Active Control of Pressure Pulsation in a Switched Inertance Hydraulic System

Pan, Min

Award date:
2012

Awarding institution:
University of Bath

Active Control of Pressure Pulsation in a Switched Inertance Hydraulic System

Min Pan

A thesis submitted for the degree of Doctor of Philosophy

University of Bath

Department of Mechanical Engineering

April 2012

ABSTRACT

The nature of digital hydraulic systems may cause pressure pulsation problems. For example, switched inertance hydraulic systems (SIHS), which are applied to adjust or control flow and pressure by a means that does not rely on dissipation of power, have noise problems due to the pulsed nature of the flow. An effective method to reduce the pulsation is important to improve system performance and increase efficiency. Although passive systems to reduce the noise have been shown to be effective in many situations, their attenuation frequency range is limited and they may be bulky. Furthermore, attenuation devices based on expansion chambers, accumulators or hoses are likely to be unsuitable for SIHS as they add compliance to the system and would impair the dynamic response. This thesis is concerned with issues relating to the development of an active noise canceller for attenuating the pressure pulsation which is caused primarily by pulsed flow from high-speed valves in SIHS.

Active control methods are widely and successfully applied in the area of structure-borne noise (SBN) and air-borne noise (ABN) cancellation. The idea is using the intentional superposition of waves to create a destructive interference pattern such that a reduction of the unwanted noise occurs. However, applications for fluid-borne noise (FBN) attenuation based on the 'Active noise control (ANC) principle' are rare due to the restriction of the hardware and experimental apparatus in previous researches.

In this thesis, an adaptive controller has been developed for active control of pressure pulsation in hydraulic system. The principle of the adaptive LMS filter and details of the controller design are described and the implementation was carried out through simulation. The designed controller was applied on a vibration test rig initially prior to the hydraulic testing in order to investigate its advantages and limitations in practice. Extensive testing on a switched inertance hydraulic rig proved that the controller, which used a piezoelectric valve with fast response and good bandwidth, is effective and that it has several advantages over previous methods, being effective for low frequency cancellation, with a quick response, and is robust and versatile.

A novel method for the accurate measurement of unsteady flowrate in a pipe was proposed. This was applied and validated on a pipe, and was shown to give good results. This method solves the difficulty for measuring the unsteady flowrate currently by using easy-measured signals, such as pressures. It can be used widely for predicting the unsteady flowrate along the pipe.

ACKNOWLEDGEMENTS

I would like to express my gratitude to all the staff of the Centre for Power Transmission and Motion Control (CPTMC) at the University of Bath who assisted in making this thesis a reality. In particular, I am grateful to my supervisors Dr. Nigel Johnston and Dr. Andrew Hillis, for their guidance, encouragement and valuable advice. Thanks are also to the technical staff of the 4E and 8E laboratories for assisting in experiments.

Many thanks go out to my friends in Bath, for their accompanying, understanding and listening to my occasional rants.

Special thanks to my parents, for their love and support.

I acknowledge the funding from the CPTMC and the Engineering and Physical Sciences Research Council for carrying out my PhD research, and the funding from the China Scholarship Council for supporting my living expenses in the UK.

This thesis is dedicated to my grandparents

CONTENTS

NOTATION

Variable	Description
A	Pipe internal cross-sectional area
A_c	Effective orifice area, switching valve closed
A_d	Amplitude of primary noise
A_{Eff}	Effective orifice area
A_L	Opening of the loading valve
A_o	Effective orifice area, switching valve open
A_{open}	Opening area of valve
A_s	Amplitude of secondary path $S(z)$
A_w	Amplitude of adaptive filter
$A(z)$	Adaptive feedforward active noise control filter
B_v	Bulk modulus in valve
B_l	Bulk modulus of pure liquid
B_t	Bulk modulus in tube
C_q	Discharge coefficient of valve
$C(z)$	Adaptive feedback active noise control filter
c	Speed of sound
$D(z)$	Z-transforms of the signals $d(n)$
d	Diameter of pipe
$d(n)$	Desired response
$\mathbf{E}(k)$	Frequency-domain block error signal
$E(z)$	Z-transforms of the signals $e(n)$
$e(n)$	Residual error signal
F	Fourier transform
F	friction term
F_c	Coulomb friction force
F_d	Sinusoidal disturbance force
F_L	System load
F_s	Cancelling force
F_v	Viscous friction force
f	Switching frequency
$H(z)$	Transfer function of the narrowband active noise control system
$I(n)$	Input of the plant $S(z)$ in time domain
i	Index
k	Number of terms in approximated friction series
L_1	Length of pipe *1*
L_2	Length of pipe *2*
l	Length of pipe
l_p	Piston stroke
M	Filter length
M_s	System mass
m	Channel index
m_i, n_i	Weighting factors in approximated friction series
nx	Divided element numbers

$O(n)$	Output of the plant $S(z)$ in time domain
P	Power spectral density of reference signal
P_A	Area of piston A
P_B	Area of piston B
P_{DF}	Delivery pressure of flow booster
P_{HP}	High supply pressure
P_{LP}	Low supply pressure
P_{SP}	Supply pressure of pressure booster
P_{RP}	Return pressure
P_i	Estimate of the average power in the *ith* frequency bin
P_t	Tank / reservoir pressure
$P(z)$	Unknown plant
$\mathbf{p}$	Cross-correlation matrix
p	Pressure
$\hat{\mathbf{p}}$	Instantaneous estimates for $\mathbf{p}$
Q	Fourier transform of flow rate
Q_c	Control flowrate
Q_{DF}	Delivery flowrate of flow booster
Q_{DP}	Delivery flowrate of pressure booster
Q_{HP}	Flowrate of high pressure supply port
Q_{LP}	Flowrate of low pressure supply port
Q_{VALVE}	Switching valve flowrate
q	Pipe flowrate
$\mathbf{R}$	Autocorrelation matrix
R	Termination impedance
R_0	Regressive wave
R_{up}	Upstream impedance
$\hat{\mathbf{R}}(\mathbf{n})$	Instantaneous estimates for $\mathbf{R}$
r	Pipe internal radius
$r_{vv}(k)$	Auto-correlation function of $v(n)$
$r_{vv'}(k)$	Cross-correlation function of $v'(n)$ and $v(n)$
$S(z)$	Secondary path dynamic
$\hat{S}(z)$	Estimated secondary path dynamic
$S(j\omega)$	Frequency response of $S(z)$
$\hat{s}_l(n)$	Estimated coefficients at time domain
$s_{vv}(z)$	Autopower spectrum of $v(n)$
$s_{vv'}(z)$	Cross-power spectrum between $v'(n)$ and $v(n)$
$\hat{s}^o(n)$	Optimum solution of $\hat{S}(z)$
t	Time
$u(n)$	Interference
V_{dA}	Dead volume of chamber A
V_{dB}	Dead volume of chamber B
V_{va}	Valve internal volume between switching orifices and inertance tube
$\mathbf{v}(\mathbf{n})$	Weight misalignment vector

$v(n)$	Zero-mean white noise
$v'(n)$	Filtered zero-mean white noise
$\hat{v'}(n)$	Estimated filtered zero-mean white noise
W	Filter tap weight
$\hat{\mathbf{W}}(k)$	Frequency-domain weight vector of block k
$\mathbf{w(n)}$	Tap weight vector
$\hat{\mathbf{w}}(k)$	Tap weight vector of block k
$\mathbf{w^o}$	Optimum filter weights vector
w_1	Weight of adaptive notch filter
w_2	Weight of adaptive notch filter
$X(z)$	Z-transforms of the signals *x(n)*
x	Switching ratio
x_f	Switching ratio of flow booster
x_p	Switching ratio of pressure booster
$\mathbf{x(n)}$	Reference input signal (vector)
$x(n)$	Reference input signal
$x_m(n)$	Reference input signal for parallel adaptive filter M
$x_0(n)$, $x_1(n)$	Reference signals for the two-weight adaptive notch filter
$\hat{\mathbf{x}}\mathbf{(n)}$	Filtered reference signal (vector)
$x_0'(n)$, $x_1'(n)$	Filtered reference signals for the two-weight adaptive notch filter
$x_{m,0}'(n)$, $x_{m,1}'(n)$	Filtered reference signals for parallel two-weight adaptive notch filter M
$Y(z)$	Z-transforms of the signals *y(n)*
$y(n)$	Output of the adaptive filter
$y'(n)$	Filtered output of the adaptive filter
z	Z-transforms
α	Frequency
β	Frequency ratio for friction terms
γ	Forgetting factor
Δt	Time step
$\delta(t)$	Impulse signal
λ	Wave length
$\lambda_{\max}$	Largest eigenvalue of the input correlation matrix **R**
μ	Convergence rate
μ	Viscosity
μ_c	Convergence rate of adaptive notch filter
μ_i	Convergence rate of fast-block LMS algorithm in the *ith* frequency bin
μ_i	Convergence rate of identification filter
$\xi(n)$	Expected value of mean-square error (MSE) / MSE cost function
$\hat{\xi}(n)$	Instantaneous estimate of the cost function ξ(n)
ρ	Density
ϕ_d	Phase of primary noise

ϕ_s	Phase of secondary path $S(z)$
ϕ_w	Phase of adaptive filter
ϕ_Δ	Phase difference between $S(z)$ and $\hat{S}(z)$
ω	Natural frequency
ω_0	Frequency of reference signal

1 Introduction

1.1 Fluid-borne noise

Fluid-borne noise (FBN) is caused primarily by unsteady flow from pumps and motors and the instability and cavitation of valves (Skaistis, 1988). Hydraulic motors may sometimes produce significant noise; the mechanism of noise generation is similar to that of pumps. The most obvious form of noise is air-borne noise (ABN), which can be detected by the ear directly. However, machines also produce structure-borne noise (SBN), which is vibration of components and mounting. Also SBN could arise as a result of unsteady forces caused by FBN (Hughes, 1981) .

FBN takes the form of pressure ripples or fluctuations in the fluid, and results in structure-borne noise (SBN) and air-borne noise (ABN). It can be propagated long distances along fluid pipelines, transmitting the noise from the pump or motor to various parts of the hydraulic system. Figure 1.1 shows the transmission of FBN, SBN and ABN of in a typical system with a pump source.

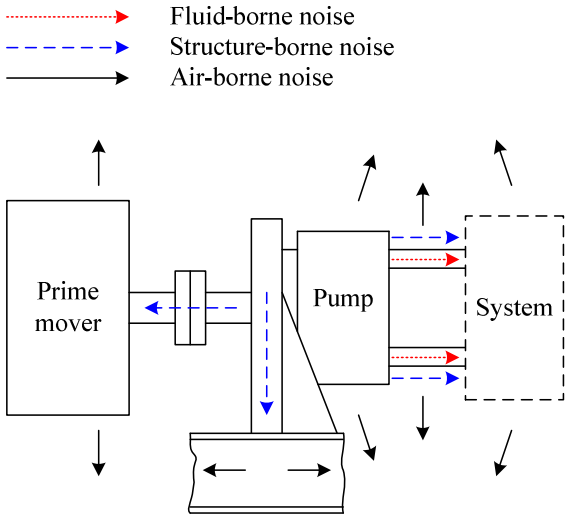

Figure 1.1 Transmission of pump source (Hughes, 1981)

Unexpected vibration is known to be potentially degrading to the stability and performance of system. Therefore, the attenuation of FBN has a significant effect on the

hydraulic system, as well as a potential cancellation of the noise source of SBN and ABN.

Hydraulic system noise can be also be important a number of other areas, notably in transport and mobile machinery. For example, hydraulic circuits in submarines can produce low frequency noise which can be transmitted great distances through the ocean and be detected by hostile surveillance systems. At the other extreme, automotive power steering systems employ simple hydraulic circuits which can cause substantial noise unless great care is taken in their design (Johnston, 1987)

1.2 Principle of active noise cancellation

A general theory of interference of waves, which was employed for active noise cancellation, was proposed by Huygens in 1690. The active noise control (ANC) system uses the intentional superposition of acoustic waves to create a destructive interference pattern such that a reduction of the unwanted noise occurs.

Figure 1.2 shows the waveforms of the primary unwanted noise, secondary antinoise, and residual noise that result when they are superimposed. The amount of primary noise cancellation depends on the accuracy of the amplitude and phase of the generated antinoise.

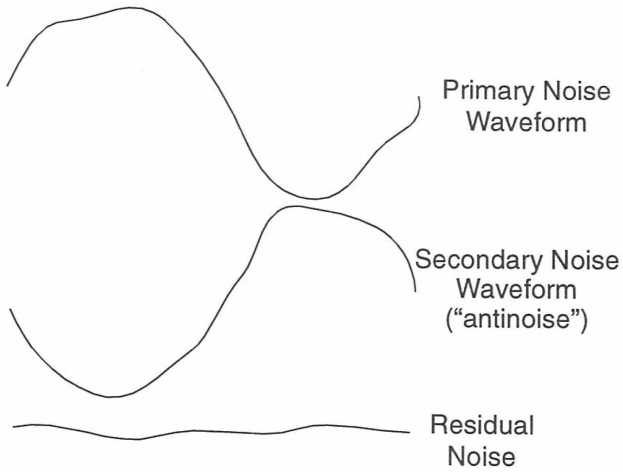

Figure 1.2 Physical concept of active noise cancellation (Kuo and Morgan, 1995)

Based on Huygens' principle, the design of acoustic ANC utilizing a microphone and an electronically driven loudspeaker to generate a cancelling sound was first filed in a 1936 patent by Lueg (1936). Since the characteristics of the acoustic noise source and the environment are time varying, the frequency content, amplitude, phase, and sound velocity of the undesired noise are nonstationary.

An ANC system must therefore be adaptive in order to cope with these variations. Adaptive filters adjust their coefficients to minimize an error signal and can be realized as transversal finite impulse response (FIR), infinite impulse response (IIR), lattice, and transform-domain filters (Haykin, 1996). The most common form of adaptive filter is the transversal filter using the least-mean-square (LMS) algorithm.

1.3 Fluid-borne noise cancellation

There are several established methods for reducing FBN in hydraulic systems. Generally speaking, these can be categorized as either active or passive.

1.3.1 Passive control of fluid-borne noise

There are several passive control methods which can be used to reduce the FBN level in hydraulic system. Normally, these can be categorized as follows (Henderson, 1981)

- Reduction of pump or motor flow ripple
- Tuning of the circuit in order to avoid resonant conditions
- Use of a silencer or pulsation damper
- Use of flexible hoses and accumulators

By reducing the pump or motor flow ripple, the pressure ripple is reduced at source. However, the pump or motor flow ripple can not normally be changed by the user except by changing its operating conditions. For example, the ripples can be reduced by using low pressure supply but this is not usually a practical solution.

Selection of a different pump with less flow ripple may be a solution to a noise problem. For instance, internal gear pumps and screw pumps generally produce low flow ripple; and external gear pumps and axial piston pumps normally generate high flow ripple. However, it is rarely possible to select a particular class of pump purely based on the

noise characteristics or attenuation in practice and the cost and other characteristics must be considered as well. Table 1.1 shows the comparative noise level of typical pumps.

Table 1.1 Comparative noise levels of typical pumps (Taylor, 1981, CPTMC fluid power course, 2009)

Noisiest	Axial piston pumps
:	External gear pumps
:	Vane pumps
:	Internal gear pumps
Quietest	Screw pumps

In the method of tuning of the overall hydraulic system, ripples are reduced by using the system anti-resonant conditions. In these conditions, the reflected pressure waves effectively cancel out the original pressure wave. The length of the pipe of system would highly affect the resonance and anti-resonance conditions. Therefore, this method requires a smart system design and good knowledge of the relationships between the circuit configuration and FBN.

Using FBN silencers or pulsation dampers is another option for cancelling FBN. It has been proved that the flow ripple reduction can be reached to 20dB to 40dB with the right fixing and usage of the noise silencers (Johnston and Edge, 1989). However a specialised silencer tends to be expensive, bulky and heavy.

Using an accumulator, the gas volume acts as a capacitor or spring, and the fluid in the neck as an inductor or mass. The gas volume and the tuning depend on the pre-charge pressure and the mean pressure and it may be ineffective as a silencer in conditions of varying pressures. Flexible hose is often a convenient and cost-effective method of reducing FBN and SBN. Because of the inherent energy dissipation of the rubber and reinforcement, the hose can be used as a device for noise attenuation. Also it can behave like a volume resonator due to its flexibility. A suitable length of flexible hose could be fitted close to the noise source to cancel the pressure pulsation in the system, however, this is usually ineffective for pressure ripple cancellation under 2 kHz (Guidelines for the Design of Quiet Hydraulic Fluid Power Systems,, 1977, Tilley, 1981)

1.3.2 Active control of fluid-borne noise

In active FBN control the pressure ripple is sensed and an anti-phase signal generated to cancel the original ripple. This is based on the principle of wave superposition which has been successfully implemented in ABN and SBN cancellation. However, applications for FBN attenuation based on the 'Active noise control (ANC) principle' are rare, although Klees filed for a patent in 1967 to introduce this principle for attenuating the periodic motion in a fluid conduit (Klees, 1967). Due to the restriction of the hardware in 1960s, the experimental results were promising but with limitations.

The active noise control methods used to reduce the FBN level in hydraulic system can be summarised as:

- Estimating and cancelling the progressive wave along the pipe (Kojima et al., 1993).
- Applying the adaptive LMS algorithm for noise cancellation (Franz and Larsen, 1996, Huebner, 1996, Phillips, 1996, Maillard et al., 1999, Horne and Hansen, 1982, Wang, 2008).

Details can be found in section 2.2.2.

1.4 Switched inertance hydraulic systems

In most fluid power hydraulic systems, the speed and force of a load are controlled by using valves to throttle the flow and dissipate the hydraulic pressure or reduce the flowrate. This is a simple but extremely inefficient method as the excess energy is lost as heat. A switched inertance hydraulic system is one of the alternative methods which can provide varied flow and pressure by a means that does not rely on dissipation of power (Brown, 1988, Johnston, 2009)

The modes of the switched inertance hydraulic system can be configured:

- The flow booster configuration;
- The pressure booster configuration.

Normally the flow booster or pressure booster consists of a high-speed switching valve with one common port and two switched ports and a long, small diameter 'inertance' tube. The principles and operation details of the two structures can be found in Chapter 6.

Ideally if the noise issues and some other practical problems of the switched inertance hydraulic system can be overcome, the device could potentially provide very significant reduction in power consumption over conventional valve controlled systems (Brown et al., 1988, Brown, 1988, Johnston, 2009). However, the noise problem may be an issue in practice due to the pulse nature of the flow.

1.5 Objectives of the research

The main objective of the research was to develop and design a noise controller for attenuating the FBN in hydraulic system. The active control method was selected and implemented in the controller. The proposed controller should be able to attenuate the FBN effectively in both a conventional and a digital hydraulic system.

The second objective was to implement the proposed controller experimentally. A vibration test rig was to be used for the initial studying of the controller performance and a switched inertance flow booster was planned for the further investigation of the controller for it being applied on a hydraulic system.

The third objective was to create an effective method to measure unsteady flowrate for analysing the flow ripple in hydraulic system. Currently it is difficult to find a simple method to estimate dynamic flowrate which is an important parameter for system studying. The proposed method should be able to predict the unsteady flowrate by using some easily measured pressure signals.

The following requirements were also considered:

- The controller must be able to attenuate the FBN to an acceptable level.
- The controller should adapt rapidly with an efficient control algorithm.
- The controller must be robust and stable in operation.
- The controller must be able to work under different working conditions of the switched inertance hydraulic system, such as different switching frequencies, changing switching ratios and varying loads.
- The unsteady flowrate measurement method should be able to estimate the flowrate effectively and accurately, although currently it is hard to find an effective method for comparison.

1.6 Scope of the thesis

Chapter 1 provides an introduction of FBN attenuation and the problem encountered. An overview of the FBN characteristics of hydraulic systems, the general methods for FBN attenuation and the overall objectives of the research are presented.

Chapter 2 presents a literature review of active noise control systems. Feedforward, feedback and hybrid control structures are discussed. The current applications for FBN attenuation are studied together with the effects from the control algorithm and system.

Chapter 3 presents the detailed theory and principle of the adaptive LMS filter. The basic theoretical background is provided and the LMS implementation for active noise control is investigated through simulation studies. A controller based on the notch filter is developed for a narrowband noise cancellation. The LMS offline and online identification and the fast block LMS online identification techniques are discussed for their advantages and limitations.

Chapter 4 describes experimental work of active vibration cancellation. The controller was applied on a vibration test rig prior to the flow booster testing in order to investigate its performance beforehand. Experience was gained and specific considerations were discussed for the further implementation for FBN cancellation based on the flow booster rig.

Chapter 5 presents the implementation of an ANC system for FBN attenuation based on a typical pump-pipe-load hydraulic system simulation by using the designed controller. The dynamics of the secondary path was investigated based on the theoretical analysis and simulations. The impulse responses with different system boundary conditions were considered. With the accurate characteristics of the secondary path, the single harmonic and multiple harmonics of FBN cancellation were applied in simulation. The stability analysis related to the changing loading condition was discussed on the basis of simulated results.

Chapter 6 describes the principle of operation of switched inertance hydraulic systems (SIHS). The system can be configured as a flow booster or a pressure booster consisting of a fast switching valve and an inertance tube. Using this system, flow and pressure can

be varied by a means that does not rely on dissipation of power. The implementation of switched inertance systems was investigated through simulation. Moreover, the method for unsteady flowrate measurement was initially validated in experiments. It provides an accurate and effective way to estimate the flow ripple along a hydraulic pipe. This is very useful for analysing the system dynamic flowrate for pressure pulsation cancellation.

The implementation of pressure pulsation cancellation based on a flow booster using the designed controller is investigated within two system arrangements, as the by-pass structure and the in-series structure, in chapter 7. The performance of the controller is studied with the application of the single harmonic and multiple harmonics cancellation of FBN. Also the system stability and robustness are discussed in terms of the switching frequency, switching ratio and load of the flow booster. Finally a comparison between the advantages and disadvantages of the by-pass and in-series structures is presented.

The results of experimental studies using the flow booster rig are presented in chapter 8. The controller is initially tested on the switched inertance hydraulic system. The performance of the controller is validated for single frequency and multiple frequencies cancellation of pressure pulsation. The robustness is investigated when the flow booster operated in different working conditions.

Finally, chapter 9 includes a discussion of the work conducted and conclusions regarding the effectiveness and robustness of the control strategy. Recommendations for future work are also included.

2 Literature review

2.1 Active noise control system

Noise problems become more and more evident as increased numbers of large industrial equipment such as engines, blowers, fans, transformers, hydraulic pumps and compressors are in use.

Noise need not be limited to air; underwater or hydro-acoustic noise is a problem in certain marine settings and could also arise in laboratory instruments and ultrasonic medical scanning applications (Fahy, 2001). The traditional approach to acoustic noise control used passive techniques such as enclosures, barriers, and silencers. For hydraulic systems, these passive silencers are valued for their high attenuation over a range of frequencies; however, they are relatively large, costly, and may be ineffective at low frequencies (Henderson, 1981).

Active noise control (ANC) involves an electroacoustic or electromechanical system that cancels the primary (unwanted) noise based on the principle of superposition; specifically, an antinoise of equal amplitude and opposite phase is generated and combined with the primary noise, thus resulting in the cancellation of both noises. An ANC system may efficiently attenuate low-frequency noise where passive methods are either ineffective or tend to be very expensive or bulky. ANC is developing rapidly because it permits improvements in noise control, often with potential benefits in size, weight, volume, and cost. Thus, application of the ANC technique is a modern supplement to conventional passive systems (Akhtar et al.). Based on the ‘ANC principle’, many works have been done successfully on the implementation for ABN and SBN cancellation, but few on FBN attenuation.

2.1.1 Control algorithm

2.1.1.1 Least mean square (LMS)

The LMS algorithm is a well-known and widely used algorithm in the stochastic gradient algorithms family. This algorithm is applied to mimic a desired filter by finding the filter coefficients that relate to producing the least mean squares of the error signal (difference between the desired and the actual signal). Widrow (1971) proposed using the instantaneous squared error instead of using the steepest descent method (Goldstein, 1965) to estimate the mean-square error. It is simple and does not require squaring, averaging or differentiating. It is a stochastic gradient descent method in that the filter is only adapted based on the error at the current time.

2.1.1.2 Filtered-X LMS (FXLMS) algorithm

The Filtered-X LMS (FXLMS) algorithm was independently derived by Burgess (1981) for ANC applications and Widrow (Widrow et al., 1981) in the context of adaptive control. It effectively solved the effect of the secondary path transfer function $S(z)$ from the output of the adaptive filter $y(n)$ to the residual error signal $e(n)$, as shown in Figure 2.1. The unknown plant $P(z)$ and the adaptive filter $W(z)$ are assumed to be driven by the same input $x(n)$, which is also used as the reference signal of the adaptive filter $W(z)$. The output of the plant $d(n)$ is the primary noise of system and the desired response for the adaptive filter. The objective of the adaptive filter $W(z)$ is to minimize the $e(n)$ by superimposing $d(n)$ and the control signal $y'(n)$ (Kuo and Morgan, 1999). With the FXLMS algorithm, the secondary path effect $S(z)$ can be eliminated ideally by placing an identical filter in the reference signal path to the weight update of the LMS algorithm. The filtered reference signal $x'(n)$ is generated by passing the reference signal through the estimated impulse response $\hat{S}(z)$ of secondary path. The block diagram of an ANC system using the FXLMS algorithm is illustrated in Figure 2.2.

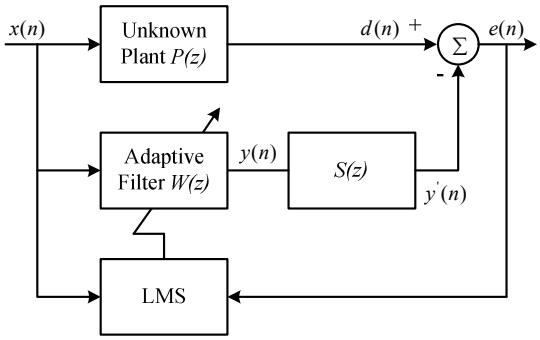

Figure 2.1 Simplified block diagram of ANC system (Kuo and Morgan, 1999)

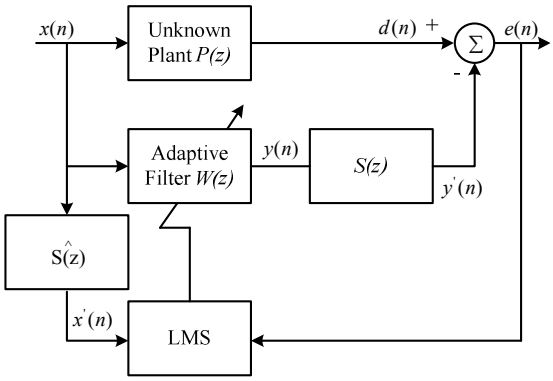

Figure 2.2 Block diagram of ANC system using the FXLMS algorithm (Widrow et al., 1981)

2.1.2 System structure

ANC is based on either a feedforward or feedback control structure. In feedforward control, a coherent reference signal detected before it propagates past the secondary antinoise (Kuo and Morgan, 1995); in feedback control, the noise attenuator attempts to cancel the noise without the benefit of a reference input (Olson and May, 1953).

2.1.2.1 Narrowband feedforward ANC system

Noise can be broadband or narrowband, which are named based on the noise energy distribution with frequency. Broadband noise is totally random and distributes its energy evenly across the frequency band, while narrowband noise concentrates most of its energy at a specific frequency or frequencies.

In a narrowband feedforward ANC system, the reference signal can be generated by measuring the fundamental frequency of the primary noise source from nonacoustic sensors, such as a tachometer in the case of rotary machine. This has the advantage of eliminating the feedback effects from the cancelling actuator back upstream, compared with using a pressure sensor for measuring the reference signal. The disadvantage is that the reference signal only tracks frequency, changes in primary noise amplitude are not tracked, so the system has to re-adapt when this happens. A block diagram of a narrowband feedforward system for ANC in a duct is shown in Figure 2.3 (Kuo and

Morgan, 1999), where the canceller controls primary noise by adaptively filtering x(*n*) with an effective control algorithm to provide antinoise for cancellation.

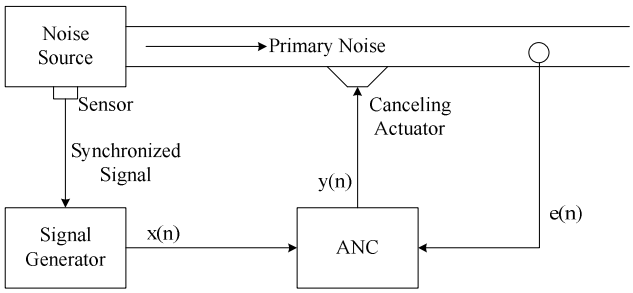

Figure 2.3 Single channel narrowband feedforward ANC system (Kuo and Morgan 1995)

Moreover, the use of an internally generated reference signal makes it capable of controlling each harmonic selectively and independently. This is because the estimated sinusoidal reference signals can be produced independently based only on the system fundamental frequency. Also many papers indicate that a lower order FIR filter could be applied by only modelling the secondary path transfer function over frequencies where harmonic tones exist in the system (Kuo and Morgan, 1995). Figure 2.4 shows a general solution for noise attenuation using a feedforward control structure.

The adaptive notch filter offers a simple narrowband noise control by using an internally generated sinusoidal reference signal. It can track the time-varying frequency of the narrowband noise effectively (Widrow et al., 2005). The use of single-frequency adaptive notch filters for ANC applications has been proposed in (Elliott et al., 2003) and they were found to be very robust. A block diagram of a single-frequency adaptive notch filter for narrowband noise cancellation is illustrated in Figure 2.4.

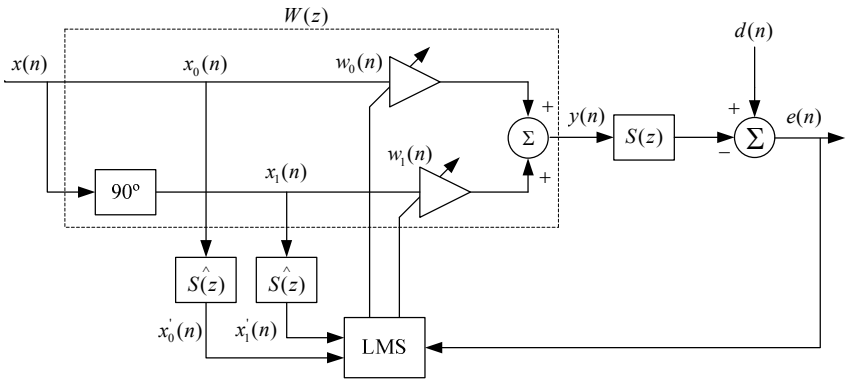

Figure 2.4 Single-frequency ANC system using FXLMS algorithm (Elliott et al., 2003)

Two sinusoidal waves $x_0(n)$ and $x_1(n)$ are used as reference signals for the two-weight adaptive notch filter and the control signal $y(n)$ is summed from the weighted reference inputs. The filter coefficients were updated on the basis of the LMS algorithm with the inputs of the residual error $e(n)$ and filtered-reference signals $x_0'(n)$ and $x_1'(n)$.

2.1.2.2 Narrowband feedback ANC system

Different from the feedforward ANC system, Olson and May (1953) proposed a nonadaptive feedback system from their "electronic sound absorber (ESB)" application. This device provides limited broadband noise attenuation over a limited frequency range. However, the feedback ANC has been explored and improved based on the encouraging results from the ESB (Eghtesadi et al., 1983, Hong et al., 1987, Dekker et al., 1989, Radcliffe and Southward, 1993, Hong et al., 1996).

In the meantime, the accelerating interests in feedback ANC began in the one-dimensional duct noise control. The concept of duct noise attenuation is illustrated in Figure 2.5. The error sensor signal $e(n)$ is returned back through a feedback ANC controller to produce attenuated signal $y(n)$ using as the secondary source. The primary noise can be attenuated through the implementation of very high loop gain (Kuo and Morgan, 1995). A narrowband feedback ANC system is more simply applied because the reference signals can be obtained from the output of an error sensor due to the predictable characteristics of the narrowband signal itself (Kuo and Morgan, 1999).

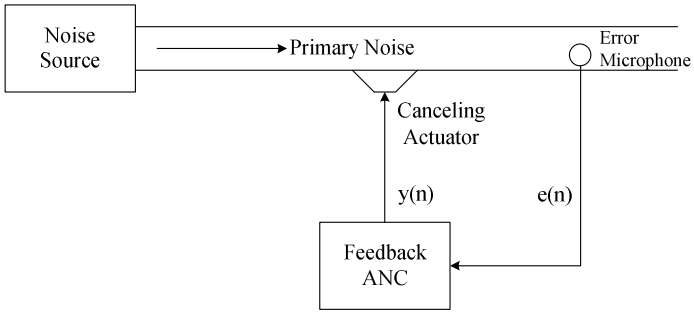

Figure 2.5 Single-channel feedback ANC system (Kuo and Morgan 1995)

It was realized that the adaptive feedback ANC system has the ability to attenuate low-frequency noise, especially when an internal reference signal is difficult to sense or generate (Kuo and Morgan, 1995). A single-channel adaptive feedback ANC was proposed by Eriksson (1991) as shown in Figure 2.6, where the secondary-path estimate $\hat{S}(z)$ is used to synthesize the reference signal $x(n)$ and to compensate for the effect of the secondary path. In fact, the reference signal is based also on the adaptive filter output $y(n)$ and error signal $e(n)$ in feedback control system.

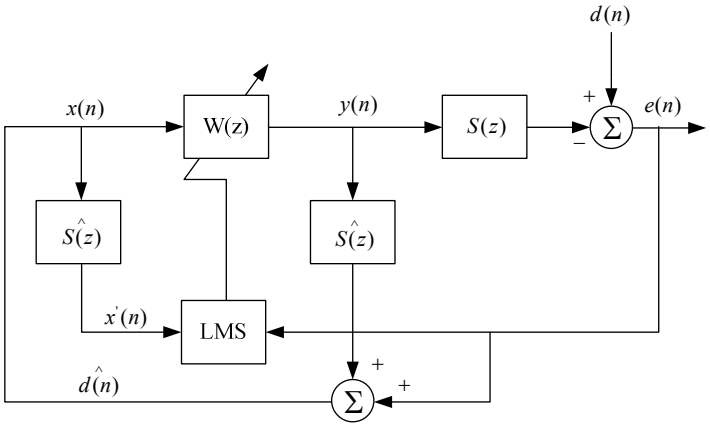

Figure 2.6 Adaptive feedback ANC system using FXLMS algorithm (Kuo and Morgan 1995)

The robustness of the adaptive feedback controller can be considered using a generalization of the complementary sensitivity function (Elliott and Sutton, 1996). The H_∞ control theory (Morari and Zafiriou, 1989) allows the design of feedback controllers to have an optimum tradeoff between giving good performance at required range of frequencies and ensuring robust stability to an assumed plant uncertainty. An alternative approach to the design of a robust feedback controller would be to gradually increase

some system parameters which could be adjusted to make the system less sensitive to plant changes (Elliott and Sutton, 1996).

Studies of the limitations of feedback in ANC have been presented by Hong and Bernstein (1998) and Freudenberg (2003) based on conventional feedback loops. In general terms, good performance requires a high loop gain, whereas robust stability requires a lower loop gain. With regard to the variation with delays in the plant in ANC system, the potential performance of the feedback control system was better than that of the feedforward system (Elliott and Sutton, 1996). Since the undesired noise is highly correlated with the estimation of secondary path, the filter for on-line identification must be inhibited when the ANC system is in operation (Kuo et al., 2010). Therefore, the development of effective on-line feedback-path modelling techniques requires further research.

2.1.2.3 Hybrid ANC

The hybrid ANC system is a combination of the feedforward and feedback control structures as shown in Figure 2.7 (Swanson, 1989). The reference sensor is set at the upstream end close to the noise source to produce a coherent reference signal for the feedforward ANC system. Sinusoidal signals synchronised with the noise source can be applied as reference inputs in a narrowband noise control system. The error sensor is placed downstream measuring the residual noise, which is used to synthesize the reference signal for the adaptive feedback ANC filter. The major advantage of hybrid ANC is the primary noise related frequency components and the predictable components in the system can both be considered in the control process. In other words, the feedforward ANC cancels undesired noise that is correlated with the reference signal, whilst the feedback ANC attenuates the predictable components of the primary noise that are not effectively detected by the reference sensor. Moreover, a lower order filter can be applied in hybrid ANC for cancellation compared with the filter used both in purely feedforward and feedback ANC systems.

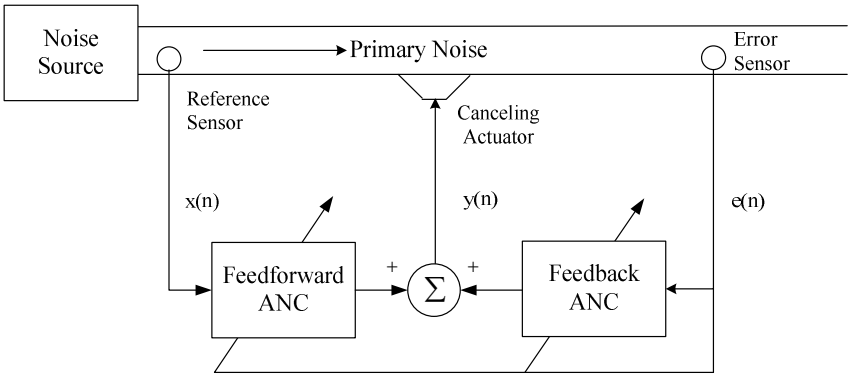

Figure 2.7 Hybrid ANC system (Swanson, 1989)

A block diagram of a hybrid ANC system using a FIR feedforward ANC with the FXLMS algorithm is illustrated in Figure 2.8, where a FIR feedforward ANC filter $A(z)$ and the adaptive feedback ANC filter $C(z)$ are combined for generating the anti-noise signal $y(n)$. The noise controller $W(z)$ is normally composed of filters $A(z)$ and $C(z)$. $A(z)$ is adapted on the filtered reference input from the reference sensor, whilst the feedback ANC filter $C(z)$ is adapted on the filtered estimated primary signal $\hat{d}(n)$. In a narrowband ANC system, the reference signal $x(n)$ can be substituted for a sinusoidal signal.

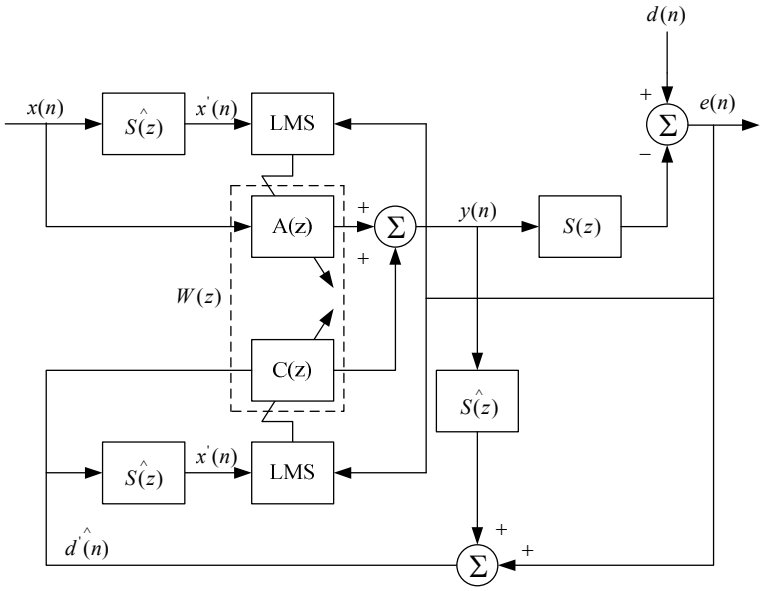

Figure 2.8 Hybrid ANC system using the FIR feedforward ANC with the FXLMS algorithm (Kuo and Morgan, 1995)

When the location and directivity of the primary noise are unknown, the hybrid ANC system performs more effectively than the feedforward or feedback controller alone

(Tseng et al., 1998). The optimum hybrid ANC controller introduced in their work has good robustness for the plant uncertainty using the technique of internal model control (IMC) and Wiener filter. Alasty et al (2002) researched hybrid ANC systems in ducts. Compared with feedforward control, the hybrid ANC controller could produce lower residual error and higher convergence rate.

The non-minimum phase (NMP) path is a problem encountered when applied to hybrid ANC system in practice. It makes it difficult to design both feedforward and feedback controllers (Yuan, 2004). The problem can be solved effectively by arranging an extra actuator to compensate the feedback damping. At the same time, it could decrease the sensitivity of the controller to uncertainties in the path models.

As the FXLMS algorithm is widely used in both feedforward and feedback control system, it is also an effective choice for use in hybrid ones. A Lyapunov-tuned LMS feedforward filter with a digital feedback system for hybrid controller was developed by Streeter (2005). The results show that the controller has considerably better noise reduction and stability at the expense of computational effort, compared with a conventional FXLMS noise attenuator. As discussed in purely feedforward and feedback ANC control, the characteristic of the secondary path has a great effect on system stability and robustness.

A hybrid ANC system which is composed of an online secondary path identification part and an acoustic feedback controller was proposed by Lopez (2010). With the help of the online secondary path estimator, the controller could be more effective when subjected to varying secondary plant and primary noise. It also was found that the hybrid system performs better in noise attenuation than the sum of independent feedforward and feedback systems at low frequencies.

2.2 Application of active control to fluid borne noise

A single-channel feedforward ANC system is ideal for one-dimensional ducts or pipework noise attenuation. The FXLMS and filtered-U recursive LMS algorithms are widely and effectively used in ANC system in ducts. In this section, firstly ANC in air

ducts will be studied. The review of some ANC applications in filled pipe systems follows, and finally the techniques of FBN attenuation are discussed

2.2.1 Air ducts

The control of noise in air ducts has received a considerable amount of attention. Snyder and Hansen (1989) presented an analytical plane-wave model for finite size realistic sources in a duct. In their work, an analytical model has adequately described the acoustic mechanism involved in power flows associated with primary and control waves in ducts. The effects of source strengths, numbers, and arrangements of anti-noise source have also been given based on overall system performance.

A feedback controller was developed for global ANC in a one-dimensional hard-walled acoustic duct (Radcliffe and Southward, 1993) with a partially dissipative boundary condition. The state-space controller effectively reduced noise levels globally rather than at a single location in duct. The state-space control technique is necessitated by the high order of the identified model (Hong et al., 1996). A modified feedback controller is introduced by applying linear quadratic Gaussian (LQG) synthesis with suitable pre-compensation to eliminate the instability of high-frequency uncertainty.

Regarding system robustness, Bai (1997) has compared feedforward and feedback ANC system for ducts, and a good feedback ANC system was developed with a reasonably accurate linear time-invariant (LTI) model for the acoustic plant. However, besides modelling errors, the variations of physical conditions, such as damping, viscosity, and temperature and radiation impedance may also result in disturbance in the duct, so that plant uncertainty became a potential problem which affects the stability and robustness directly (Bai and Lin, 1998).

The noise itself, which often arises from dynamical systems in many practical applications, could be nonlinear and deterministic or stochastic. The performance of linear ANC system would be degraded under this situation, so that nonlinear active controllers might be required in cases where the actuators used in ANC systems exhibit nonlinear characteristics (Strauch and Mulgrew, 1998, Bouchard et al., 1999, Efe and Kaynak, 2000, Tan and Jiang, 2001).

Recent studies have been focused on the robust control aspects of ANC in ducts. The H_∞ control theory provides an efficient way to design a robust controller with achievable performance and good robustness. Lin (2002) proposed a method using linear quadratic Gaussian (LQG) control with an H_∞ approach for a robust ANC design of a one-dimensional acoustic duct. Some experimental results of LQG control were presented by Petersen and Pota (2002). Application of a H_∞ hybrid active controller which is designed by frequency domain methods is presented by Wu (2005). With the introduction of hybrid systems and H_∞ theory, the system robustness to disturbances and plant uncertainties has been improved. The stability of closed loop feedback ANC in a duct system has also been considered with the effects of the dynamics of time-delay systems (Haraguchi and Hu, 2009). A delay differential equation was introduced for analyzing stability and the optimal distance between secondary path actuator and error sensor was obtained.

2.2.2 Fluid-filled pipe

In 1967, Klees filed for a patent for introducing the principle of destructive interference to attenuate the periodic motion in a fluid conduit (Klees, 1967). This may be the first 'ANC concept' that was applied to cancel noise in a fluid. After that, Crouse presented an active attenuation system which can be used for attenuating pressure pulsation in a liquid flowing in a pipe (Crouse, 1988). An actuator was introduced in this system for generating pulsation in the pipe in order to attenuate the pressure pulsations.

Kojima proposed an active noise attenuator for FBN in filled-fluid piping systems, and good experimental results were achieved (Kojima et al., 1993). The basic principle of this method is using an upstream real-time progressive wave signal to generate an anti-phase wave to attenuate the flow ripples by using the concept of wave superposition. This method is highly relied on the accuracy of the real-time progressive wave. The dynamic flowrate was estimated by using finite difference approximations using pressure which required the measuring transducers to be close together, limiting the bandwidth and the accuracy. Moreover, wave propagation and unsteady friction effects are not considered in the calculation. This may cause inaccurate flowrate estimation, easily resulting in system instability. An alternative technique for estimating the unsteady flowrate is using a wave propagation model (Johnston and Pan, 2010) which

has no restriction on the bandwidth and transducer spacing. Unsteady friction is also considered. More accurate estimated flowrate can be achieved by using this method, which could be used as an enhancement to Kojima's method.

In the mid-1990s, many applications and apparatuses have been proposed for the purpose of FBN cancellation using ANC method (Franz and Larsen, 1996, Huebner, 1996, Phillips, 1996). Maillard studied the active control of pressure pulsation in piping system where the FXLMS was used as the control algorithm (Maillard et al., 1999). The design and testing of a non-intrusive fluid wave actuator for the control was presented in this report and considerable cancellation results (about 20dB) were achieved. Horne and Hansen (1982) and Wang (2008) also successfully applied the adaptive FXLMS algorithm to attenuate the periodic noise produced by pumps in piping system. The structure was based on the feedforward control system. It has been proved that the FXLMS algorithm with an estimated secondary path $S(z)$ could attenuate the FBN in a simple hydraulic system. However, the validation was based on a servovalve as an anti-noise actuator. It limited the cancellation to the low frequency range. Also the servovalve is sensitive to contamination.

2.3 Practical problems

2.3.1 Effects of secondary path

Off-line modelling can be used to estimate secondary path dynamics during the initial training stage for most ANC applications. However, on-line modelling may be required for some practical applications which involve fast changing conditions.

For the on-line modelling technique, the accuracy of the estimated secondary path model is significant for system stability and robustness (Eriksson and Allie, 1989). Boucher and Elliott (1991) studied the effect of convergence speed on phase errors in $S(z)$ identification. It can be concluded that the limit for convergence of noise attenuation is when the phase error in the secondary path model is approximately 90º. This is because the poles of the secondary transfer function come closer to the unit circle. Moreover, the convergence and stability of the system becomes dependent on the calculation delay for phase errors beyond 70º. When the phase error is less than

approximately 45º, the filter is relatively unaffected. For narrowband signals, errors in the estimation of the secondary path transfer function can be considered as amplitude errors and phase errors respectively (Snyder and Hansen, 2002). The power of the filtered reference signal is changed proportionally with the amplitude error and algorithm convergence rate is affected by the phase error in the range of ±90º.

Kuo and Vijayan (1997) proposed a method to eliminate interference during online modelling of secondary path. An optimized adaptive prediction error filter is introduced with delays which are dependent upon the harmonics of the undesired noise and upon the identification filter. It is effective for compensating the modelling error in the case of narrowband noise cancellation. Many researchers focused on the approaches of compensating or eliminating the modelling error to achieve a better performance and faster convergence by adding extra filters for error compensation (Zhang et al., 2001, Zhang et al., 2003, Lan et al., 2002b, Lan et al., 2002a, Akhtar et al., 2004, Akhtar et al., 2005, Akhtar and Mitsuhashi, 2009) and modifying the LMS algorithm which is used for identification (Akhtar, Abe et al. 2004; Akhtar, Abe et al. 2005; Akhtar and Mitsuhashi 2009)

There may also be computation and measurement errors and system uncertainties. The IMC (Tseng et al., 1998, Kaiser et al., 2003, Lin and Luo, 2002) and H_∞ optimal control (Bai and Lin, 1997, Bai and Lin, 1998, Petersen and Pota, 2002, Wu and Lee, 2005, Yuan, 2003) have been successfully applied in the design of robust ANC systems in ducts. Both simulated and experimental results show these approaches are effective for noise cancellation with plant uncertainties.

2.3.2 Frequency mismatch

In many practical applications, the frequencies of the internally generated reference sinusoidal signal may be different to the actual frequencies of primary noise due to the time-varying characteristics of noise sources and the frequency measurement hardware or algorithm. This frequency difference is referred to as frequency mismatch (FM) in narrowband ANC systems (Xiao et al., 2004b, Sakai and Hinamoto, 2005). FM could degrade the performance of ANC systems even if there is just a small frequency difference.

According to previous research, the performance of an ANC system using the FXLMS algorithm degrades noticeably for FM of 1%. In order to eliminate the FM effect, a robust narrowband ANC system, which is composed of an magnitude phase adjustment (MPA) and the FM compensator, was proposed by Xiao (2004b). This makes it possible to remove the FM effects with an acceptable expense of computation. The dynamics of the narrowband ANC systems with the FM and the steady-state performance were analysed for the real-valued sinusoidal signals using the averaging technique (Xiao et al., 2004a). Sakai and Hinamoto (2005) analysed the LMS algorithm with tonal reference signals based on the adaptive noise control system. The equivalent transfer function technique (Glover Jr, 1977) was also used for the investigation of FM effects for FXLMS algorithm with sinusoidal reference signals (Hinamoto and Sakai, 2007).

Further research has focused on the area of FM and improved control algorithms for fast convergence and superior robustness. A fast filtered-X RLS (FXRLS) algorithm (Xiao et al., 2005) was modified to compensate for the effects of FM by incorporating a second-order AR model which is updated by using an LMS or RLS algorithm. Compared with a conventional FXLMS algorithm, the FXRLS-based ANC system was found to be more robust for the system being subjected to the FM. This method effectively improves the system performance with FM in reference signal. But the RLS algorithm requires of the order of L^2 operations where L is the order of the filter, and it is more complex than the FXLMS algorithm.

The applications of narrowband ANC with FM effects have also been considered practically. Kuo and Nallabolu analysed the frequency error in electronic mufflers when using an internally synthesized reference signal in the system (Kuo and Nallabolu, 2007). They explained that the worst performance of noise reduction results from increased FM in terms of the steady-state transfer function of the controller from the primary noise to the residual noise.

Jeon and Chang (2010) presented the robustness of a narrowband ANC system. This research investigated the effects of FM combined with the phase error of the estimated secondary-path model. It was the first attempt to consider the overall effects for the active periodic noise cancellation. Before their work, many papers (Hinamoto and Sakai, 2007) considered FM for an ANC system with the ideal secondary-path transfer

function and also considered convergence analysis without considering FM effect (Hinamoto and Sakai, 2005).

FM is a new consideration in the narrowband ANC system in recent years. Many promising results have been achieved both from the theoretical analysis and lab experiments with the consideration of FM. However, effective solutions still remain to be developed for practical applications.

2.3.3 Nonlinearities

Nonlinearities in the system may degrade the performance of a linear ANC method in a practical system. In fact, the noise generated from a dynamical system and the secondary path of an ANC system may both exhibit nonlinear characteristics. The linear techniques used to attenuate such noise may exhibit degradation in performance, and hence yield poor control accuracy and stability both of the identification of secondary-path and primary noise cancellation.

A feedforward neural network (NN) using active adaptive algorithm was successfully applied for linear and nonlinear vibration systems by Snyder and Tanaka (1995), where two NN were implemented: one was applied as a controller and the other one was used for modelling the cancellation path transfer function. The NN controller is able to compensate for the introduction of harmonics by the secondary-path actuator and distorted reference signal. However, the consistency and predictability of the system cannot be clearly demonstrated by using this nonlinear NN controller. A combined linear and nonlinear model was implemented for active nonlinear noise control in a linear duct (Strauch and Mulgrew, 1998). The controller exploits the predictability of the input signal to eliminate the effects of using a nonminimum phase actuator as secondary path. However, based on this combined structure, problems appeared for filter convergence speed and system computation load. In order to avoid these problems, an improved training of the NN was proposed (Bouchard et al., 1999) by introducing a novel heuristical algorithm for the same NN control structure. The simulation results show that a faster convergence speed was achieved by the use of nonlinear recursive-least-squares techniques and a lower computational load was obtained.

One of the disadvantages in the artificial NN training process is the lack of stabilizing forces, the existence of which prevents the unbounded growth in the adjustable parameters. This fact is closely related to the internal dynamics of the trainning strategy (Efe and Kaynak, 2000). A combination of the error back propagation (EBP) with variable structure system (VSS) was implemented to adjust parameters to achieve a steady state solution for system stability. In the mean time, the FXLMS based NN structure for nonlinear ANC system, such as Volterra filtered-X LMS (VFXLMS), filtered-s least mean square (FSLMS), neural-based filtered-X least-mean-square algorithm (NFXLMS) (Tan and Jiang, 2001, Das and Panda, 2004, Chang and Luoh, 2007), etc., has been proposed for its high robustness and easy implementation. It indicated that the FSLMS algorithm performs better than VFXLMS in terms of MSE and an evaluation of the computational requirements. It also shows that the FSLMS algorithm has an advantage over VFXLMS when the length of secondary path filter is less than 6. In order to simplfy the system structure and parameters learning process, a generalized filtered-X gradient descent algorithm based on an integrated evaluation criterion was developed to adaptively adjust the weights of the controller for attenuating the nonlinear and non-Gaussian noises (Zhang et al., 2010)

2.4 Concluding remarks

Subsequent to this review, the noise attenuator for FBN cancellation would be designed with the following considerations:

- The feedforward ANC structure was determined for pressure pulsation control in this research for its easy implementation and stability, although the feedback and hybrid ANC structures have been shown to be promising in many applications. The adaptive notch filter was chosen for FBN attenuation as a typical case of narrowband noise cancellation.
- The FXLMS filter with LMS system identification technique was selected for detailed investigation due to its effectiveness and robustness applied in ABN and SBN attenuation. Successful implementations based on these algorithms are highly promising for the application of FBN attenuation in hydraulic system.
- The LMS time-domain and frequency-domain identification techniques would be studied on the comparison of the performance and limitations when these were implemented for FBN attenuation based on hydraulic systems.

- Effects from the accuracy of secondary path identification would be considered carefully in the controller design. Also effects from the frequency mismatch and system nonlinearities need to be considered based on experimental results.

3 Adaptive controller design

In this chapter, the derivation of least-mean-square (LMS) algorithm is studied. The LMS algorithm is a linear adaptive filtering algorithm, which generally consists of a filtering process and an adaptive process. The implementation of the LMS algorithm in the areas of active noise control is discussed and a widely used modified filtered-X LMS algorithm is introduced. Comparative simulation studies were investigated in terms of narrowband noise cancellation. The LMS filter has been found to offer a stable and robust solution for periodic noise attenuation. Different approaches for secondary path identification are validated and compared. The fast-block LMS (FBLMS) algorithm was found to have fast computation and high robustness in comparison with the conventional LMS algorithm.

3.1 Least-mean square algorithm

The least-mean square (LMS) algorithm is a linear adaptive filtering algorithm, which generally consists of a filtering process and an adaptive process (Haykin, 1996). In general there are two filter structures that can be applied for adaptive filtering: finite impulse response (FIR) and infinite impulse response (IIR) structures. The general block diagram of an adaptive FIR filter is shown in Figure 3.1(a), where $d(n)$ is a desired response, $y(n)$ is the actual output of a digital filter driven by a reference input signal $x(n)$, and the error $e(n)$ is the difference between $d(n)$ and $y(n)$.

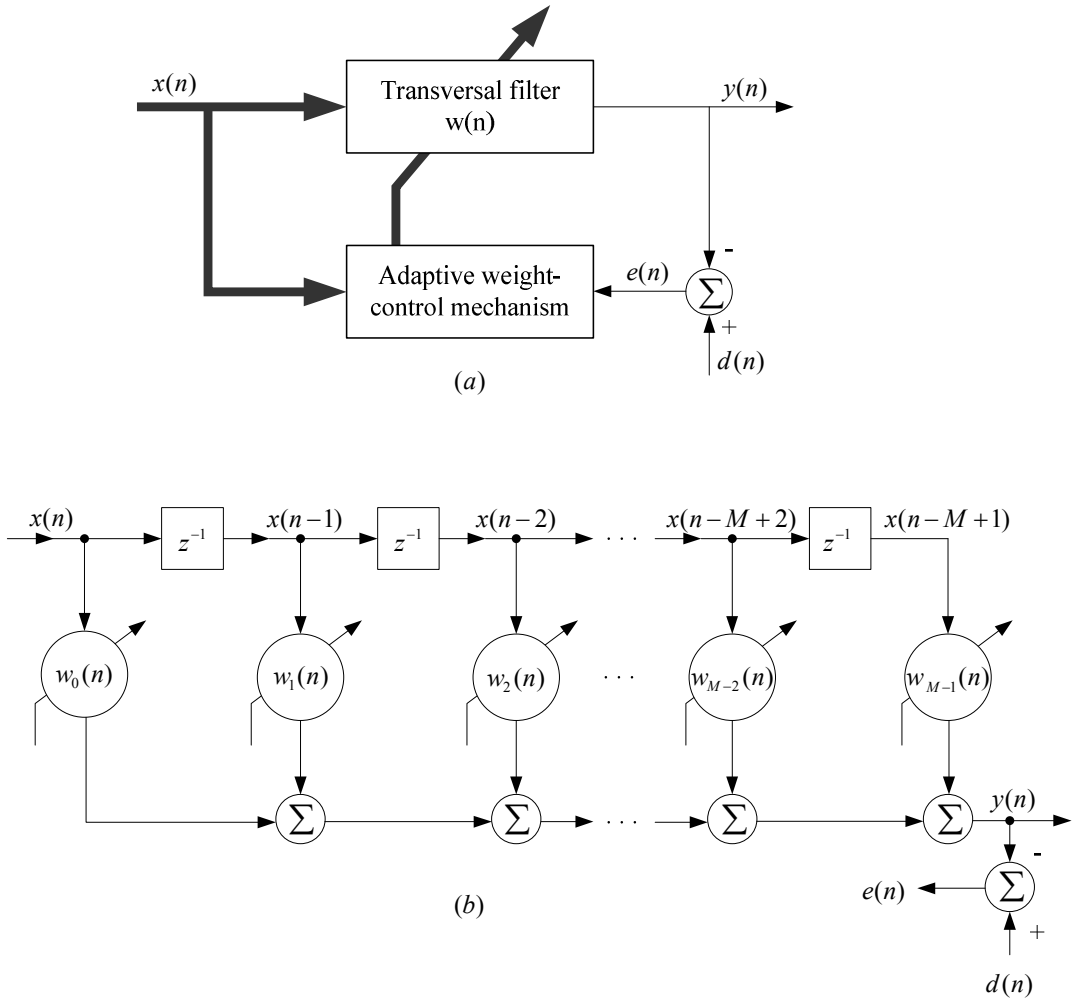

Figure 3.1 (a) Block diagram of adaptive transversal filter (b) Detailed structure of the transversal filter component (Haykin, 1996)

Details of the transversal filter component are presented in Figure 3.1(b). The tap inputs $x(n)$, $x(n\text{-}1)$, …, $x(n\text{-}M\text{+}1)$ form the elements of the M-by-1 tap-input vector $\mathbf{x}(n)$**,** where M-1 is the number of delay elements; The coefficients of tap weight vector $\mathbf{w}(n)$ = $[w_0(n), w_1(n),\ldots,w_{M\text{-}1}(n)]$ are updated using the adaptive algorithm to minimise a measured error signal $e(n)$. These tap weights operate as a gain on their respective tap inputs and the output of each gain is summed to produce the filter output $y(n)$ given by the equation 3.1:

$$y(n) = \mathbf{w}^T(n)\mathbf{x}(n) = \mathbf{x}^T(n)\mathbf{w}(n) \tag{3.1}$$

The output $y(n)$ is compared with the desired response $d(n)$, which results in the difference error signal:

$$e(n) = d(n) - y(n) = d(n) - \mathbf{w}^T(n)\mathbf{x}(n) \tag{3.2}$$

Taking the square of equation 3.2 gives:

$$e^2(n) = d(n)^2 - 2d(n)\mathbf{w}^T(n)\mathbf{x}(n) + \mathbf{w}^T(n)\mathbf{x}(n)\mathbf{x}^T(n)\mathbf{w}(n) \tag{3.3}$$

The expected value of mean-square error (MSE) of $e(n)$ can be defined as

$$\xi(n) = E[e^2(n)] \tag{3.4}$$

For an adaptive FIR filter, $\xi(n)$ will depend on the M filter weights $w_0(n)$, $w_1(n)$, …, $w_{M-1}(n)$. Assuming that the adaptive weight vector $\mathbf{w}(n)$ is a deterministic sequence, then the MSE performance function (cost function) can be determined from equation 3.2, giving

$$\xi(n) = E[d^2(n)] - 2\mathbf{p}^T\mathbf{w}(n) + \mathbf{w}^T(n)\mathbf{R}\mathbf{w}(n) \tag{3.5}$$

where $\mathbf{p}$ is the cross-correlation vector of desired signal $d(n)$ to input $\mathbf{x}(n)$

$$\mathbf{p} = E[d(n)\mathbf{x}(n)] = [r_{dx}(0) \quad r_{dx}(1) \quad \cdots \quad r_{dx}(L-1)]^T \tag{3.6}$$

where

$$r_{dx}(k) = E[d(n)x(n-k)] \tag{3.7}$$

and $\mathbf{R}$ is the input autocorrelation matrix, which is given as

$$\mathbf{R} = E[\mathbf{x}(n)\mathbf{x}^T(n)]$$

$$= \begin{bmatrix} r_{xx}(0) & r_{xx}(1) & \cdots & r_{xx}(L-1) \\ r_{xx}(1) & r_{xx}(0) & \cdots & r_{xx}(L-2) \\ \vdots & \cdots & \ddots & \vdots \\ r_{xx}(L-1) & r_{xx}(L-2) & \cdots & r_{xx}(0) \end{bmatrix} \tag{3.8}$$

where

$$r_{xx}(k) = E[x(n)x(n-k)] \tag{3.9}$$

From Equation 3.5, it can be seen that the MSE is a quadratic function of the tap weights $\mathbf{w}(n)$, assuming the tap-input $\mathbf{x}(n)$ and the desired response $d(n)$ are jointly stationary. For each value of the tap weights vector $\mathbf{w}(n)$, there is a corresponding value of MSE. The MSE values associated with $\mathbf{w}(n)$ form an (M+1) dimensional space (MSE surface). For M=2, this corresponds to error surface in a three dimensional space (Wang, 2008).

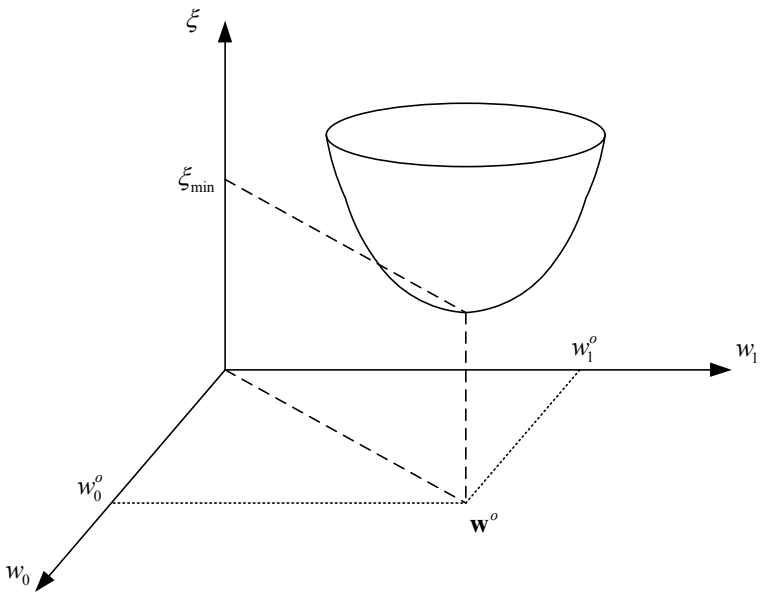

Figure 3.2 Three dimensional performance surface, $M = 2$ (Kuo and Morgan, 1995)

Figure 3.2 shows a typical 3-D error surface for the case $M = 2$. The filter coefficients vector $\mathbf{w}^o = [w_0^o \quad w_1^o]^T$ is the optimal weight value and ξ_{min} is the minimum mean-square error. It can be concluded that the optimum filter $\mathbf{w}^o$ minimizes the MSE cost function $\xi(n)$ (Kuo and Morgan, 1995). Taking the gradient of the cost function $\xi(n)$ on the performance surface:

$$\nabla\xi(n) = \begin{bmatrix} \dfrac{\partial\xi(n)}{\partial w_0(n)} \\ \dfrac{\partial\xi(n)}{\partial w_1(n)} \\ \vdots \\ \dfrac{\partial\xi(n)}{\partial w_{M-1}(n)} \end{bmatrix} = -2\mathbf{p} + 2\mathbf{R}\mathbf{w}(n) \tag{3.10}$$

Setting $\nabla\xi(n) = 0$ in equation 3.10 to obtain the optimal solution for the filter coefficients

$$\mathbf{w}^o = \mathbf{R}^{-1}\mathbf{p} \tag{3.11}$$

The computation of the ideal optimal solution is intensive as it requires continuous estimation of the autocorrelation matrix **R** and the cross-correlation vector **p**.

Substituting the optimum weight vector $\mathbf{w}^o$ from equation 3.11 to equation 3.5, the minimum MSE can be obtained as follows:

$$\xi_{\min} = E[d^2(n)] - \mathbf{p}^T \mathbf{w}^o \tag{3.12}$$

Combining equation 3.12 with equation 3.5 and 3.11 gives the MSE as

$$\xi(n) = \xi_{\min} + [\mathbf{w}(n) - \mathbf{w}^o]^T \mathbf{R}[\mathbf{w}(n) - \mathbf{w}^o] \tag{3.13}$$

Defining the weight misalignment vector $\mathbf{v}(n)$ as the difference between the adaptive filter tap weight and the optimal solution,

$$\mathbf{v}(n) = \mathbf{w}(n) - \mathbf{w}^o \tag{3.14}$$

Equation 3.13 can be re-written as follows

$$\xi(n) = \xi_{\min} + \mathbf{v}(n)^T \mathbf{R}\mathbf{v}(n) \tag{3.15}$$

The quadratic form of $\xi(n)$ with respect to $\mathbf{v}(n)$ indicates that the error surface is concave and possesses a unique minimum $\xi(n)$ value. The LMS algorithm employs the well known steepest descent algorithm to converge upon the optimal solution. The successive adjustments applied to the weight vector **w** are in the direction of steepest descent – that is, in a direction opposite to $\nabla\xi(n)$.

The concept of steepest descent can be expressed in the following algorithm:

$$\mathbf{w}(n+1) = \mathbf{w}(n) - \frac{\mu}{2}\nabla\xi(n) \tag{3.16}$$

where μ is a positive real constant used to control stability and the rate of descent to the minimum MSE value.

In reality, it is not possible to evaluate the gradient vector, since that would require prior knowledge of both the correlation matrix **R** of the tap inputs and the cross-correlation vector **p** between the tap inputs $x(n)$ and the desired response $d(n)$. Consequently, the gradient vector must be estimated from the available data when the system operates in an unknown environment.

The simplest choice of estimators is to use instantaneous estimates for **R** and **p** that are based on sample values of the tap-input vector and desired response, defined respectively by

$$\hat{\mathbf{R}}(n) = \mathbf{x}(n)\mathbf{x}^T(n) \tag{3.17}$$

and

$$\hat{\mathbf{p}}(n) = d(n)\mathbf{x}(n) \tag{3.18}$$

where ($\hat{}$) denotes the instantaneous estimate.

The instantaneous estimate of the cost function $\xi(n)$ is

$$\hat{\xi}(n) = E[d^2(n)] - 2\hat{\mathbf{p}}(n)^T\mathbf{w}(n) + \mathbf{w}^T(n)\hat{\mathbf{R}}(n)\mathbf{w}(n) \tag{3.19}$$

Differentiating this estimate with respect to $\mathbf{w}(n)$, an instantaneous estimate of $\hat{\nabla}\xi(n)$ is obtained:

$$\hat{\nabla}\xi(n) = -2d(n)\mathbf{x}(n) + 2\mathbf{x}(n)\mathbf{x}^T(n)\mathbf{w}(n) \tag{3.20}$$

Substituting the estimate of Equation 3.20 for the gradient vector $\nabla\xi(n)$ in the steepest descent algorithm described in Equation 3.16, gives

$$\begin{aligned} w(n+1) &= w(n) - \frac{\mu}{2}(-2d(n)\mathbf{x}(n) + 2\mathbf{x}(n)\mathbf{x}^T(n)\mathbf{w}(n)) \\ &= w(n) + \mu\mathbf{x}(n)[d(n) - \mathbf{x}^T(n)\mathbf{w}(n)] \end{aligned} \tag{3.21}$$

which is the LMS recursive algorithm.

Three basic relations can be used to describe the LMS algorithm simply and equivalently as follows (Simon, 1996):

1. *Filter output*

$$y(n) = \mathbf{w}^T(n)\mathbf{x}(n) \tag{3.22}$$

2. *Error signal*

$$e(n) = d(n) - y(n) \tag{3.23}$$

3. *Filter coefficients adaptation*

$$\mathbf{w}(n+1) = \mathbf{w}(n) + \mu\mathbf{x}(n)e(n) \tag{3.24}$$

A signal-flow graph representation of the LMS algorithm in the form of a feedback model is shown in Figure 3.3.

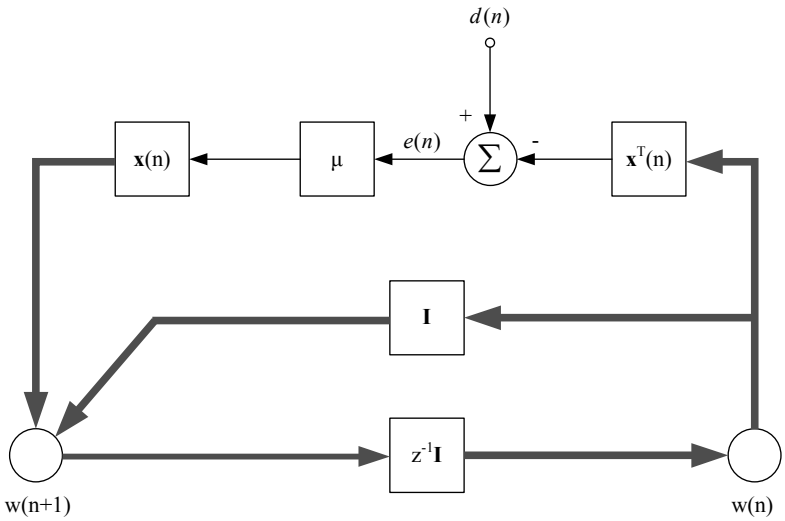

Figure 3.3 Signal-flow graph representation of the LMS algorithm (Haykin, 1996)

It can be seen that, at each iteration or time update, the LMS algorithm requires knowledge of the most recent values: $\mathbf{x}(n)$, $d(n)$ and $\mathbf{w}(n)$. The iterative procedure is started with an initial guess $\mathbf{w}(0)$.

The condition for stability of the LMS algorithm is (Kuo and Morgan, 1995)

$$0 < \mu < \frac{2}{\lambda_{\max}} \tag{3.25}$$

where $\lambda_{\max}$ is the largest eigenvalue of the input correlation matrix $\mathbf{R}$.

The stability condition on μ given in Equation 3.25 is not practical to apply because computation of $\lambda_{\max}$ is complex when the filter length M is large. Therefore, in practical application, it is desirable to estimate $\lambda_{\max}$ using a simple method. Feuer and Weinstein (1985) showed that the convergence of the mean-square error for Gaussian signals requires:

$$0 < \mu < \frac{2}{3MP_x} \tag{3.26}$$

where

$$P_x = E[x^2(n)] \tag{3.27}$$

and M is the length of tap-weights.

Equation (3.26) shows the upper bound on μ is inversely proportional to M. It can be seen that a large order filter requires a small convergence rate μ. Since μ is also inversely proportional to the power of input signals, a small μ is required for a signal with a high power.

3.2 Filtered-X Least-mean square algorithm

Figure 3.4 shows a block diagram of a standard cancellation system employing the conventional LMS algorithm. In this structure, the introduction of the actuator dynamics $S(z)$ into a controller will generally cause instability (Elliott and Nelson, 1985). This is because the error signal is not ideally "aligned" in time with the reference signal due to the presence of $S(z)$.

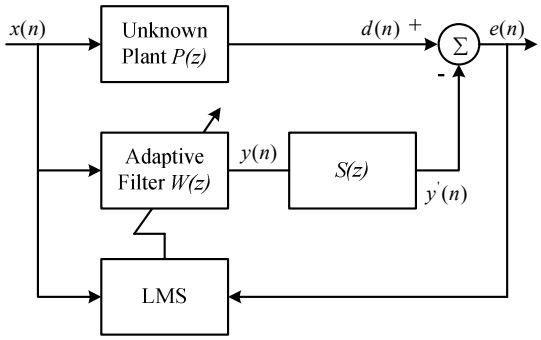

Figure 3.4 Simplified block diagram of ANC system (Elliott and Nelson, 1985)

Morgan (1980) proposed a solution which is placing an identical filter in the reference signal path to the weight update of the LMS algorithm to solve this problem. The reference signal is filtered so as to compensate for the effect of the secondary path in the adaptation loop. This algorithm is widely realized and named filtered-X LMS (FXLMS) algorithm, as shown in Figure 3.5.

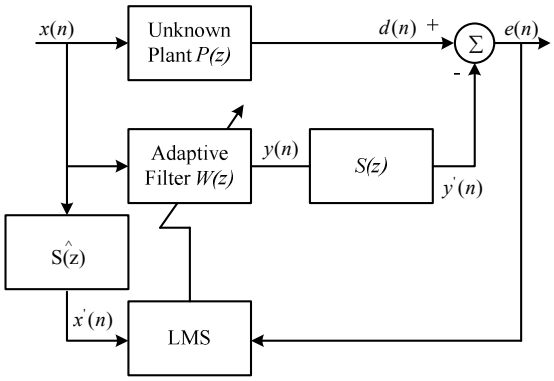

Figure 3.5 Block diagram of ANC system using the FXLMS algorithm (Morgan, 1980)

The error signal is given by the equation:

$$E(z) = D(z) - Y(z)S(z) = X(z)(P(z) - W(z)S(z)) \tag{3.28}$$

where $E(z)$,$D(z)$,$Y(z)$ and $X(z)$ are the z-transforms of the signals $e(n)$,$d(n)$,$y(n)$ and $x(n)$.

When the error signal $e(n)$ is close to zero, as $E(z) = 0$:

$$W(z) = \frac{P(z)}{S(z)} \tag{3.29}$$

With the estimated secondary path $\hat{S}(z)$, the LMS algorithm given in equation 3.24 now becomes:

$$\mathbf{w}(n+1) = \mathbf{w}(n) + \mu \mathbf{x}'(n)e(n) \tag{3.30}$$

where $\mathbf{x}'(n) = [x'(n) \quad x'(n-1) \quad \cdots \quad x'(n-m)]$ is the filtered reference signal $x(n)$ by using $\hat{S}(z)$, and is expressed as follows:

$$\mathbf{x}'(n) = \hat{s}^{T}(n)\,\mathbf{x}(n) \tag{3.31}$$

From equation 3.29, 3.30 and 3.31, it can be seen that the effect from secondary path transfer function $S(z)$ can be compensated by using filtered reference signal.

So for $E(z) = 0$,

$$W(z) = P(z) \tag{3.32}$$

This can be expressed using the block diagram of LMS algorithm in Figure 3.6 where the actuator dynamic $S(z)$ is ideally eliminated.

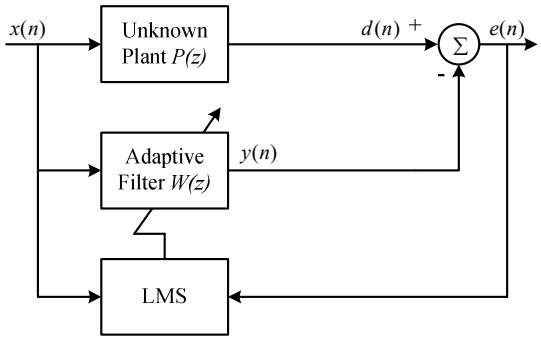

Figure 3.6 Conventional LMS block diagram (Morgan, 1980)

3.3 Secondary path identification

Assuming that the characteristics of $S(z)$ are time-invariant, the off-line modelling technique can be applied to estimate the secondary path dynamics $S(z)$. For this technique, the process data is first stored in a data storage medium then transferred to a controller and evaluated. In situations where the secondary path $S(z)$ is unknown and time-varying, the identification must proceed in parallel with the cancellation algorithm. Two methods are commonly employed to achieve the on-line system identification:

1. Auxiliary random noise technique;

This approach was firstly proposed by Eriksson (Eriksson and Allie, 1989) for ANC and applied successfully for ABN and SBN cancellation (Bao et al., 1993a, Kuo and Vijayan, 1997, Gan and Kuo, 2002, Zhang et al., 2001, Lan et al., 2002). It involves injection of auxiliary random noise into the system in order to estimate the dynamics of secondary path $S(z)$. The power of the auxiliary signal should be small in comparison with the power of the primary noise. Also the auxiliary signal should be a zero-mean signal which is independent of the primary noise (Bao et al., 1993b). The advantage of this method is that $\hat{S}(z)$ obtained by the model at all frequencies is signal-independent. This brings the benefit of fast response of the controller to the changes of the system primary noise (Bao et al., 1993b). However, the introduction of unrelated auxiliary noise can affect the overall noise cancellation.

2. Overall modelling algorithm (without auxiliary random noise).

The overall on-line secondary path modelling algorithm also uses a LMS filter to estimate secondary path $S(z)$ dynamics. This algorithm has the capability to model the

secondary path $S(z)$ with another adaptive filter which is used for eliminating the identification bias (Sommerfeldt, 1989, Eriksson, 1991, Kuo and Morgan, 1995) instead of using an additional excitation signal. The $\hat{S}(z)$ obtained by the model is dependent on the frequency content of the primary noise. It means that $\hat{S}(z)$ will change if the primary noise varies. This can slow the convergence of the cancellation filter and reduce the robustness of system.

These approaches with and without auxiliary noise injection both can be applied in secondary path identification (Eriksson and Allie, 1989, Kuo and Morgan, 1995). The comparison of on-line identification approaches was presented by Bao (1993b) and it concluded that the technique using auxiliary noise is more reliable and effective. The convergence of the auxiliary noise technique is faster than that of the overall modelling technique, especially when the primary noise path changes. More details in the application of the auxiliary random noise technique will be described in this section. White noise was employed as an ideal training signal in system identification since it has a constant spectral density at all frequencies.

3.3.1 LMS offline identification technique

The structure of off-line identification technique is shown in Figure 3.7, where uncorrelated white noise $v(n)$ is internally generated as the input to a secondary source $S(z)$, and an adaptive filter $\hat{S}(z)$ is used to model the secondary path.

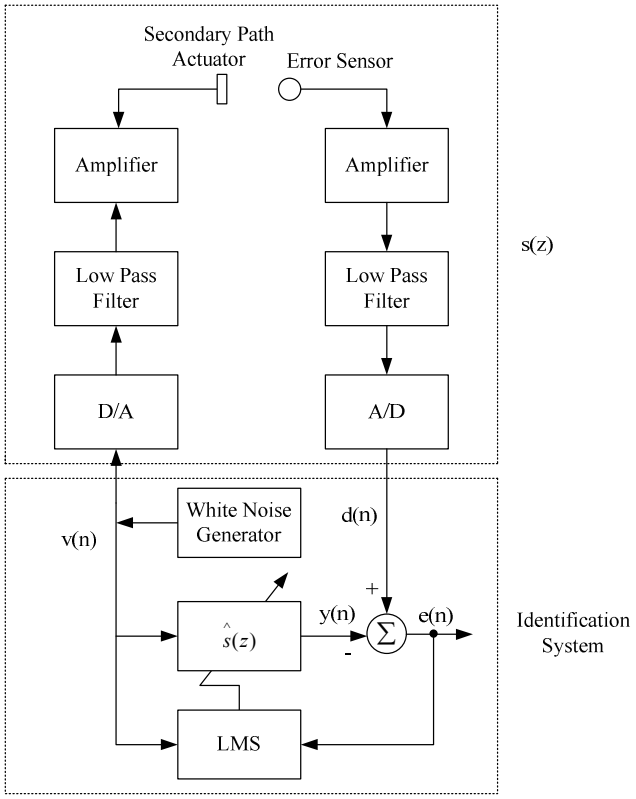

Figure 3.7 Block diagram of off-line identification technique (Kuo and Morgan, 1995)

The adaptive filter output is $y(n)$ which can be expressed as

$$y(n) = \sum_{l=1}^{L-1} \hat{s_l}(n)\, v(n-l) \tag{3.33}$$

where $\hat{s_l}(n)$ is the l^{th} coefficient of the estimated secondary path $\hat{S}(z)$ at time n.

Using the conventional LMS algorithm coefficients update

$$\hat{s_l}(n+1) = \hat{s_l}(n) + \mu v(n-l)e(n) \tag{3.34}$$

where $e(n)$ is the error signal as $e(n) = d(n) - y(n)$.

Equation 3.33 is applied for each iteration until the power of $e(n)$ is minimized and the adaptive filter $\hat{s}(z)$ converges to the optimum solution.

In order to validate secondary path identifications by using the conventional LMS algorithm, a simplified plant $S(z)$ is represented by a second-order continuous transfer function $S(s)$ with 0.1ms sample time step:

$$S(s) = \frac{\lambda \omega_n^2}{s^2 + 2\xi\omega_n s + \omega_n^2} \tag{3.35}$$

with gain $\lambda = 1$, damping ratio $\xi = 0.8$ and natural frequency $\omega_n = 628$ rad/s;

The standard system identification technique is introduced for results comparison of secondary path identification. Random noise is employed as the driving signal for actuator $S(z)$. The output $O(n)$ and input $I(n)$ signals of plant $S(z)$ are recorded and transformed to frequency domain by using Fast Fourier Transform (FFT) technique. The frequency response can be obtained by:

$$S(j\omega) = \frac{O(j\omega)}{I(j\omega)} \tag{3.36}$$

where $O(j\omega)$ and $I(j\omega)$ are the Fourier transforms of output and input signals. This is used as theoretical frequency response of plant in following analysis.

Figure 3.8 shows the comparison of frequency response of secondary path $S(z)$ by using the standard system identification technique and LMS offline identification technique. The length of the adaptive filter was 256 and the convergence rate was 70 at the sample frequency of 10 kHz.

Good agreement is obtained between the results and it is shown that the LMS off-line identification technique described in Figure 3.7 is effective for using to identify the dynamics of unknown plant.

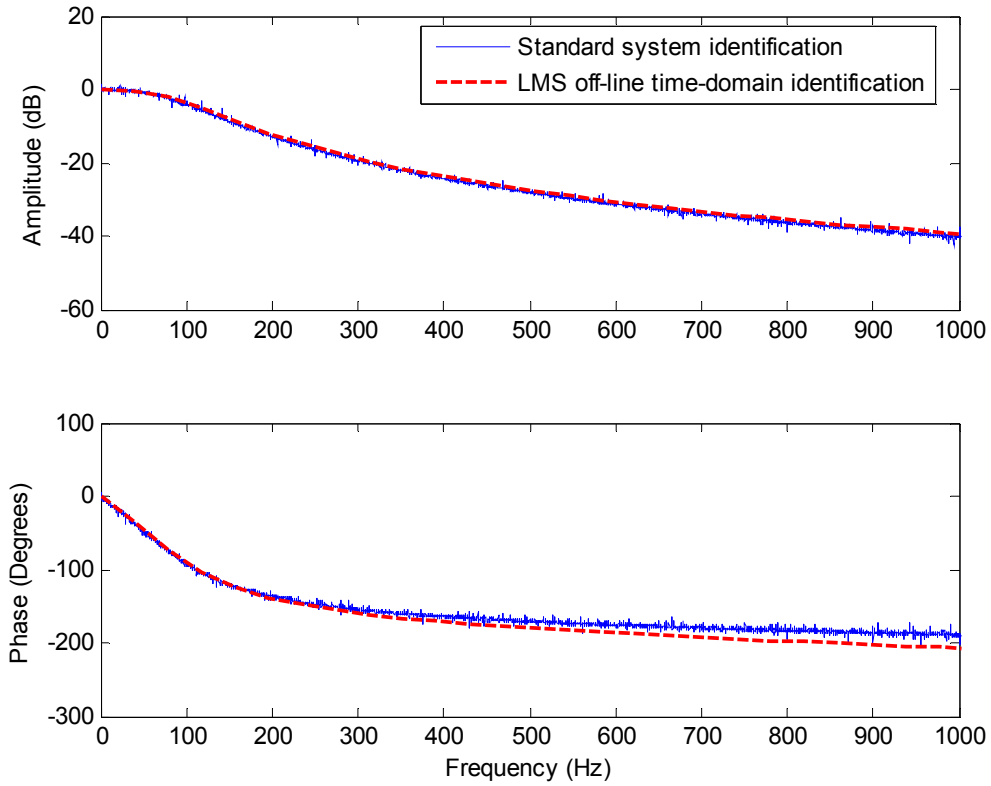

Figure 3.8 Comparison of frequency responses of secondary path $S(z)$ using standard system identification technique and the LMS offline time-domain identification technique.

3.3.2 LMS online identification technique

Figure 3.9 shows the block diagram of FXLMS using on-line identification technique. A zero-mean white noise $v(n)$ is added to the secondary signal $y(n)$ produced by the ANC filter $w(z)$ to drive the secondary source. The adaptive filter $\hat{S}(z)$ is connected in parallel with the secondary path to model $S(z)$. Hence the estimated secondary path $\hat{S}(z)$ is updated according to:

$$\hat{s_l}(n+1) = \hat{s_l}(n) + \mu v(n-l)[e(n) - \hat{s_l}(n)v(n-l)] \tag{3.37}$$

The residual error is

$$e(n) = d(n) - y'(n) - v'(n) \tag{3.38}$$

where

$$y'(n) = s(n)y(n) \tag{3.39}$$

$$v'(n) = s(n)v(n) \tag{3.40}$$

An estimate of Equation 3.40 is obtained from the estimated filter $\hat{S}(z)$ as

$$\hat{v}'(n) = \hat{s}(n)v(n) \tag{3.41}$$

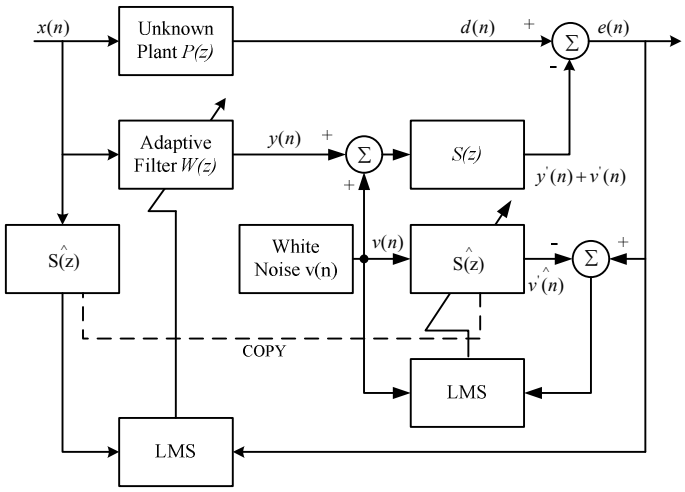

Figure 3.9 Filtered-X LMS block diagram with on-line identification technique (Kuo and Morgan, 1995)

3.3.2.1 Effects from auxiliary random noise

In order to investigate the effects from the white noise $v(n)$ in Figure 3.9, a signal $u(n)$ is used to define the component of the error $e(n)$ as follows:

$$\begin{aligned} u(n) &= d(n) - s(n)y(n) \\ &= [p(n) - s(n)w(n)]x(n) \end{aligned} \tag{3.42}$$

where $p(n)$, $s(n)$ and $w(n)$ are the impulse response of $p(z)$, $s(z)$, and $w(z)$ at time n. It can be seen that $u(n)$ is dependent on the primary noise $x(n)$ and uncorrelated to the white noise $v(n)$.

Therefore, a simplified block diagram of the system identification algorithm is illustrated in Figure 3.10, where $u(n)$ is defined in Equation 3.42. This simplified model is similar to the standard system identification form as shown in Figure 3.6. In this case, $u(n)$ could be seen as an interference, which is uncorrelated with the driving signal $v(n)$ (Kuo and Morgan, 1995).

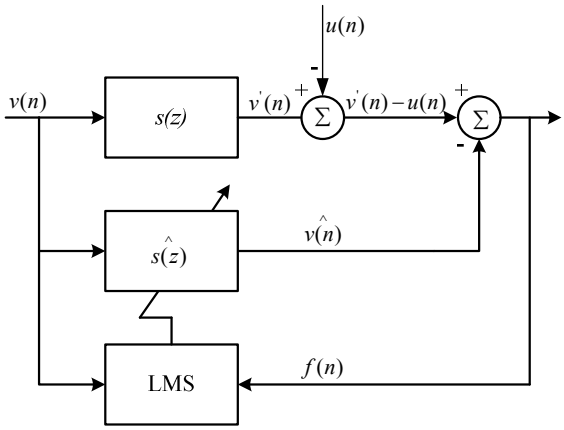

Figure 3.10 Simplified block diagram of system identification with additive random noise technique (Kuo and Morgan, 1995)

Assuming that $\hat{S}(z)$ has sufficient order, the optimum solution of $\hat{S}(z)$ is the ratio of the cross-power spectrum between ($v'(n)$-$u(n)$) and $v(n)$ to the autopower spectrum of $v(n)$ (Oppenheim and Schafer, 1989, Widrow and Stearns, 1985), as shown in Equation 3.43.

$$\hat{s^o}(z) = \frac{s_{vv'}(z)}{s_{vv}(z)} \tag{3.43}$$

where $s_{vv'}(z)$ is the cross-power spectrum between $v'(n)$ and $v(n)$, which is defined as the z-transform of the cross-correlation function $r_{vv'}(k)$, and $s_{vv}(z)$ is the autopower spectrum of $v(n)$, which is defined as the z-transform of the auto-correlation function $r_{vv}(k)$.

From Figure 3.10,

$$r_{vv'}(k) = E[v'(n)v(n-k)] = E[(s(n)v(n))v(n-k)] = s(n)r_{vv}(k) \tag{3.44}$$

Therefore,

$$s_{vv'}(z) = s(z)s_{vv}(z) \tag{3.45}$$

Substituting Equation 3.45 into Equation 3.43, it yields

$$\hat{s^o}(z) = s(z) \tag{3.46}$$

It shows that the optimum solution of $\hat{S}(z)$ is unaffected by the interference $u(n)$. But the convergence speed of the adaptive algorithm will be affected by the presence of $u(n)$ (Kuo and Morgan, 1995).

Figure 3.11 shows the frequency response of secondary path $S(z)$ by using on-line identification technique. A sinusoidal signal $x(t) = 0.1\sin(40\pi t)$ was employed as the primary noise $x(n)$. The length of the adaptive filter was 256 and the convergence rate was μ=70 with a sample frequency of 10 kHz, which are as similar to those applied in the offline identification in section 3.2.2.1. However, the simulation time used in the online technique is 5 times (50s) that of offline ones (10s). For comparison, the results in Figure 3.8 were also plotted. It can be seen that amplitude and phase differences occurred around the high frequency range (650Hz – 1000Hz). This is because of the inaccuracy of impulse response of $S(z)$ obtained from the LMS filter. The accuracy can be improved by applying longer simulation time and increasing the magnitude of white noise and the value of convergence factor for the identification filter.

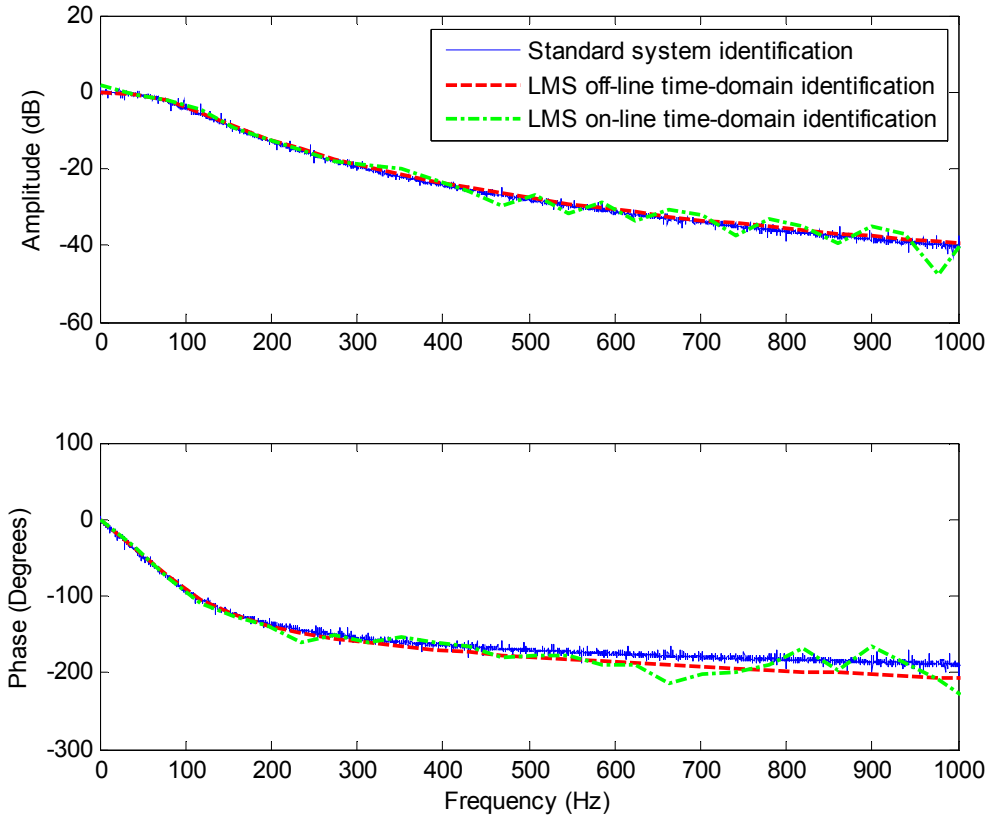

Figure 3.11 Frequency response of secondary path $S(z)$ by using on-line time-domain identification techniques.

On the other hand, the use of a time-domain filter can cause problems with the on-line system identification since the estimated $\hat{S}(z)$ can be corrupted by residual error signal which contains components uncorrelated with the reference signal. This can increase the convergence time of the cancellation filter and result in instability. Moreover, a constant uniform convergence rate is used for all frequency components in the time-domain technique. This means the selected convergence rate has to be small enough to give stable results for all cancellation frequencies. The fast-block LMS (FBLMS) algorithm which operates in the frequency domain can solve this problem and improve the robustness and efficiency of the system identification.

3.3.2.2 Effects of length of identification filter

The selection of the filter length is very significant for system performance. For secondary path identification, a high order filter is preferred in order to achieve accurate secondary path dynamics. However, it may result in more computational cost.

The transfer function (3.35) was used to investigate the effect of the filter length in the identification process. The same convergence rate was applied with different lengths. Figure 3.12 shows the impulse responses of the secondary path S(z) with different lengths of filters. As can be seen, the filter with the length of 256 provided a whole and clear impulse response of S(z). In contrast, an incomplete impulse response, which the shape of the impulse response was captured correctly, but the end being truncated, was obtained with the filter of the length of 64. This inaccuracy may cause instability of the noise controller due to the incomplete information of the secondary path.

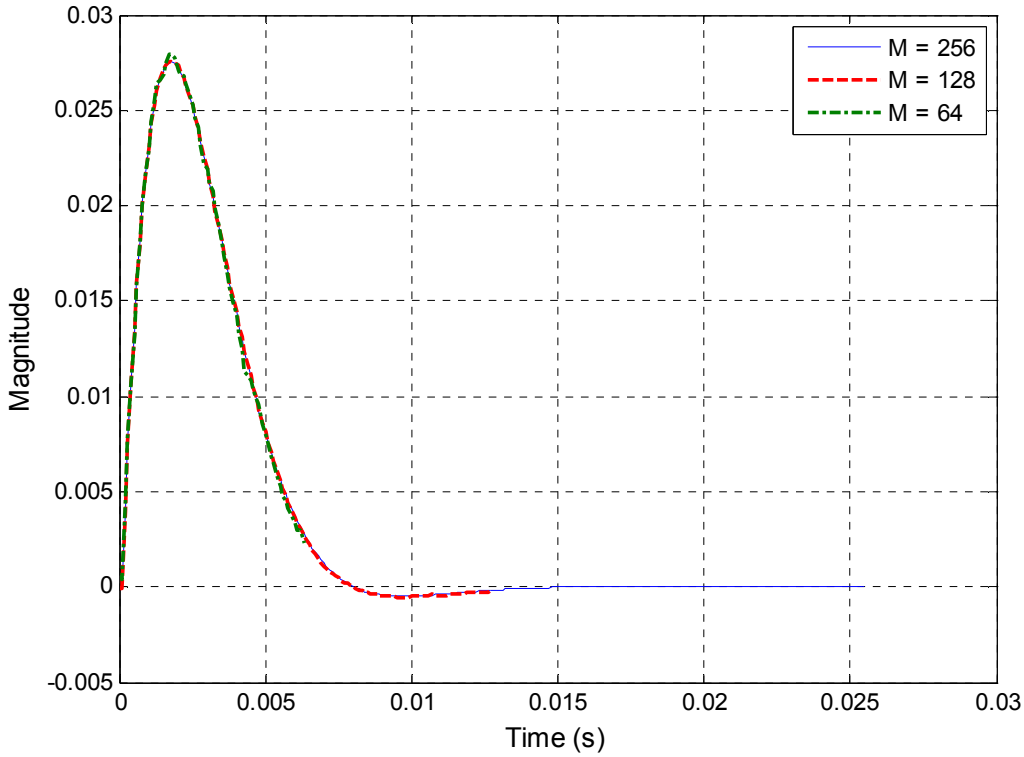

Figure 3.12 Impulse responses of the secondary path S(z) by using different lengths of filters

Figure 3.12 shows the frequency responses of the secondary path S(z). The density of the points in the same frequency range was different based on the results of using different filter lengths. With the same sampling rate, the filter of 256 orders has twice of the sampling points than the filter of 128 orders. However, the upper bound on the convergence rate μ of the former has to be smaller than the latter. This could slow down the speed of the identification process. Therefore, a compromise should be made between the accuracy of identification and the computation of the system.

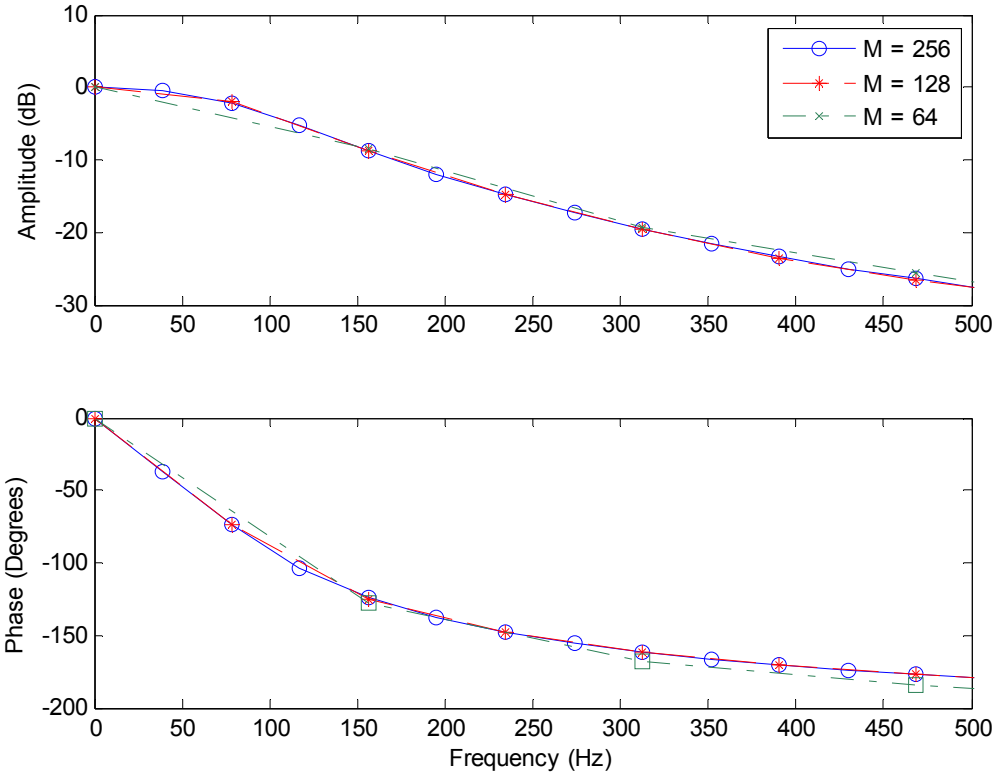

Figure 3.13 Frequency response of the secondary path S(z) by using different lengths of filters

3.3.2.3 Fast-block Least-mean square algorithm

The block diagram of fast-block least-mean square (FBLMS) algorithm is shown in Figure 3.14 (Clark et al., 1981).

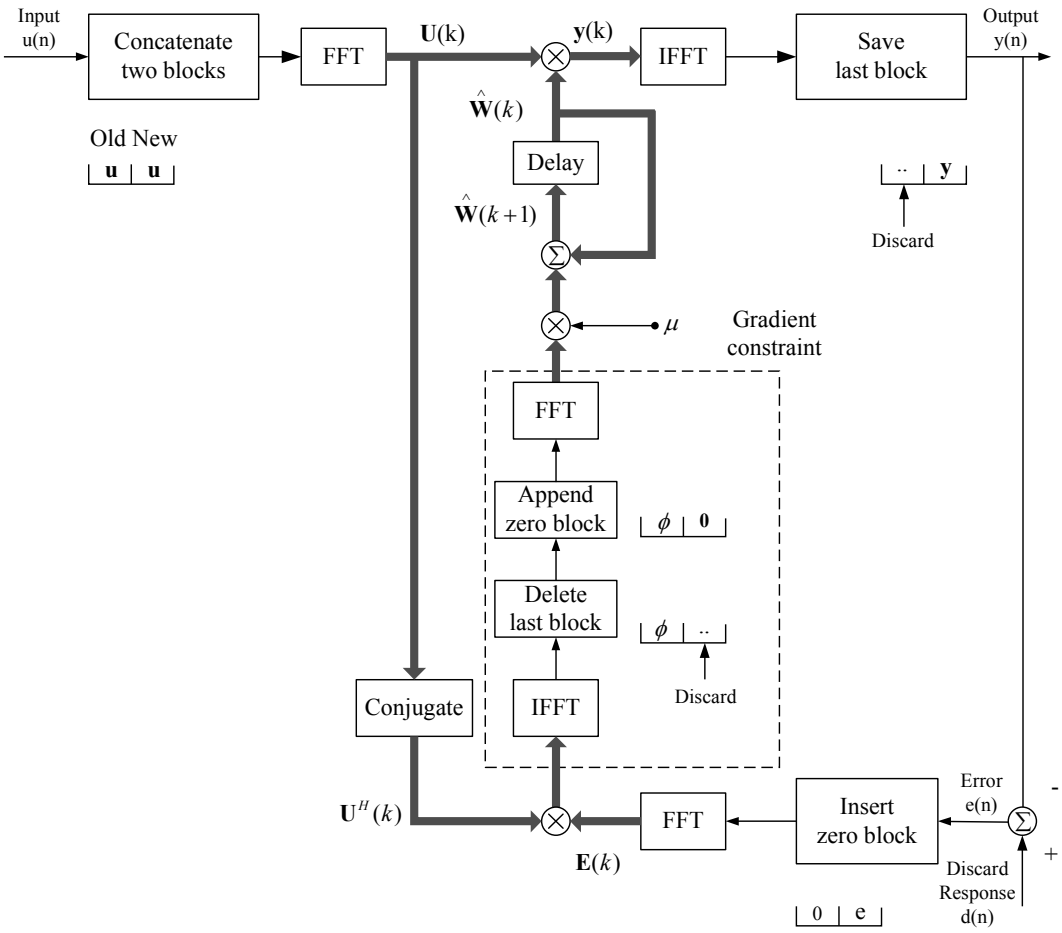

Figure 3.14 Block diagram of FBLMS identification algorithm (Clark et al., 1981)

The overlap-save method provides an efficient procedure for fast convolution. The discrete Fourier transform is applied for the computation of linear convolution (Oppenheim and Schafer, 1989). This is a common method for nonadaptive filtering. Although the filter can be implemented with any amount of overlap, the use of 50 percent overlap, which means the block size equals the number of weights, is the most efficient (Simon, 1996).

The M tap weights of the filter are padded with an equal number of zeros, and an N-point FFT is used for the computation, where

$$N = 2 \cdot M \tag{3.47}$$

Thus let the N-by-1 vector

$$\hat{\mathbf{W}}(k) = FFT\begin{bmatrix} \hat{\mathbf{w}(k)} \\ \mathbf{0} \end{bmatrix} \tag{3.48}$$

where $\hat{\mathbf{w}}(k)$ is the tap-weight vector and $\mathbf{0}$ is the M-by-1 null vector. $\hat{\mathbf{W}}(k)$ is the frequency-domain weight vector which is twice as long as the time-domain weight vector $\hat{\mathbf{w}}(k)$. k refers to the block index.

From Figure 3.12, the $\hat{\mathbf{W}}(k)$ updating for block number k is defined as

$$\hat{\mathbf{W}}(k+1) = \hat{\mathbf{W}}(k) + \mu \mathrm{FFT}\begin{bmatrix} \phi(k) \\ \mathbf{0} \end{bmatrix} \tag{3.49}$$

in which $\phi(k) = \text{first } M \text{ elements of IFFT}[\mathbf{U}^H(\mathrm{k})\mathbf{E}(\mathrm{k})]$.

$\mathbf{U}(k)$ is the two successive blocks of input data obtained by FFT

$$\mathbf{U}(k) = diag\{FFT[\underbrace{u(kM-M),...,u(kM-1)}_{(k-1)th\ \ block}, \underbrace{u(k),...,u(kM+M-1)}_{kth\ \ block}]\} \tag{3.50}$$

and the frequency-domain block signal $\mathbf{E}(k)$

$$\mathbf{E}(k) = \mathrm{FFT}\begin{bmatrix} \mathbf{0} \\ e(k) \end{bmatrix} \tag{3.51}$$

where *diag* donates an N-by-N diagonal matrix.

The convergence rate of the FBLMS algorithm can be improved by assigning a different step size to each tap weight without affecting the minimum mean-square error (Simon, 1996). The improvement is achieved by compensating for variations in the average signal power across the individual frequency bins. The step-size parameter μ becomes a function of the power spectral density (PSD) of the reference signal.

$$\mu_i = \frac{\alpha}{P_i}, \quad i = 0,1,...,2M-1, \tag{3.52}$$

where α is a constant and P_i is an estimate of the average power in the i^{th} frequency bin.

P_i can be estimated by using a first order low-pass filter as follows

$$P_i(k) = \gamma P_i(k-1) + (1-\gamma)\left|U_i(k)\right|^2, \qquad i = 0,1,...,2M-1. \tag{3.53}$$

$U_i(k)$ is the input applied to the i^{th} weight in the FBLMS algorithm at time k, γ is a forgetting factor chosen in the range $0 < \gamma < 1$.

The weights updating equation (3.49) for block number k can be modified as

$$\hat{\mathbf{W}}(k+1) = \hat{\mathbf{W}}(k) + \alpha \text{FFT}\begin{bmatrix} \phi(k) \\ \mathbf{0} \end{bmatrix}$$

$$\phi(k) = \text{first } M \text{ elements of IFFT}[\mathbf{D}(k)\mathbf{U}^H(k)\mathbf{E}(k)] \tag{3.54}$$

where $D(k) = diag[P_0^{-1}(k), \quad P_1^{-1}(k), \quad ..., \quad P_{2M-1}^{-1}(k)]$.

Thus, a lower adaption rate is applied to the frequency bins containing signal power relating to the uncancelled pressure ripple components and corruption of the estimate $\hat{S}(z)$ is reduced.

Figure 3.15 shows the comparison of the frequency responses by using LMS online and FBLMS online techniques. The length of the filter was 512 and the simulation time was 10s with a sample frequency of 10 kHz. As can be seen, good agreement was achieved between the results by using standard system identification and FBLMS online techniques. For the LMS online technique, the amplitude and phase differences occurred at the frequency of 19.53Hz, which is caused by the effect from the primary noise. This shows the FBLMS online technique is more efficient than the LMS online technique for the secondary path identification when the system has extra disturbance.

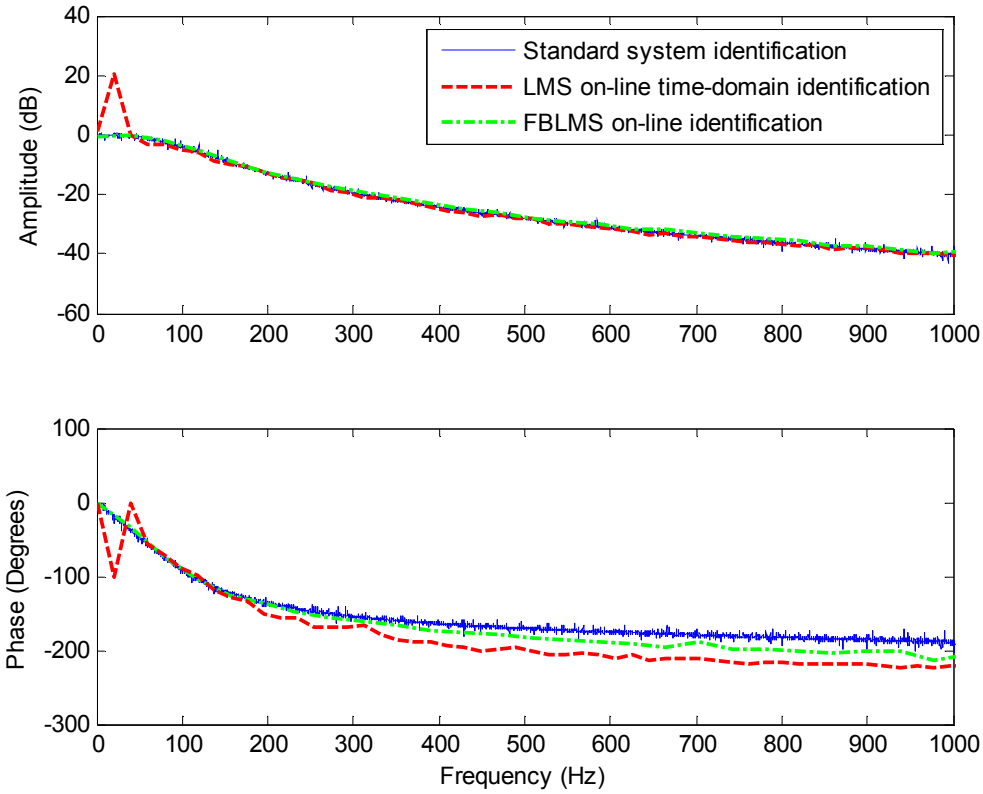

Figure 3.15 Frequency response of secondary path $S(z)$ by using LMS on-line and FBLMS on-line techniques

3.4 Active narrowband noise cancellation

The LMS adaptive filter described in sections 3.2 and 3.3 can be applied to either broadband or narrowband noise cancellation. Broadband noise may be totally random and distributes its energy across the frequency band. By contrast, narrowband noise concentrates most of its energy at specific frequencies. For the case of broadband cancellation the filter length must be sufficiently long to adequately model the impulse response of the system dynamics. Therefore, the filter length could be a function of the damping of the system and the sampling rate. For narrowband cancellation the LMS algorithm could be specialized as an adaptive notch filter, which removes the primary spectral components within a narrowband centred about the measured reference frequency. Simulation studies are included in this section to gain an understanding of the function, performance and stability of the algorithms for cancelling narrowband noise.

3.4.1 Single-frequency cancellation using the FXLMS algorithm

In narrowband feedforward ANC system, the reference signal can be generated by detecting the fundamental frequency of the primary noise from nonacoustic sensors, such as a tachometer or accelerometer. This reference signal is completely unaffected by the feedback effects from secondary source (Kuo and Morgan, 1995), which effectively eliminates the feedback effects caused by the anti-phase signal.

When a sinewave is employed as the reference signal of the controller, the LMS algorithm becomes an adaptive notch filter, which is able to eliminate the primary spectral component that has the same frequency as the reference signal. This means the centre frequency of the notch filter depends on the sinusoidal reference signal, whose frequency is equal to the frequency of the primary sinusoidal noise. Therefore, the noise at that frequency can be attenuated. Also the adaptive notch filter has the advantage of tracking the exact frequency of the interference adaptively. In practice, a very narrow notch is usually desired in order to eliminate the noise without seriously affecting the signal characteristics.

Figure 3.16 shows the block diagram of Filtered-X adaptive notch filter for narrowband noise cancellation. Two orthogonal components $x_0(n)$ and $x_1(n)$ are used as reference signals for the two-weight adaptive notch filter and the control signal $y(n)$ is summed from the weighted reference inputs. For the frequency present in the reference signal, the adaptive weight vector $\mathbf{w(n)} = [w_0(n), w_1(n)]$ is required for cancellation.

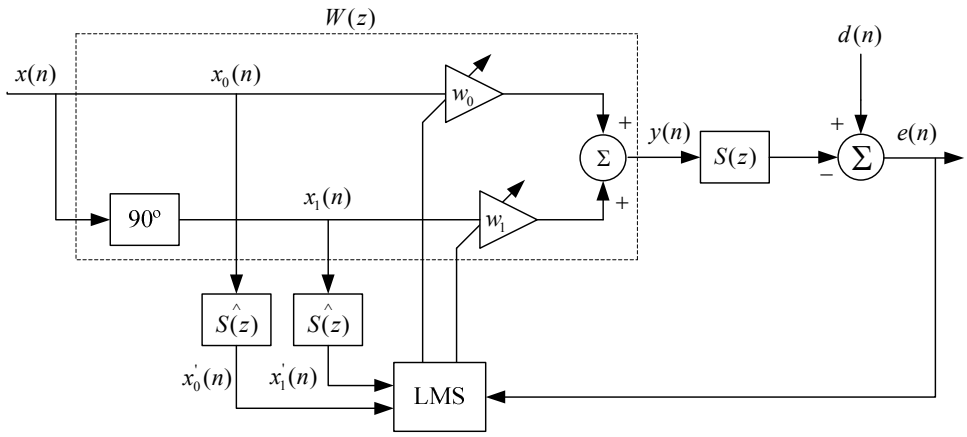

Figure 3.16 Single-frequency ANC system using FXLMS algorithm (Elliott et al., 2003)

The weights are updated by the equations:

$$\mathbf{w}_0(n+1) = \mathbf{w}_0(n) + \mu \mathbf{x}_0^{'}(n)e(n) \tag{3.55}$$

$$\mathbf{w}_1(n+1) = \mathbf{w}_1(n) + \mu \mathbf{x}_1^{'}(n)e(n) \tag{3.56}$$

where $\mathbf{x}_0^{'}(n)$ and $\mathbf{x}_1^{'}(n)$ are the reference signals filtered by the cancellation path estimate $\hat{S(z)}$.

The reference input can be defined as

$$x(n) = A\cos(\omega_0 n\Delta t) \tag{3.57}$$

at the reference frequency ω_0 .A is the amplitude of $x(n)$ and Δt is the fixed sampling interval.

Assuming the primary noise

$$d(n) = A_d \cos(\omega_0 n\Delta t + \phi_d) \tag{3.58}$$

and the estimated cancellation path $\hat{S(z)}$ equals to the actual value $S(z)$, the error signal at the frequency ω_0 can be given as

$$e(n) = A_d \cos(\omega_0 n\Delta t + \phi_d) - AA_w A_s \cos(\omega_0 n\Delta t + \phi_w + \phi_s) \tag{3.59}$$

where A_w and ϕ_w are the amplitude and phase of adaptive filter at ω_0 , and A_s and ϕ_s are the amplitude and phase of cancelling path $S(z)$, respectively.

When the error signal $e(n)$ is zero, the optimal controller can be achieved. In this case, the required controller magnitude and phase response can be expressed as

$$A_w = \frac{A_d}{AA_s} \tag{3.60}$$

and

$$\phi_w = \phi_d - \phi_s \tag{3.61}$$

So the adaptive filter $W(z)$ is employed to compensate the amplitude and phase difference between the primary noise and the cancelling signal.

The cancelling signal $y(n)$ is given by:

$$y(n) = w_0(n)\mathbf{x}_0(n) + w_1(n)\mathbf{x}_1(n) \tag{3.62}$$

It was shown by Kuo and Morgan (1995) that the equivalent closed-loop transfer function between the primary noise d(n) and the error output $e(n)$ is

$$H(z)=\frac{1}{1+\dfrac{S(z)Y(z)}{E(z)}}=\frac{z^2-2z\cos(\omega_0\Delta t)+1}{z^2-2z\cos(\omega_0\Delta t)+1+\beta S(z)[z\cos(\omega_0\Delta t-\phi_s)-\cos\phi_s]} \tag{3.63}$$

where

$$\beta=\mu A^2 A_s \tag{3.64}$$

and A_s and ϕ_s are the magnitude and phase of the cancellation path dynamics $S(z)$ at the frequency ω_0. $Y(z)$ and $E(z)$ are the z transform of the cancelling signal $y(n)$ and error signal e(n).

Figure 3.17 shows the magnitude and phase responses of $H(z)$ for $\mu=0.1$ and $\mu=0.01$ for frequency ω_0.

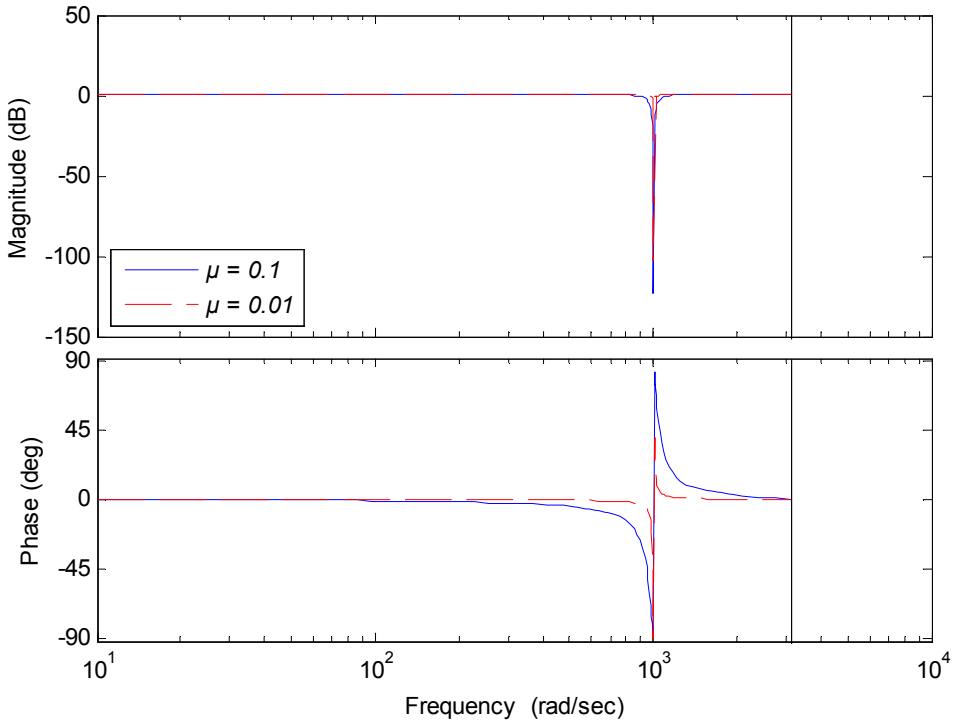

Figure 3.17 Magnitude and phase response of $H(z)$

The responses are the form of a notch filter with the notch frequency equal to 1000 rad/s. The secondary-path transfer function $S(z)=1$, thus, $A_s=1$ and $\phi_s=0$. The amplitude of

reference signal $A = 1$. The value of μ determines the width of the notch. It can be seen that the notch becomes sharper when μ decreases.

The accuracy of the estimated secondary path $\hat{S}(z)$ can be deduced with slow adaptive convergence speed ($\beta \to 0$). In this case the transfer function of the narrowband ANC system becomes

$$H(z) = \frac{z^2 - 2z\cos(\omega_0 \Delta t) + 1}{z^2 - [2\cos(\omega_0 \Delta t) - \beta\cos(\omega_0 \Delta t - \phi_\Delta)]z + 1 - \beta\cos\phi_\Delta} \tag{3.65}$$

where

$$\phi_\Delta = \phi_s - \phi_{s'} \tag{3.66}$$

is the phase difference between $S(z)$ and $\hat{S}(z)$ at the frequency ω_0.

The stability of $H(z)$ can be investigated by analysing the pole locations of this second-order system. For small β, $H(z)$ has complex conjugate poles at radius

$$r_p = \sqrt{1 - \beta\cos\phi_\Delta} \tag{3.67}$$

Since μ, A, $A_s > 0$, the radius of the pole can be greater than 1 only if $\cos\phi_\Delta$ is negative. Therefore, the stability condition can be given by

$$\cos\phi_\Delta > 0 \tag{3.68}$$

or

$$-90^\circ < \phi_\Delta < 90^\circ \tag{3.69}$$

This shows that the phase difference between $S(z)$ and $\hat{S}(z)$ must not exceed 90º for system stability.

3.4.2 Multiple harmonics cancellation using the FXLMS algorithm

Periodic noise usually contains tones at the fundamental frequency and at several harmonic frequencies. These multiple sinusoidal interferences can be cancelled by extension of the basic adaptive notch filter technique to multiple notches. For the case in which the undesired primary noise contains M harmonics, M two-weight adaptive filters

can be connected in parallel to cancel these periodic components. Figure 3.18 shows the configuration of parallel narrowband ANC system.

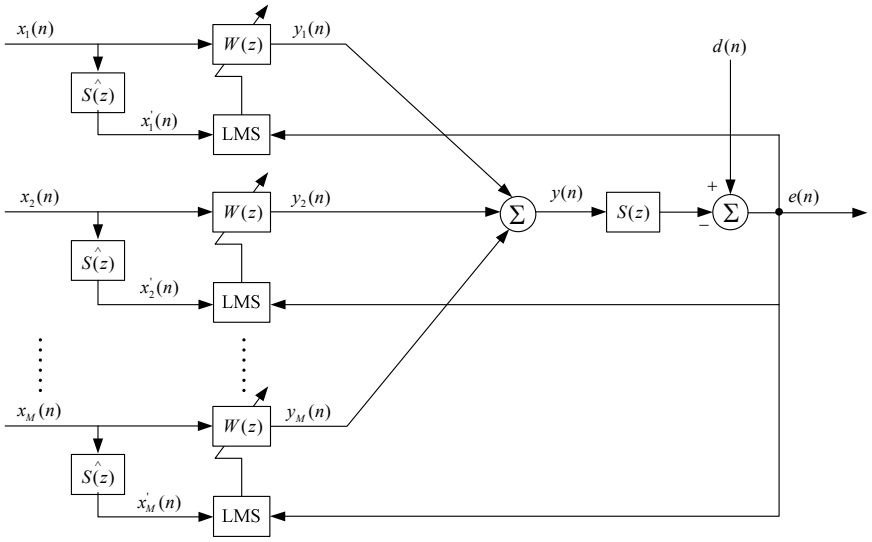

Figure 3.18 Multiple-frequency ANC system using FXLMS algorithm in parallel

The reference inputs are now given by

$$x_m(n) = A_m \cos(\omega_m n\Delta t), \quad m = 1, 2, ..., M. \tag{3.70}$$

The cancelling signal is a sum of M adaptive filter outputs

$$y(n) = \sum_{m=1}^{M} y_m(n), \qquad m = 1, 2, ..., M. \tag{3.71}$$

$$y_m(n) = w_{m,0}(n)\mathbf{x}_{m,0}(n) + w_{m,1}(n)\mathbf{x}_{m,1}(n) \tag{3.72}$$

where $x'_{m,0}(n)$ and $x'_{m,1}(n)$ are the filtered reference signals with 90º phase difference.

The filter weights can be updated based on FXLMS algorithm

$$w_{m,0}(n+1) = w_{m,0}(n) + \mu x'_{m,0}(n)e(n), \qquad m = 1, 2, ...M \tag{3.73}$$

$$w_{m,1}(n+1) = w_{m,1}(n) + \mu x'_{m,1}(n)e(n), \qquad m = 1, 2, ...M \tag{3.74}$$

in which m is the channel index.

3.5 Simulation studies for active noise cancellation

3.5.1 Single frequency cancellation

A simulation model was created using MATLAB Simulink. The primary noise was modelled as a sinusoidal signal $d(n) = \sin(40\pi n\Delta t)$.

3.5.1.1 Single frequency cancellation using the LMS offline identification technique

The LMS offline technique was applied firstly to validate the performance of controller. The dynamics of secondary path $S(z)$ used were shown in Figure 3.8. The convergence rate of the adaptive notch filter was $u_c = 5\times10^{-4}$ and the sampling frequency was 10 kHz. Results of cancellation plotted in the time domain are shown in Figure 3.19, where good cancellation was obtained after a short adaptive period.

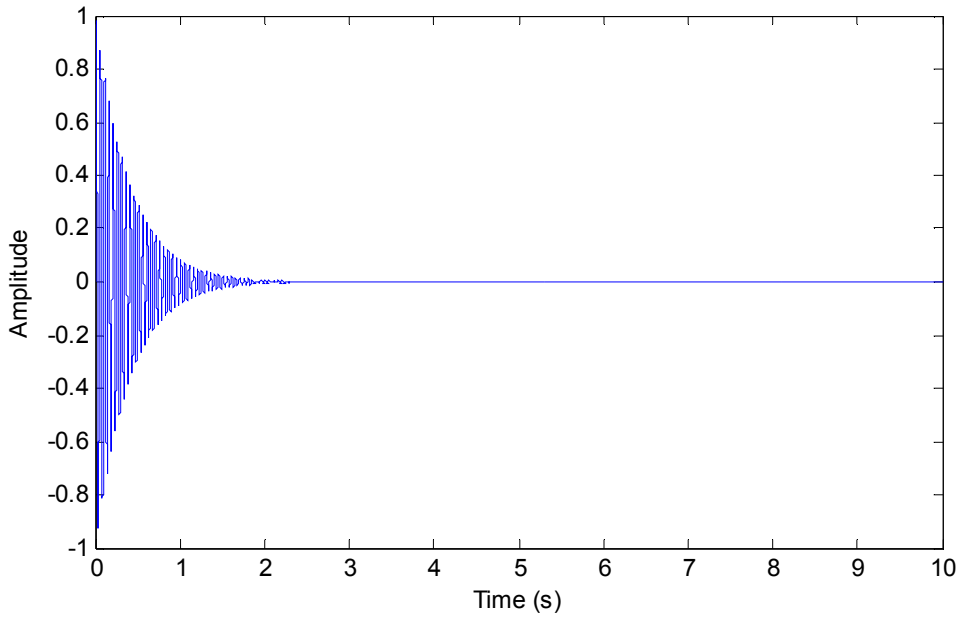

Figure 3.19 Cancellation of primary noise by using LMS offline technique

3.5.1.2 Single frequency cancellation using the LMS online identification technique

The LMS online time-domain technique was then implemented using white noise with a variance of 1×10^{-5} for secondary path $S(z)$ identification. The filter length was 512 and

the convergence factors for identification and noise cancellation were $\mu_i = 1\times10^{-2}$ and $\mu_c = 5\times10^{-4}$. Figure 3.20 shows the cancellation achieved by using LMS online time-domain technique. It can be seen that the adaptive period is longer than using offline technique, although the convergence factors are equal. For clear explanation, the tap weights of the adaptive notch filter are plotted for comparison of using LMS offline and online time-domain techniques in Figure 3.21. It is clearly shown that about 5s adaptive time is required for LMS online technique and only half that for offline technique. The optimum weights obtained at the end are $w_1 = 0.9$ and $w_2 = 0.3$ in both cases.

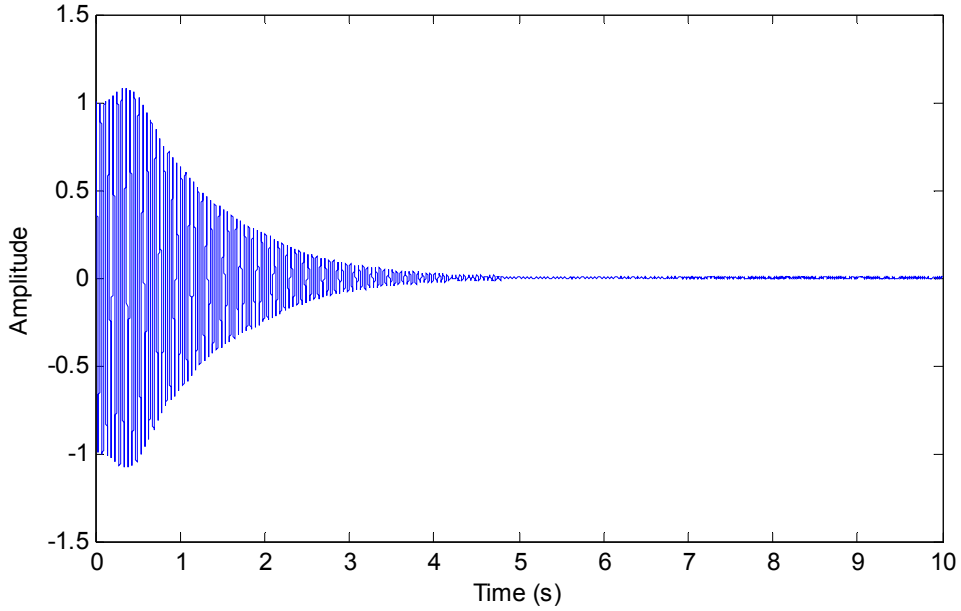

Figure 3.20 Cancellation of primary noise by using LMS online time-domain technique with 10s

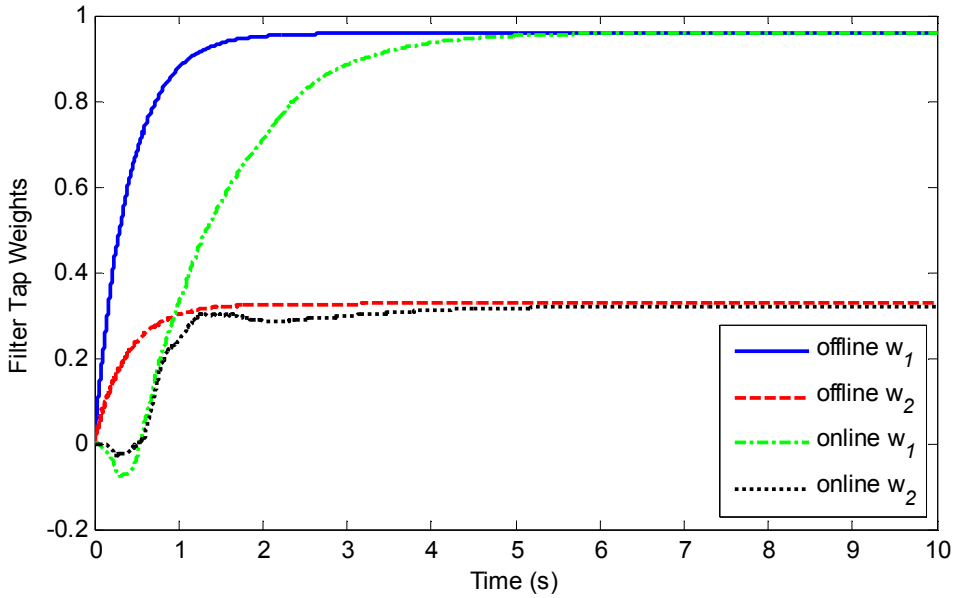

Figure 3.21 Tap weights of adaptive notch filter.

It is worth mentioning that the dynamics of the secondary path $S(z)$ achieved from the identification filter which worked in parallel with the cancellation process were inaccurate in this case. Figure 3.22 shows the frequency response of $S(z)$. It can be seen that the phase difference at the frequency of 20Hz is nearly 30 degrees. The noise canceller can still give good performance in terms of the stability conditions (equation 3.61). However, the system is sensitive to the disturbance and may even become unstable when the parameters change slightly. The phase and amplitude differences are the result of the disturbance from the primary noise. The power of primary noise was much greater than the power of white noise, which caused the inaccuracy and slow convergence of the identification filter.

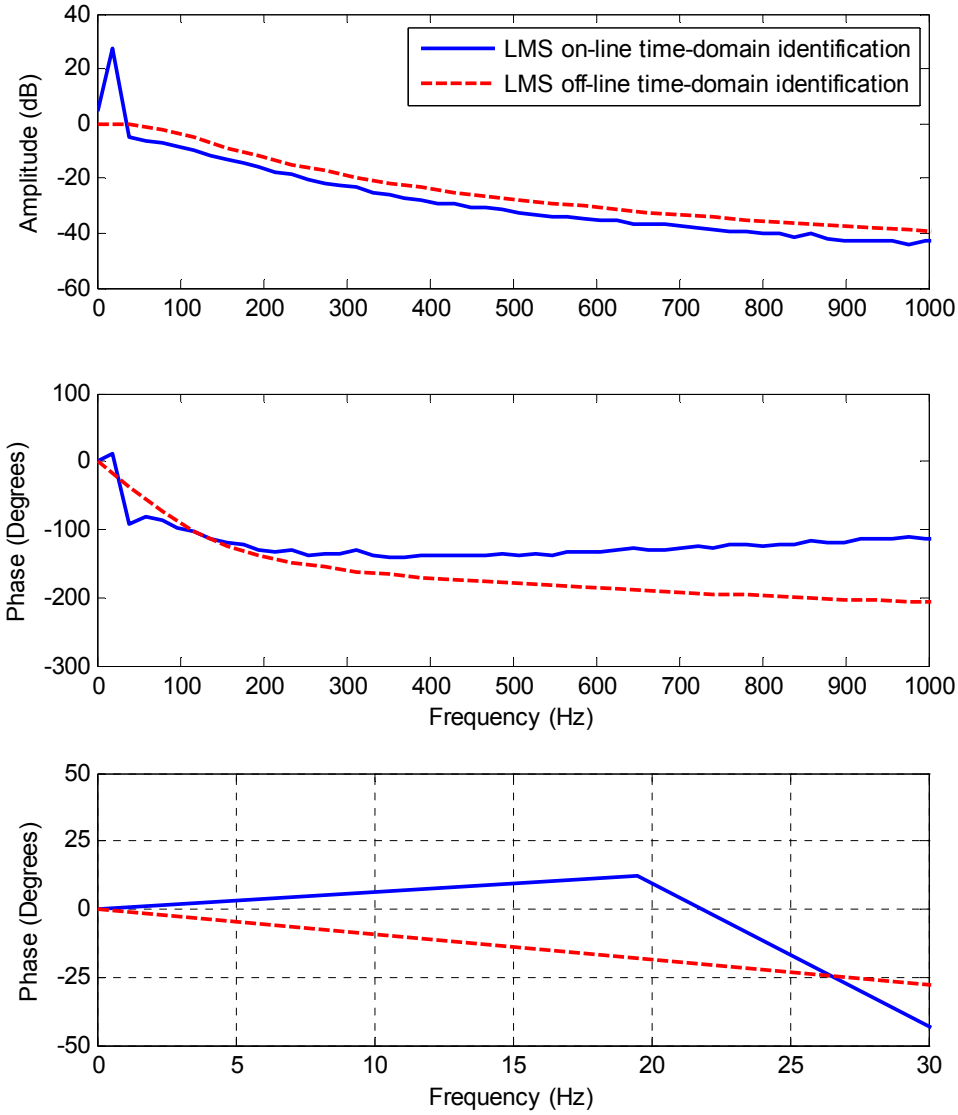

Figure 3.22 Frequency response of secondary path $S(z)$ achieved by using LMS online identification technique

Two methods could be used to eliminate this problem. One is switching on the identification filter alone before switching on the primary noise and controller. This process can help to get accurate secondary path dynamic beforehand, which would be less affected by the primary noise. The other way is to lengthen the simulation time and increase the power of the white noise and the convergence factor of the identification filter. This is effective to obtain more accurate secondary path dynamics at the expense of longer processing time and worse performance of cancellation. Moreover, the convergence factor is also limited by the stability criterion of the system itself. Therefore, a compromise should be made according to the specific conditions. Figure

3.23 gives the results of attenuation by applying LMS online time-domain technique using a white noise with a variance of 5×10^{-4} and a convergence factor of μ_i=1×10^{-1} for identification. The convergence rate of the controller ($\mu_c = 5\times10^{-4}$) remains the same as in the previous case. The simulation time increased from 10s to 30s. As can be seen, the adaptive process is more stable than the previous case. This is because the achieved dynamics of the secondary path $S(z)$ are much more accurate and are able to effectively be used in the FXLMS control algorithm. Moreover, a short period 2s at the beginning is applied for identification without the primary noise and attenuator. The details of the secondary path are plotted in Figure 3.24, where the results are more close to the one achieved from the offline technique, although there are still slight amplitude and phase differences in the high frequency range.

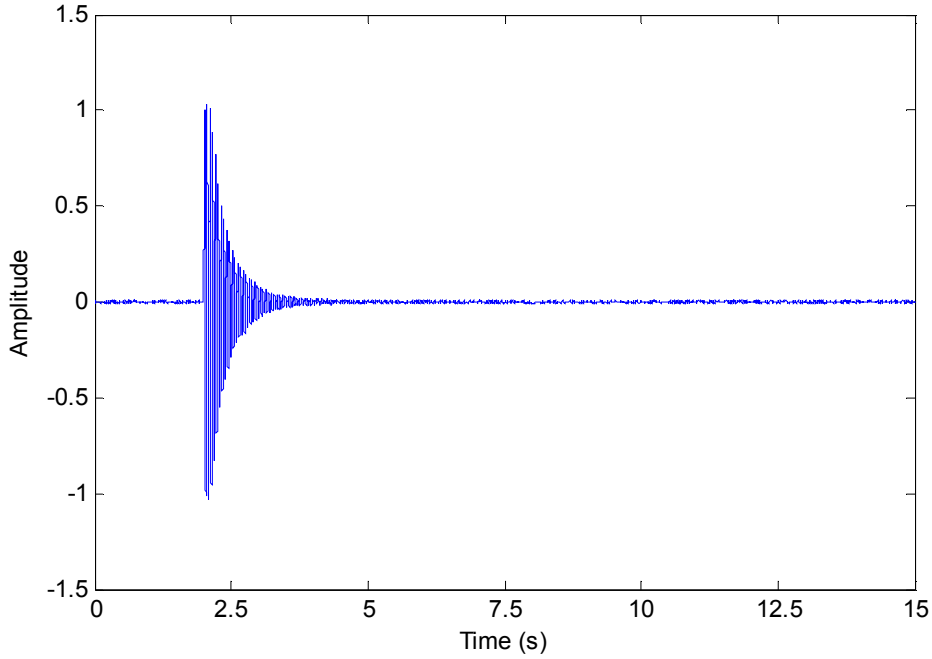

Figure 3.23 Cancellation of primary noise by using LMS online time-domain technique with 15s

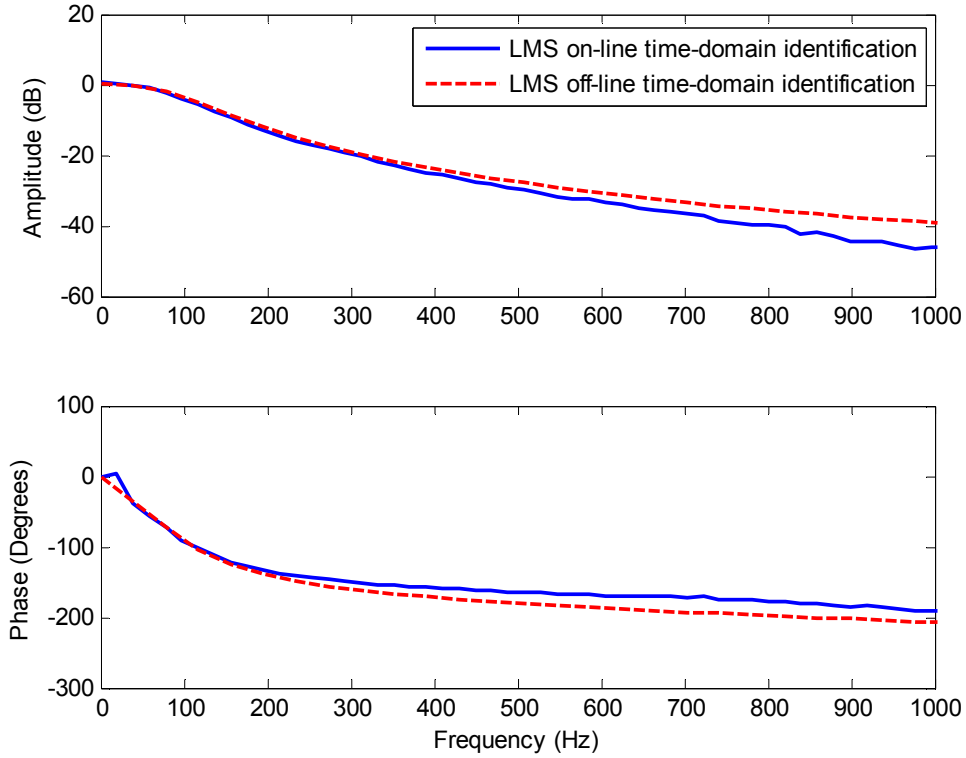

Figure 3.24 Amplitude and phase characteristics of secondary path $S(z)$ with longer simulation time and larger white noise and convergence factor for identification

3.5.1.3 Single frequency cancellation using the FBLMS online identification technique

The FBLMS online frequency-domain technique was also used for secondary path identification. Similar simulation parameters to the first LMS online time-domain technique were re-applied. The variance of white noise was 1×10^{-5} and the convergence rate of the controller was $\mu_c = 5\times10^{-4}$. The simulation time was 10s. The amplitude and phase characteristics of secondary path $S(z)$ are plotted in Figure 3.25, where good agreement was achieved. As can be seen from Figure 3.26, a short period 2s was also employed for identification at the beginning of the processing and good noise cancellation was obtained. Therefore, the FBLMS algorithm is an effective and robust solution for secondary path identification in the online technique.

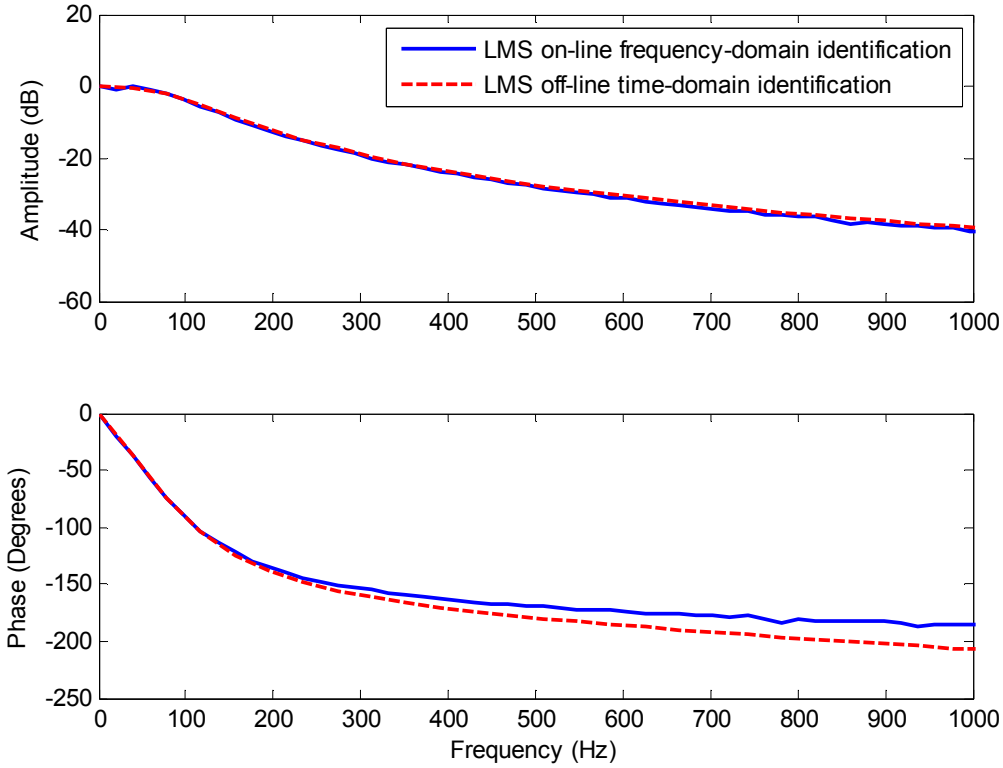

Figure 3.25 Amplitude and phase characteristics of secondary path $S(z)$ by using FBLMS frequency-domain identification technique

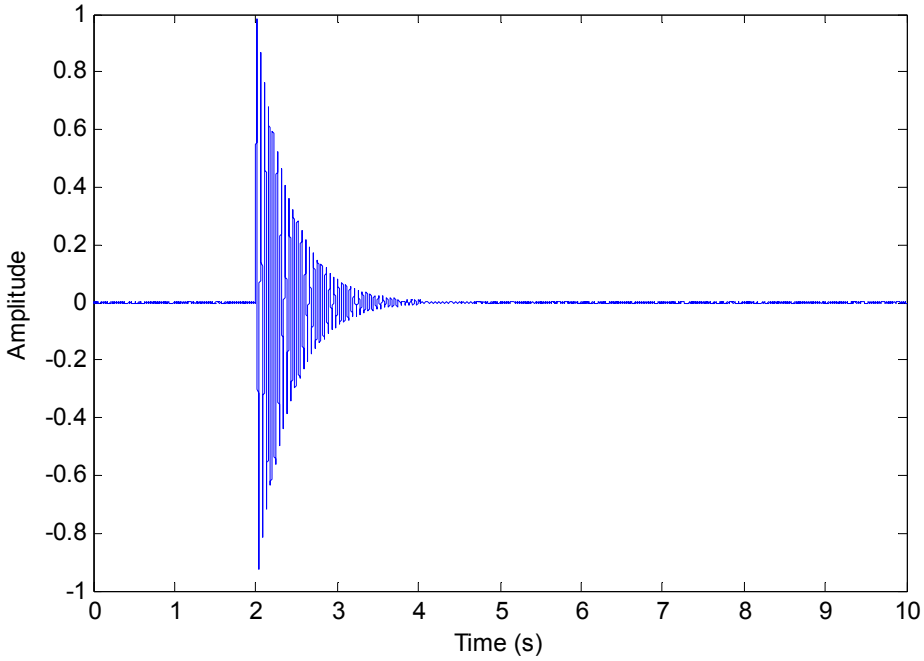

Figure 3.26 Cancellation of primary noise by using FBLMS online frequency-domain technique with 10s

To conclude, the LMS offline time-domain technique is effective for single frequency noise cancellation. An efficient and stable FXLMS noise canceller has been modelled and successfully tested with specific cases in Simulink. Moreover, the LMS online time-domain technique is studied by using different approaches, which were compared based on the same simulated parameters. It can be concluded that the LMS time-domain technique is able to achieve the expected results at the expense of larger residual error and longer computation time. In addition, the FBLMS online technique is an improved approach which could give stable and accurate results and fast computation for secondary path identification in noise attenuation systems.

3.5.1.4 Discussion

The simulated results show that the performance of a noise attenuator depends mainly on two factors: the accuracy of the secondary path identification and the convergence speed of the cancellation filter. The convergence rate of the cancellation filter would benefit from accurate estimates of secondary path dynamics which are used to filter the reference signal. The secondary path characteristic is represented as an impulse response by using weight taps within the LMS technique. The Fast Fourier Transform (FFT) was used to obtain the frequency response based on the impulse response.

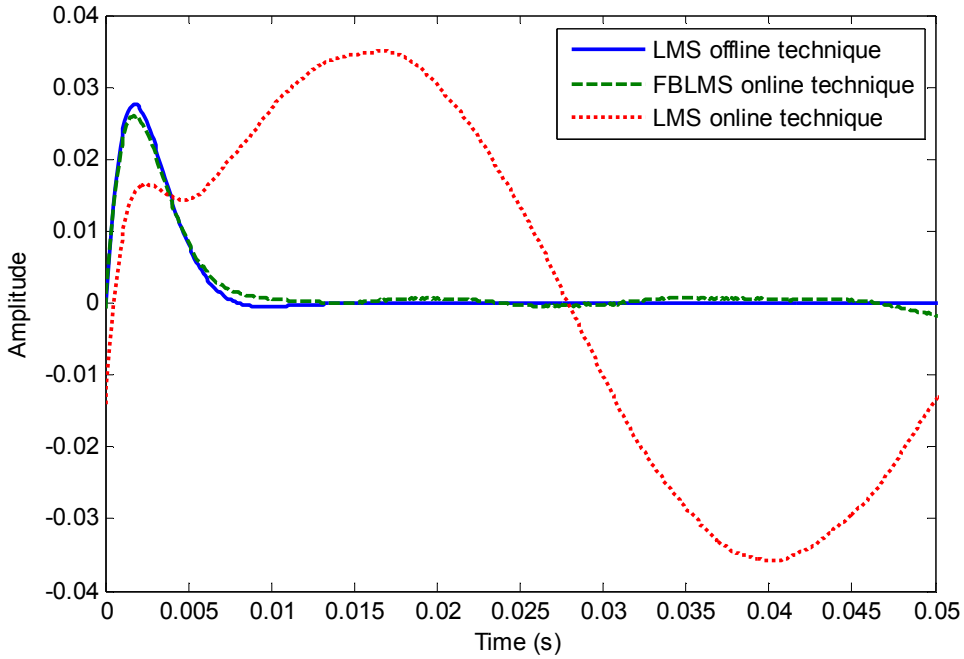

Figure 3.27 Impulse responses of the secondary path identification by using different LMS techniques

Figure 3.27 shows the impulse responses of the secondary path dynamics estimated using different LMS techniques. It can be seen that the result from the FBLMS online method is much closer to the result using the LMS offline technique and both of them converged to a small value. On the other hand, the impulse response obtained by using the LMS offline technique did not converge but had oscillations with a frequency of 20Hz due to the primary noise. This may cause instability of the identification filter or even destabilise system stability when the noise attenuator operates.

3.5.2 Multiple harmonics cancellation

In practice, the real system doesn't only contain a single harmonic but contains multiple harmonics. The structure of a multiple harmonic cancellation system was modelled based on Figure 3.16 and the offline and online identification techniques were applied separately for comparison. The primary noise was modelled as

$$d(n) = \sum_{k=1}^{5} \sin(40k\pi n\Delta t) \tag{3.75}$$

The fundamental frequency of the system was 20Hz and 5 harmonics (20Hz, 40Hz, 60Hz, 80Hz and 100Hz) were taken into consideration.

3.5.2.1 Multiple harmonics cancellation using the LMS offline identification technique

The LMS offline technique was applied to validate the performance of the attenuator for multiple harmonic cancellation. The dynamics of secondary path $S(z)$ are shown in Figure 3.8. Different convergence rates of the sub-controller (adaptive notch filter) were used as listed in Table 3.1, and the sampling frequency was 10kHz. The result of cancellation is plotted in Figure 3.28, where good cancellation was obtained after a short adaptive period.

Table 3.1 Convergence rates used for difference harmonics using LMS offline time-domain technique

Frequency (Hz)	20	40	60	80	100
Convergence rate μ_c	5×10^{-4}	6×10^{-4}	7×10^{-4}	8×10^{-4}	8×10^{-4}

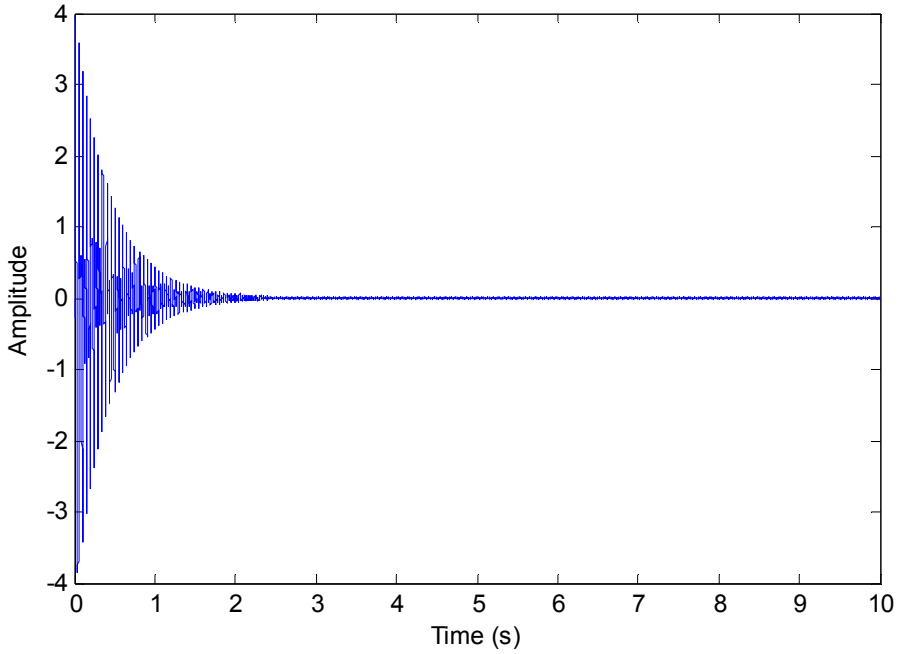

Figure 3.28 Multiple frequency cancellation of primary noise by using LMS offline time-domain technique with 10s

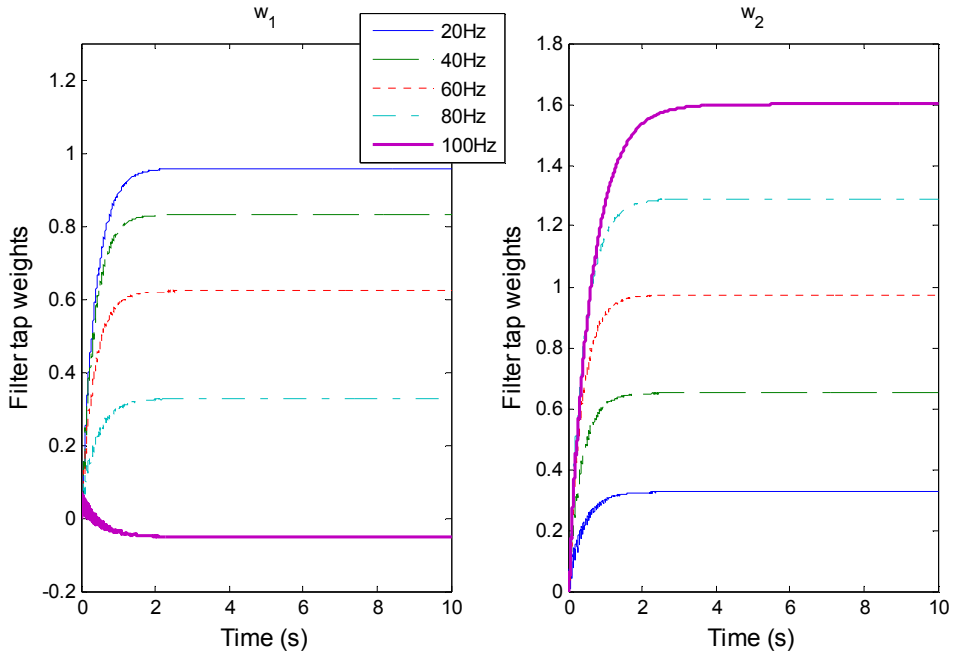

Figure 3.29 Filter tap weights of different sub-controllers using LMS offline technique

Figure 3.29 shows the filter weights of different sub-controllers. It can be found that after 2s the filters converged and the tap weights reached the optimal values which are described in Table 3.2.

Table 3.2 optimal values of weights for different harmonics using LMS offline time-domain technique

Frequency (Hz)	20	40	60	80	100
Optimal value of w_1	0.9579	0.8317	0.6215	0.3271	-0.0513
Optimal value of w_2	0.3262	0.6508	0.9724	1.289	1.6000

3.5.2.2 Multiple harmonics cancellation using the LMS online identification technique

The LMS online technique was applied for the same primary noise source as shown in Equation 3.67. The cancellation result is plotted in Figure 3.30. The first 15s was used for LMS offline identification without switching on the primary noise and noise controller. This can help the system achieve stable performance when the primary noise is introduced (Wang, 2008). The variance of white noise was 5×10^{-4} and the convergence rate for secondary path identification was 9×10^{-2}. Compared with the value used for single harmonic cancellation, the convergence rate was much smaller in this case. This is due to the consideration of system stability; large convergence rate may destabilise the controller at some frequency bins when the disturbance contains different frequency components. The convergence rates of the sub-controller (adaptive notch filter) that were used are listed in Table 3.3.

Table 3.3 Convergence rates used for difference harmonics using LMS online time-domain technique

Frequency (Hz)	20	40	60	80	100
Convergence rate μ_c	8.5×10^{-6}	8.5×10^{-6}	9×10^{-6}	9×10^{-6}	1×10^{-5}

As can be seen, the noise amplitude increased by a factor of two after few seconds, although the adaptive controller adjusted the weights efficiently and successfully and achieved good cancellation later. However, the residual error still contained the components of the primary noise, which means the noise control filter didn't converge completely and the weights didn't come to the optimal values in this case. This would introduce the potential risk of system instability. The weights w_1 and w_2 are plotted in Figure 3.31 and the steady state values are listed in Table 3.4.

Table 3.4 Value of weights for different harmonics using LMS online time-domain technique

Frequency (Hz)	20	40	60	80	100
value of w_1	-0.9583	-0.3259	-0.6416	-0.3726	0.0337
value of w_2	-0.8316	-0.6505	-1.0110	-1.3000	-1.647

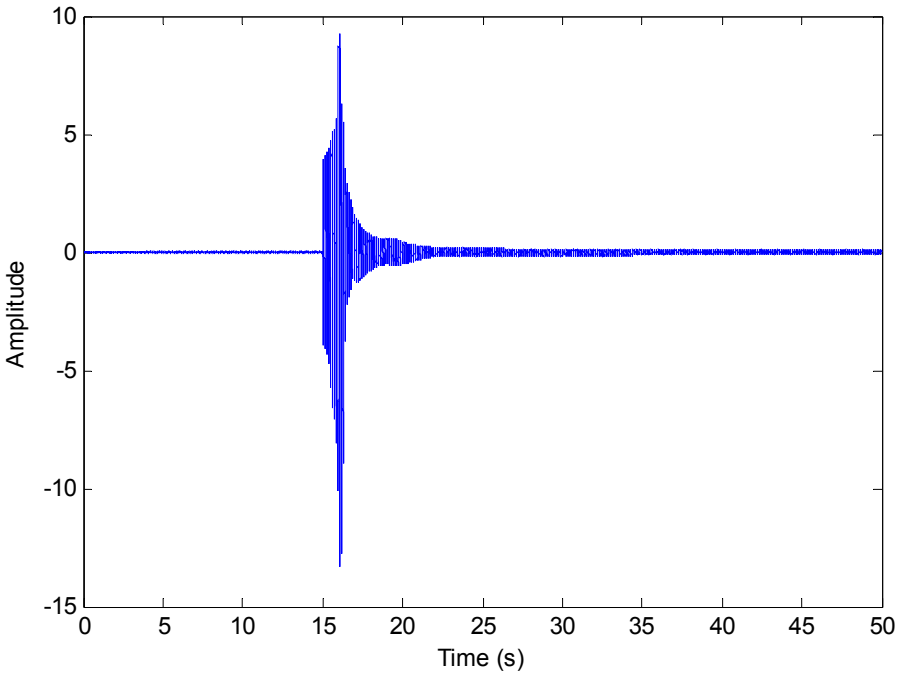

Figure 3.30 Multiple harmonics cancellation of primary noise by using LMS online time-domain technique with 50s

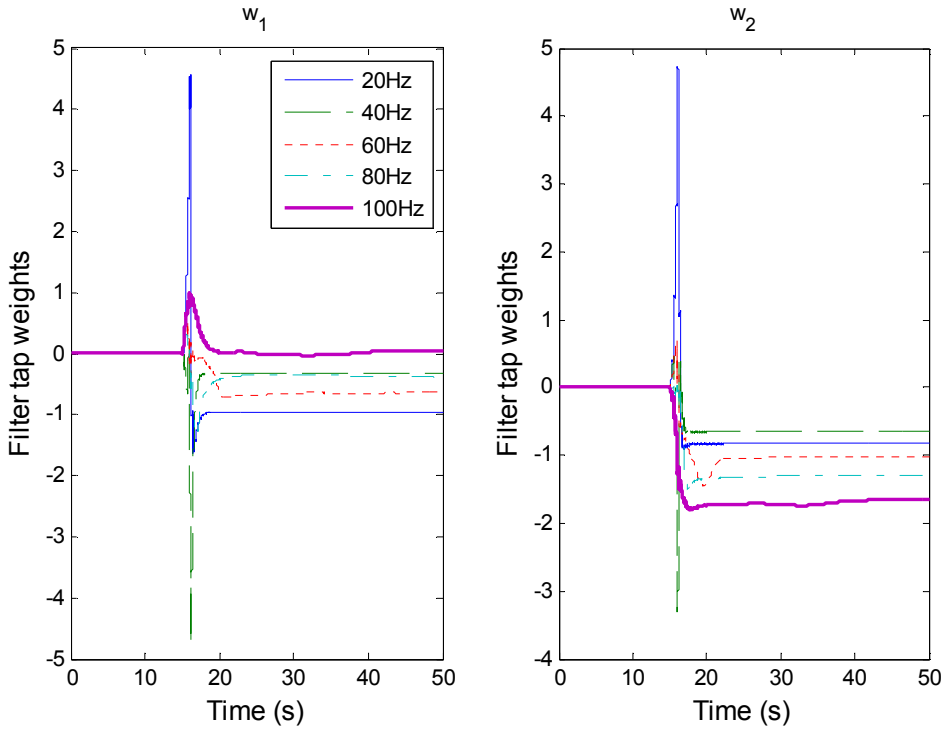

Figure 3.31 Filter tap weights of different sub-controller using LMS online technique

System stability can also be affected by the convergence factors of the noise control filters. It can be noticed that the convergence rates used for the LMS online technique were much smaller than for the LMS offline technique. This is because the selection of the convergence rates has to be a compromise to the inaccurate amplitude and phase which were achieved from the LMS online identification in order to get stable performance. The frequency response using the LMS online technique is shown in Figure 3.32.

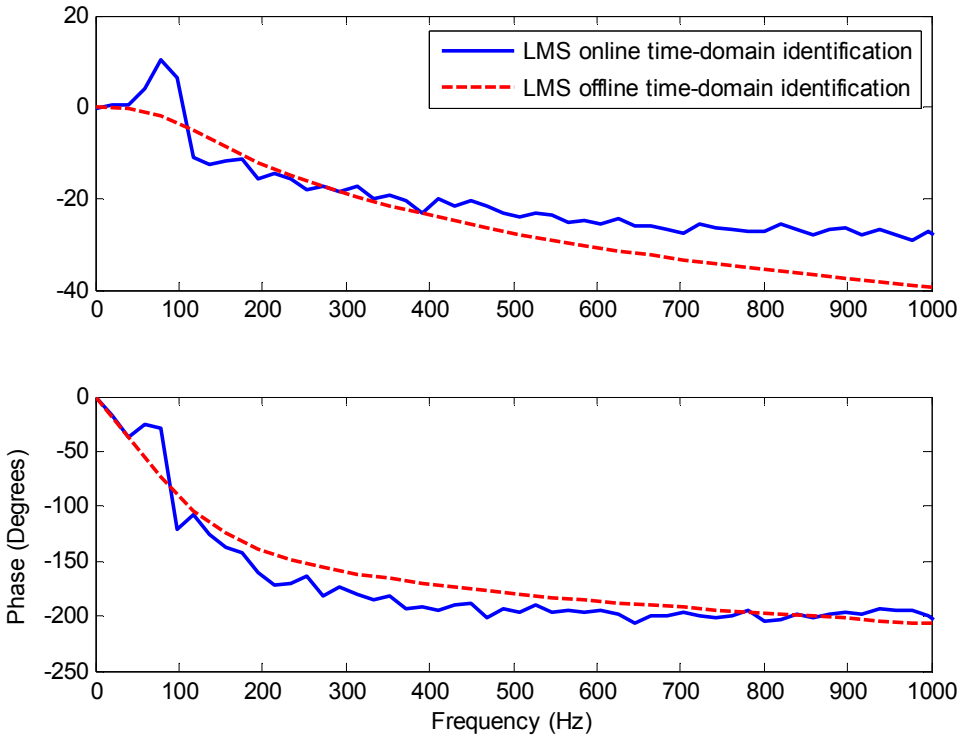

Figure 3.32 Amplitude and phase characteristics of secondary path using LMS online time-domain identification technique

The FBLMS online technique was applied using the same model parameters as used in the LMS offline technique test for multiple harmonic cancellation. The results are shown in Figure 3.33, where good cancellation was achieved in 10s. The variance of the white noise was 1×10^{-5} and the convergence rates are listed in Table 3.5.

Table 3.5 Convergence rates used for difference harmonics using FBLMS online frequency-domain technique

Frequency (Hz)	20	40	60	80	100
Convergence rate μ_c	5×10^{-4}	6×10^{-4}	7×10^{-4}	8×10^{-4}	8×10^{-4}

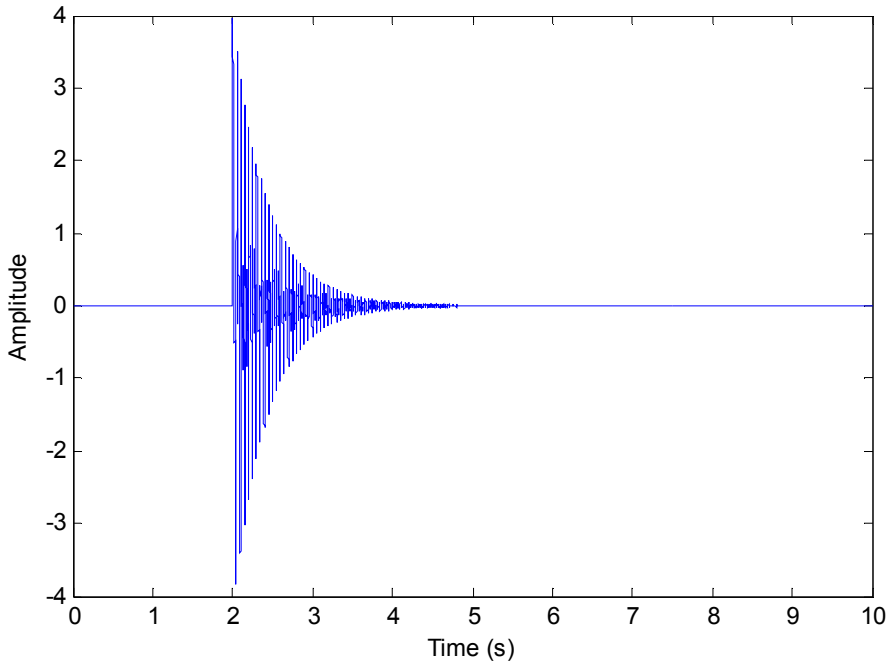

Figure 3.33 Multiple frequency cancellation of primary noise using FBLMS online frequency-domain technique

Figure 3.34 shows the filter tap weights of different sub-controller. It can be seen that the weights adapted at the beginning of 2s after switching on the controller then reached to the stable values. The weights values are listed in Table 3.6. Compared with Table 3.2, it can be said that the optimal tap weights were obtained. This is mainly because a stable and accurate estimate of secondary path dynamics was achieved by using the FBLMS online technique.

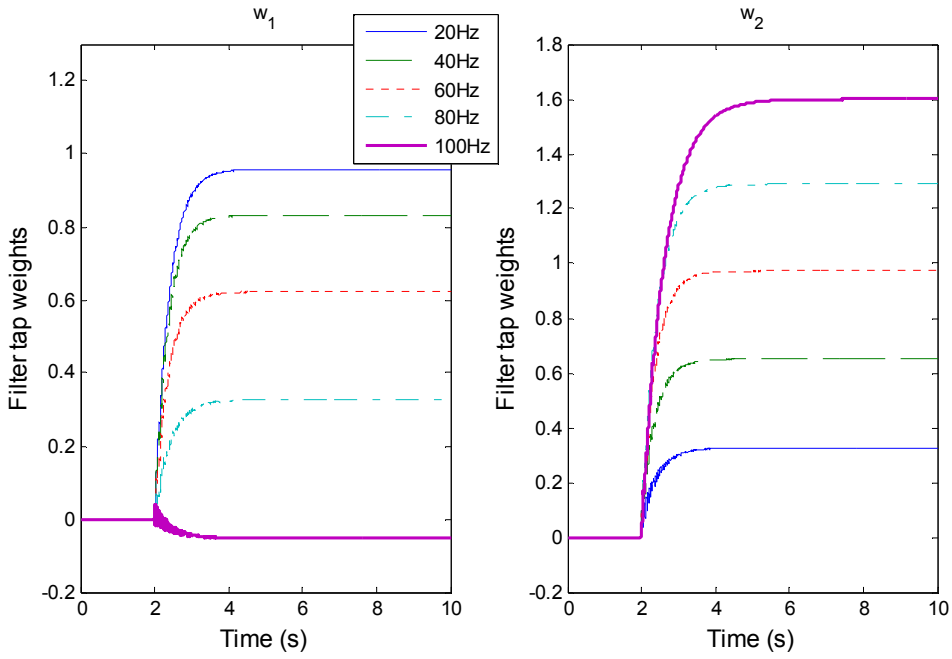

Figure 3.34 Filter tap weights of different sub-controller using FBLMS online frequency-domain technique

Table 3.6 Weight values for different harmonics using FBLMS online frequency-domain technique

Frequency (Hz)	20	40	60	80	100
value of w_1	0.9579	0.8317	0.6215	0.3270	-0.0513
value of w_2	0.3262	0.6508	0.9725	1.289	1.6

The frequency response of the secondary path is shown in Figure 3.35 where good agreement was obtained between the curves achieved from the LMS offline technique and FBLMS online technique, especially at the low frequency range.

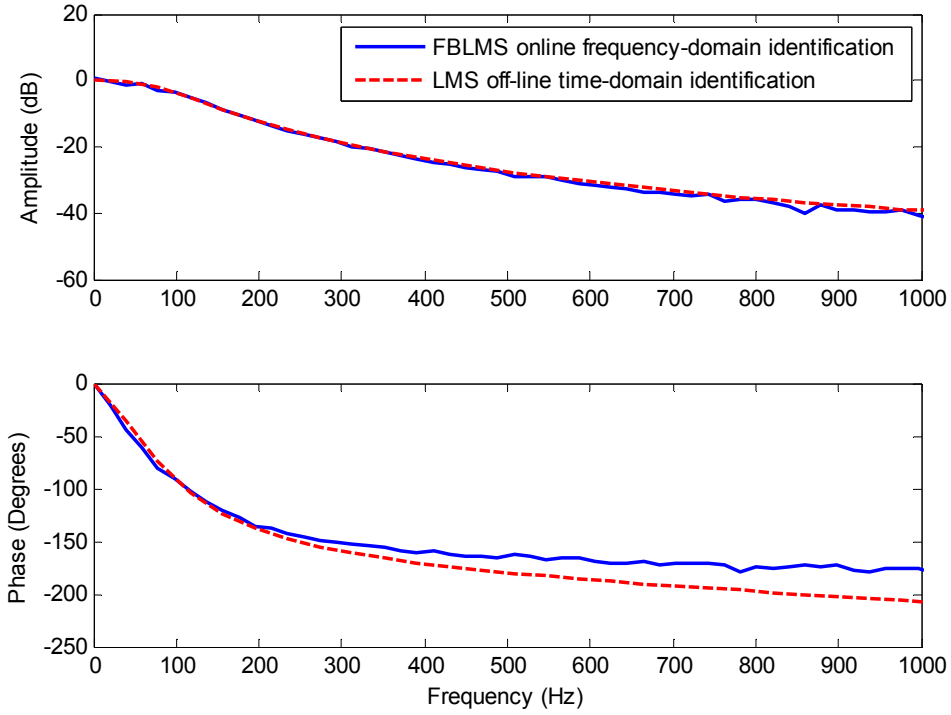

Figure 3.35 Amplitude and phase characteristics of secondary path using FBLMS online frequency-domain technique

To conclude, multiple harmonic frequencies can be cancelled by using parallel adaptive notch filters with the FXLMS algorithm. Different convergence rates were employed for different notch filters. The performance of the noise attenuator is highly related to the accuracy of the secondary path identification. The LMS offline technique is effective to achieve a good estimate of the dynamics of the secondary path, but has the disadvantage that it cannot respond to time-varying system dynamics. For the online technique, the LMS time-domain method is sensitive to the disturbance from the noise components. This may cause slow convergence speed of the identification filter and poor performance of the noise cancellation. As an alternative technique, the FBLMS frequency-domain method is much more stable and robust under the same conditions. Good cancellation and stable results were achieved by using this algorithm.

3.6 Concluding remarks

The derivation of the FXLMS algorithm has been introduced. The implementations of FXLMS for active narrowband noise control have been investigated via simulation examples. Base upon these investigations the FXLMS algorithm with FBLMS

frequency-domain online system identification has been proved as the most appropriate combination due to its robustness to destabilising signal content. This was applied and validated in the experimental studies described in Chapter 4 and 8.

4 Experimental studies: vibration rig tests

The FXLMS controller was applied to a vibration rig in order to gain an understanding of the real-time implementation and performance of the control strategy prior to hydraulic testing. The controller was initially applied to an engine mount vibration system to cancel a single frequency. Next multiple harmonics are introduced in undesired noise, and finally the performance of controller for a sudden frequency change is investigated.

4.1 Experimental rig

An experimental rig used for research into the adaptive control of active engine mounts (Hillis, 2005) was re-applied for the purpose of an initial investigation of the controller for the following issues before a hydraulic rig was available for further testing and experiments:

- Real-time implementation issues;
- Control of narrowband noise;
- Effects and potential problems.

Figure 4.1 shows a schematic of the electronic hardware of test rig.

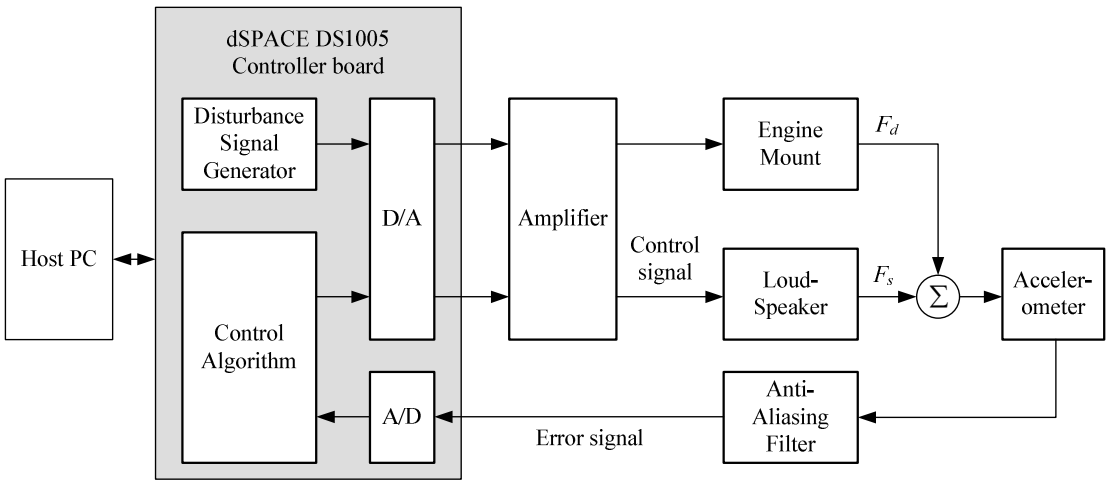

Figure 4.1 Schematic of the electronics hardware of test rig (Hillis, 2005)

A schematic diagram of the test rig is shown in Figure 4.2.

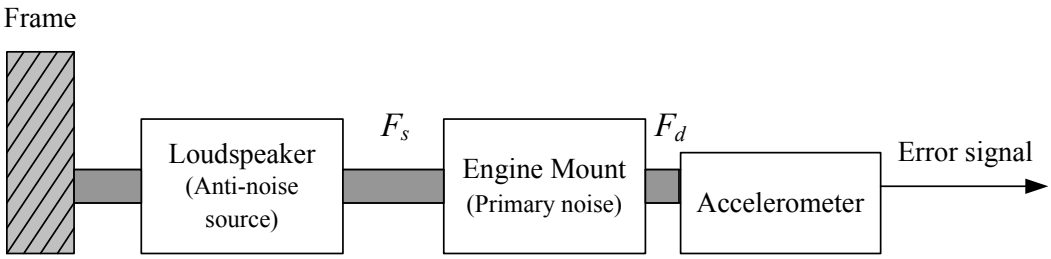

Figure 4.2 Schematic of the test rig

The active engine mount was used to generate sinusoidal disturbance forces F_d simulating an undesired source, and was limited to operation in the range of 10Hz to 700Hz using a low-pass filter. The signal used to generate these disturbances was either generated by the dSPACE system, or by a function generator. The cancelling force F_s was generated by the loudspeaker and was dependent upon the control signal supplied by the control algorithm. A Europower EP1500 amplifier and an accelerometer were used and the FXLMS algorithm was implemented using a dSPACE DS1005 controller board sampling at a time step of 0.3ms. A photograph of the test rig is shown in Figure 4.3.

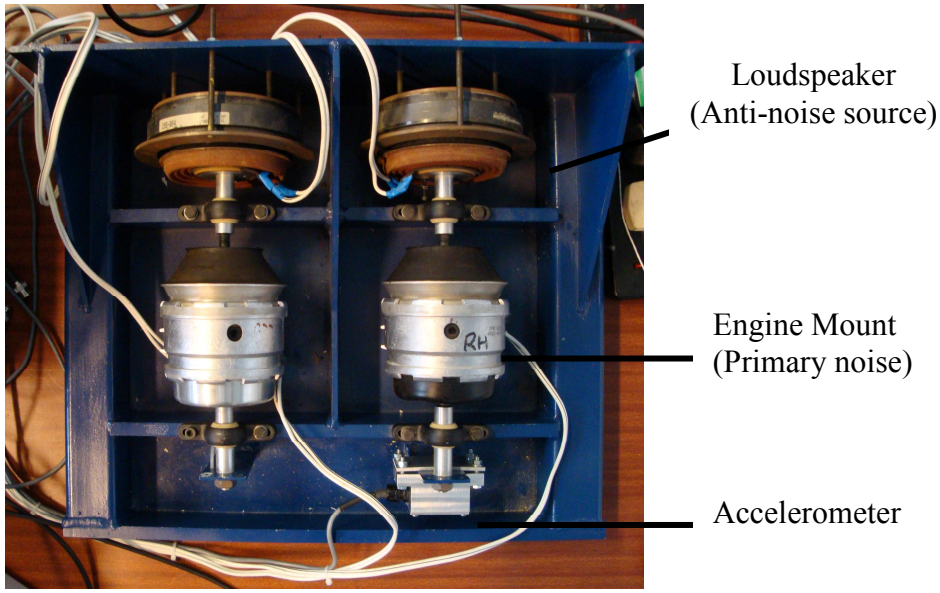

Figure 4.3 Photograph of the experimental rig

4.2 System identification

The characteristics of the experimental rig were determined using standard system identification method. The output $O(n)$ and input $I(n)$ signals of an unknown system

driven by a random noise were recorded and transformed to frequency domain by using Fast Fourier Transform (FFT) technique. The frequency response can be obtained by:

$$S(j\omega) = \frac{O(j\omega)}{I(j\omega)} \tag{4.1}$$

where $O(jw)$ and $I(jw)$ are the Fourier transforms of output and input signals.

Under laboratory conditions, a low level white noise source (0-1000Hz) was generated within the controller board and used as the actuator signal. The input and output voltages of the loudspeaker were recorded and applied to estimate the system characteristics. For the purpose of comparison, a frequency analyzer was used to obtain the frequency response of secondary path by sweeping a sinusoidal signal through a range of frequencies.

Figure 4.4 shows the frequency response of the loudspeaker achieved from standard system identification technique and frequency analyzer. The amplitude and phase response agreed well apart from some points with environmental noise.

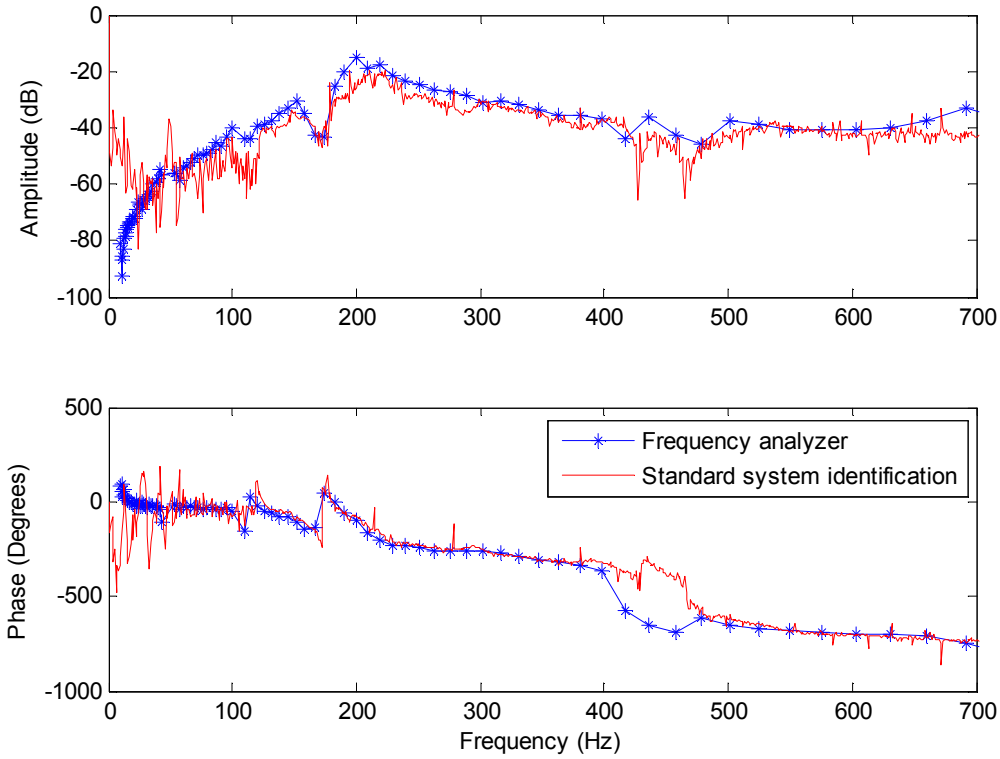

Figure 4.4. Magnitude and phase response of the loudspeaker using frequency analyzer and standard system identification technique

The LMS off-line technique was implemented to validate the effectiveness for secondary path identification. The length of FIR filter was 512 which is long enough to capture the characteristics of the secondary path. Figure 4.5 shows the impulse response of the loudspeaker using the LMS offline technique. The FFT technique was applied for transforming the impulse response of the loudspeaker to frequency response.

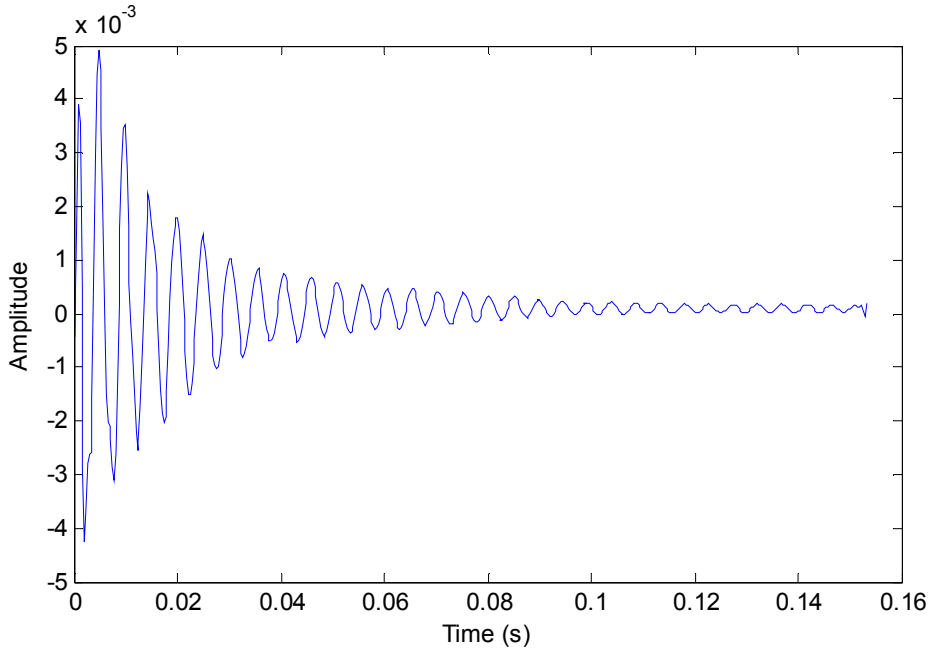

Figure 4.5 Impulse response of secondary path actuator

The amplitude and phase responses of loudspeaker achieved from FIR filter are shown in Figure 4.6, where the LMS offline time-domain and FBLMS offline techniques were used for identification. It can be seen that good agreement was obtained between the experimental result and the result from the frequency analyser in the range of frequency from 10Hz to 480Hz. The peak magnitude occurred at nearly 200Hz. It is also can be seen a phase shift becomes obvious for the frequencies above 500Hz. This is because the FIR filter used to achieve the impulse response of loudspeaker was not completely converged, or the length of filter was not long enough to capture the whole characteristics of the secondary path actuator, so that phase errors occurred after doing FFT technique for frequency analysis. The frequency resolution was also affected by the length of the impulse response. The longer the length of the filter, the more accurate frequency response could be achieved.

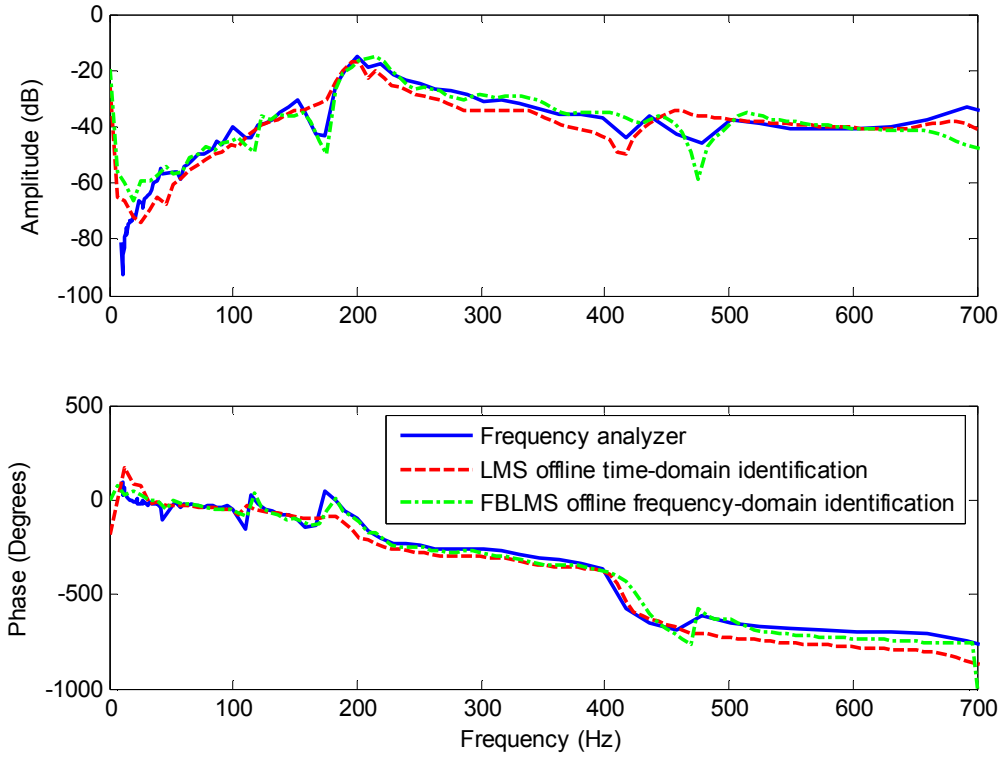

Figure 4.6 Frequency response of secondary path using LMS filter for identification

4.3 Experiments with narrowband noise cancellation

4.3.1 Frequency estimator implementation

As stated in chapter 3, the noise controller requires a reference signal at the precise disturbance frequency to generate the accurate anti-phase signal. In practice, the frequency components included in the disturbance are unknown and not specific in most cases, so that it is difficult to specify the frequency of reference signal before switching on the controller. One of the options to solve this problem is using a tachometer or sensor to detect pulse edges that could be used to calculate the disturbance frequency indirectly. In the following tests an auxiliary port of function generator is used to simulate the signal from external devices. The frequency estimator was built using functional blocks in Simulink.

The basic principle of the frequency estimator is illustrated in Figure 4.7. When an edge is detected an interrupt is triggered and the counter is read and reset. The count is a measure of the elapsed time between pulses and hence a measure of the disturbance

frequency. A low pass filter is employed to smooth the value of frequency which is then used to form reference signals with the dSPACE algorithm.

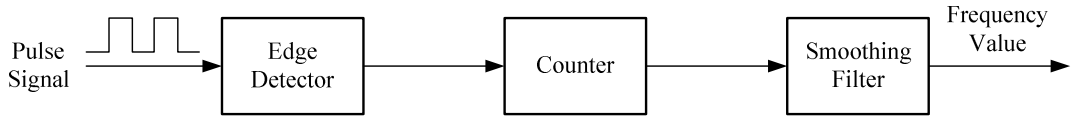

Figure 4.7 Schematic of the implementation of frequency estimator

The frequency estimator was found to be sufficiently accurate for its intended purpose in the test rig, although inaccuracy occurred at high frequencies as the sampling frequency of the dSPACE 1005 controller board was not high enough to catch these frequency components. However, it was also found to be capable of tracking sudden frequency changes.

4.3.2 Single frequency cancellation

In this section a 200Hz disturbance was applied and the controller was switched on with zero initial gains. The amplitude of the residual error signal using secondary path model obtained from off-line identification process is shown in Figure 4.8, where the vibration cancellation achieved was more than 30dB at the frequency of 200Hz. A voltage signal with the amplitude of 1V was used as the reference signal in the data processing. The convergence rate μ_c of the cancellation filter was 1×10^{1} and the sample frequency was 3333Hz.

The 3dB bandwidth B of the adaptive notch filter can be estimated by using the following equation (Haykin, 1996):

$$B \approx \frac{\mu M A^2}{2} \text{ rad/s} \tag{4.2}$$

where μ is the convergence rate, M is the filter length and A is the magnitude of the filtered reference signal.

Therefore,

$$B \approx \mu A^2 \tag{4.3}$$

where

$$A = A_r A_s^{'} \tag{4.4}$$

and $A_s^{'}$ is the magnitude of the estimated cancellation path dynamics $\hat{S}(z)$.

Using equation (4.3), the bandwidth of the notch filter with the frequency of 200Hz, where the secondary path magnitude $A_s^{'}$ is 0.1, can be estimated as 0.02Hz.

The convergence rate μ_c was selected based on equation 3.26. The variance of the filtered reference signal can be estimated and is 0.005. In this case, the theoretical convergence rate μ_c should be below 67. Consider the system stability, 1×10^{1}, which is about one sixth of the upper bound value, was chosen as the convergence rate of the cancellation filter.

Small disturbances also existed at the frequency of 400Hz and 600Hz, although only a 200Hz sinusoidal signal was used for driving engine mount. Particularly, the noise was reinforced rather than cancelled at 600Hz and the amplitude of error was increased by approximately 20dB, but it is still small compared with the peak amplitude at the frequency of 200Hz. These effects are not found in simulation, so are believed to be the results of non-linear behaviour of the rig.

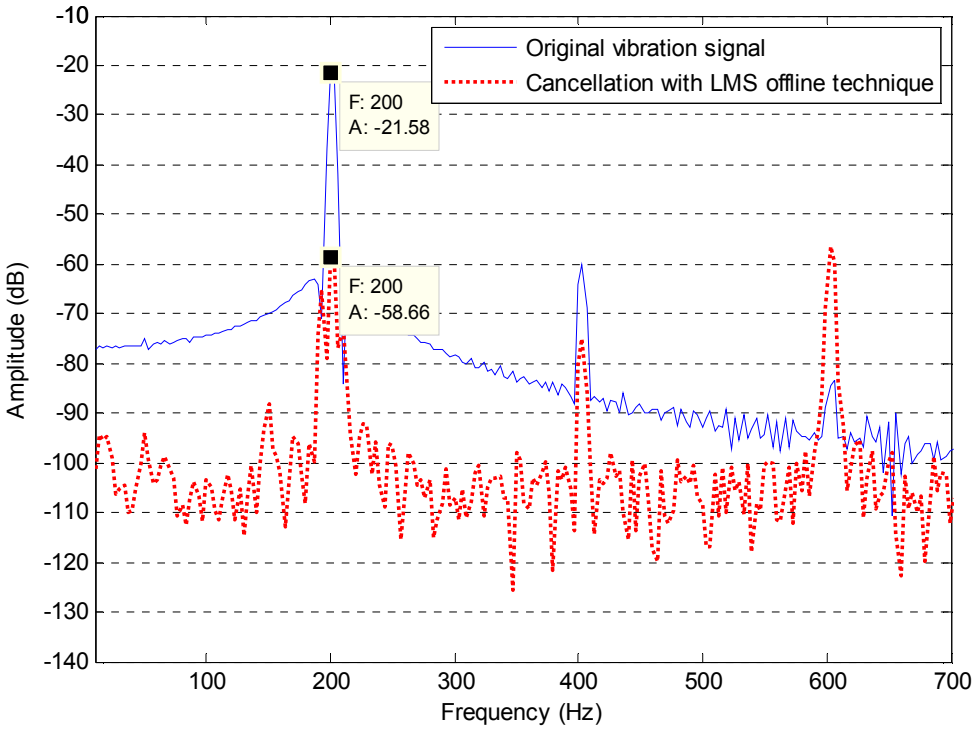

Figure 4.8 Experimental results of vibration cancellation at 200Hz using LMS offline identification technique

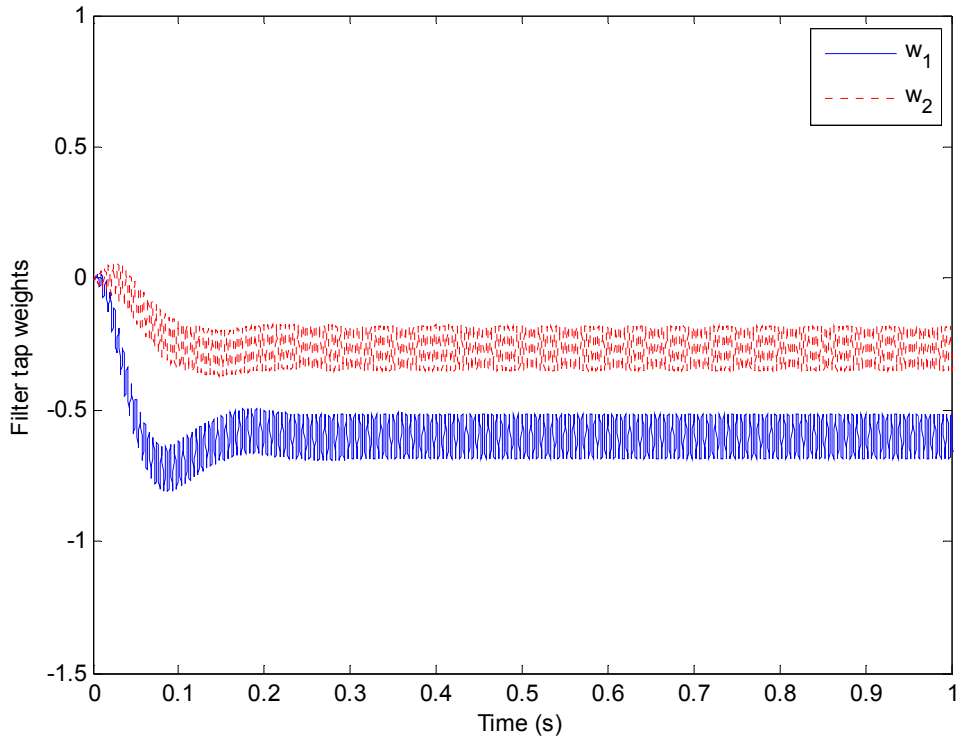

Figure 4.9 LMS weights following controller switch-on

The convergence behaviour of the filter coefficients using the FXLMS algorithm is shown in Figure 4.9 in which the mean values of weights w_1 and w_2 equal to -0.27 and -0.60 respectively. It can be said that after the controller converged the system could remain stable with the constant gains unless other external disturbances occurred.

The on-line identification technique was implemented and the identical parameters were re-applied as used in the off-line system. A white noise with variance of 1×10^{-4} was introduced as a training signal in the secondary path modelling. The length of the filter was 512 and the convergence rate μ_i for updating estimated model $\hat{S}(z)$ was 1×10^{-2}.

For the on-line identification, the convergence rate μ_i would be 100 times less than using the off-line identification (Kuo and Morgan, 1995). Equation 3.26 is the estimation based on the off-line system. The range of μ_i needs to be modified to satisfy the following expression:

$$0 < \mu_i < \frac{2}{300MP_x} \tag{4.5}$$

where P_x is normally the variance of the white noise for identification.

Therefore,

$$0 < \mu < 0.1302$$

based on the filter length of 512 and power of the white noise of 1×10^{-4} in this case.

Considering the system stability, 1×10^{-2} which is one-thirteenth of the upper bound value, was chosen as the convergence rate of the cancellation filter. In practice, it is experienced that one should use the small value at the beginning of the on-line identification and increase to one-third of the upper bound value for faster convergence rate later. This can help to maintain stable performance and obtain a reasonably fast convergence speed.

Figure 4.10 shows the magnitude and phase responses of secondary path by using the FBLMS online identification technique. It can be observed that amplitude offsets and phase shifts occurred below the frequency of 150Hz. In other words, the performance of

controller might degrade at low frequency (below 150Hz) due to the inaccurate estimated model of secondary path, or in the worse case, the system might become unstable eventually.

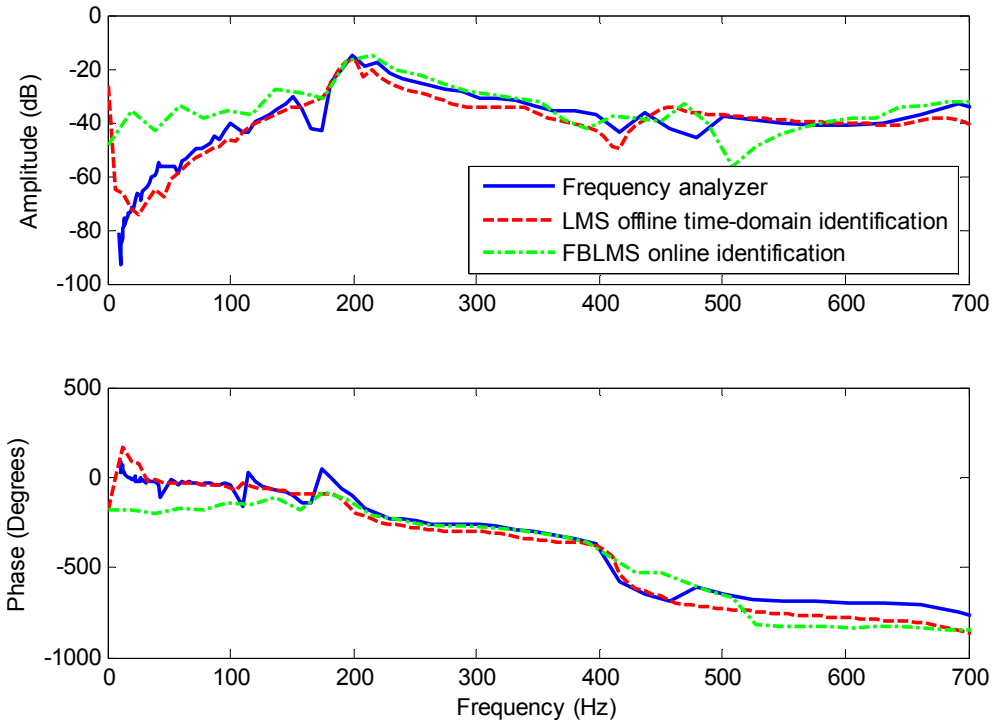

Figure 4.10 Comparisons of magnitude and phase responses of loudspeaker using offline and online time-domain identification techniques

The vibration at the frequency of 200Hz was cancelled following the controller switch-on as shown in Figure 4.11, where the online identification filter was applied. The level of cancellation obtained was approximately the same (around 30dB) as the results in Figure 4.7. This is because the magnitude and phase characteristics at 200Hz achieved by using FBLMS online identification technique are quite close to the results achieved by using the offline method. It also can be seen the amplitudes at higher harmonics were reduced at the same time. This is probably caused by the effects of the cancellation of fundamental frequency or the varying behaviour of the system itself.

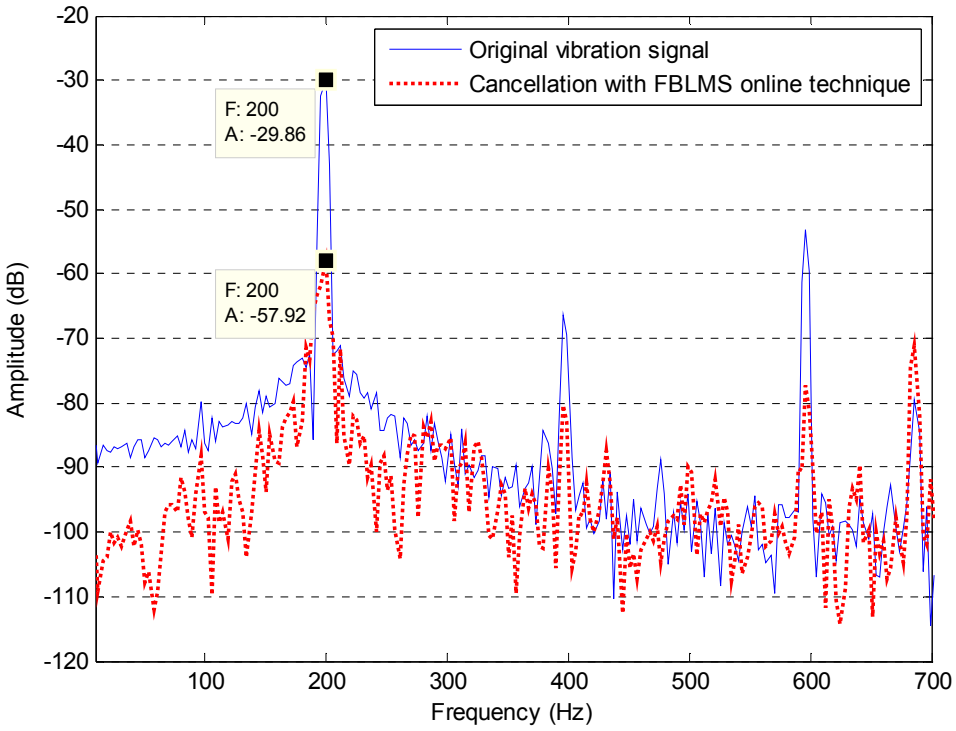

Figure 4.11 Experimental result of vibration cancellation at 200Hz using LMS online time-domain identification technique

Figure 4.12 shows the filter weights during the adaptive period. Stable adaption is seen and the gains settle to near constant values after 6s. The values of weight are about -0.27 and -0.61, respectively, which are quite close to the values plotted in Figure 4.9, although longer adaptive time is needed in online identification case. A digital high-pass filter was designed with 1Hz cut-off frequency to eliminate the offset of the signal achieved from the accelerometer. This can help to remove the weights' oscillations as plotted in Figure 4.9. The mathematical deduction and explanation of the effects of accelerometer offset can be found in Appendix 1.

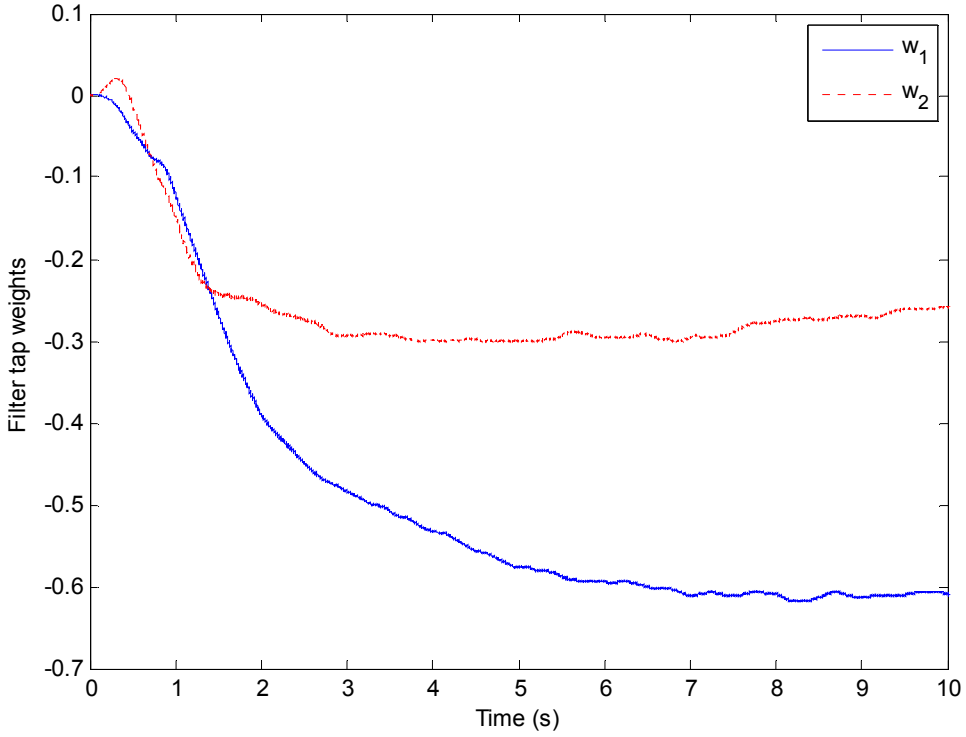

Figure 4.12. LMS weights following controller switch-on

4.3.3 Multiple harmonics cancellation

In these tests two extra harmonic disturbances were imposed on the system. For each additional harmonic to be cancelled, an additional controller was used. A square signal from the function generator was employed to drive the engine mount in order to generate extra disturbances at odd harmonics. The ratio of the pulse width of the square wave to the signal period was fixed at 0.5, which made the system contain only odd harmonics. The fundamental frequency was set to 100Hz and the disturbances at 300Hz and 500Hz were taken into consideration. The convergence rates of each harmonic are listed in Table 4.1.

Table 4.1 Convergence rates used for difference harmonics using FBLMS online frequency-domain technique

Frequency (Hz)	99.9	303	506
Convergence rate μ_c	1×10^{2}	1×10^{0}	1×10^{0}

The amplitude response of errors at frequency of 100Hz, 300Hz and 500Hz after

cancellation is shown in Figure 4.13. It can be found that the frequencies at cancellation had small offsets relative to the expected values. This may be caused by two reasons: one is because the inaccuracy from the signal generator itself; the other is because the length of the error signal used for FFT is not long enough compared with the sample frequency of 3333Hz. Thus, the inaccuracy occurred. However, it was sufficient for proof of the noise cancellation principle. As can be seen, the average level of cancellation achieved was more than 20dB with the maximum peak cancellation of 30.4dB occurring at 500Hz, but the noise was reinforced at frequencies of 200Hz (and integer multiples of 200Hz). Again, these effects might be the results of non-linear behaviour of the rig. Tests also have been done to solve these undesired effects by simply introducing into the system an additional attenuator for 200Hz disturbance with a convergence rate of 2×10^{1}. The cancellation result is shown in Figure 4.14. Because of hardware limitations, still only three sub-controllers with frequencies of 100Hz, 200Hz and 300Hz were applied in the system. It can be seen that substantial levels of cancellation at the frequency of 100Hz and 300Hz were achieved and the cancellation for the disturbance at 200Hz worked effectively.

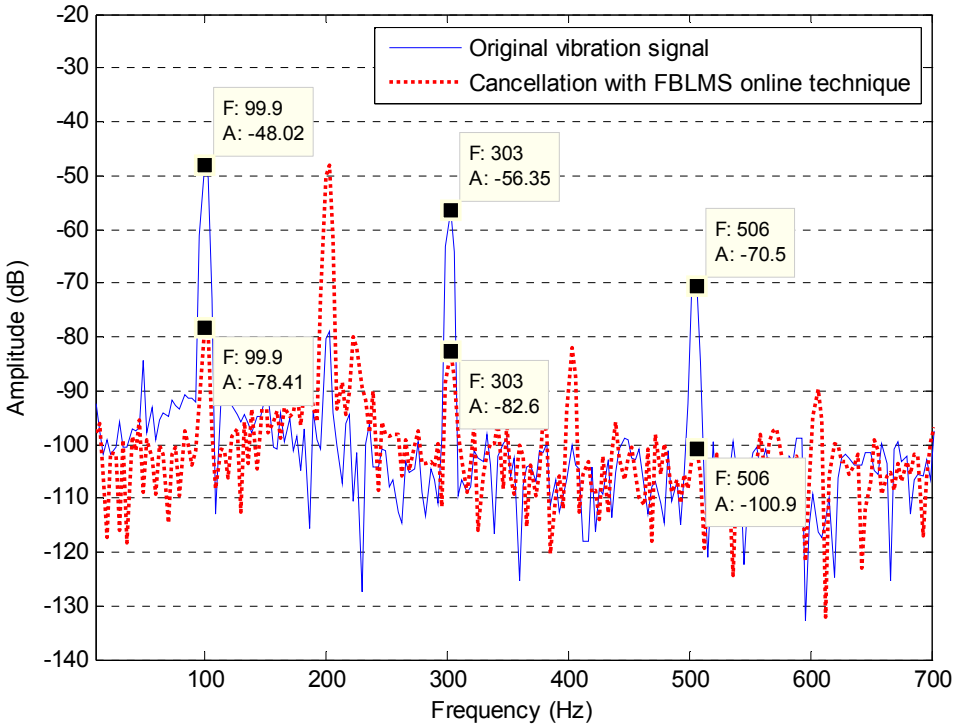

Figure 4.13. Experimental results of multiple harmonics cancellation

It can be expected that the average level of vibration in the system would decrease

eventually with enough controllers in parallel for cancelling different harmonics of undesired noise.

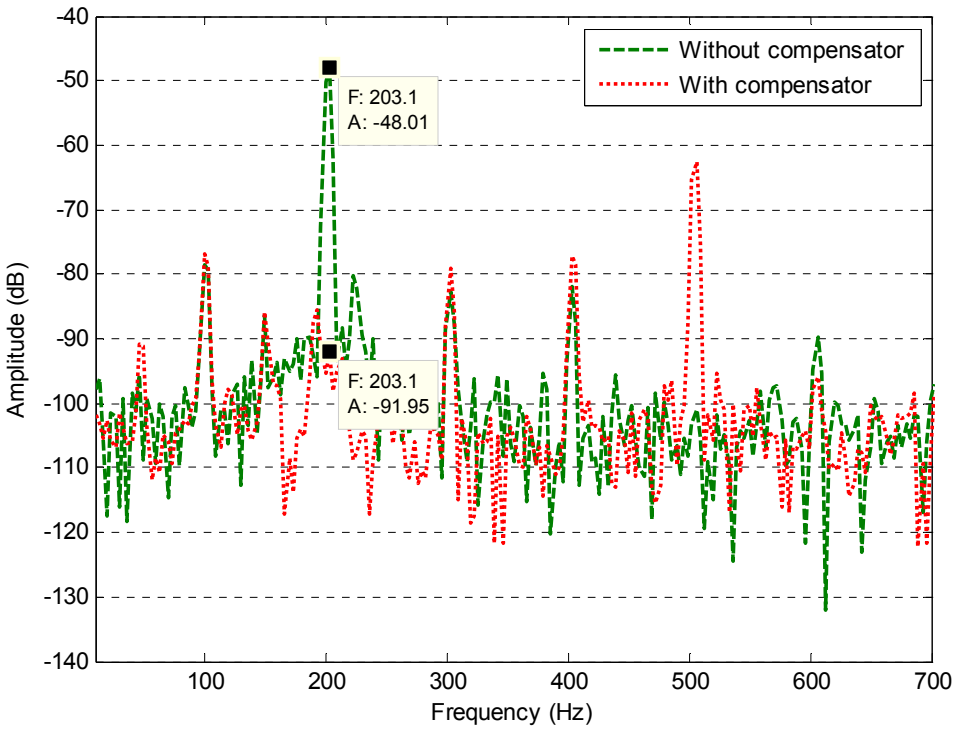

Figure 4.14. Experimental results of multiple harmonics cancellation with cancellation at 200Hz

4.3.4 Changes in frequency

The stability and robustness of the system were investigated using disturbances with sudden changes in the fundamental frequency. The frequency was varied manually from 101.6Hz to 148.3Hz, then to 194.9Hz over 30 seconds. Two transient periods were chosen to be long enough to validate the response of the FXLMS controller for the system being changed. Figure 4.15 shows the residual error with changes in frequency. The convergence rate for each controller is listed in Table 4.2.

Table 4.2 Convergence rates used for different fundamental frequency and the related harmonics in experiment

	Fundamental Frequency (Hz)	Multiple harmonics based on fundamental frequency (Hz)	
Frequency (Hz)	101.6	201.6	303.2
	148.3	296.5	444.8

	194.9	391.5	586.4
Convergence rate μ	1×10^{1}	1×10^{1}	1×10^{0}

It can be concluded that the controller performed effectively with good response speed and noise cancellation. These results have also been analyzed in frequency domain in Figure 4.15.

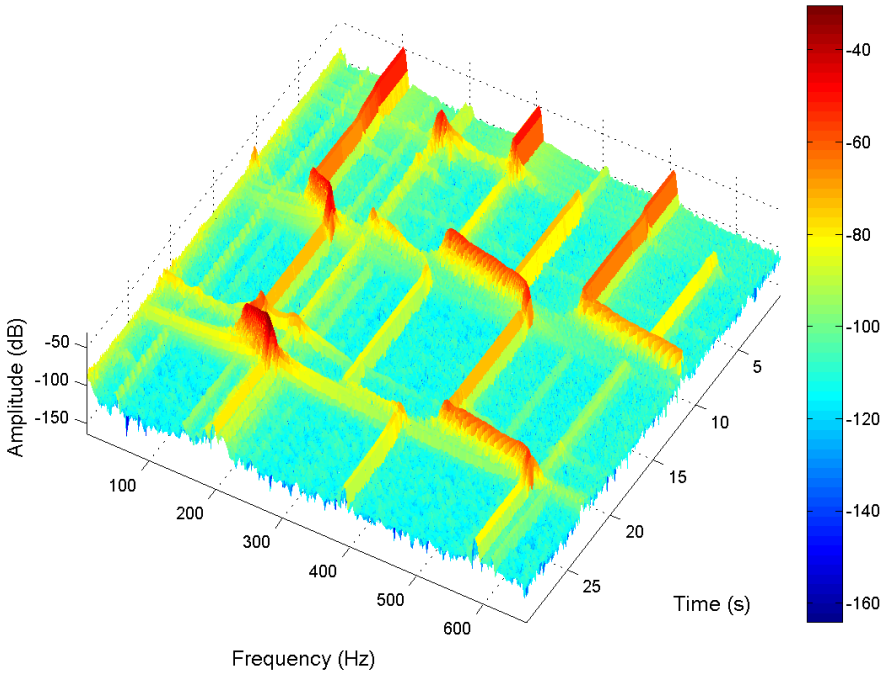

Figure 4.15 Residual error with transient fundamental harmonic from 101.6Hz to 148.3Hz, then to 194.9Hz over 30s

Figure 4.16 (a) (b) and (c) show the amplitude of error with the fundamental frequency of 101.6Hz, 148.3Hz and 194.9Hz respectively, before and after cancellation. It can be observed that the amplitude of every tone of the detected signal was decreased and the average level of vibration cancellation was more than 15dB during frequency transition. As can be noticed, the cancellation in this test was less than previous tests. This is because smaller convergence rates were selected for the cancellation filters in terms of system stability. Since the fundamental frequency was varied in every 10s, the selected convergence rates need to satisfy all the conditions with different fundamental frequency. Therefore, the compromise should be made between cancellation performance and system stability.

It also can be noted that a peak has appeared at near 190Hz which is larger than the uncancelled amplitude of 201.6Hz in Figure 4.16(a). This unexpected peak occurred occasionally, and the reason may be related to the system non-linear behaviour. However, no such peak occurred with the fundamental frequencies of 148.3Hz and 194.9Hz, as shown in Figure 4.16 (b) and (c).

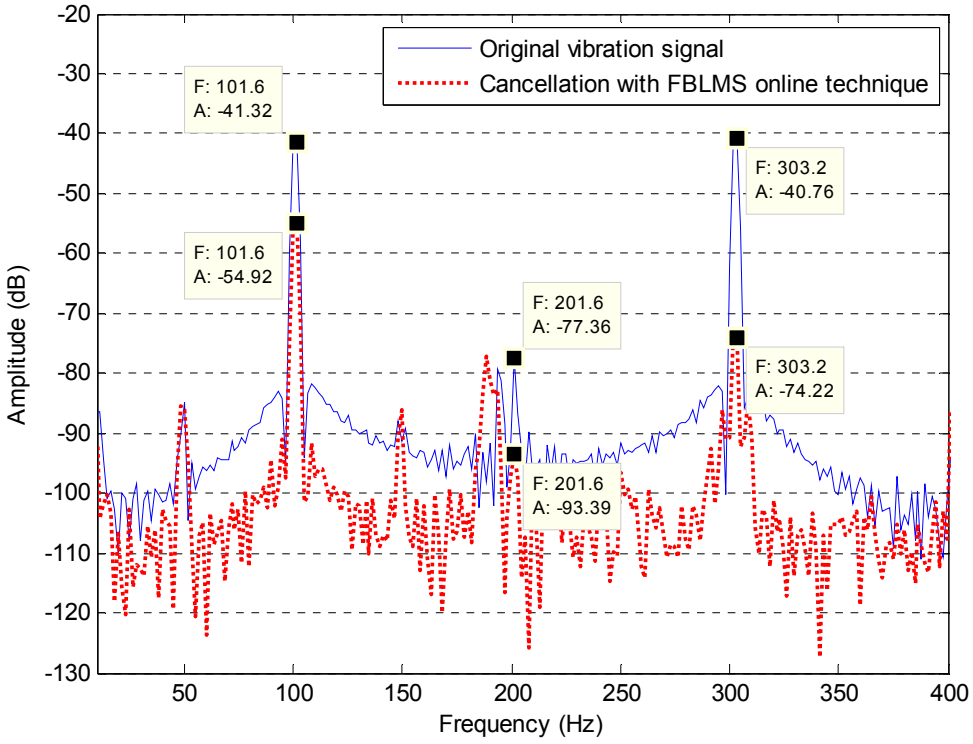

(a) Fundamental frequency = 101.6Hz

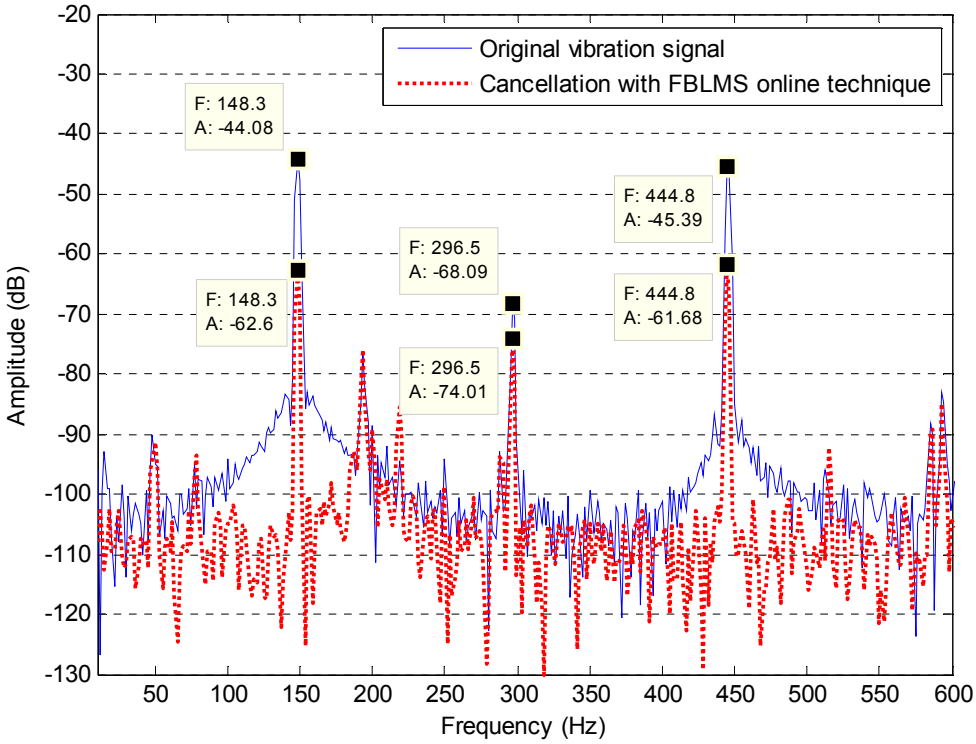

(b) Fundamental frequency = 148.3Hz

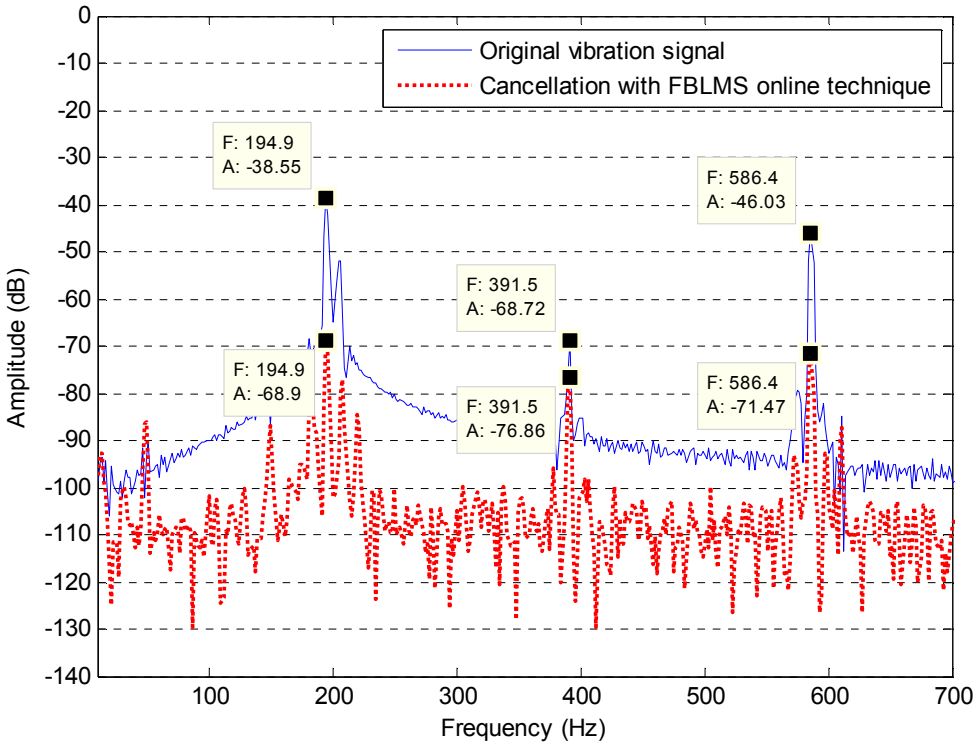

(c) Fundamental frequency = 194.9Hz

Figure 4.16 Magnitude responses with fundamental frequency changing from 100.8Hz to 148.4Hz then to 195.4Hz, plotted in frequency domain

4.4 Problems and discussion

The FXLMS feedforward controller is designed by using an adaptive notch filter combined with a secondary path identification filter. Two different identification techniques were effectively applied in the system. The use of FBLMS frequency-domain identification technique substantially improved the robustness of the overall controller. The controller could achieve approximately 20dB cancellation on average under different experimental conditions. The disadvantages of the designed controller associated with the system identification component are concluded as follows:

- The controller is sensitive to the accuracy of estimated secondary path model. The errors from the phase characteristic of estimated model can not be eliminated completely based on the general structure of ANC system, particularly for the case of using online identification technique.
- The performance of noise controller could degrade with inaccurate secondary path model and negative effects from internal or external system.
- The frequencies achieved from frequency estimator can be different than the actual frequencies of noise due to the external measurement errors. The estimator is also limited by the system sampling frequency. The small frequency mismatch could degrade the performance of the controller.
- The disturbances generated from the dynamic system and the secondary path system exhibit nonlinear characteristics at some situations. The linear FXLMS algorithm used to attenuate such disturbances may exhibit degradation in performance, and hence yield poor control accuracy and stability both of the identification of secondary path modelling and noise cancellation.

Since this vibration experimental rig was used to test the effectiveness of designed controller prior to hydraulic testing, the following statements will be considered about the controller when it comes to be modified for use in a hydraulic system:

- An effective compensator for improving the accuracy of secondary path model might be necessary in the system, or alternative system identification signals that contain only frequencies in a range of system operation could be used with the FXLMS algorithm.

- A modified controller is necessary in terms of some effects from the hydraulic system itself, such as pipeline length, delay from fluid transition, and arrangement of transducers etc. The modified controller may further improve the robustness and stability of the system.
- An alternative frequency estimator could be designed based on dSPACE Timing and Digital I/O board directly, which make it possible to achieve more accurate disturbance frequency values through hardware.
- It may be useful to conduct a study with the purpose of eliminating non-linear system effects, but the analysis and experiments are still focused on the performance of a linear system.

4.5 Concluding remarks

The experimental work described in this section forms a successful development and implementation study for the active control of engine mount vibration. An effective and stable FXLMS noise controller has been developed and successfully tested with a test rig, where it has been shown to be capable of controlling signal frequency component, multiple harmonic frequencies and frequency transition with single-in-single-out system. The disadvantages of the designed controller have been discussed. Hence in future work it would be valuable to investigate a robust system which is capable to apply in hydraulic system testing. Some further considerations have also been presented.

5 Active control of fluid-borne noise in piping systems

In this chapter, the implementation of the designed controller for attenuating FBN in a piping system was investigated. Different system boundary conditions were applied for studying the varying system dynamics. Computer simulations show that the designed controller is effective and robust for cancelling FBN. The system stability was discussed based on the controller performance when it was operated in the varying working conditions.

5.1 System structure

A hydraulic piping system is presented to investigate FBN cancellation using the designed controller, as shown in Chapter 3.

The structure of a piping system is shown in Figure 5.1. It consists of a pump, a loading valve and two pipes arranged in series. A pressure transducer is placed at the downstream line to capture the error signal $e(n)$ for noise cancellation. The pump was modelled using a sinusoidal signal generator for pressure ripples and a fixed value for constant pressure supply. The pipeline was modelled using a pipeline wave propagation model. The effect of the loading valve was demonstrated by using different impedances of the end of system.

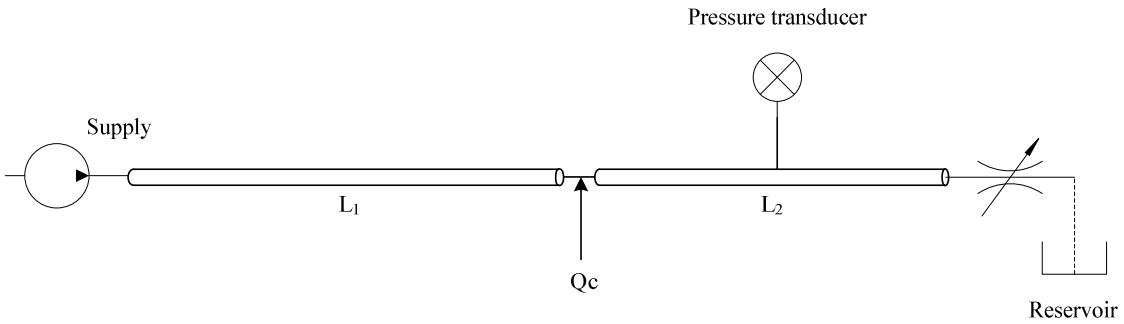

Figure 5.1 Schematic of a simple piping system

5.2 Secondary path dynamics

5.2.1 Impulse responses

As stated in Chapter 3, the accuracy of secondary path identification is significant to the FXLMS algorithm. It is based on the performance of LMS identification filter which is represented by the impulse response of the aimed system. Generally speaking, the impulse response of a dynamic system is its output when presented with a brief impulse signal which is defined as:

$$\delta(t-t_0)=\begin{cases}\lim\limits_{\varepsilon\to 0}\dfrac{1}{\varepsilon} & t_0-\dfrac{\varepsilon}{2}\le t\le t_0+\dfrac{\varepsilon}{2}\\ 0 & \text{otherwise}\end{cases} \tag{5.1}$$

The function works like a sampling gate at t_0,

$$\int_{t_1}^{t_2} f(t)\delta(t-t_0)dt=\begin{cases}f(t_0) & t_1<t_0<t_2\\ 0 & \text{otherwise}\end{cases} \tag{5.2}$$

Assuming Q_c is the control flow of the piping system as shown in Figure 5.1, an impulse flowrate is applied as the driving signal to study the ideal impulse response of the system.

Different boundary conditions of the piping system could affect the impulse response due to the wave propagation in the system. A standard orifice equation was used to model the secondary actuator generating a flowrate impulse signal, as shown in Equation (5.3).

$$Q_V = A_{Eff}\sqrt{\frac{2|\Delta P|}{\rho}}\,\mathrm{sgn}(\Delta P) \tag{5.3}$$

The area $A_{Eff}=C_q A_{open}$, where C_q is the discharge coefficient and A_{open} is the opening area of the valve. Equation 5.3 shows a non-linear characteristic of the valve.

Figure 5.2 shows the schematic of 21 nodes pipe model with control flow. The selection of the number of nodes is dependent on the frequencies of interest in the pipe model. In this chapter, frequencies under 1000Hz were considered.

The length of pipe in the model was defined using the following equation:

$$L = c \times (n-1) \times dt \tag{5.4}$$

where L is the length of the tube, n is the number of nodes and dt is the sample rate and c is the speed of sound.

The sample rate was selected to 0.1ms to ensure accuracy and wide frequency bandwidth. Thus, 21 nodes were selected with the pipe length of 2.6m.

In this model, the pipe length L_1 was 1.82m and L_2 was 0.78m and the pressure transducer was arranged at the position of 2.21m. The simulation parameters are listed in Table 5.1.

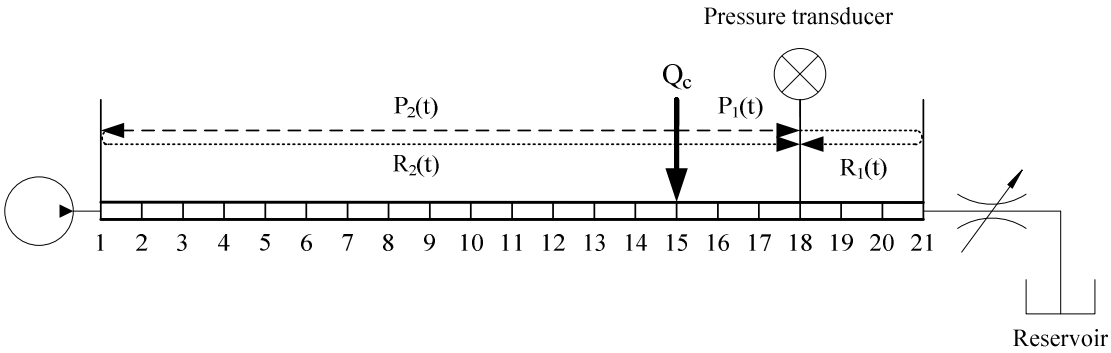

Figure 5.2 Schematic of 21 nodes pipe model

Table 5.1 Simulation parameters

Length l	2.6 m
Diameter d	0.01 m
Viscosity μ	30 cSt
Density ρ	870 kg/m^3
Speed of sound c	1300 m/s
Number of nodes	21
Grid spacing	0.13 m
Friction terms k	4
Pressure "transducer" location	2.21m (node 17)

Figure 5.3 shows the system impulse response when the termination impedance was equal to the characteristic impedance of the system, $R = 1.44 \times 10^{10}$ Ns/m^5. The system was driven by an impulse flowrate $Q_c = 1 \times 10^{-3}$ at 2s. The upstream boundary was 0 bar representing the open end condition. Thus, the system boundary condition was the open-reflectionless (termination impedance equals to characteristic impedance). A first peak

occurred at 2.0003s. This is caused by the distance between the position of the transducer and the injecting point of control flow. The spacing between these two positions was 0.39m, which is three times the gird spacing. The reflection also occurred at the upstream open end which caused the 0.0027s delay with a negative peak at 2.0031s.

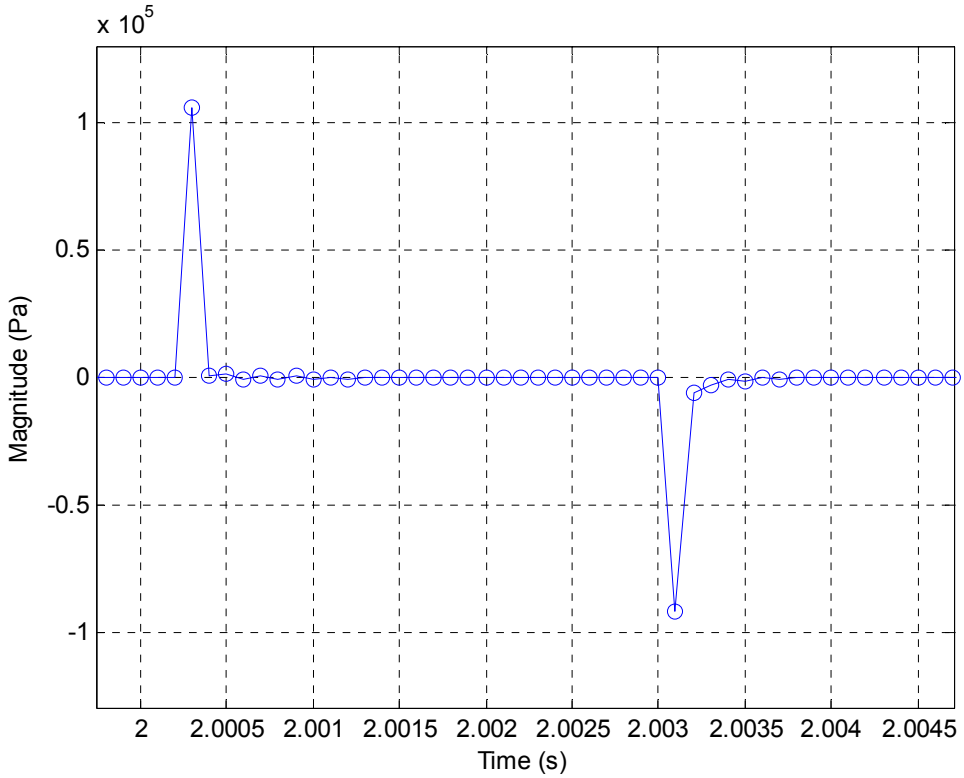

Figure 5.3 Impulse response of piping system when the termination impedance equals the characteristic impedance

When it comes to the open-open ends boundary condition (termination impedance $R = 1.44 \times 10^8$ Ns/m^5), the wave refection changed and the natural frequency of the system can be calculated as follows:

$$\omega = \frac{C}{2 \cdot L} \tag{5.5}$$

The natural frequency of this system was 250Hz. The impulse response is shown in Figure 5.4.

Reflections occurred at both the upstream and downstream ends. The first negative peak occurred at 2.0009s due to the regressive wave R_1 reflection from the downstream end. After that, a negative reflection produced by the regressive wave R_2 was detected at

2.0031s, and so on.

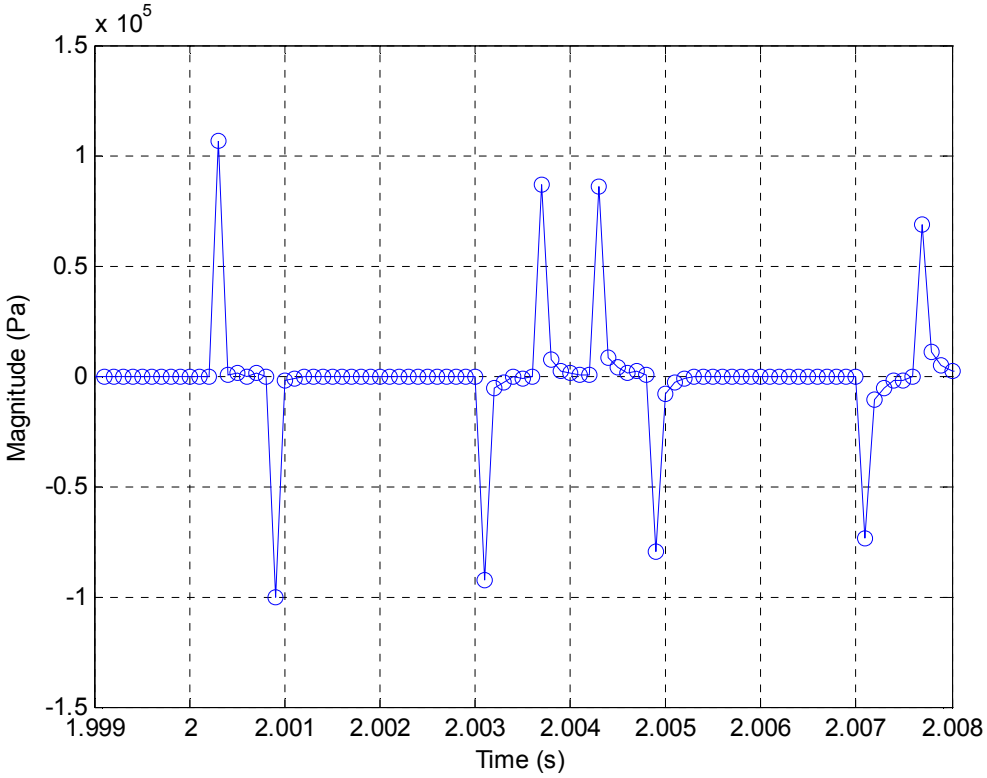

Figure 5.4 Impulse response of piping system with open-open boundary condition

Consider the open-closed ends boundary condition, the downstream termination impedance was $R = 1.44 \times 10^{12}$ Ns/m^5 and the upstream pressure was 0 bar. The natural frequency of system was 125Hz in theory, which is based on Equation 5.6:

$$\omega = \frac{C}{4 \cdot L} \tag{5.6}$$

Figure 5.5 shows the system impulse response with open-closed boundary condition. The peaks occurred at 2.0003s, 2.0009s, 2.0031s and 2.0037s due to the reflections from the downstream and upstream ends.

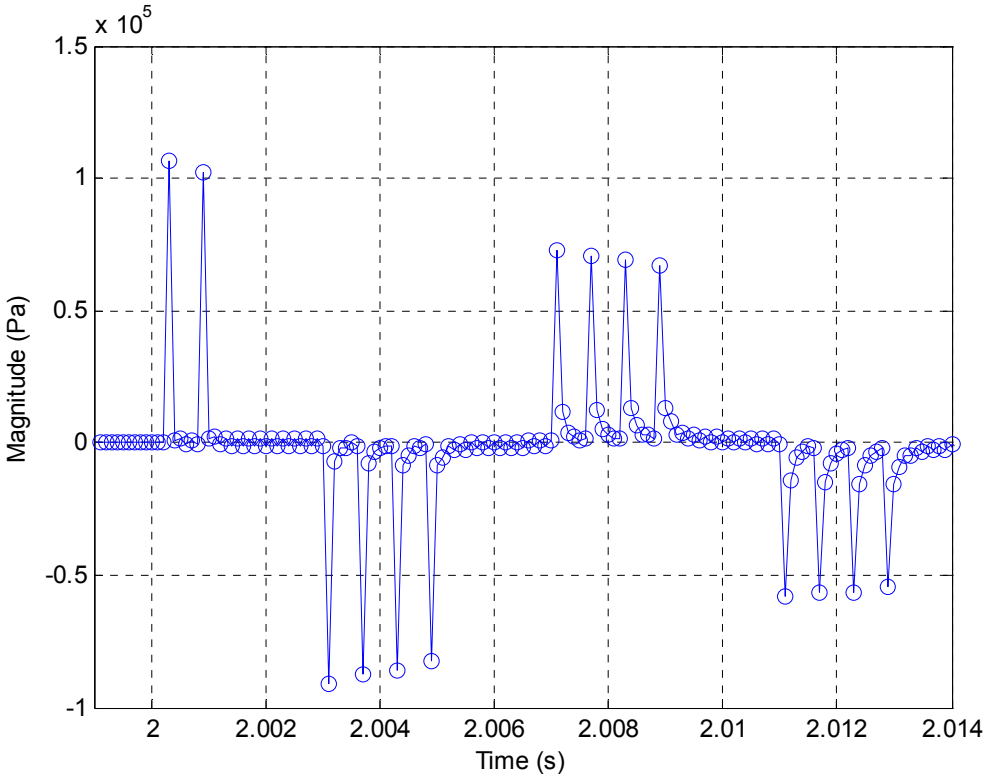

Figure 5.5 Impulse response of piping system with open-closed boundary condition

Setting the upstream and termination impedance $R_{up} = R = 1.44 \times 10^{12}$ Ns/m^5, which represents the closed-closed ends boundary condition of system, the natural frequency of system was 250Hz again, which can be calculated through Equation 5.5. The impulse response is plotted in Figure 5.6.

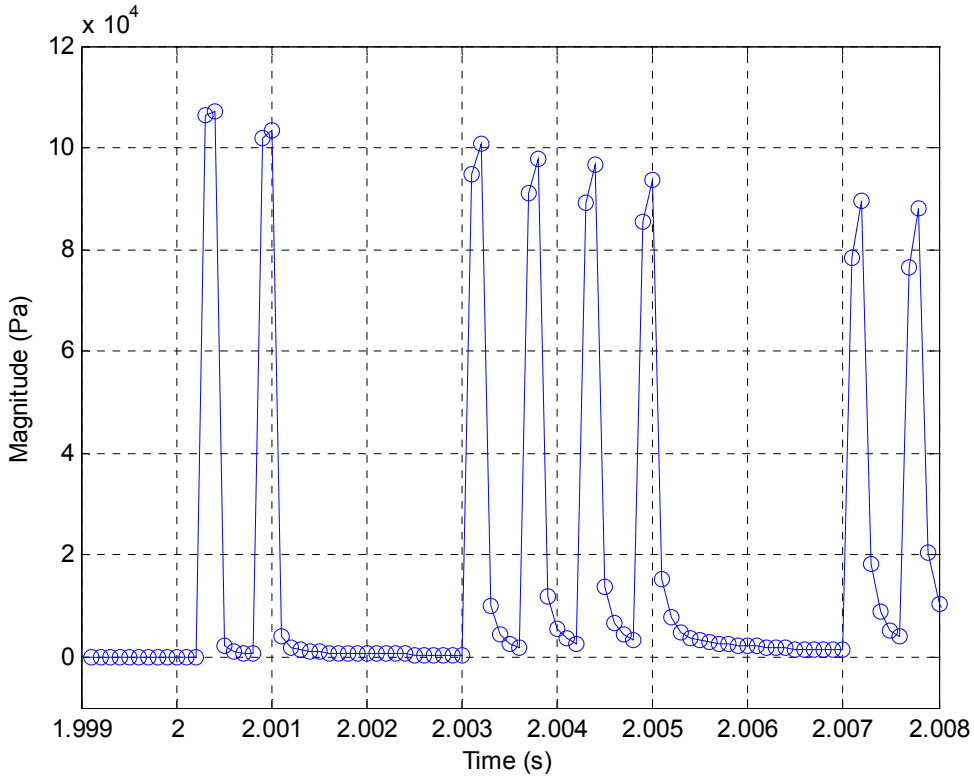

Figure 5.6 Impulse response of piping system with closed-closed boundary condition

Figure 5.3 - 5.6 presented the impulse responses based on a standard ideal orifice equation. In practice, the dynamic of the actuator could also affect the system impulse responses.

An arbitrary second-order continuous transfer function $S(s)$ with 0.1ms sample time step was introduced to demonstrate the actuator dynamics with gain $\lambda = 1$, damping ratio $\xi = 0.8$ and natural frequency $\omega_n = 628$ rad/s:

$$S(s) = \frac{628^2}{s^2 + 1004.8s + 628^2}$$

Figure 5.7 shows the impulse response of piping system including actuator dynamics by applying different boundary conditions. Impulse response 1 represented the open-characteristic impedance boundary condition; Impulse response 2 represented the open-open boundary condition; Impulse response 3 represented the open-closed boundary condition; and Impulse response 4 represented the closed-closed boundary condition. As can be seen, the frequencies of impulse responses 2 and 4 were equal, and twice the frequency of impulse response 3. Besides, the mean pressure value of impulse response

4 was much higher than other results. This is because of the closed-closed boundary condition which caused additional fluid to be injected into a closed volume.

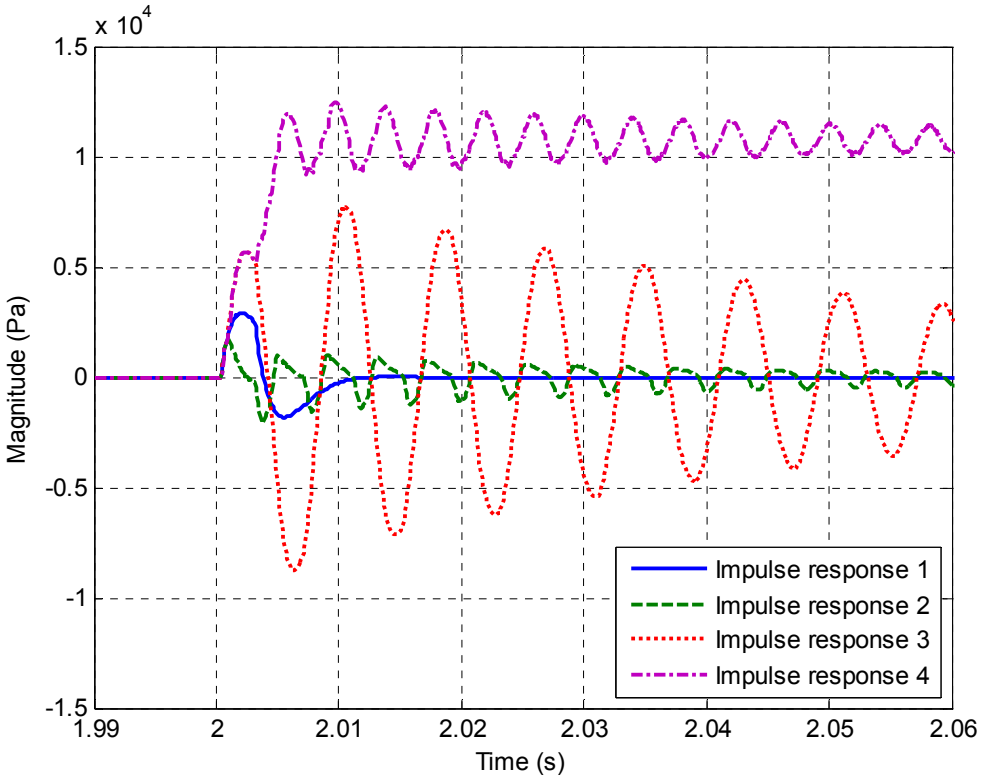

Figure 5.7 Impulse responses of piping system achieving by applying different boundary conditions

The impulse response of the secondary path has been investigated based on different system boundary conditions in this section. It has been shown that the secondary path dynamics are highly related to the system upstream and downstream boundary conditions. The secondary path actuator dynamics can also affect the system amplitude and phase. In practice, these two factors may change system dynamics and degrade the controller performance or even result in the system instability.

5.2.2 Secondary path dynamics using the LMS identification technique

The LMS identification technique was used to obtain the impulse response of piping system. The filter length was 256 and the sample frequency was 10 kHz. The result was compared with the one achieved by applying ideal impulse flow signal. Good agreement

was obtained as shown in Figure 5.8 where the open-reflectionless boundary was applied in the system.

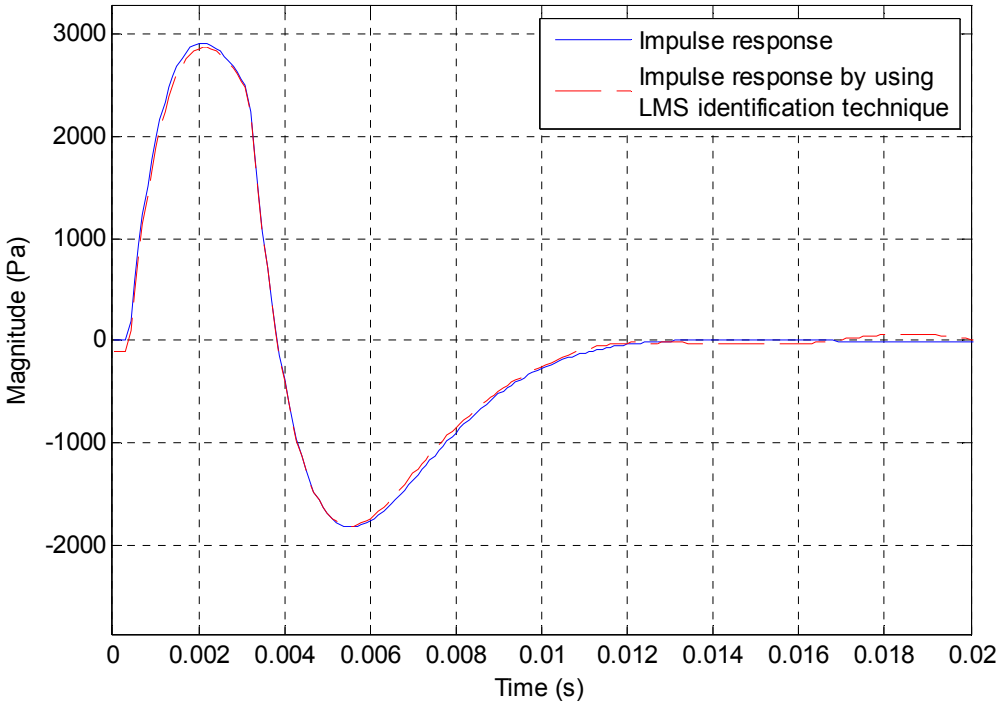

Figure 5.8 Comparison of impulse responses of piping system by using LMS identification technique with open-characteristic impedance boundary condition

Figure 5.9 shows the impulse response of piping system with the open-open boundary condition. The filter length was 1024 and the sample frequency was 10 kHz. It can be seen that the length of the identification filter was too short to capture all of the characteristics of the system. This may cause instability when it applies the noise attenuator which is highly related to the accuracy of the secondary path dynamics.

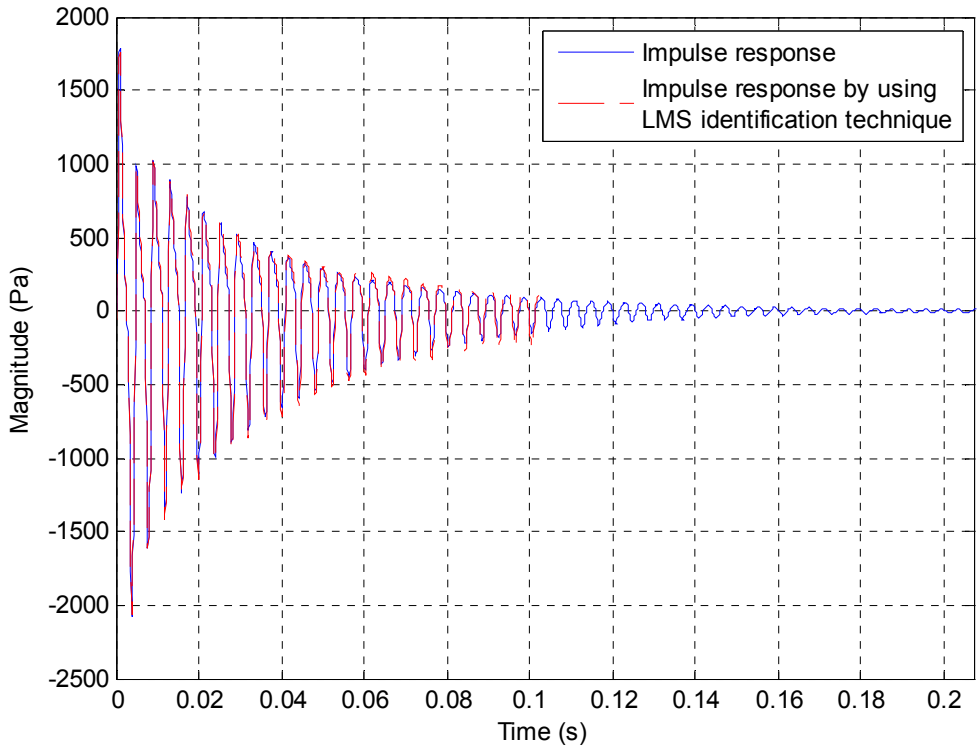

Figure 5.9 Comparison of impulse response of piping system by using LMS identification technique with open-open boundary condition

In conclusion, the step response and impulse response of a piping system were studied with different upstream and downstream boundary conditions. Comparison between the impulse responses achieved from LMS identification technique and ideal driving impulse signal were investigated. From the simulated results, it can be concluded that the LMS identification technique is effective to identify the dynamics of a piping system and achieve accurate results. However, in some situations, a compromise needs to be made between the computation and the accuracy of the identification filter in terms of the selection of filter length.

5.3 Simulation studies

A simulation model was created using MATLAB Simulink. The performance of the designed noise attenuator was studied based on the hydraulic model in Figure 5.1 in terms of ability of noise cancellation, stability and robustness of controller. Figure 5.10 shows the FXLMS arrangement for the case of single frequency cancellation in a piping system. The initial downstream boundary resistance was fixed at 1.44×10^{10} Ns/m^5. The opening of the control valve was 0.01cm^2 and the discharge coefficient of the valve was

0.7. The supply pressure was 10bar and the amplitude of pressure ripple was 1 bar with the frequency of 40Hz. Other related simulation parameters are the same as listed in Table 5.1. Figure 5.11 shows the original FBN detected at the downstream pressure transducer in 0.4s.

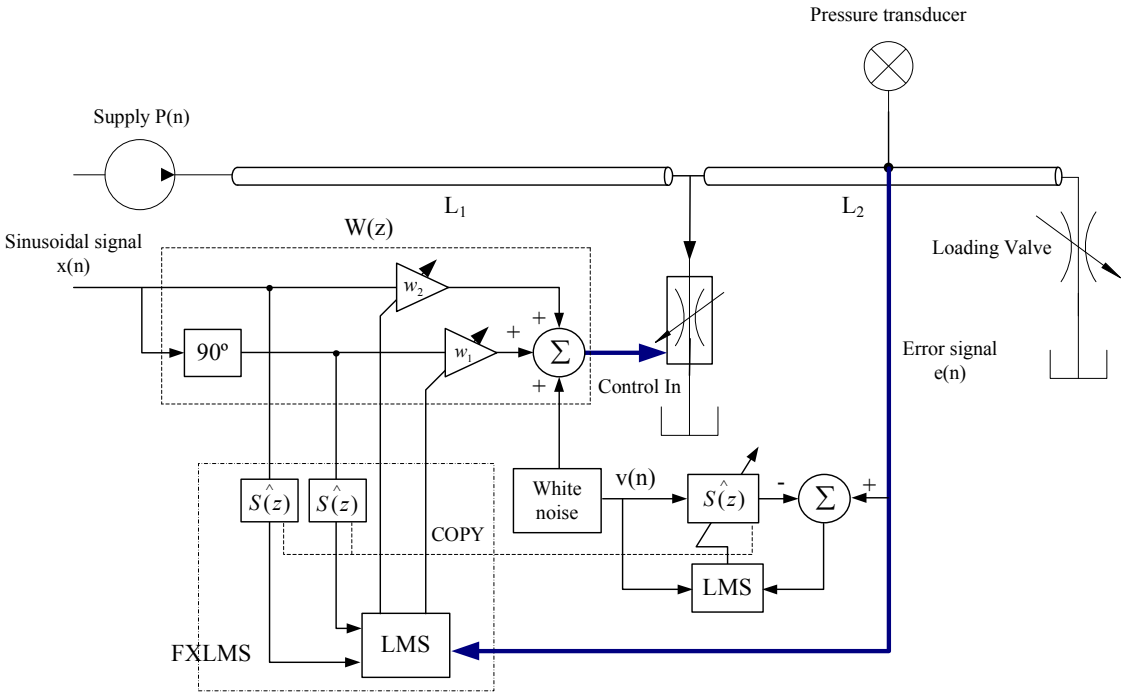

Figure 5.10 Single-frequency ANC system using FXLMS algorithm in a piping system

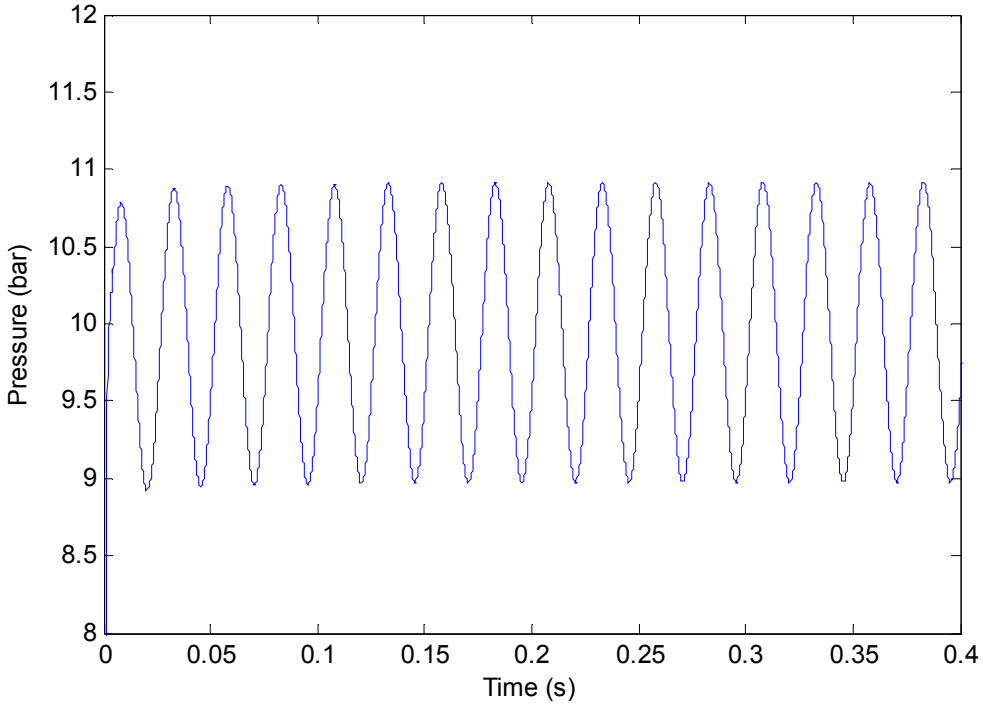

Figure 5.11 Modelled original pressure pulsation

5.3.1 Secondary path identification

The noise attenuator was applied by using LMS offline and FBLMS online identification techniques separately. Figure 5.12 plots impulse responses of secondary path $S(z)$. As can be seen, the impulse response achieved with FBLMS online technique agreed well with the one with LMS offline technique apart from some random oscillations around the zero position. This may be caused by the small convergence rate and power of white noise used for the identification filter. Also, a longer simulation time could be helpful for improving the accuracy of the impulse response. The frequency responses of $S(z)$ are shown in Figure 5.13 where the amplitude and phase characteristics match well expect for some phase differences in the high frequency range.

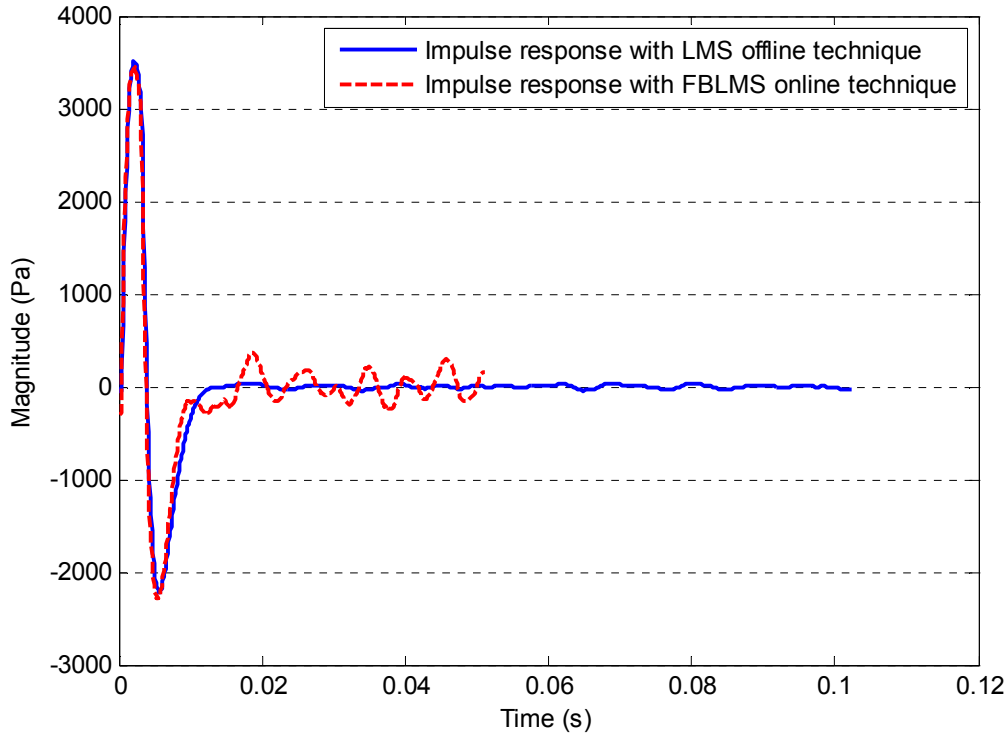

Figure 5.12 Impulse response of secondary path S(z)

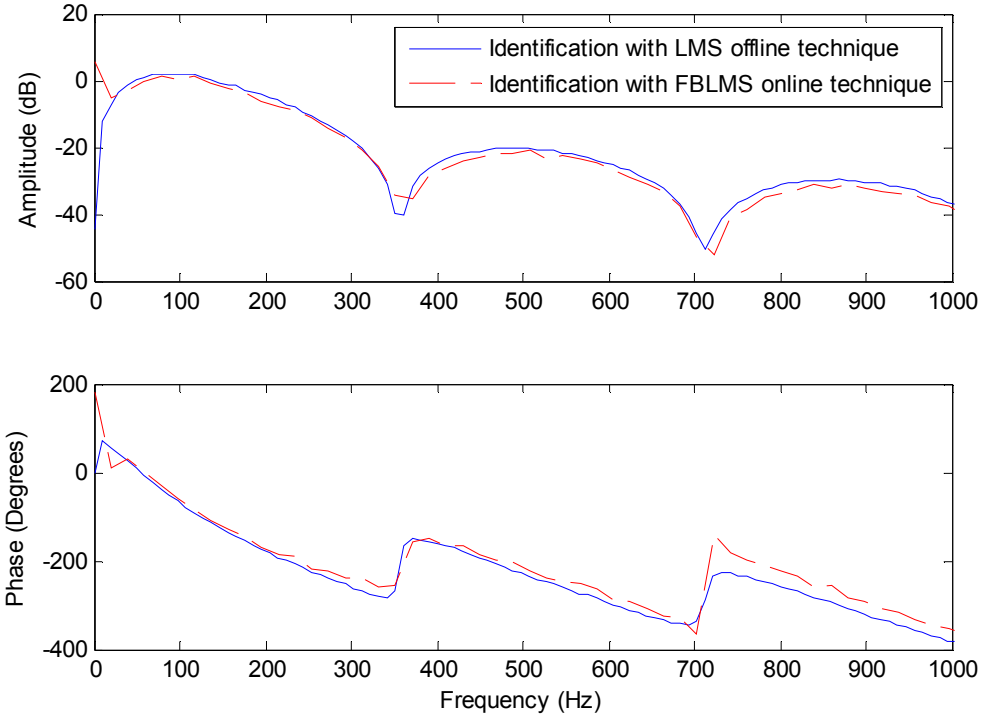

Figure 5.13 Amplitude and phase characteristics of secondary path achieved using LMS offline identification technique

5.3.2 Single frequency cancellation

5.3.2.1 Single frequency cancellation using the LMS offline identification technique

The FBN cancellation by using LMS offline identification technique is shown in Figure 5.14. The secondary path dynamics plotted in Figure 5.13 were used for the FXLMS algorithm. The convergence rate for the cancellation filter was 5×10^{-20}. It appeared that good cancellation was achieved after 1s adaptive time. The weights of the notch filter are plotted in Figure 5.15 (a).

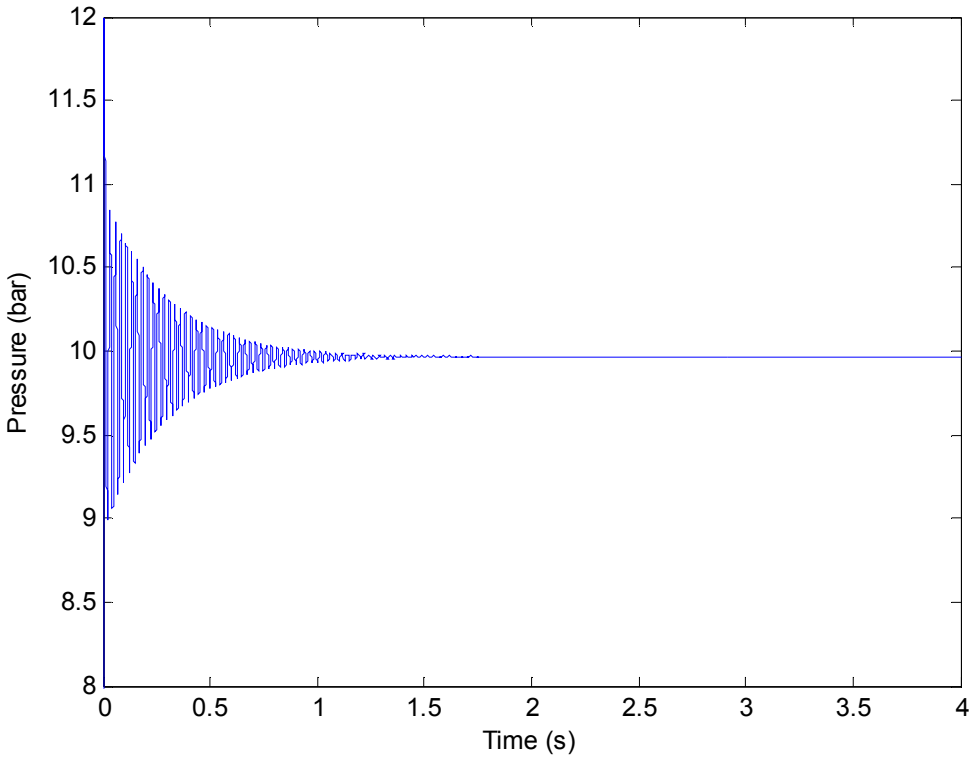

Figure 5.14 Pressure pulsation cancellation by using LMS offline identification technique

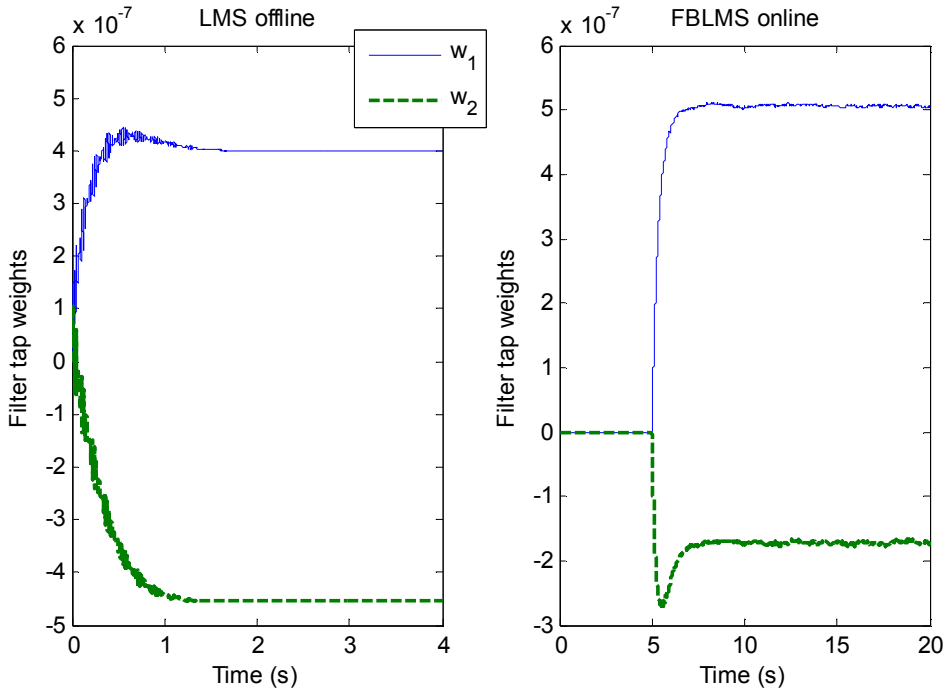

(a) (b)

Figure 5.15 Tap weights of cancellation filter

5.3.2.2 Single frequency cancellation using the LMS online identification technique

For the case of using FBLMS online technique, the same convergence rate 5×10^{-20} was used for noise cancellation filter. The variance of white noise applied for identification was 1.25×10^{-13} and the length of the identification filter was 512. Figure 5.16 shows the pressure ripple cancellation using FBLMS online identification technique. At the beginning of 5s, the noise attenuator and pressure pulsation were switched off in order to obtain accurate secondary path dynamics $S(z)$ for filtered reference signals. When the pressure ripple was switched on, the noise controller was operated synchronously for reducing pressure pulsation. It can be seen that the noise attenuator is able to decrease the noise effectively and stably within only 1s adaptive time. However, the residual error signal included the white noise which was introduced for system identification. This may be a disadvantage of using FBLMS online technique, but the power of white noise can be smaller as long as it is enough for achieving an accurate identification of secondary path $S(z)$.

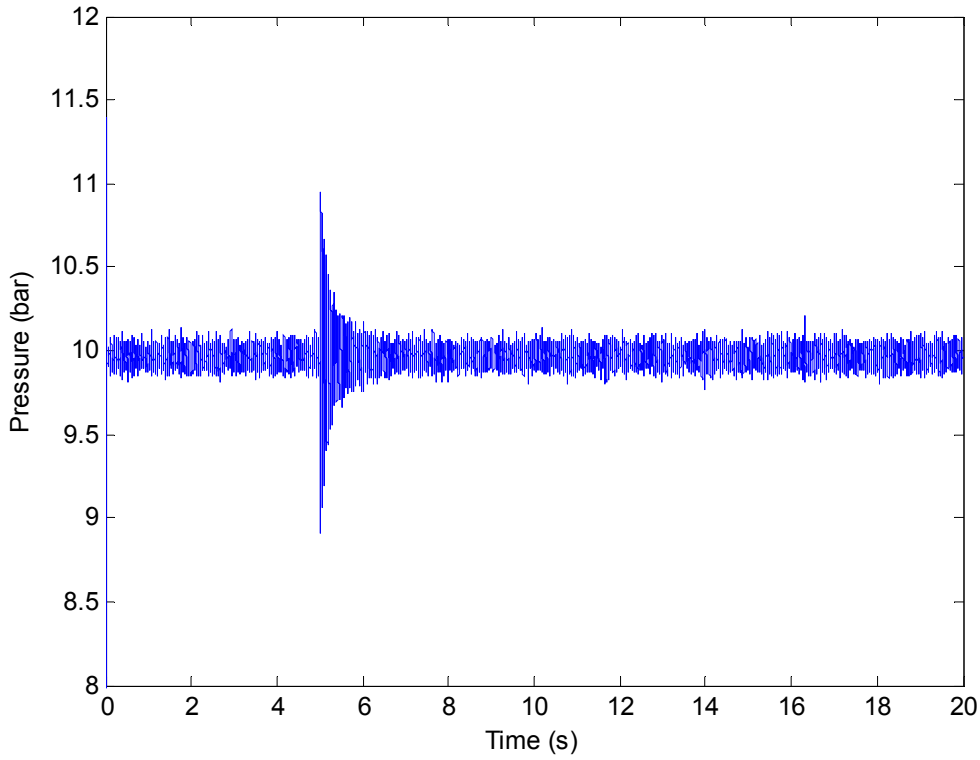

Figure 5.16 Pressure pulsation cancellation by using FBLMS online identification technique

Figure 5.15 (b) shows the tap weights of the adaptive notch filter. The weight taps controlled the instantaneous valve opening in the process of cancellation to generate an appropriate anti-phase signal with a fixed valve opening of 0.01 cm^2. Ideally, with the same convergence rate for noise attenuator and amplitude of $S(z)$ at the cancelled frequency, the weights of notch filter should be the same using LMS offline and online techniques. However, it can be found that the weight w_1 and w_2 in Figure 5.15 (b) were different from w_1 and w_2 plotted in Figure 5.15 (a). This is because the $S(z)$ used for LMS offline and FBLMS online techniques were not exactly similar at the frequency of 40Hz. Thus, minor differences of the weights of notch filters occurred at cancellation.

5.3.3 Multiple harmonics cancellation

The flow ripple of a pump or the pressure ripple created in a hydraulic circuit normally is a periodic waveform, which can be considered as the summation of a number of sinusoidal components or harmonics. In this case, a noise attenuator for multiple harmonics cancellation was applied. Two more sinusoidal signals of frequency 80Hz and 120Hz were introduced to model the pressure ripple with multiple harmonics. The termination boundary condition remained the same as before. Figure 5.17 shows the cancellation of pressure pulsation with multiple harmonics using LMS offline identification technique. The convergence rates used for the sub-controller (adaptive notch filter) are listed in Table 5.3.

Table 5.3 Convergence rates used for different harmonics using LMS online time-domain technique

Frequency (Hz)	40	80	120
Convergence rate μ_c	5×10^{-20}	5×10^{-20}	5×10^{-20}

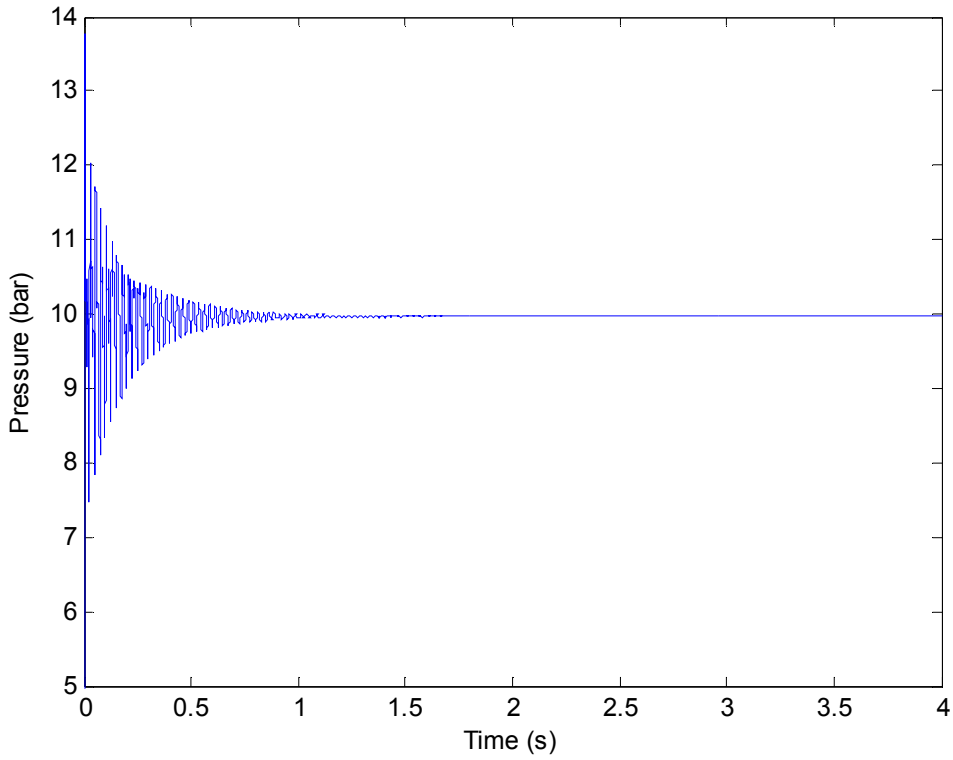

Figure 5.17 Pressure pulsation with multiple harmonics cancellation by using LMS offline identification technique

The filter weights of different sub-controllers are shown in Figure 5.18.

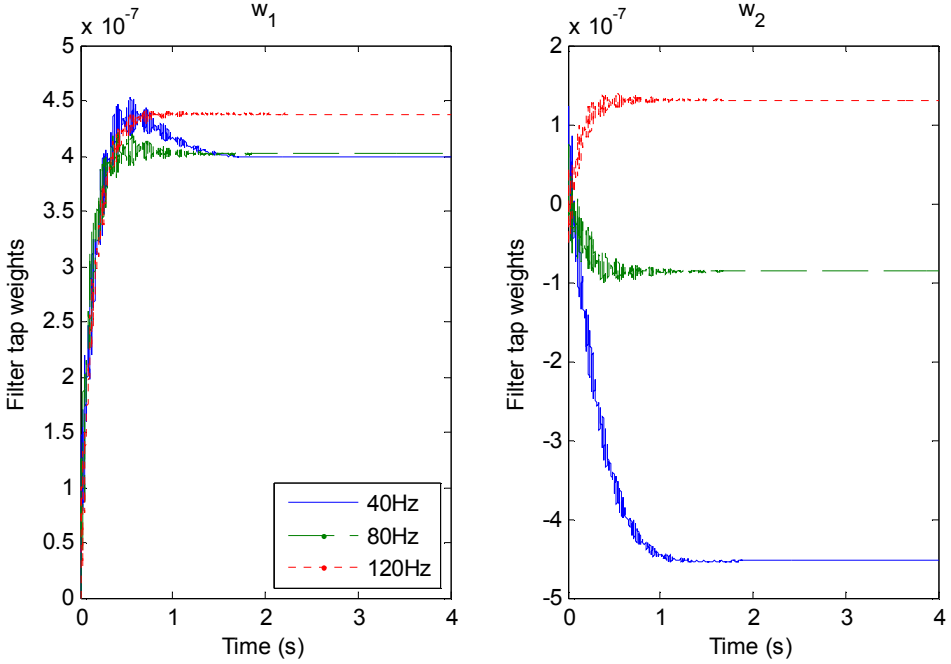

Figure 5.18 Filter tap weights of different sub-noise controller by using LMS offline technique

5.3.4 Stability analysis

In practice, the downstream boundary condition of the system may vary according to specific working requirements or loading conditions. To investigate the system stability, the performance of the noise attenuator for the system functioning in a variety of operating conditions was considered and modelled by changing the status of the downstream loading valve. The impedance of the termination was changed from 1.44×10^{10} Ns/m^5 to 1.44×10^{12} Ns/m^5, then to 1.44×10^{8} Ns/m^5, which represented the loading valve opening changed from small opening to fully closed, then to wide open. A step signal was used to model the sudden changes of system. In order to simplify the system, only one harmonic (fundamental frequency = 40Hz) was considered for noise attenuation. The FBLMS online identification technique was implemented to identify the secondary path characteristics when the system dynamics varied. The robustness and response speed of system were studied by analysing the changing of the notch filter weights.

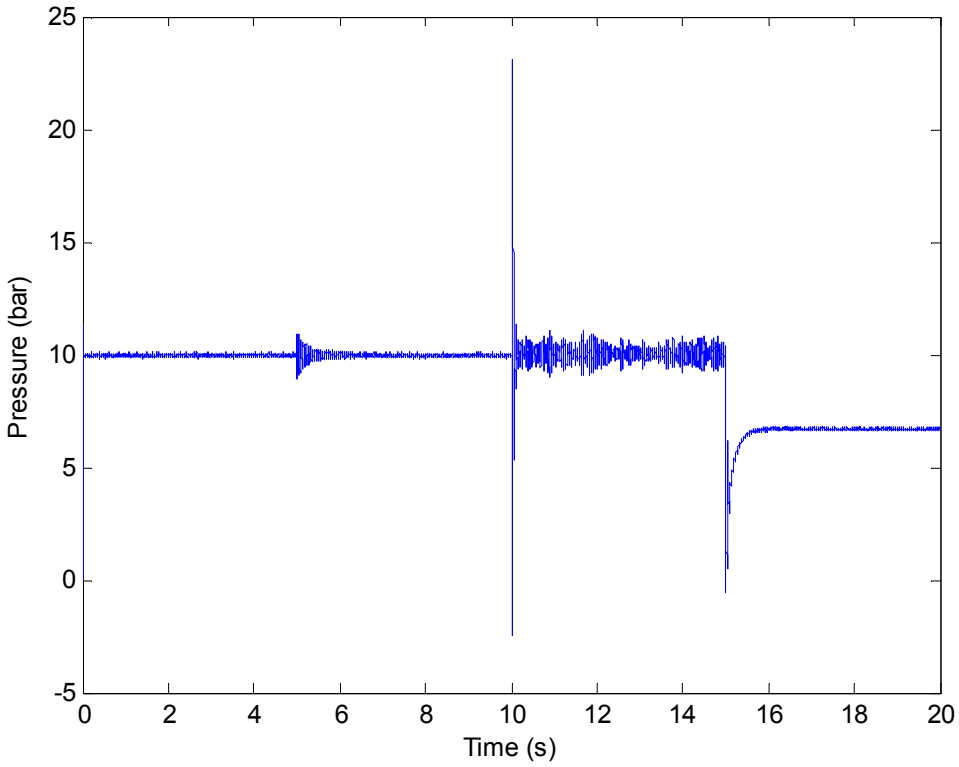

Figure 5.19 Cancellation of pressure pulsation using FBLMS online identification method with changing downstream boundary condition

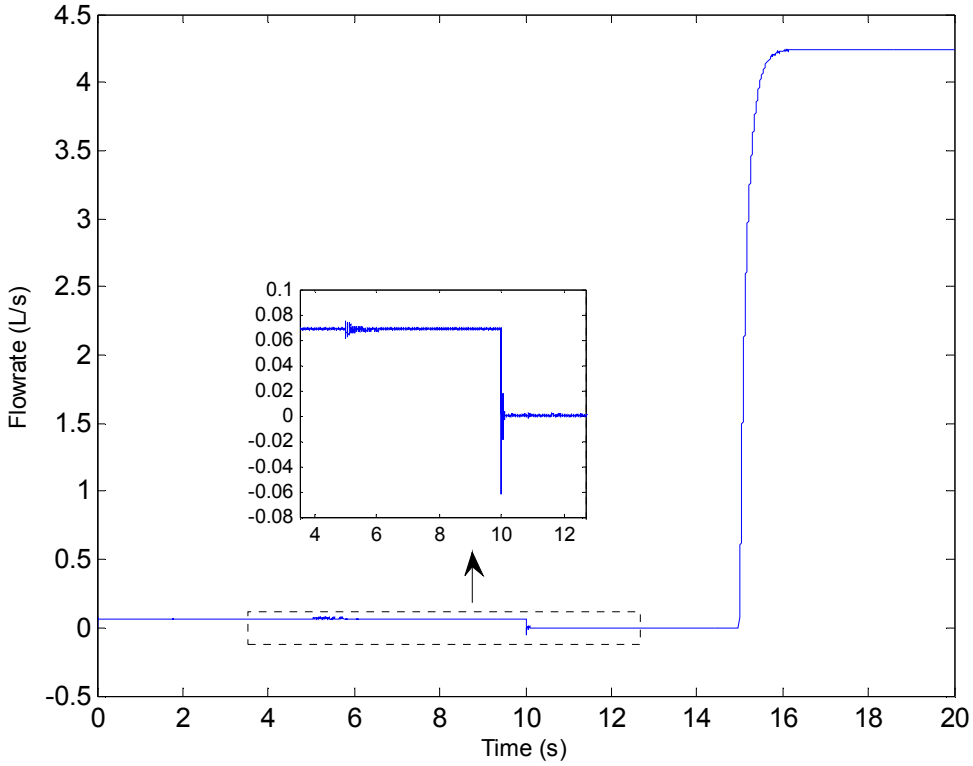

Figure 5.20 Cancellation of flow ripples using FBLMS online identification method with changing downstream boundary condition

Figure 5.19 shows the cancellation of pressure pulsation by using FBLMS online identification method. The boundary condition changed at 10s and 15s. It can be seen that good noise cancellation was obtained and the system performed stably with the varying downstream boundary conditions. The first 5s was used for secondary path identification without disturbance from pressure ripple and noise attenuator in order to achieve more accurate dynamic result for the FXLMS control algorithm. At 10s, the loading valve was suddenly closed, which caused the increasing mean pressure and large pressure pulsation in the system. The loading valve was then opened quickly at 15s and the mean pressure of the system decreased to 6.6bar. The system flowrate is shown in Figure 5.20. As can be seen in Figure 5.19 - 5.20, the noise controller performed robustly and cancelled the ripple with fast response, although the residual ripple increased by the reflection of wave propagation in the period of 10s to 15s.

Figure 5.21 plots the weights of the notch filter with the varying boundary conditions. The average adaptive time was fast and about 1.5s. At 10s, the controller adapted

quickly due to the small characteristics changes of the system. It can be seen that the weights adapted slower with more than 2s after 15s. This is because a re-adaption process is needed when the amplitude of the pulsation in the system changed with the system characteristics. From Figure 5.19 – 5.21, it can be concluded that the noise cancellation filter can adapt quickly and perform effectively for the system being subjected to the sudden condition changes.

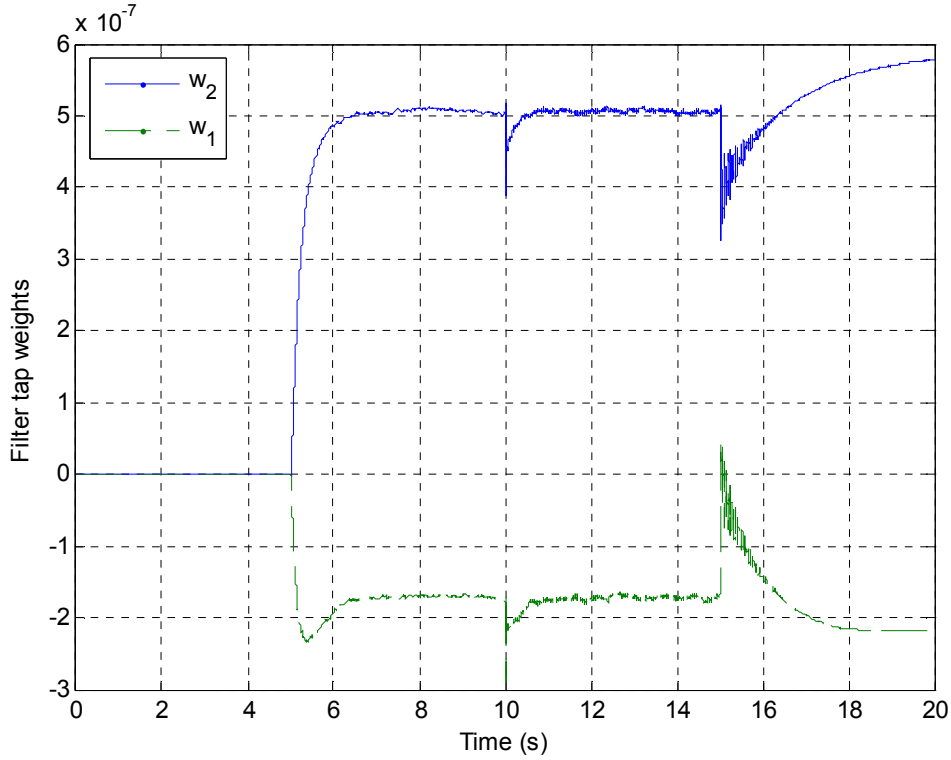

Figure 5.21 Weight taps of cancellation filter with the varying downstream boundary conditions

5.4 Concluding remarks

The implementation of the designed noise controller for cancelling FBN in a piping system was investigated through simulations in this chapter. Different system boundary conditions were applied for studying the varying dynamics of the secondary path. The LMS algorithm was evaluated and validated for obtaining the accurate impulse response of secondary path with the comparison of the theoretical results. The controller performance was investigated via simulation in term of attenuation ability, robustness and stability with the varying working conditions. Simulated results show an excellent cancellation was achieved and the controller is able to perform robustly with changing loading conditions. It can be concluded that the proposed controller is capable of

obtaining good FBN cancellation effectively and robustly based on a pump-pipe-loading valve hydraulic system.

6 Switched inertance hydraulic systems

In this chapter, the principle of operation of switched inertance hydraulic systems is studied. The system can be configured as a flow booster or a pressure booster consisting of a high-speed switching valve and an inertance tube. Using this system, flow and pressure can be varied by a means that does not rely on dissipation of power. Simulated results show good performance of both flow booster and pressure booster, although noise may be a problem which needs be considered for system efficiency. The method of unsteady flowrate measurement was applied to estimate the dynamic flowrate on a pipe line rig. Experimental results show that the method is effective to estimate the unsteady flowrate of system which is very useful for analysing the system characteristics and for investigating the methods of pressure pulsation cancellation.

6.1 Introduction

In most fluid power hydraulic systems, the speed and force of a load are controlled by using valves to throttle the flow and dissipate the hydraulic pressure or reduce the flowrate. This is a simple but extremely inefficient method as the excess energy is lost as heat. The switched inertance hydraulic system (SIHS) is one of the alternative methods which can provide varied flow and pressure by a means that does not rely on dissipation of power. This SIHS could be used in a number of configurations, all of which are commonly required in hydraulic fluid power systems (Johnston, 2009):

- To produce a modulated pressure and flow from a fixed pressure supply. This would behave like a proportional valve. It may be used for controlling the speed and force of one or more devices from a constant pressure supply.
- To produce a variable controlled flow from a fixed capacity pump. This would behave like a fixed capacity pump with a pressure compensated flow control valve, or like a variable capacity pump. This may be used to control the speed of a hydraulic motor.
- To produce a variable flow at a constant, controlled pressure from a fixed capacity pump. This would behave like a pressure compensated pump. This is

commonly required when several loading devices are required to be operated in parallel from a common supply (Johnston, 2009).

Brown presented a number of switched reactive devices with good simulated results and successful experimental validations (Brown et al., 1988, Brown, 1988). The theory and principle of SIHS and its application are investigated in the following sections.

6.2 Principle of operation

An initial investigation of the performance of three-port and four-port SIHSs was presented by Johnston (2009). Two modes, a flow booster and a pressure booster, can be configured by reversing the inlet and outlet connections in a three-port SIHS. It consists of a high-speed switching valve with one common port and two switched ports and a long, small diameter 'inertance' tube.

6.2.1 Flow booster configuration

Figure 6.1(a) shows the arrangement of a flow booster. The three-port switching valve has one common port and two switched ports. The common port is connected alternately to high pressure (HP) supply port and then the low pressure (LP) supply port. When one switched port is connected to the common port, the other switched port is closed off. The common port is connected to the 'inertance' tube, which performs the function of the inductor in the electrical circuit as shown in Figure 6.1(b), causing flow to continue when there is no power input. The switching valve, inertance tube and accumulator correspond to a switch, inductor and capacitor respectively in electrical circuits.

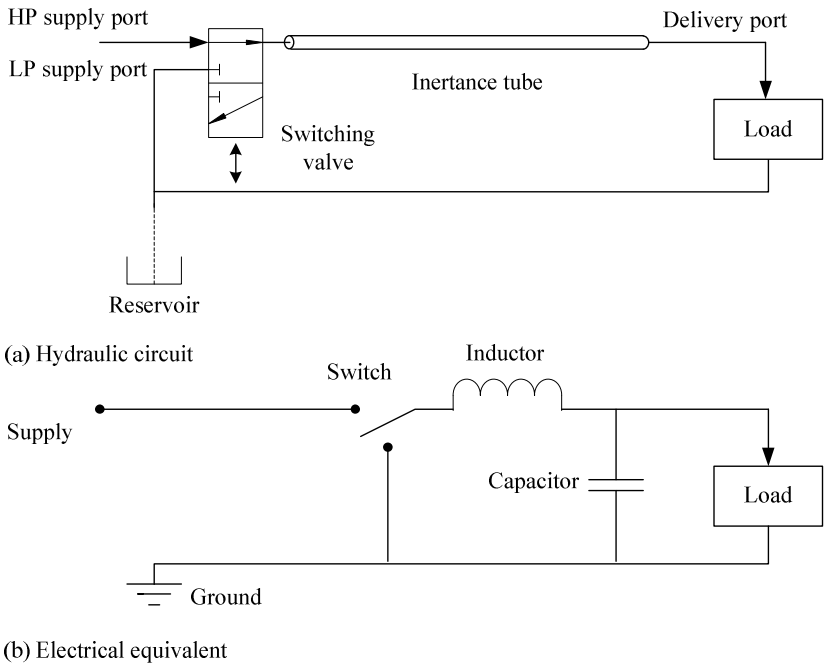

Figure 6.1 Schematic diagram of flow booster arrangement (Johnston, 2009)

While the SIHS works, the switching valve performs cyclically and rapidly such that the supply and boost ports are opened alternately. The delivery port might connect to a loading system. When the valve is connected to the HP supply port, flow passes form the HP supply port to the delivery port and a high speed fluid occurs in the inertance line. When the valve is open to the LP supply port, fluid is drawn from the LP supply port to the delivery port by large momentum of the fluid in the inertance line. As long as the valve is switched quickly, the delivery flow will only reduce slightly due to small deceleration of fluid velocity during this phase, as shown in Figure 6.2.

The flowrate into the HP supply port (Q_{HP}) and LP supply port (Q_{LP}) takes the form of a series of 'on-off' pulses, whereas the flowrate from the delivery port (Q_{DF}) is relatively steady and roughly equal to Q_{HP} and Q_{LP} during the 'on' cycle, as shown in Figure 6.2. It can be seen that the mean HP supply flowrate is lower than the delivery flow.

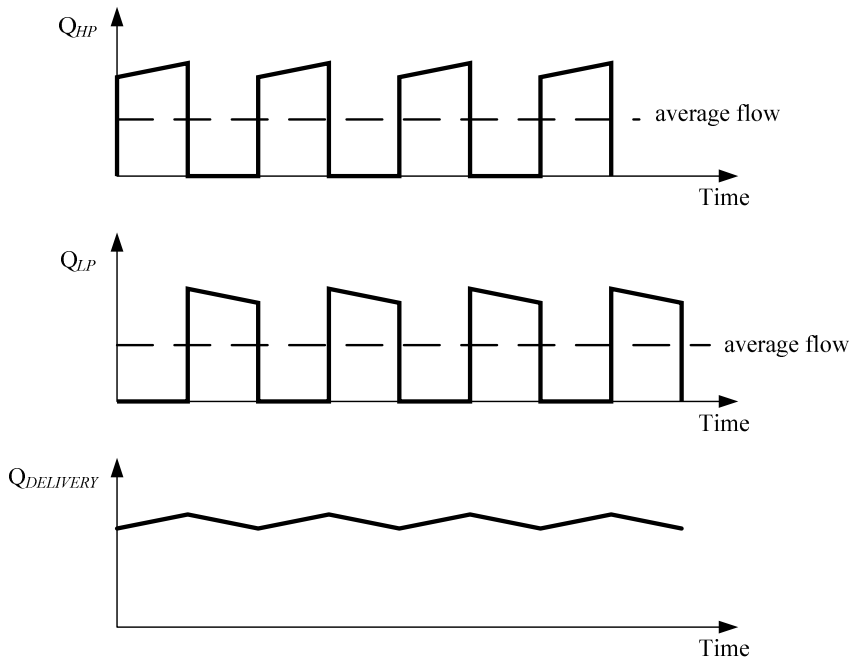

Figure 6.2 Idealized operation of flow booster (Johnston, 2009)

Regarding the form of 'on-off' pulses, the delivery flowrate and pressure can be varied by adjusting the ratio of time between the HP supply port open to LP supply port open. Ideally, assuming operation with no losses, the relationship between delivery flow and mean HP supply flow can be written as:

$$Q_{DF} = \frac{Q_{HP}}{x} \tag{6.1}$$

where x is the percentage of the valve cycle during which the valve is connected to the HP supply ($0 \le x \le 1$). Equation 6.1 demonstrates that the delivery flow is higher than the mean HP supply flowrate from the other side.

The relationship between delivery pressure and supply pressure for ideal operation is given by Equation 6.2:

$$P_{DF} = xP_{HP} + (1-x)P_{LP} \tag{6.2}$$

As can be seen, the delivery pressure is lower than the HP supply pressure. If x is increased, the delivery flow decreases but the delivery pressure increases. In practice, the actual delivery flow and pressure will be less than the ideal Q_{DF} and P_{DF} due to leakage and friction losses.

6.2.2 Pressure booster configuration

Figure 6.3(a) shows the configuration of a pressure booster. Different from the flow booster, one supply port is used to connect to a high pressure source and two outlet ports which are a delivery port and a low pressure port are for a load at high pressure and a reservoir at low pressure respectively. The valve switches cyclically and rapidly such that the delivery and return ports are opened alternately.

Assuming the switching ratio is 0.5, the supply pressure can be calculated as

$$P_{SP} = \frac{P_{DP} + P_{RP}}{2} \tag{6.3}$$

where P_{DP} is the delivery pressure and P_{RP} is the return pressure ($P_{RP} \le P_{SP} \le P_{DP}$).

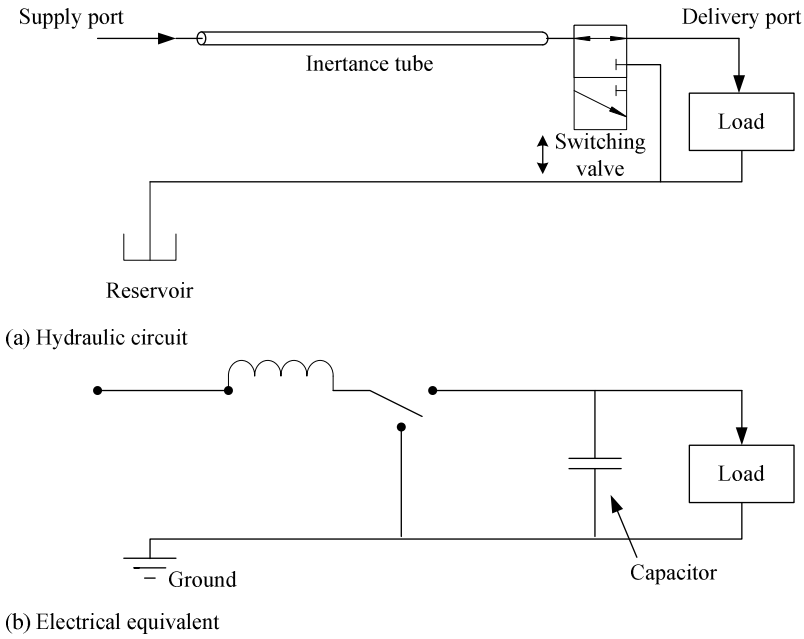

Figure 6.3 Schematic diagram of pressure booster arrangement (Brown, 1988)

When the valve switches to the delivery port, flow passes from the supply port to the delivery port where the pressure is higher than supply pressure, so the flow in the inertance tube decelerates. When the valve switches to the low pressure port, flow passes from supply port to low pressure port where the pressure is lower than supply pressure, so the fluid in the inertance tube accelerates.

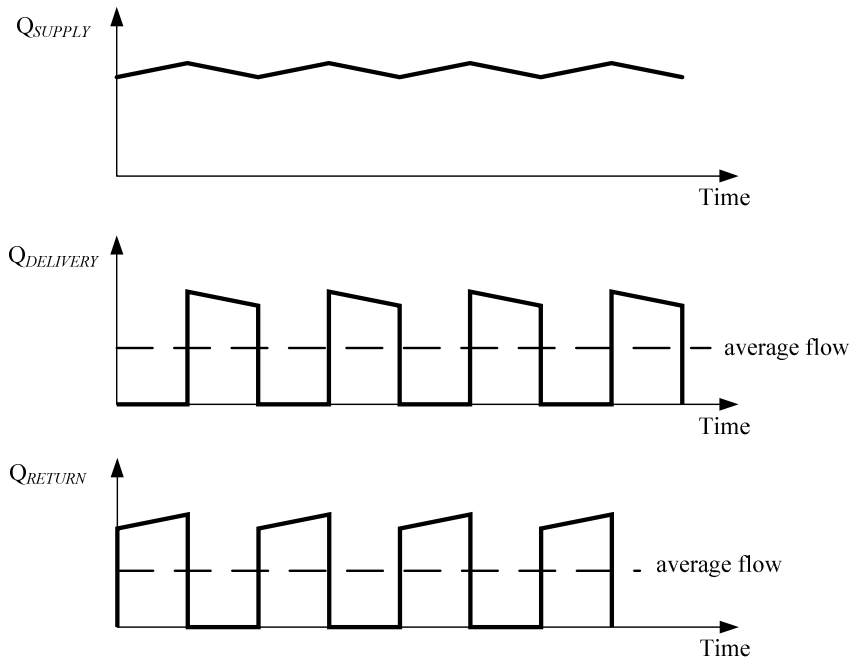

Figure 6.4 Idealized operation of pressure booster (Johnston, 2009)

Regarding the form of 'on-off' pulses, the delivery flowrate and pressure can be varied by adjusting the ratio of time between the HP supply port open and LP supply port open. Ideally, assuming the operation with no losses, the relationship between delivery flow and mean HP supply flow can be written as:

$$Q_{DP} = xQ_{SP} \tag{6.4}$$

where x is the percentage of the valve cycle during which the valve is connected to the delivery port ($0 \le x \le 1$). The delivery flow is smaller than the supply flow.

The relationship between delivery pressure and supply pressure for ideal operation is given by Equation 6.2:

$$\begin{aligned} P_{DP} &= \frac{P_{SP}}{x} - \frac{(1-x)P_{RP}}{x} \\ &= \frac{(P_{SP} - P_{RP})}{x} + P_{RP} \end{aligned} \tag{6.5}$$

If x is increased, the delivery flow increases but the delivery pressure decreases.

It can be said that the flow and pressure boosters may be efficient for controlling the flow and pressure without much energy loss by careful design of the SIHS. However, the noise problem is an issue as noted by Brown et al.(1988) and Johnston (2009) for

these two configurations. This is because the pulsed nature of a high speed switching valve introduces pressure ripple into the inlet and outlet lines in SIHS. Passive systems to reduce the noise have been shown to be effective at some points, but they require tuning to specific systems and the attenuation frequency range is limited and they may be bulky. The implementation of active noise cancellation using designed and modified controller on SIHS was studied and is discussed in Chapter 7. This chapter presents research of SIHS performance in terms of switching ratio and loading requirement.

6.3 Simulation studies

6.3.1 Flow booster

A flow booster model was created using MATLAB Simulink.

The switching valve flow was modelled using the standard orifice equation, as shown in Equation (6.6):

$$Q_{VALVE} = A_{Eff}\sqrt{\frac{2|\Delta P|}{\rho}}\,\mathrm{sgn}(\Delta P) \tag{6.6}$$

The closed valve port was modelled using Equation 6.6 as well but with a very small area to represent leakage. The area A_{Eff} was assumed to vary linearly between the open and closed areas over 1% of a complete cycle. A loading valve was modelled using this equation with the area $A_{Eff} = C_d A_{open}$, where C_d is the discharge coefficient and A_{open} is the opening area of the valve.

The volume between the switching valve and the inertance tube was modelled using Equation 6.7

$$P = \frac{B}{V}\int (Q_{VALVE} - Q_{TUBE})dt \tag{6.7}$$

The Transmission Line Method (TLM), which was developed by Kruz (1994) and modified by Johnston (2006, 2012) to include unsteady or frequency-dependent friction, was applied for modelling the inertance tube. The wave propagation effects can be accurately represented by this model over a wide frequency range.

Simulink's 'ode23tb' solver ('stiff/TR-BDF2') was used in this simulation. This was found to be reasonably efficient and stable. Parameters for the model are listed in Table 6.1.

Table 6.1 Parameters for simulations

Bulk modulus in valve B_v	10^9 Pa
Density ρ	870 kg/m^3
Viscosity μ	20 cSt
Switching frequency f	200 Hz
Effective orifice area A_o, switching valve open	1.44 cm^2
Effective orifice area A_c, switching valve closed	0.03 mm^2
Valve internal volume between switching orifices and inertance tube, V_{va}	10 cm^3
Discharge coefficient of the loading valve	0.7
Inertance tube length l	1 m
Inertance tube diameter d	7 mm
Bulk modulus in tube B_t	1.6×10^9 Pa
Number of unsteady friction terms	4

Figure 6.5 shows the supply, delivery and return flowrates of the flow booster with ratio $x = 0.5$. The theoretical curves stated the ideal flowrates without the wave propagation effects. The high pressure supply was fixed at 100 bar, and the low pressure supply (return) at 10 bar. The opening area of the loading valve was 1 cm^2 which represented the valve was in fully open status and small loading was forced on the system. It can be seen that the flowrate into the HP was about 4.6 L/s in acceleration and the flowrate into the LP was also close to 4.6 L/s in deceleration during the 'on' cycle. The delivery flowrate is relatively steady and roughly equal to 4.6 L/s when the switching frequency was 200Hz.

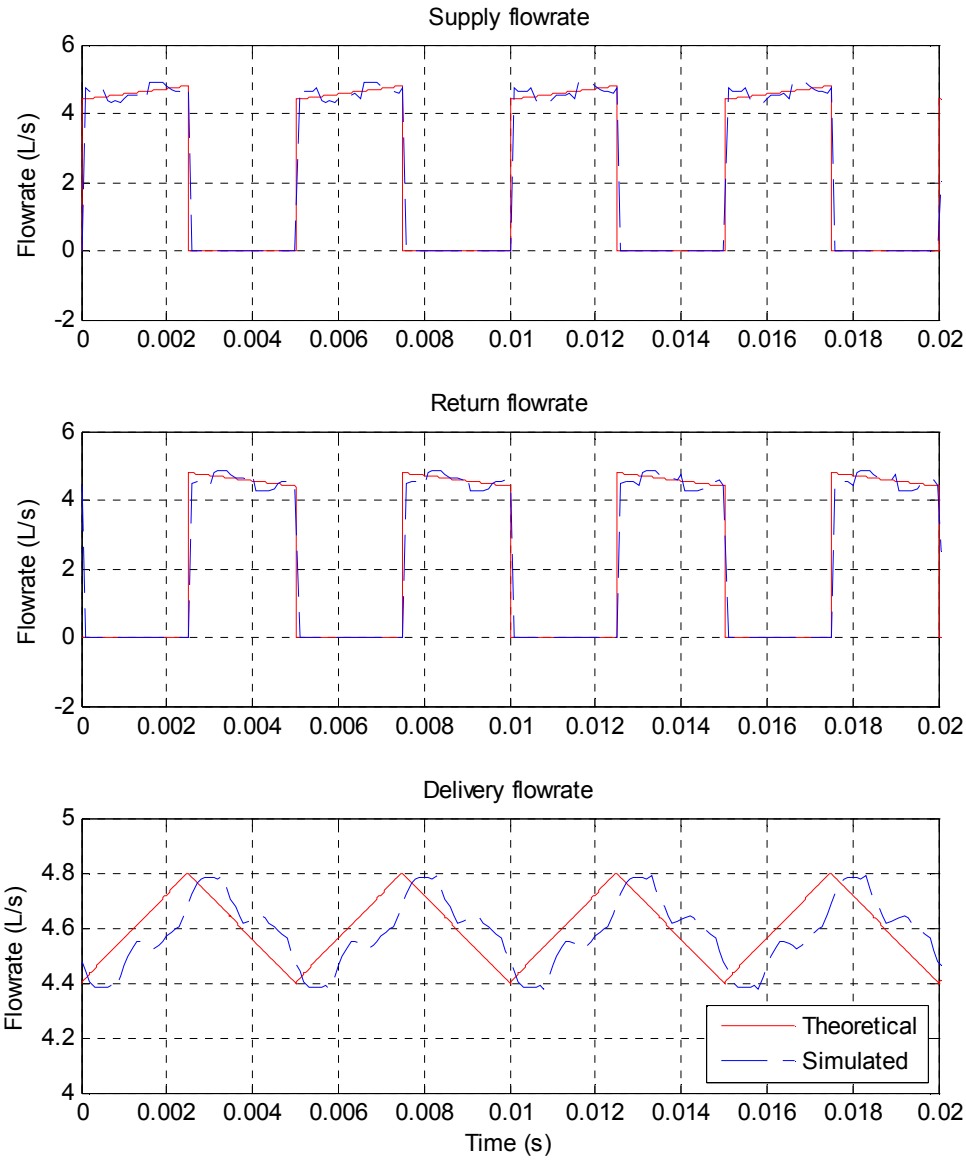

Figure 6.5 Simulated results of flow booster with switching ratio equal to 0.5

Adjusting the switching ratio to 0.7, the outlet flowrate varied to about 5.4 L/s, as shown in Figure 6.6. It can be concluded that the flow booster is effective for boosting delivery flowrate with lower supply by using different ratios.

As can be seen from Figure 6.5 and Figure 6.6, the delivery flowrate has 0.7ms delay compared with the theoretical curve. This is caused by the wave transition along the l m inertance tube. The speed of sound was 1356 m/s which is determined by the bulk modulus in the tube and fluid density.

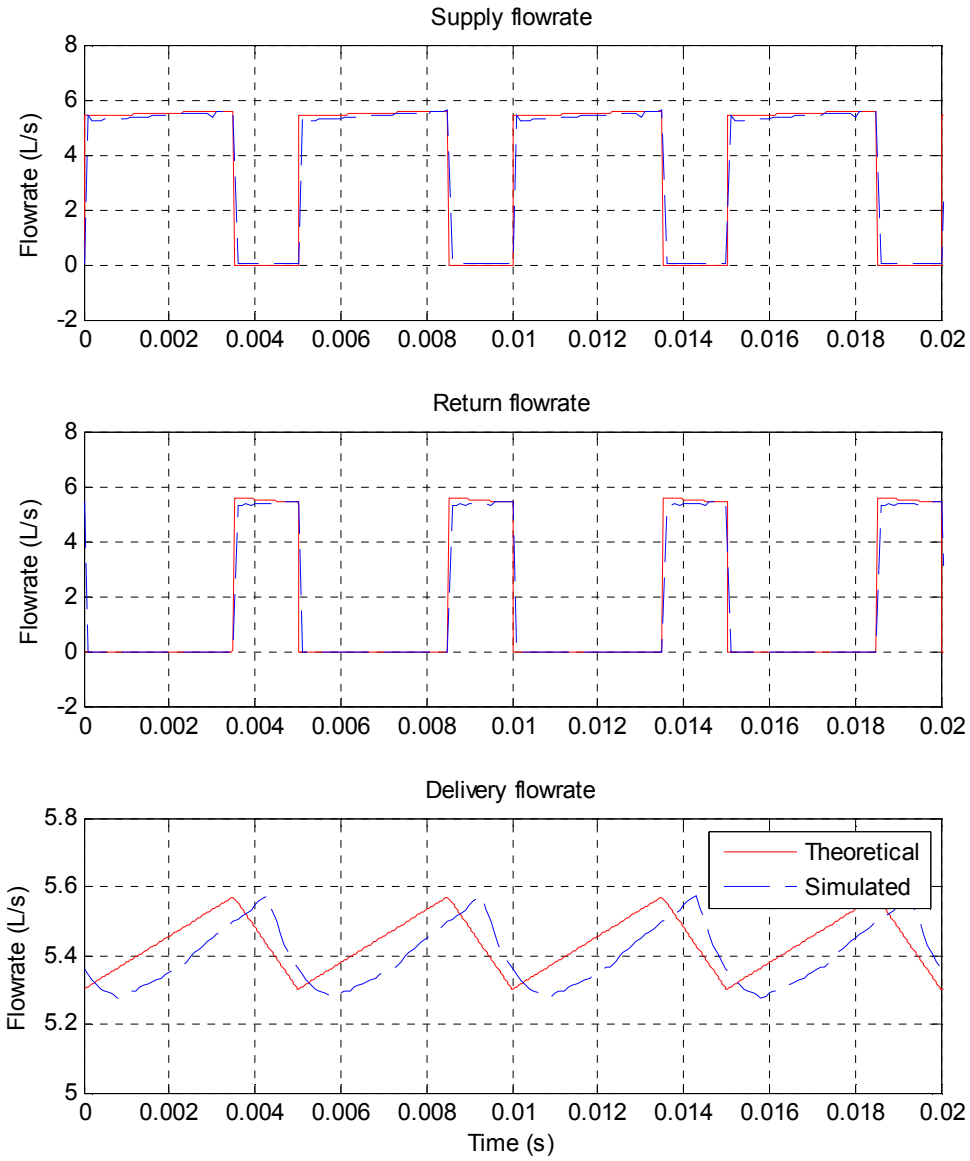

Figure 6.6 Simulated results of flow booster with switching ratio equal to 0.7

The delivery pressure is affected by the switching ratio and loading of system. Simulated results are shown in Figure 6.7, for a range of opening of loading valve. The switching ratio was fixed at 0.5. The opening was ramped from zero at 1s to 0.5cm^2 over a period of 5 seconds. A second order low pass filter was used with a 6 Hz cutoff frequency to eliminate the noise of delivery flowrate and pressure. As can be seen, the system went to steady state after 0.3s. The delivery pressure was about 55 bar at 0.3s when the delivery flowrate was ideally 0 L/s. This pressure is equal to the theoretical value calculated using Equation 6.2. The resistance of the tube and valve could also cause pressure drop between the supply port and delivery port. It can be noted that the

delivery pressure decreased with the increasing flowrate. The supply and return flowrates at the last 0.02s are shown in Figure 6.8, where the delivery flowrate was boosted over 3L/s. The results demonstrate that the flow booster can be used as a pressure source with a boosted flowrate which would be beneficial when a high flowrate is required.

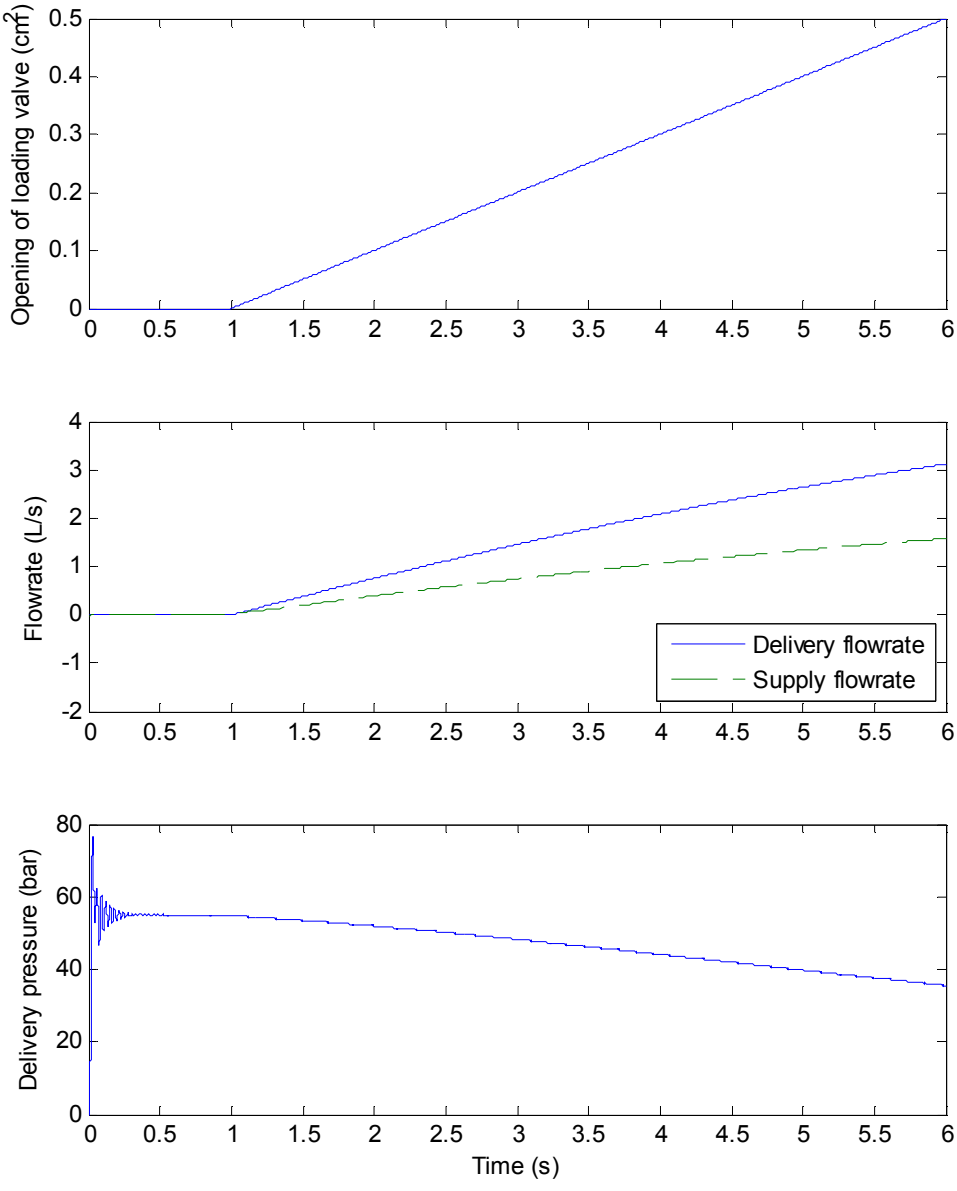

Figure 6.7 Delivery flowrate and pressure with varying loading

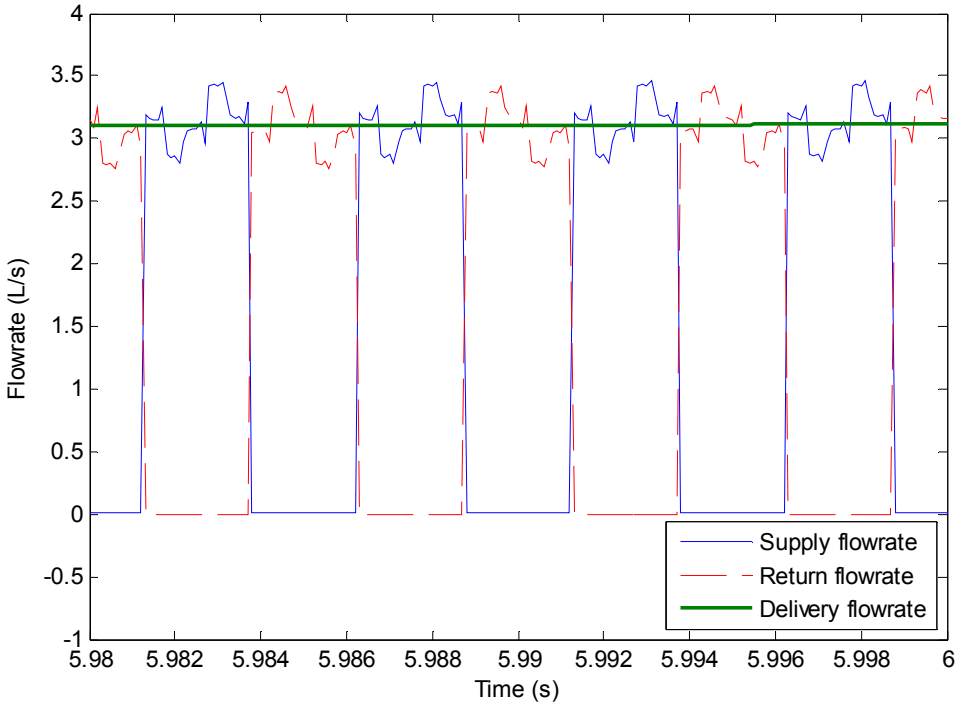

Figure 6.8 Supply and return flowrate of the flow booster

The flow booster could also be implemented to act like a proportional valve to produce a modulated pressure and flow from a constant pressure by means of adjusting the switching ratio. Simulations were performed of the response of flow booster whilst changing the valve switching ratio x from 0 to 1 with a ramp up and ramp down profile. The opening of loading valve was 0.01 cm^2 which represents the downstream end nearly closed.

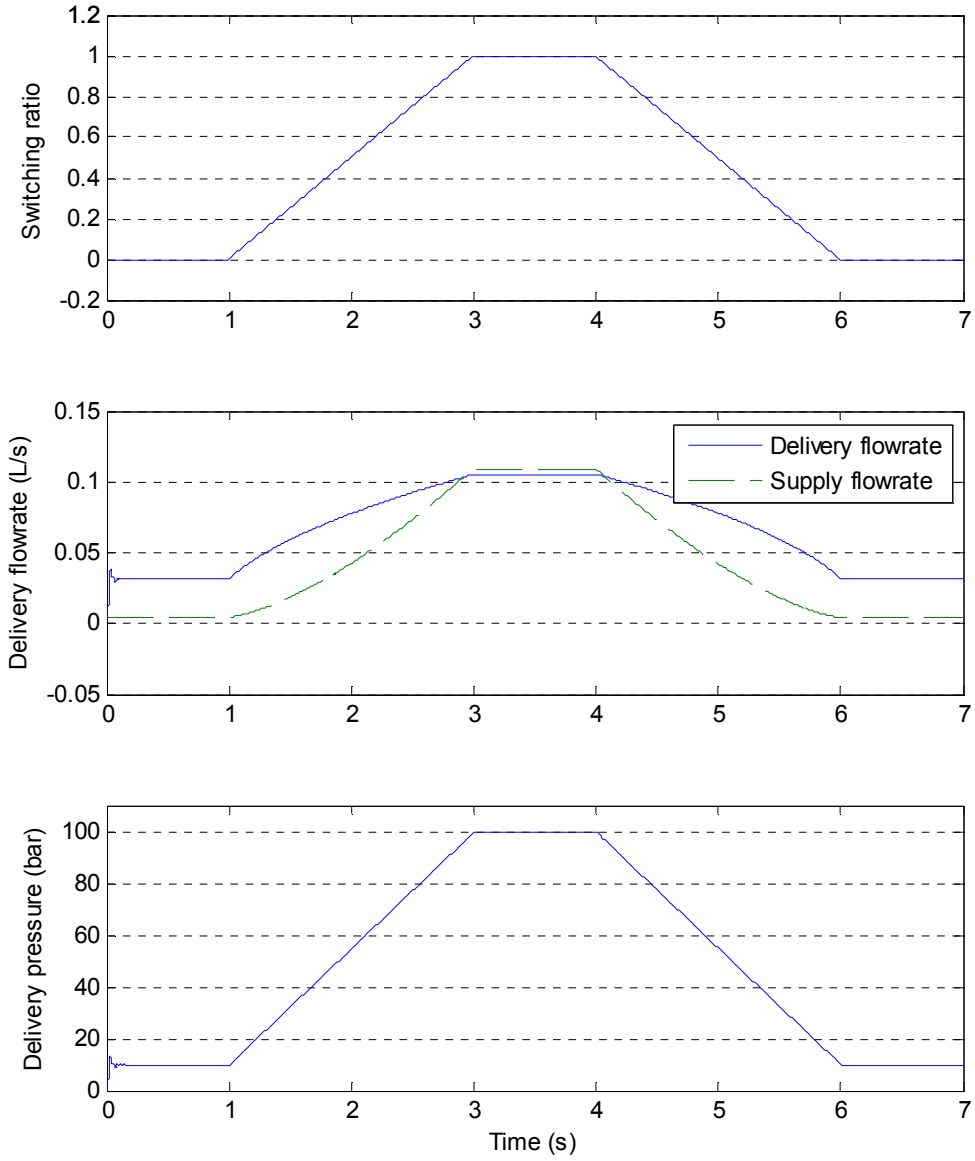

Figure 6.9 Delivery flowrate and pressure with varying switching ratio in 7s

Figure 6.9 plots the relationship of delivery flowrate and pressure with switching ratio. It can be noticed that the delivery pressure and flowrate went up gradually as a result of the increasing ratio and dropped with the decreasing ratio. Therefore, it can be concluded that the flow booster is able to adjust the speed and force of devices from a constant pressure supply and return line.

A conventional system was assumed and simulated with the supply pressure of 100bar and flowrate of 7L/min according to the requirements of delivery flow in order to

discuss the efficiency of the flow booster. Using the conventional supply source, the delivery flowrate and pressure would be adjusted by applying a proportional valve. Figure 6.10 shows the system efficiency using the flow booster and the proportional valve. It can be seen that the efficiency achieved from the flow booster was higher than using the proportional valve. It can be expected that ideally using the flow booster is more efficient than the conventional method.

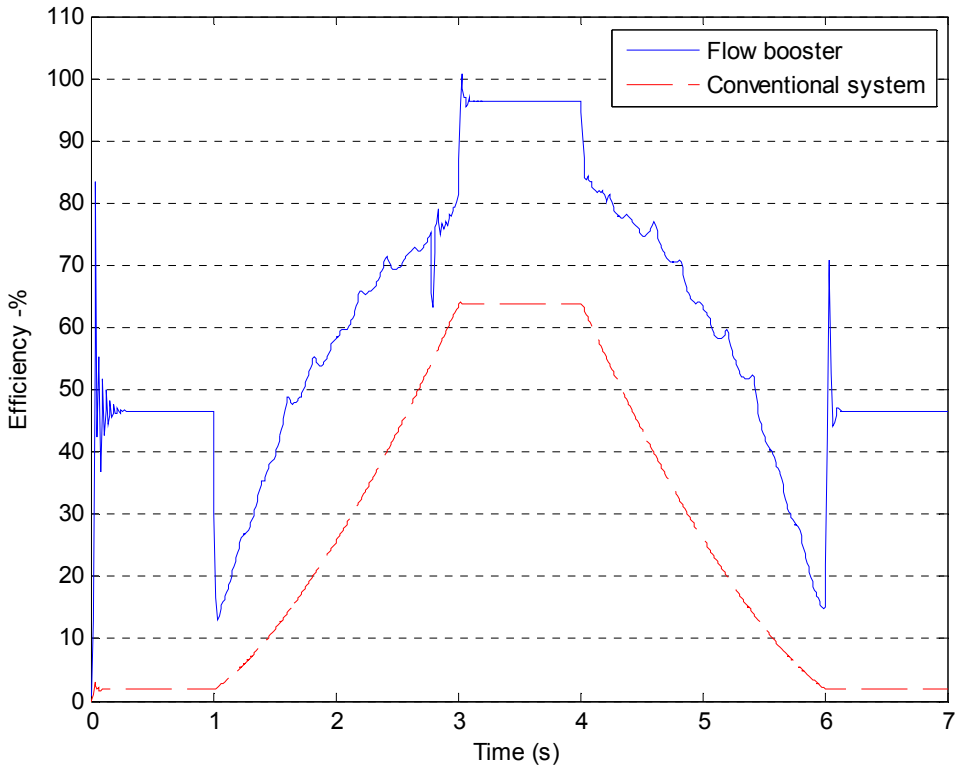

Figure 6.10 Efficiency and power loss of the system

6.3.2 Pressure booster

A pressure booster model was created in which the inertance tube, volume and switching valve were modelled using the same equations as the flow booster. Simulation parameters used for flow booster were re-applied to the pressure booster.

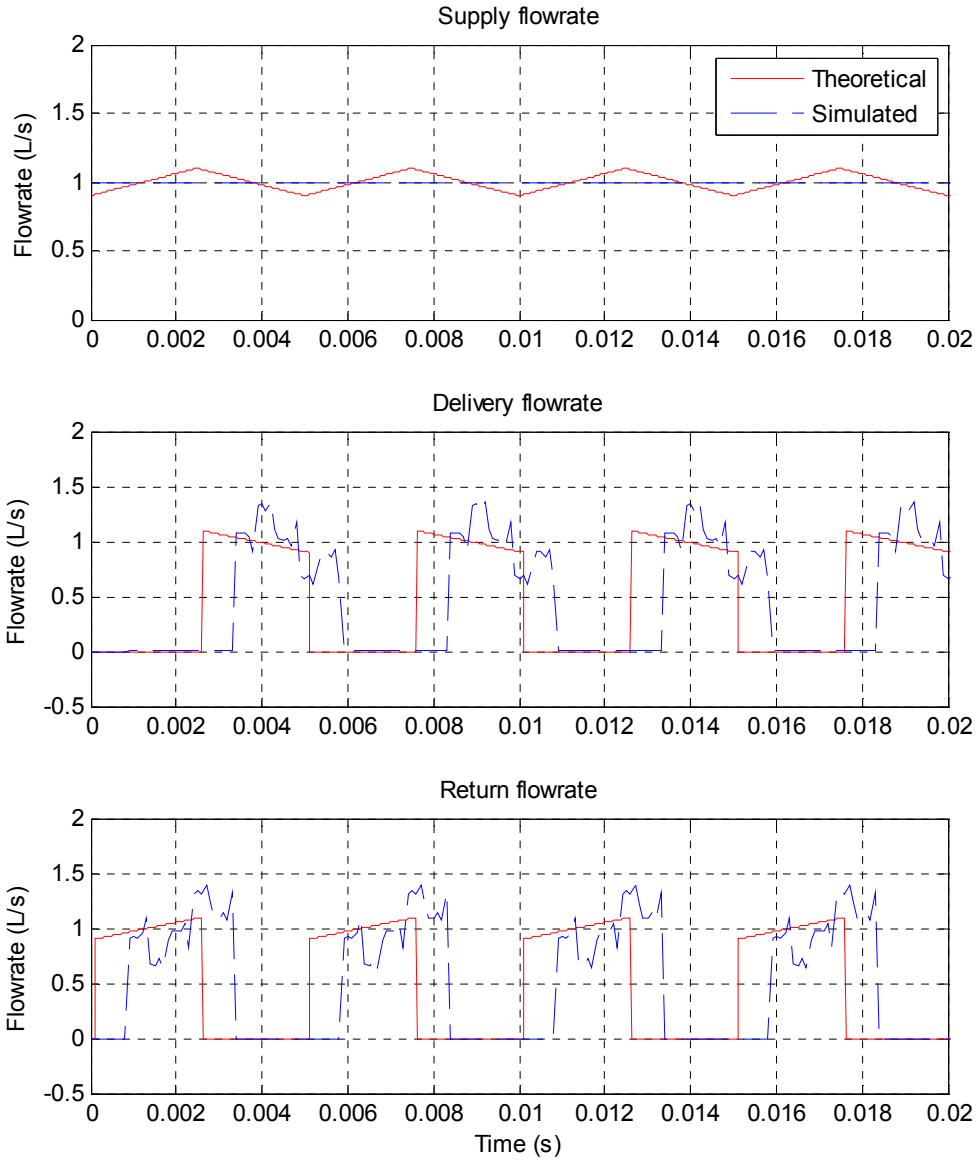

Figure 6.11 Simulated results of pressure booster with switching ratio equals 0.5

Figure 6.11 shows the simulated results of pressure booster with ratio $x = 0.5$. The supply flowrate was fixed at 1 L/s, and the load pressure and return pressure were at 100 bar and 10 bar respectively. The opening area of the loading valve was 1 cm^2. It can be seen that the delivery flowrate and return flowrate take the form of a series of 'on-off' pulses, whereas the flowrate from the delivery port is 1 L/s during the 'on' cycle.

The switching ratio can affect the delivery flowrate and supply pressure. Figure 6.12 shows the supply and delivery pressures with the ratio equal to 0.5 and 0.3 respectively. The inlet flowrate Q_{SP} was 1 L/s. As can be noted, the pressure delivered was higher

than the pressure supplied, which means the load pressure can be maintained at high pressure (100 bar) with a lower supply pressure.

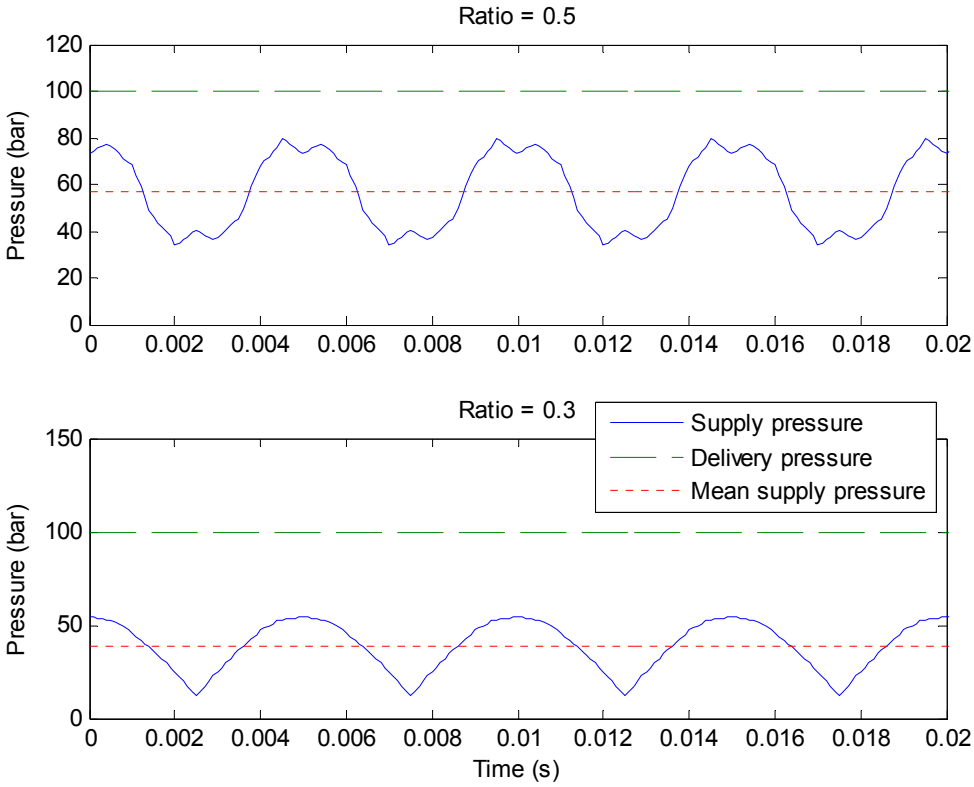

Figure 6.12 Simulated results of pressure booster with constant supply flowrate

Figure 6.13 shows the performance of pressure booster whilst changing the valve switching ratio x from 0 at 2s to 1 at 2.2s with a ramp up and ramp down signal. A second order low pass filter was used with a 6Hz cutoff frequency to eliminate the noise in the delivery pressure and flowrate. The response is reasonably linear. It can be seen that the outlet pressure of 100 bar is maintained while the supply pressure is low (about 10 bar) at low delivery flowrate.

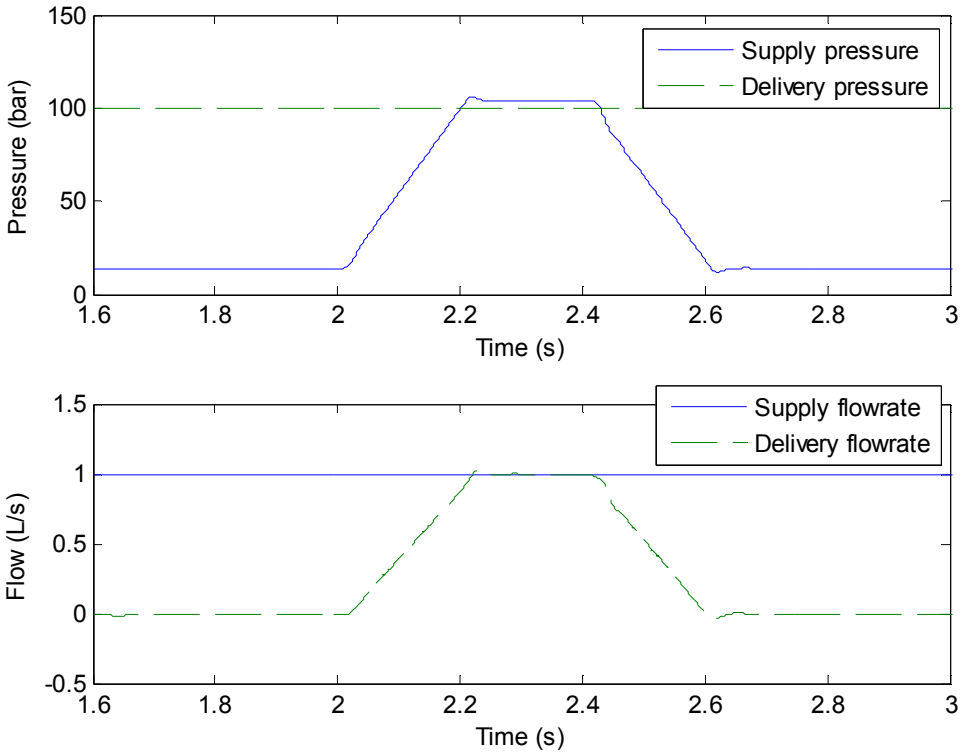

Figure 6.13 Performance of pressure booster with changing switching ratio

6.4 Unsteady flowrate measurement

A novel method was proposed by Johnston and Pan (2010) to estimate the unsteady flowrate based on the wave propagation model using measured pressures as boundary conditions (Appendix 3). The estimation of dynamic flowrate is significant for the theoretical analysis of pipe system and practical applications. However, it is difficult to obtain the dynamic flowrate in practice. Many systems and methods have been proposed as the means to obtain the unsteady flowrate by determining the velocity of fluid, such as the hot wire anemometer, laser Doppler velocimetry and particle image velocimetry. These methods are expensive and sophisticated, and they are particularly ill-suited to use on an industrial site. In this section, the proposed method was validated in the experiments.

The three-transducer method was applied to a pipe rig to estimate the unsteady flowrate at certain positions. Three transducers were arranged along the pipe with unequal spacing, as shown in Figure 6.14. The length of the tube was 7.9m with the diameter of 7.1mm. The supply pressure was fixed at 50 bar in experiments. The boundary

conditions of the ends were determined by a proportional valve and a needle valve, which were arranged at the upstream end and downstream respectively.

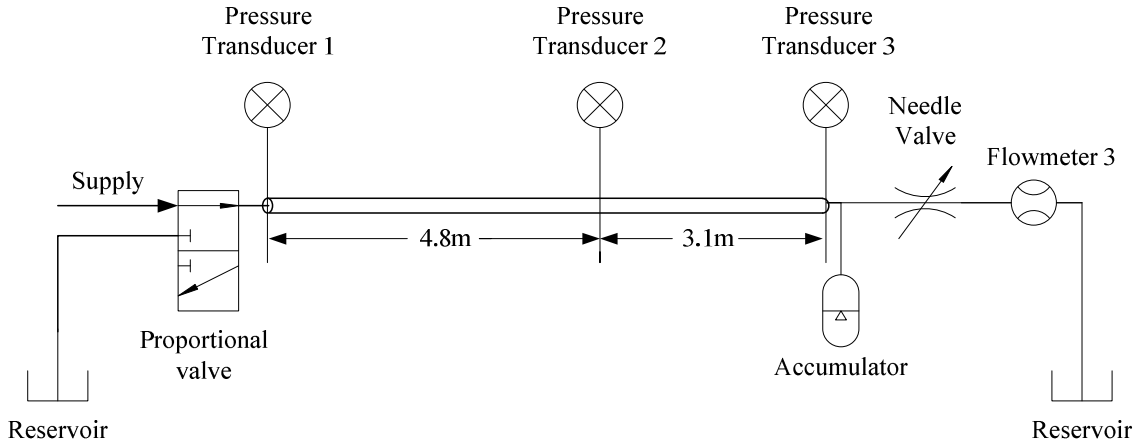

Figure 6.14 Schematic of the test rig

The proportional valve was controlled by a step voltage signal which was stepped from 2V to 0V at 1s. This means that the valve was switched off and the upstream end was completely closed after 1s, although a small leakage is expected of the valve itself. An accumulator was used to maintain constant pressure at load.

A pipeline model with the same boundary conditions and parameters of experiments was built in order to estimate the unsteady flowrate via simulation. The estimated flowrate would be used for comparison of the experimental results as it would be difficult to evaluate the measurement accuracy by other means currently.

Parameters used in the model are listed in Table 6.2.

Table 6.2 Simulation parameters

Length of pipe model *1* l_1	4.725m (node equals 36)
Length of pipe model *2* l_2	3.105m (node equals 24)
Diameter d	7.1 mm
Viscosity μ	72 cSt
Density ρ	870 kg/m^3
Speed of sound c	1350 m/s
Grid spacing	0.13 m
Friction terms k	4
Time step Δt	0.1 ms
Simulation time t	2 s

For a clear demonstration and explanation, pressures measured from the transducer *1, 2* and *3* as shown in Figure 6.14 were named the upstream pressure, middle-stream pressure and downstream pressure respectively. In the simulation, the measured upstream pressure was used as the upstream boundary condition of the system. Three measured and simulated pressures at steady operating conditions are shown in Figure 6.15 to Figure 6.17. As can be seen, the experimental and simulation results match well except for a small mean pressure difference which may result from the MOC model itself.

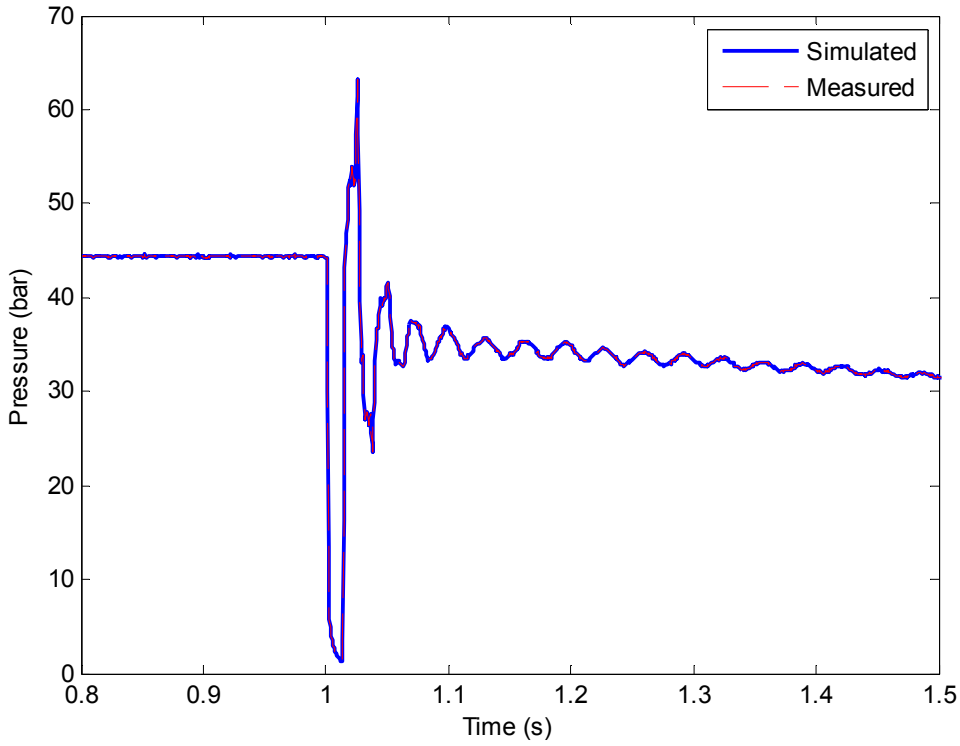

Figure 6.15 Experimental and simulated upstream pressures

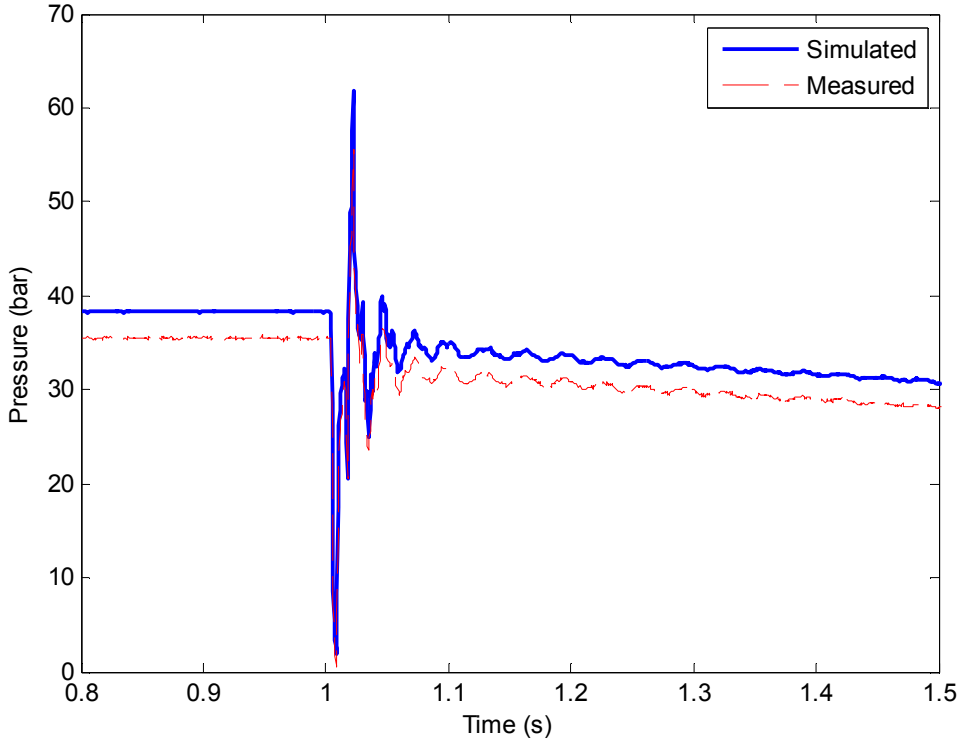

Figure 6.16 Experimental and simulated mid-stream pressures

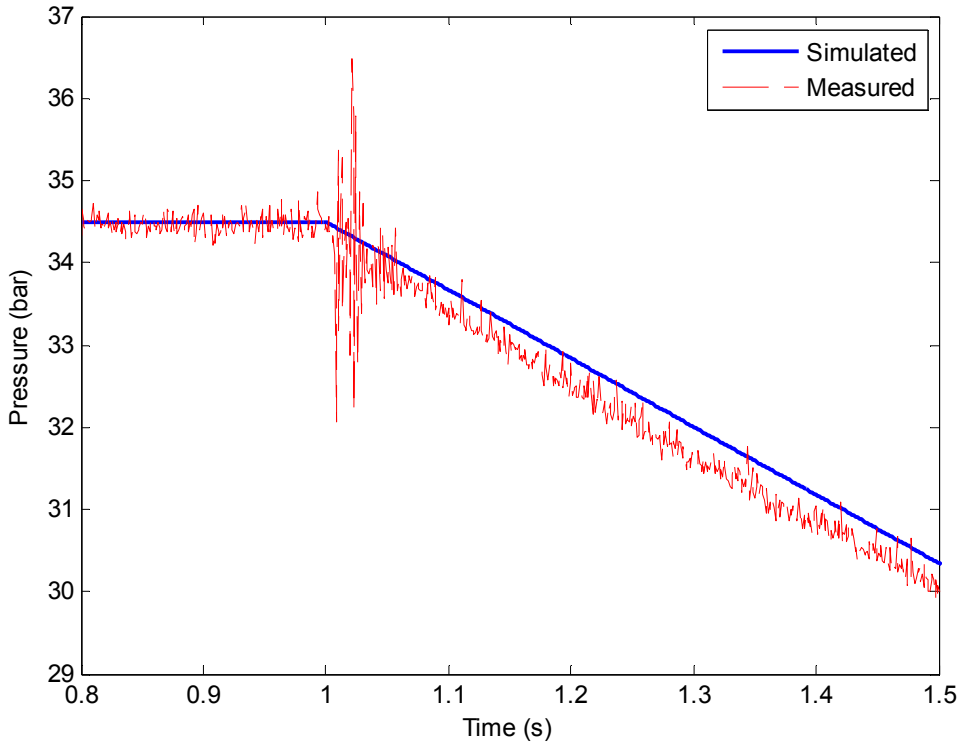

Figure 6.17 Experimental and simulated downstream pressures

Figure 6.18 to Figure 6.20 show the unsteady flowrate measured at upstream, middle-

stream and downstream positions by using the three-transducer technique. It can be seen the simulated and experimental unsteady flowrates at steady operating conditions agree well except for a small mean flowrate difference at the upstream and downstream positions. This method may have a disadvantage of inaccurate mean flowrate measurement because it is based on a wave propagation model and is less effective for steady state measurement.

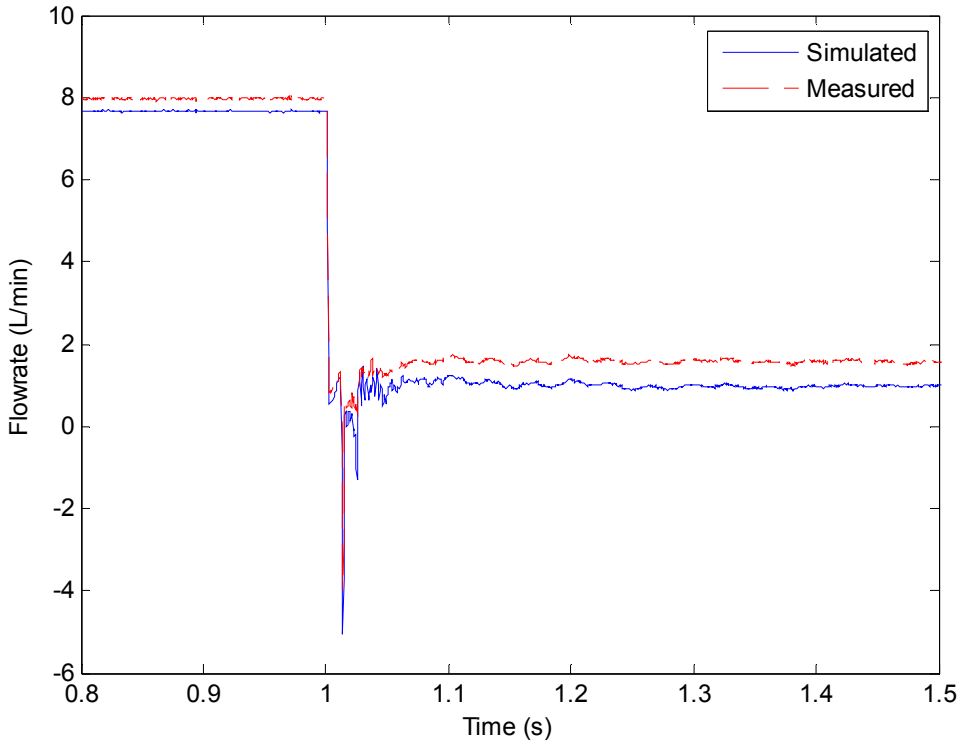

Figure 6.18 Experimental and simulated upstream flowrate

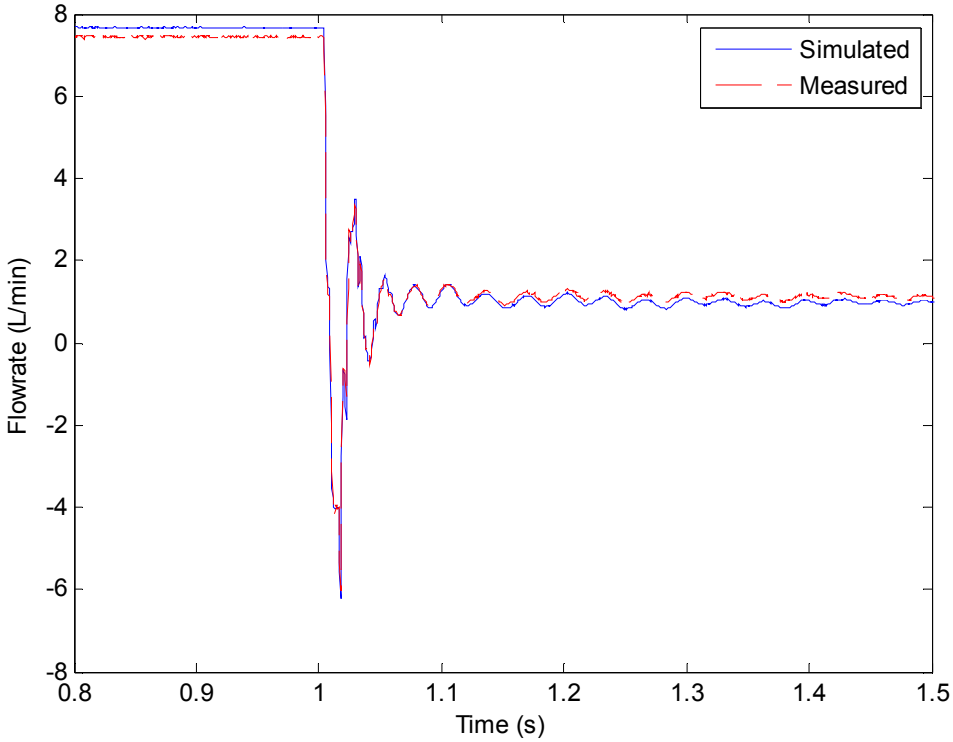

Figure 6.19 Experimental and simulated middle-stream flowrate

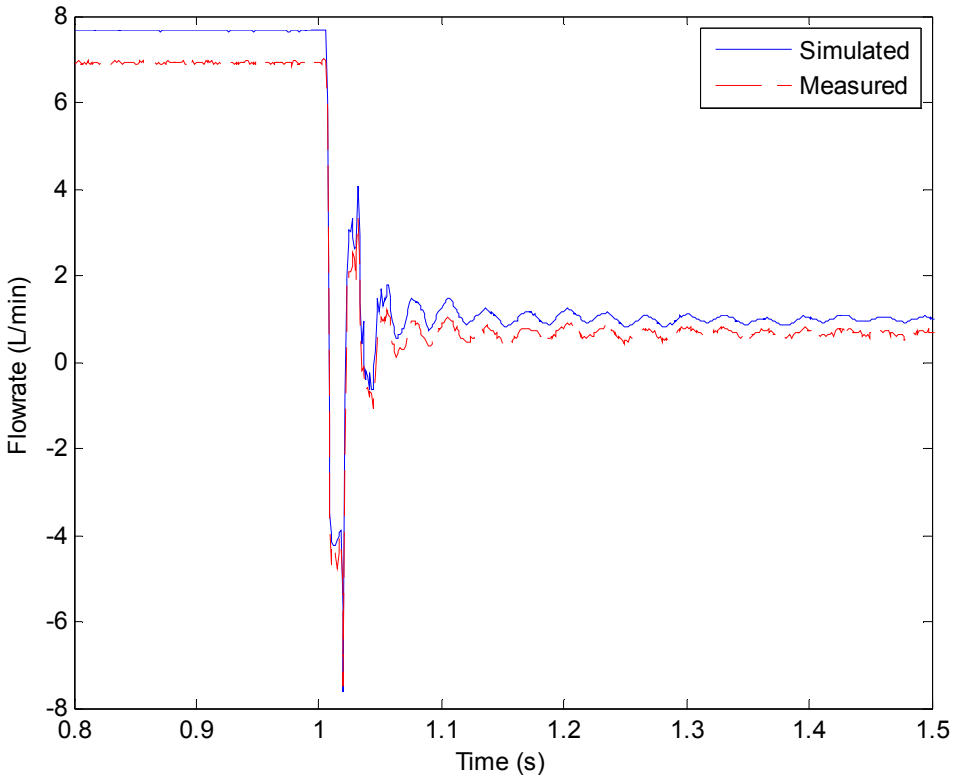

Figure 6.20 Experimental and simulated downstream flowrate

To conclude, the proposed unsteady flowrate measurement method was validated and proved for its effectiveness of estimating the instantaneous flowrate along the pipe. The experimental results show an acceptable accuracy of flowrate can be achieved comparing with the simulated results. However, it is difficult to find an effective method in experiments currently for comparison. With this method, the dynamic flowrate of the system can be estimated, which is very useful for studying and analyzing the characteristics of conventional piping systems and SIHSs. For a SIHS, this method can be also used for attenuating the pressure pulsation based on Kojima's method. A more accurate dynamic flowrate can be applied for attenuation instead of estimating the flow from the pressure gradient which has the limited bandwidth and inaccurate problem. This will be applied in future work.

6.5 Concluding remarks

The principle and operation of switched hydraulic system has been introduced in this chapter. The flow booster and pressure booster models were built and investigated via simulation. Results show that the SIHS works as expected. However, because of the pulse nature of the flow during the valve switching, the noise problems may be an issue. The details of pressure pulsation problem and the implementations of noise cancellation are described in the next chapter. Experiments of unsteady flowrate measurement were also presented. Good agreement occurred between the simulated and experimental results. It proved experimentally that the proposed method is effective for measuring the unsteady flowrate in a hydraulic piping system.

7 Simulation of pressure pulsation cancellation for a fast-switching system

The implementation for pressure pulsation cancellation in a flow booster system based on a fast switching valve has been investigated within two different arrangements, which were named as the by-pass structure and the in-series structure. The by-pass structure represented the noise canceller arranged in parallel with the flow booster and system load; whilst for the in-series structure the controller was arranged in line with the main system. Simulated results show that excellent cancellation of pressure pulsation was achieved using the noise attenuator with both structures and the average cancellation obtained was 40dB. Moreover, the system stability and robustness were investigated in term of the switching frequency, switching ratio and load of a flow booster. Good and reliable results were obtained for the flow booster subjected to varying working conditions. Finally a comparison of the advantages and limitations of the by-pass and in-series structures is presented.

7.1 Noise source

In a switched inertance hydraulic system, the pulsed nature of a high speed switching valve could introduce pressure pulsation into the inlet and outlet lines. Figure 7.1 shows a typical delivery pressure wave from a flow booster. In this case, the pressure of the high supply line was 100 bar, and the pressure of the return line was 10 bar. A square wave was used as a driving signal for the fast switching valve. The switching frequency of the valve was 200Hz and the switching ratio was 0.5. When the square wave is during the ‘1’ cycle, the switching valve is connected to the high supply pressure port; when the square wave is during the ‘-1’ cycle, the switching valve is connected to the reservoir or the return port. As can be seen, pressure pulsation occurred in the system when the high-speed valve switched.

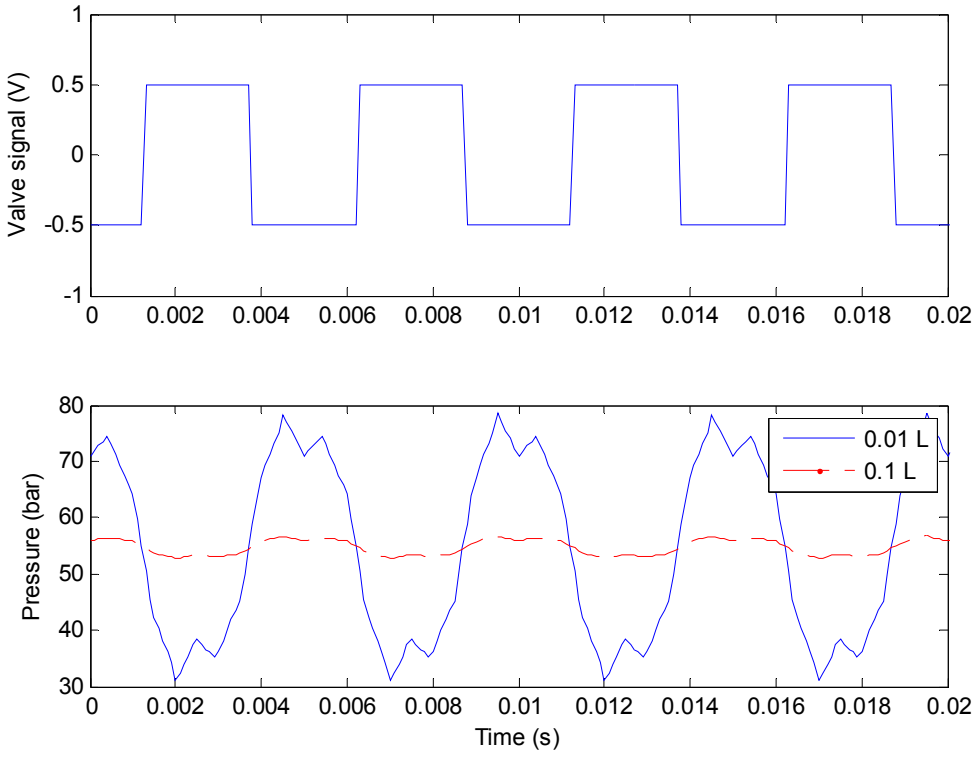

Figure 7.1 Simulated Pressure pulsation generated from a flow booster system with different sizes of accumulator

Many approaches could be used to decrease the pressure pulsation in hydraulic systems (Johnston and Tilley, 2003, Johnston, 2007). Generally speaking, there are passive and active control methods. Passive control methods have been proved for their effectiveness of noise cancellation in specific cases, but their attenuation frequency range is limited and they may be bulky, such as an expansion chamber silencer and large accumulator. As can be seen in Figure 7.1, accumulators with different volumes were applied for decreasing the FBN in the flow booster in simulation. It can be noted that the larger volume accumulator is more effective to reduce the pressure ripple and maintain a constant delivery pressure. However the accumulator would impair the system dynamic response as it adds compliance to the system. By contrast, active devices can potentially be effective at a much wider range of frequencies and system designs without affecting the system dynamics. The active method of fluid-borne noise (FBN) cancellation has been proven successfully in experimental results using a servo-valve (Wang, 2008). It is envisaged that the use of a faster secondary path actuator, such as piezoelectric actuated valve, would give improved performance.

7.2 System arrangement

Two different arrangements of FBN cancellation can be implemented on a flow booster system. These are the by-pass structure and the in-series structure, which are named based on the arrangement of the noise attenuator. The by-pass structure is that the noise attenuator is arranged in parallel with the noise source as a by-pass branch, whilst for the in-series structure the noise attenuator is positioned in line with the noise source of the system.

7.2.1 By-pass structure

Figure 7.2 shows a schematic of the by-pass structure. A pressure transducer was arranged at the conjunction of the tube and noise canceller to detect the residual delivery pressure $e(n)$ of the system. When the noise attenuator was switched off, the pressure transducer measured the pulsed delivery pressure produced by the flow booster directly. A loading valve was fixed at the downstream end to adjust the load of the system.

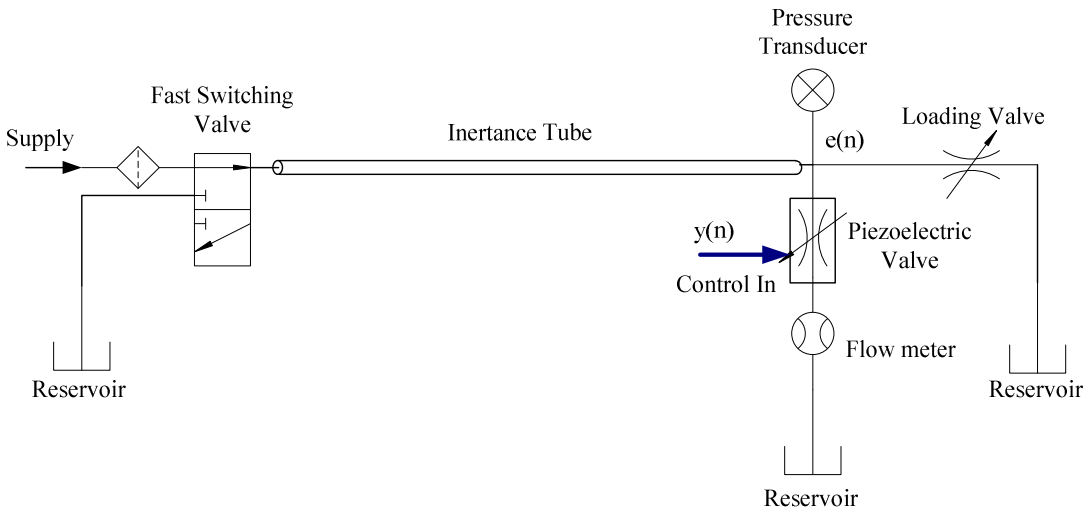

Figure 7.2 Schematic of the by-pass structure based on a flow booster system

7.2.2 In-series structure

The in-series structure, in which the noise attenuator was arranged in series with the noise source, pressure transducer and system load, is shown in Figure 7.3. The pressure transducer was arranged after the noise controller to ensure a constant delivery pressure for the system.

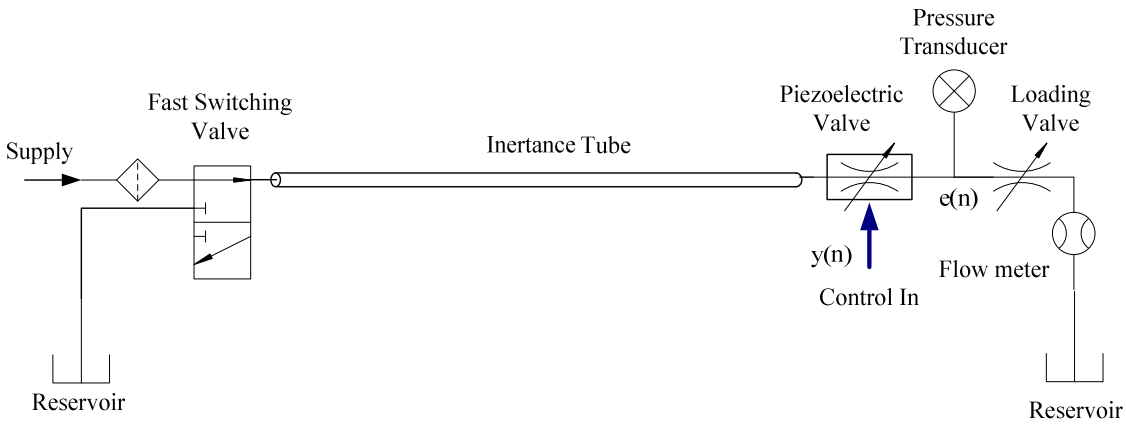

Figure 7.3 Schematic of the in-series structure based on a flow booster system

The noise attenuator was applied to generate a signal which has the same amplitude and opposite phase of the pressure ripple in flow booster in both by-pass structure and in-series structure. The by-pass structure results in an extra flow requirement, whilst the in-series structure results in an extra pressure requirement. Comparisons of the advantages and disadvantages of by-pass and in-series structures are described in section 7.5 of this chapter.

7.3 Implementation for pressure pulsation cancellation with a by-pass controller

The by-pass structure was implemented for pressure pulsation attenuation based on a flow booster. The performance of the designed noise canceller was investigated in terms of the switching frequency, switching ratio and load of system.

7.3.1 Secondary path identification

The knowledge of the secondary path $S(z)$ is significant to the FXLMS algorithm as mentioned in Chapter 3. $S(z)$ is usually estimated off-line then transferred to a controller and evaluated in real-time applications in which $S(z)$ is initially unknown and time-invariant. However, $S(z)$ is unknown and time-varying with different conditions in flow booster system, so it is necessary to perform simultaneous on-line identification and cancellation. In the following, both offline and online LMS approaches were investigated for $S(z)$ identification with the flow booster system.

7.3.1.1 LMS offline identification technique

The LMS offline identification method was applied with a fixed supply source, which means the switching valve was connected to a constant supply pressure without switching. The supply pressure was 100 bar and the tank pressure was 1 bar. A 1 m length inertance tube with a diameter of 0.7 cm was used in the system and the opening of loading valve was 0.1 cm^2. In order to show the dynamics of the piezoelectric valve, a second order transfer function

$$G(s) = \frac{628^2}{s^2 + 2 \times 0.8 \times 628s + 628^2} \tag{7.1}$$

was chosen to demonstrate the valve characteristics with a standard orifice equation (equation 6.6) and the opening of the piezoelectric valve was 0.02 cm^2 in simulation.

The impulse response of the secondary path $S(z)$ using the LMS offline technique is shown in Figure 7.4. The length of the LMS filter was 256 and the sample frequency was 10 kHz. It can be seen that the impulse response converged completely after 0.015s. The standard deviation of white noise was $1 \times 10^{-5} m^2$ and the convergence factor of the identification filter was $\mu = 1$. Parameters chosen were a compromise between the system stability and speed of computation. The simulation time was 15s.

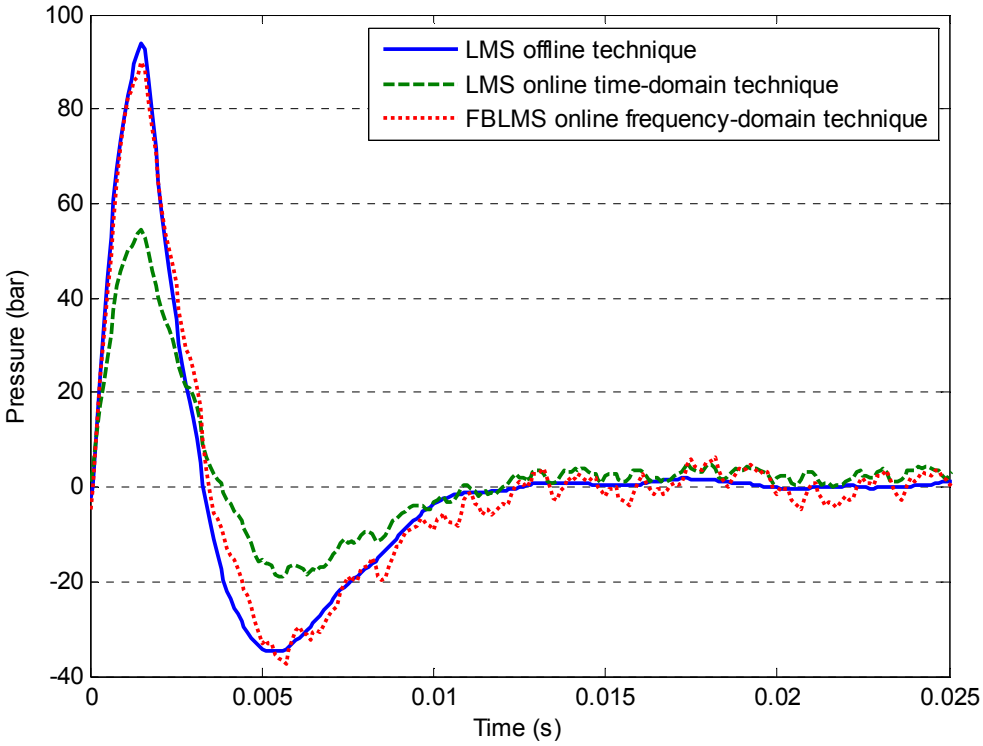

Figure 7.4 Impulse response of secondary path $S(z)$ of flow booster

7.3.1.2 LMS online identification technique

In the case of the LMS online method, in principle, the estimated $\hat{S}(z)$ is unaffected by interference from pressure pulsation, but the convergence speed of the adaptive algorithm would be affected by the presence of interference, as shown in equations 3.43 – 3.46.

The switching ratio x_f was fixed at 0.5 and flow booster switching frequency was 40Hz, introducing pulsed pressure ripples into the system. The high supply pressure was 100 bar and low supply pressure was 10 bar. The same parameters were re-applied for secondary path $S(z)$ identification by using LMS online technique and the result is shown in Figure 7.4. It can be noted that the impulse response was not converged eventually within 15s, although the same convergence factor was applied. This is caused by the interference from the pressure pulsation, which also might result in

system instability. Smaller convergence rate and longer simulation time could be helpful for the potential instability.

On the other hand, as mentioned and validated in Chapter 3, the FBLMS online frequency-domain algorithm could be a more robust and efficient option for $S(z)$ identification in the condition of the fast-speed valve switching cyclically from high pressure port to low pressure port. It can be seen from Figure 7.4 that the impulse response obtained by using the FBLMS online identification method is similar to the result from LMS offline method. The results show that the FBLMS algorithm is able to obtain an accurate secondary path dynamic in a flow booster within the pressure pulsation.

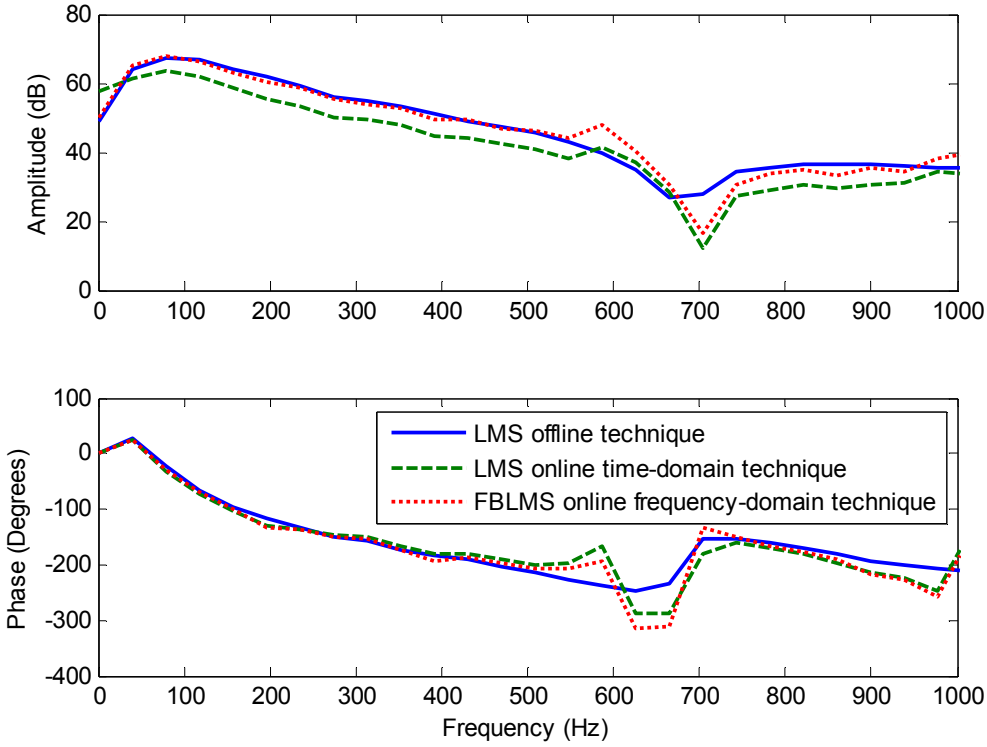

Figure 7.5 Amplitude and phase characteristics of secondary path $S(z)$ of flow booster

Figure 7.5 shows the frequency responses of $S(z)$ which is transformed from impulse responses by using FFT. The phases agree well using LMS offline, LMS online time-domain and FBLMS online techniques, although differences of amplitude occurred between the results from LMS offline technique and the other two approaches. However,

the differences could be compensated in the use of the LMS adaptive algorithm of the identification filter.

In conclusion, the LMS offline and FBLMS online techniques both are effective for $S(z)$ identification in the flow booster system. The FBLMS online identification process can be operated with or without pressure ripples from the switching valve, although the convergence speed of the adaptive filter might decrease. In practice, pressure pulsation occurs when the fast-speed valve switches. Therefore, the FBLMS online technique is more practical for the solution of secondary path identification of a flow booster in a real application.

7.3.2 Active pressure pulsation cancellation

The designed noise attenuator, which consists of an identification filter and a two weights notch filter for cancellation, was implemented for pressure pulsation attenuation in a flow booster. This section firstly describes the performance of the noise attenuator for single frequency and multiple harmonics cancellation. The stability and effectiveness were investigated next in terms of the controller performance when the switching frequency of the fast-speed valve was changed. Finally, the effects of varying switching ratio and system loading were studied. Figure 7.6 shows the schematic of pressure pulsation cancellation based on a flow booster system with a by-pass controller. Two switched ports were connected to a high supply pressure and a low supply pressure alternately, which was based on the driving signal produced by a pulsed wave generator. The control algorithm of the noise attenuator is designed based on Simulink blocks, where the FXLMS algorithm was applied to generate an adaptive control signal to the piezoelectric valve.

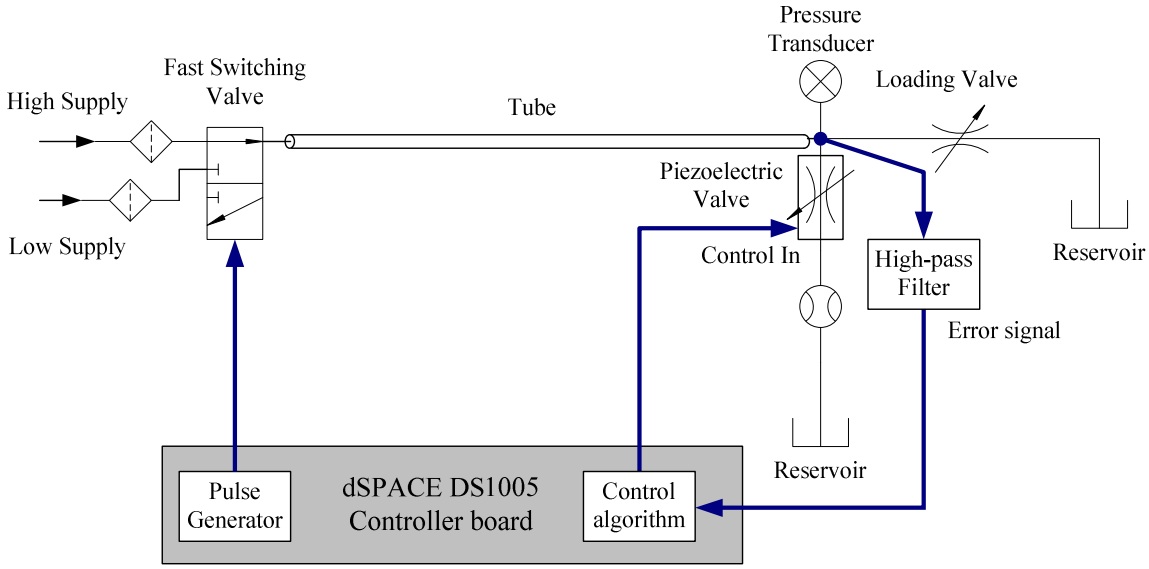

Figure 7.6 Schematic of the by-pass structure based on a flow booster system with noise attenuator

A digital Butterworth high-pass filter was designed with a cutoff frequency of 3 Hz to eliminate the mean pressure value measured from the pressure transducer. Figure 7.7 shows the magnitude and phase characteristics of the high-pass filter.

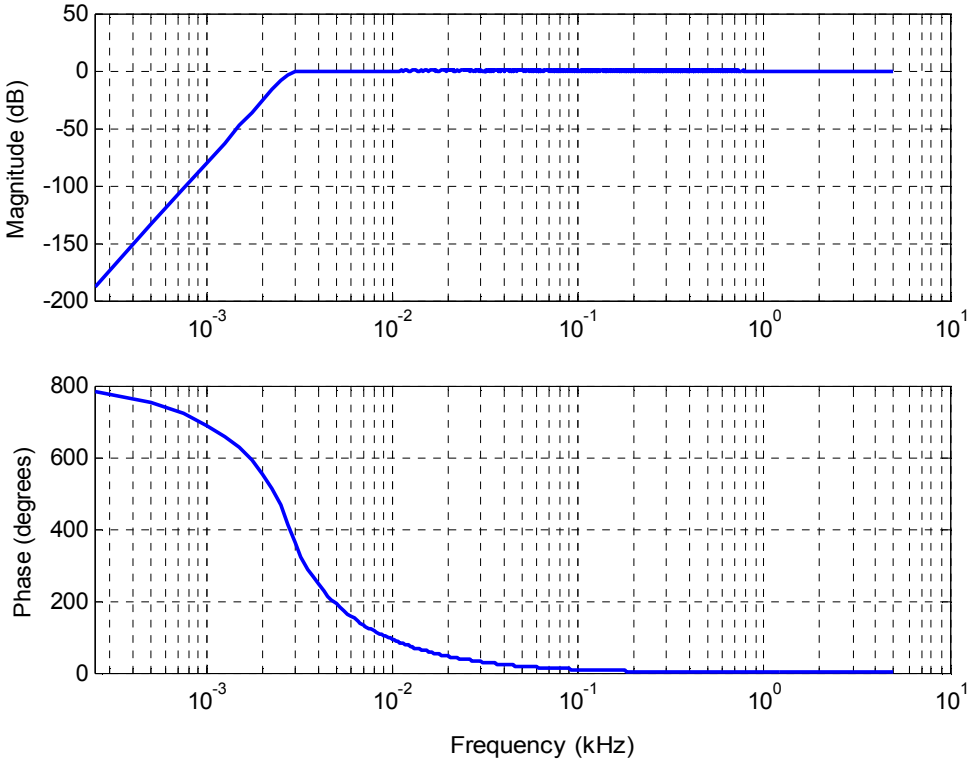

Figure 7.7 Magnitude and phase responses of the designed high-pass filter

It is known that the introduction of the filter could cause phase delay which may affect the performance of the control system. But this would be considered automatically in the characteristics of secondary path $S(z)$ in the designed controller.

7.3.2.1 LMS offline method for single frequency cancellation

The simulation model was set up to represent the system as shown in Figure 7.6. Parameters for the model are listed in Table 7.1.

Table 7.1 Parameters for simulations

Bulk modulus in valve B_v	10^9 Pa
Density ρ	870 kg/m^3
Viscosity μ	20 cSt
Switching frequency f	40 Hz
High supply pressure P_{HP}	100 bar
Low supply pressure P_{LP}	10 bar
Reservoir pressure P_t	1 bar
Effective orifice area A_o, switching valve open	1.44 cm^2
Effective orifice area A_c, switching valve closed	0.03 mm^2
Valve internal volume between switching orifices and inertance tube, V_{va}	10 cm^3
Discharge coefficient of the loading valve	0.7
Opening of the loading valve A_L	0.1 cm^2
Opening of the piezoelectric valve A_{piezo}	0.02 cm^2
Inertance tube length l	1 m
Inertance tube diameter d	7.1 mm
Bulk modulus in tube B_t	1.6×10^9 Pa
Number of unsteady friction terms	4

The switching ratio of the fast-speed valve was 0.5. The secondary path dynamics $S(z)$ were identified using the LMS offline technique as shown in Figure 7.5. For the noise attenuator, the initial values of the weights equal zero.

A leakage factor of 0.9999 was used in this work to mitigate the coefficients overflow problem resulted from limited precision of the hardware (Cioffi, 1987). When a fixed-point adaptive notch filter was implemented for computation of filter coefficients, quantization errors occurred due to the limited range and precision of the fixed-point data type (LabVIEW, 2008). Over time, these quantization errors might accumulate until an overflow in the filter coefficients occurred. The leaky LMS algorithm provides a compromise between minimizing the mean-square error and containing the energy in

the impulse response of the adaptive notch filter (Widrow and Stearns, 1985) . It results in increasing computation cost and degradation in performance.

The convergence factor of the noise canceller was $\mu_c = 3\times10^{-22}$. Simulated results of FBN cancellation using LMS offline identification method for a single frequency are shown in Figure 7.8, for a switching frequency $f = 40\,\text{Hz}$. A Hamming window was used to minimize the maximum side lobe in spectral analysis. It can be seen that the pressure pulsation was decreased by 44dB at the frequency of 40Hz. The amplitude of background noise increased to -40dB after cancellation. This might be the result of the adaptive control signal itself which introduces reference signals to the system resulting in the power of the background noise increasing.

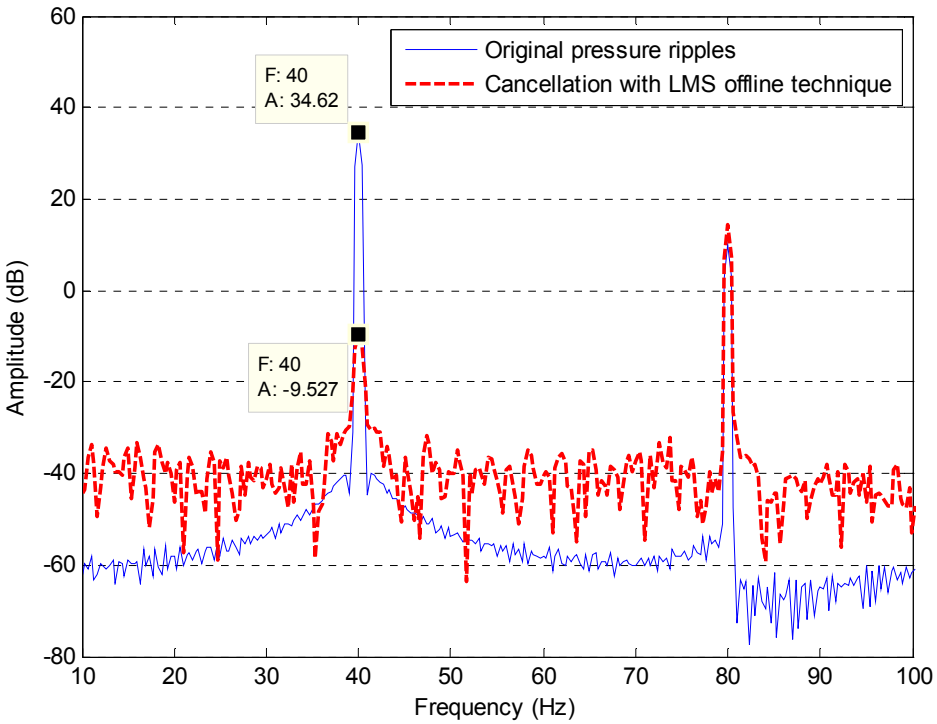

Figure 7.8 Single frequency cancellation using LMS offline technique

7.3.2.2 FBLMS online method for single frequency cancellation

Next the FBLMS online technique was applied in combination with the noise canceller with FXLMS algorithm. To achieve accurate identification results, a period of 10s without switching was introduced, which means the high-speed valve was driven by a constant voltage and the port was connected to a fixed pressure supply in the initial

conditions. After 10s, the high-speed valve switched cyclically and alternately to the HP port and LP port, and large pressure pulsations were generated in the system. The frequency responses of the secondary path at 5s and 20s are shown in Figure 7.9. The phases agree well and amplitude differences occur at different times due to the incomplete filter convergence. The amplitude difference can be compensated by increasing the convergence factor of the cancellation filter. It is also said the amplitude could obtain to its theoretical value within a longer simulation time. By contrast, the good agreement of phase is significant and is a requirement for the FBLMS algorithm and system stability.

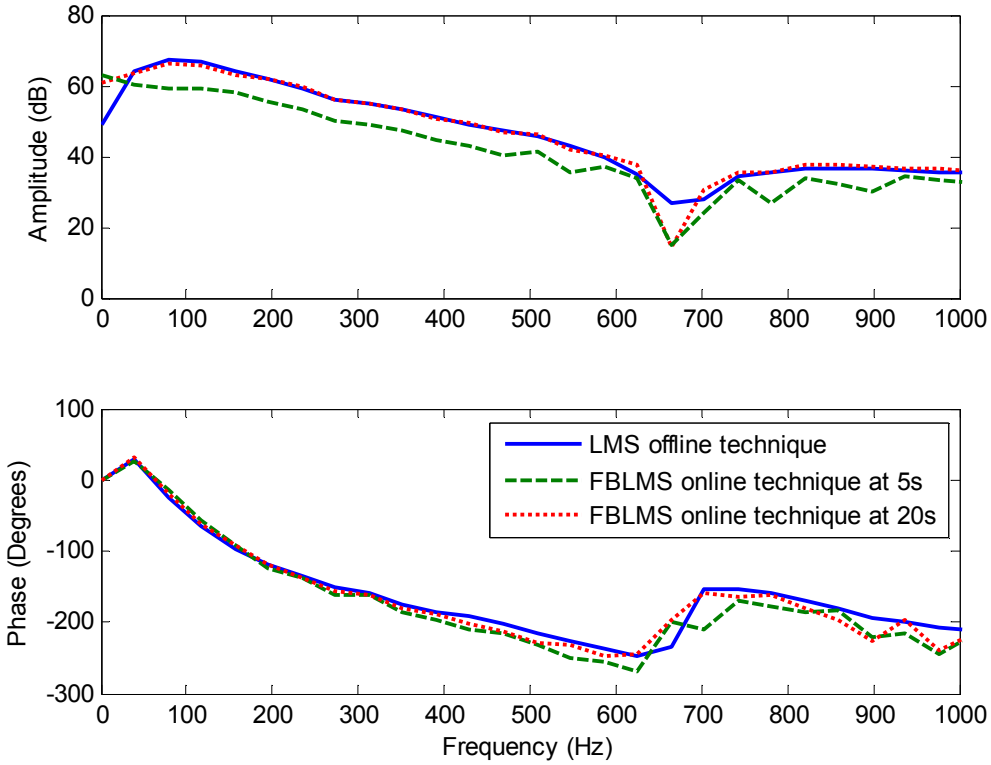

Figure 7.9 Amplitude and phase characteristics of secondary path $S(z)$ of flow booster system

The cancellation is plotted in Figure 7.10, where the amplitude of pressure pulsation dropped from 33 dB to -6.2 dB at the fundamental frequency. It can be seen that the background noise of original pressure ripples rise to -40 dB compared to Figure 7.9 where the power was around -60dB. This is because of the introduction of the white noise for online secondary path identification. This could be acceptable since the background noise still remained at a low power level compared with the peak amplitude

of the harmonics. The magnitude of 80Hz component increased about 5dB, which may be caused by the system non-linear characteristics.

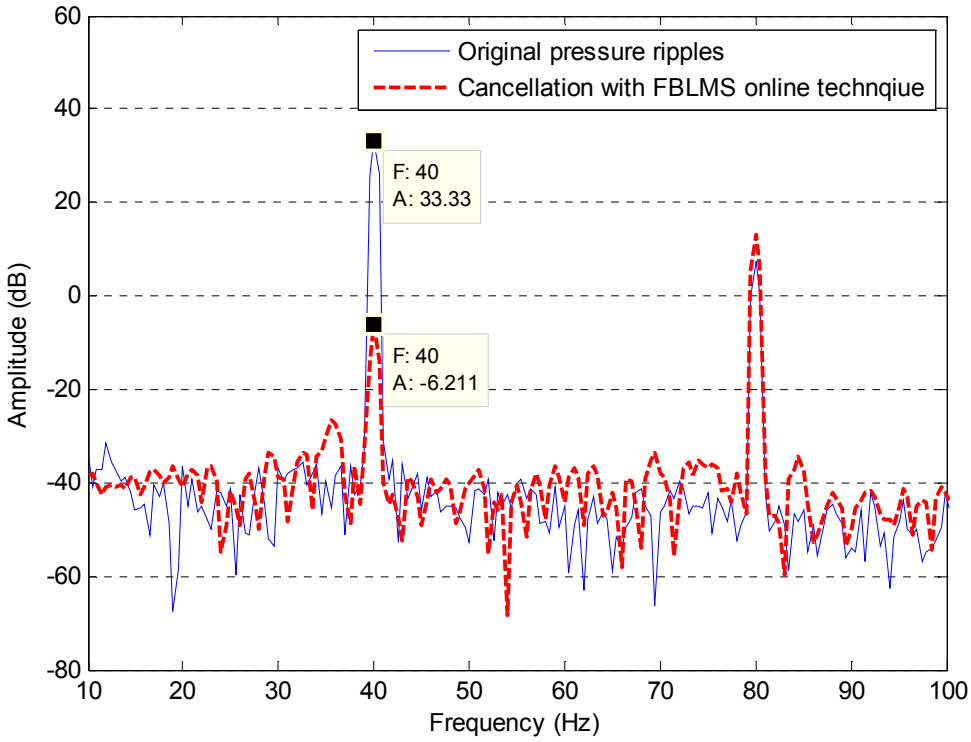

Figure 7.10 Single frequency cancellation using FBLMS online technique

7.3.2.3 LMS offline method for multiple harmonics cancellation

As discussed in the previous section, a single-frequency component can be cancelled by a simple two-weight adaptive filter. For the case in which the pressure pulsation contains multiple harmonics, two-weight adaptive filters can be connected in parallel to attenuate these narrowband components. Different convergence factors were applied in the paralleled adaptive notch filters of different frequencies, as listed in Table 7.2. Now the cancelled frequencies were multiples of the fundamental frequency of 40Hz and five harmonics were considered.

Table 7.2 Convergence rates used for different harmonics by using LMS offline time-domain technique

Frequency (Hz)	40	80	120	160	200
Convergence rate μ_c	3×10^{-22}	8×10^{-24}	8×10^{-24}	1×10^{-22}	7×10^{-22}

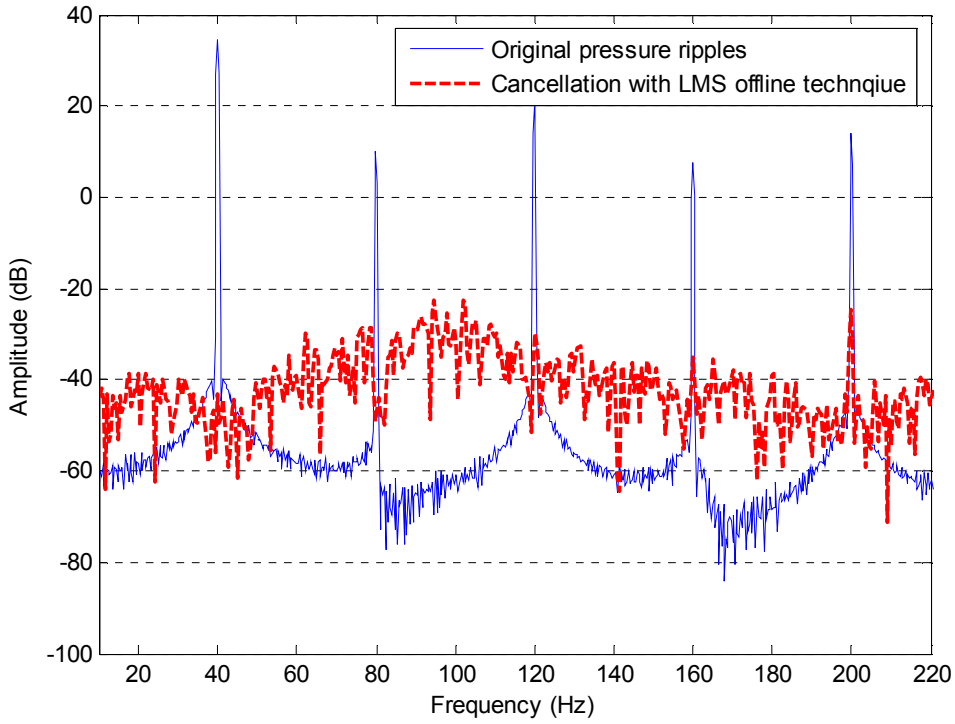

Figure 7.11 Multiple harmonics cancellation of pressure pulsation using LMS offline time-domain technique

Figure 7.11 shows the multiple harmonics cancellation of pressure pulsation using the LMS offline technique. The amplitudes of the original pressure pulsation and the pressure pulsation after cancellation at different frequencies are listed in Table 7.3. The maximum cancellation of 77.6 dB was achieved at the fundamental frequency of 40Hz. Compared to the result in Figure 7.8, the cancellation has been increased by 33.4 dB with the same convergence rate used for 40Hz in single frequency cancellation. This might be caused by the effects from the error signal measured from the downstream pressure transducer (Yang et al., 2009). For the single frequency cancellation, the error signal contained the higher harmonics to which could restrict the performance of cancellation due to less efficient updating of filter coefficients. It can be found that the attenuations at the frequencies of 80 Hz, 120Hz, 160Hz and 200Hz were effective and the average cancellation was roughly 50dB.

Table 7.3 Results of cancellation at different frequencies using LMS offline time-domain technique

Frequency (Hz)	40	80	120	160	200
Original pressure pulsation (dB)	34.6	10.2	21.9	7.5	14.2
After cancellation (dB)	-43.0	-48.9	-30.0	-35.0	-24.4
Total cancellation (dB)	77.6	59.1	51.9	42.5	38.6

Figure 7.12 shows the filter tap weights of different sub-controllers. The filter coefficients are plotted at 0.025s time interval in 10s. It can be noted that after 2s the filters converged and the tap weights reached their optimal values which are listed in Table 7.4.

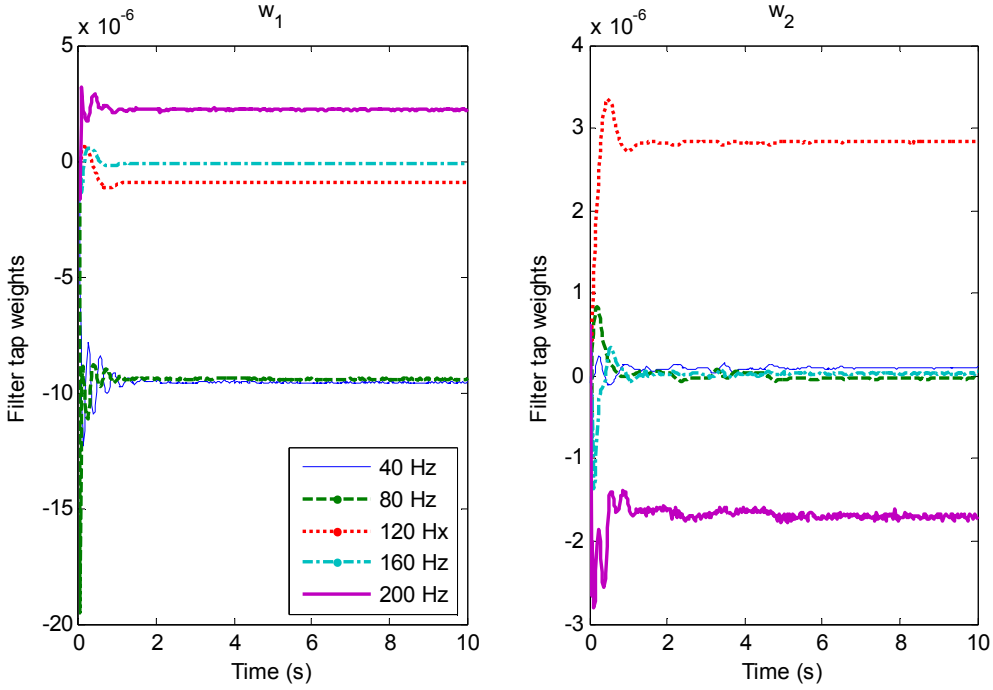

Figure 7.12 Filter tap weights of different sub-controller using LMS offline technique

Compared with the results in Figure 3.26, the weights plotted in Figure 7.12 had some oscillations even with the controller maintained at the steady state. Although a high-pass filter was designed to eliminate these effects beforehand (mathematical deduction can be found in Appendix 1), there still were interferences from the uncancelled high frequencies which could introduce unexpected oscillations into the system. Some of the

mean values were taken to represent the estimated optimal weights of the sub-controllers, as shown in Table 7.4.

Table 7.4 optimal value of weights for different harmonics using LMS offline time-domain technique

Frequency (Hz)	40	80	120	160	200
Optimal value of w_1	-9.57×10^{-6}	-9.42×10^{-6}	-9.15×10^{-7}	-1.13×10^{-7}	2.21×10^{-6}
Optimal value of w_2	9.66×10^{-8}	-2.65×10^{-8}	2.82×10^{-6}	2.35×10^{-8}	-1.71×10^{-6}

7.3.2.4 FBLMS online method for multiple harmonics cancellation

Using the FBLMS online identification method, the convergence rates listed in Table 7.2 were re-applied to the noise attenuator with an online identification filter. The FBN attenuation using the FBLMS online technique is shown in Figure 7.13 where the cancellations were achieved at 5 harmonics. The attenuations at 80Hz and 120Hz were less than 20dB which were only half of the cancellation of the LMS offline technique. The reason could be the inaccuracy of the secondary path identification. The frequency responses of secondary path in the range of 0Hz to 300Hz are shown in Figure 7.14 where the amplitude differences can be noticed clearly from the frequency of 40Hz to 160Hz. As said before, these differences could be compensated by introducing suitable gain values for different frequencies with appropriate control algorithms. For simplicity, these also could be realized by increasing the weights of sub-controllers which are used for cancellation of specific harmonics. However, it may bring out the instability of the notch filter for exceeding its stable convergence limits at a specific frequency (Kuo and Morgan, 1995).

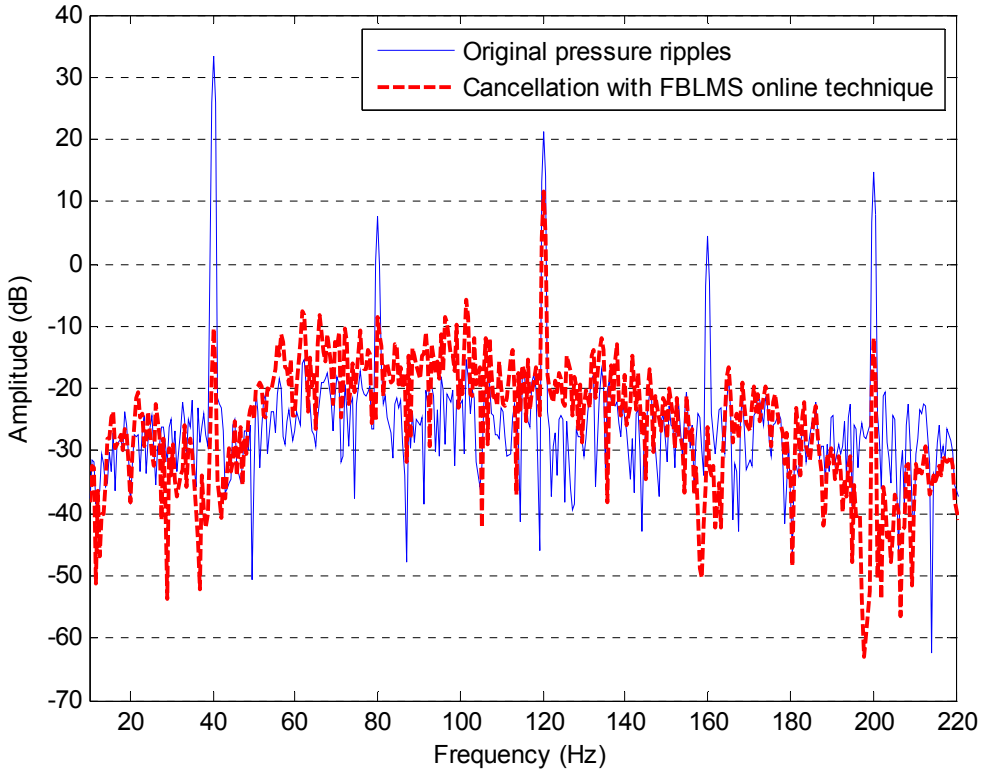

Figure 7.13 Multiple harmonics cancellation of pressure ripple using FBLMS online technique

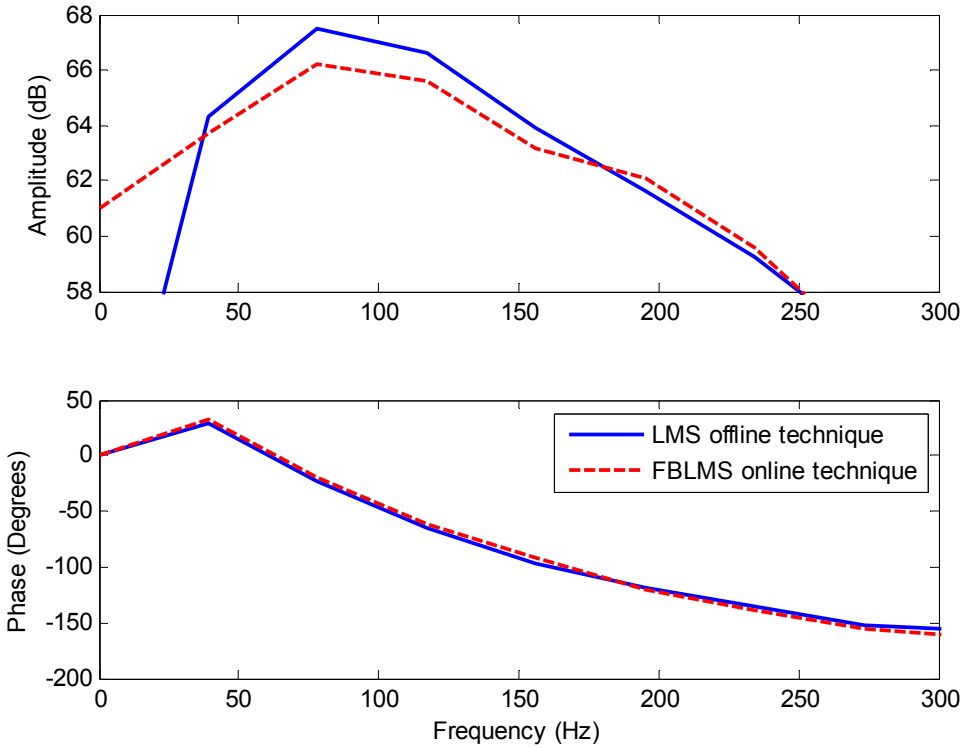

Figure 7.14 Comparison of amplitudes and phases achieved using LMS offline and FBLMS online technique

The modified convergence rates of the controller are shown in Table 7.5 and the cancellation is plotted in Figure 7.15.

Table 7.5 Convergence rates used for different harmonics by using FBLMS online frequency-domain technique

Frequency (Hz)	40	80	120	160	200
Convergence rate μ_c	3×10^{-22}	9×10^{-24}	1.5×10^{-22}	1×10^{-22}	7×10^{-22}

As can be seen, the amplitudes after cancellation at the frequencies 80Hz and 120Hz were reduced by -10dB within the larger convergence rates. A compromise should be made between the cancellation and system stability since the online identification method would introduce a risk of instability due to the use of auxiliary signal and the varying characteristics of secondary path. Table 7.6 shows the amplitudes of the original pressure and the total cancellation.

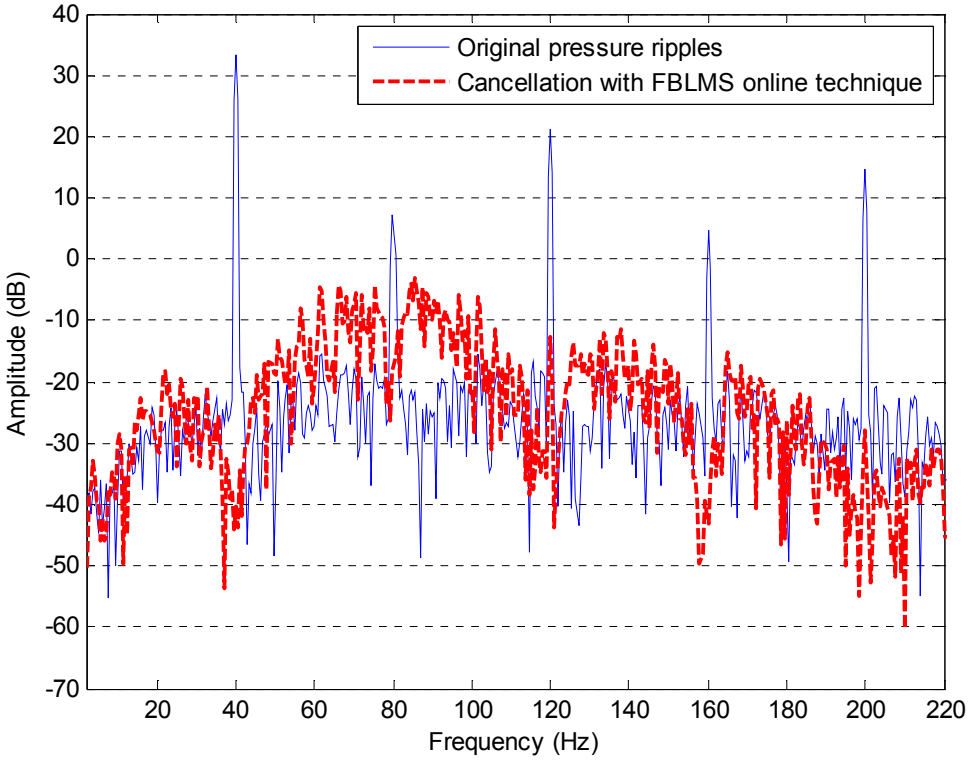

Figure 7.15 Multiple harmonics cancellation of pressure ripple using FBLMS online technique with the modified convergence rates

Table 7.6 Results of cancellation at different frequencies using FBLMS online frequency-domain technique

Frequency (Hz)	40	80	120	160	200
Original pressure pulsation (dB)	33.3	7.3	21.2	4.8	14.7
After cancellation (dB)	-40.2	-18.1	-12.6	-43.1	-27.9
Total reduction (dB)	73.5	25.4	33.8	47.9	42.6

In conclusion, the LMS offline and FBLMS online techniques are effective for secondary path identification of the flow booster. The FXLMS algorithm was applied for the single and multiple harmonics cancellation in combination with the offline and online identification methods respectively. Good cancellation was achieved with these two approaches. It can be concluded that the designed controller is suitable and effective for pressure pulsation cancellation of the flow booster.

7.3.2.5 FBLMS online method for multiple harmonics cancellation with a transient switching frequency

The switching frequency f may vary according to different working conditions and application requirements. It can be noticed that the frequencies of the flow booster that need to be cancelled would change with the switching frequency of the high speed valve.

Figure 7.16 shows spectrograms of the pressure pulsation cancellation during a frequency transient. The original pressure ripple is plotted in Figure 7.16 (a) and the residual pressure pulsation after cancellation is shown in Figure 7.16 (b). The switching frequency of the valve was varied from 80 Hz to 20 Hz over 20s with steps of 20 Hz. A step signal is employed to model the sudden frequency changing. The sub-controllers for different frequencies were all fully adapted before the frequency was changed. As can be noted, the noise canceller with five sub-controllers arranged in parallel is able to adapt to the changing conditions quickly and obtain good cancellation at the target frequencies.

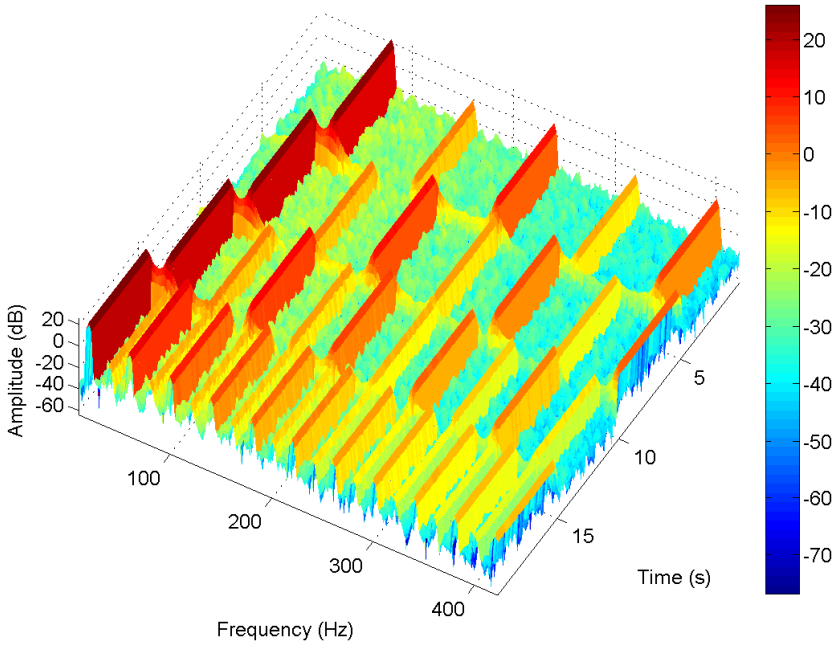

[a] Original pressure pulsation

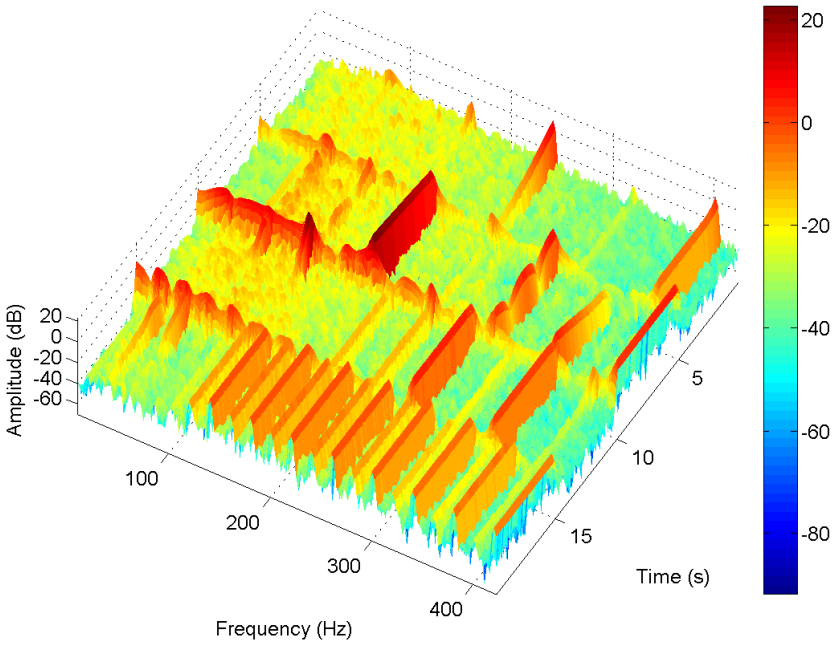

[b] After cancellation using the designed noise canceller with fixed convergence factors

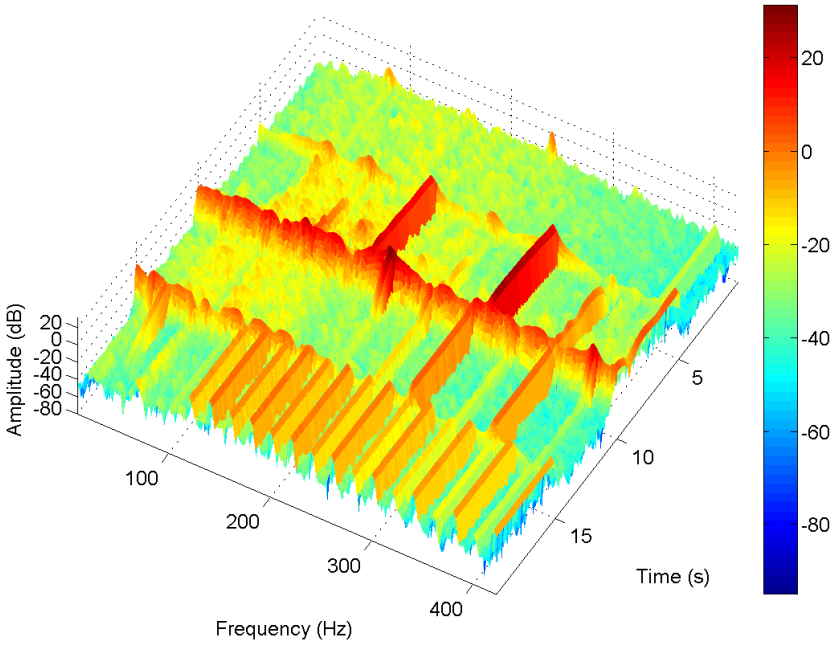

[c] After cancellation using the designed noise canceller with modified convergence factors

Figure 7.16 Spectrograms showing transient cancellation of 5 harmonics with step changes in the fundamental frequency from 80Hz to 20Hz over 20s

The controller needs to re-adapt with the varying switching frequency. The cancellation is not achieved directly because the frequency of the reference signals for the attenuator would change synchronously based on the switching frequency. A re-adaption process is needed for attenuation. This can be seen as a disadvantage of the narrowband noise cancellation structure as the re-adaption process may result in less effectiveness of the controller or even system instability.

From Figure 7.16 (b), the pressure harmonics after cancellation at the frequencies of 180Hz and 240Hz from 5s to 10s are still apparent. This is because fixed convergence rates were applied for different harmonics with the varying switching frequency. This is a compromise between the cancellation and controller stability. Table 7.7 (a) shows the values applied for the convergence factors of sub-filters. Theoretically the more obvious attenuation could be achieved using more appropriate convergence factors for different harmonics. As can be seen from Figure 7.16 (c), the pressure amplitudes after cancellation at some frequencies were lower than the results using uniform convergence factors. The convergence factors are presented in Table 7.7 (b) where the modified values (in bold and underlined) were applied for the 3^{rd} and 5^{th} harmonics. The amplitudes after cancellation at 180Hz and 240Hz were lower than the results in Figure 7.16(b), although the amplitudes are still significant due to the consideration of system stability.

Table 7.7 (a) Convergence rates used for different harmonics with varying switching frequency

	Fundamental Frequency (Hz)	Harmonics of fundamental frequency (Hz)			
Frequency (Hz)	80	160	240	320	400
	60	120	180	240	300
	40	80	120	160	200
	20	40	60	80	100
Convergence rate μ	1×10^{-22}	5×10^{-23}	1×10^{-23}	2×10^{-22}	3×10^{-23}

Table 7.7 (b) Modified convergence rates used for different harmonics with varying switching frequency

	Fundamental Frequency (Hz)	Harmonics of fundamental frequency (Hz)			
Frequency (Hz)	80	160	240	320	400
Convergence rate μ	1×10^{-22}	5×10^{-23}	**6×10^{-23}**	2×10^{-22}	**5×10^{-21}**
Frequency (Hz)	60	120	180	240	300
Convergence rate μ	1×10^{-22}	5×10^{-23}	**1.5×10^{-23}**	2×10^{-22}	**6×10^{-23}**
Frequency (Hz)	40	80	120	160	200
Convergence rate μ	1×10^{-22}	5×10^{-23}	**3×10^{-23}**	2×10^{-22}	**3×10^{-23}**
Frequency (Hz)	20	40	60	80	100
Convergence rate μ	1×10^{-22}	5×10^{-23}	**2×10^{-22}**	2×10^{-22}	**4×10^{-22}**

The tap weights of the sub-controllers for fundamental frequency and the 3rd harmonics cancellation are plotted in Figure 7.17 where two weights w_1 and w_2 of the filter adapted with the changing conditions and obtained their optimal values quickly with a short period re-adaption. The weights for the fundamental frequency are presented as $w_1(f)$ and $w_2(f)$ and for the 3rd harmonic are described as $w_1(3f)$ and $w_2(3f)$ in Figure 7.17. It can be seen that the designed controller has excellent ability for pressure pulsation cancellation and good robustness for adapting with the varying conditions.

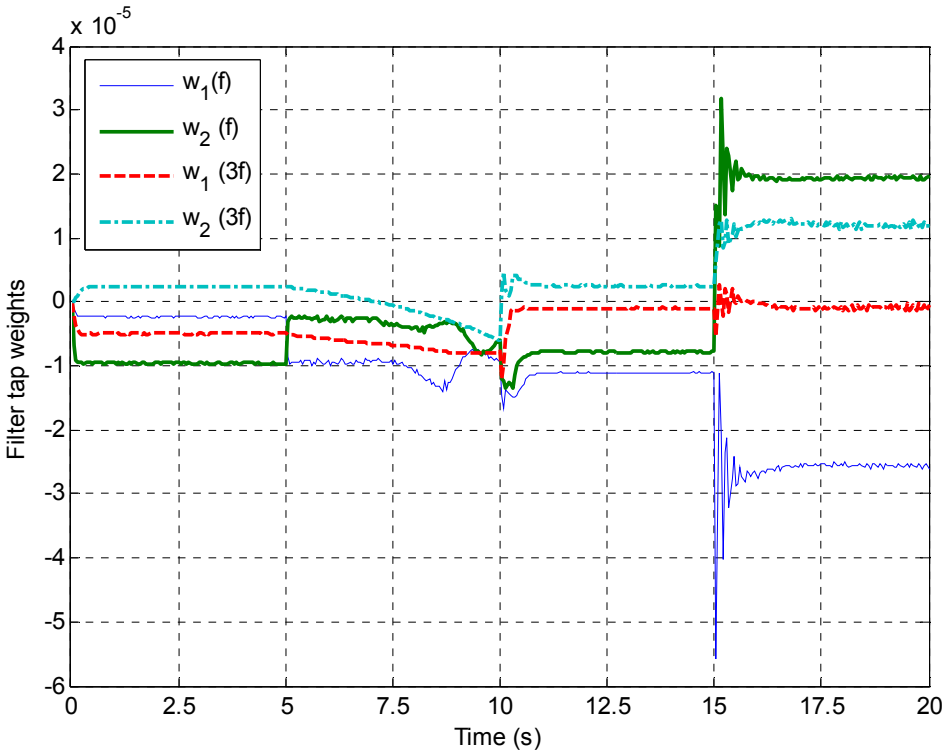

Figure 7.17 Filter tap weights of the sub-controller for fundamental frequency and 3rd harmonic with varying switching frequency

7.3.2.6 FBLMS online method for multiple harmonics cancellation with a transient switching ratio

The switching ratio x is used to adjust the delivery flow and pressure of flow booster in terms of system load in practice. However, the changing of ratio may affect the controller performance due to the varying of pressure and flowrate of system. The characteristics of the disturbance could also be changed with varying switching ratio.

Firstly the investigation of secondary path dynamics with different ratios was discussed with a fixed loading condition. Theoretically the relationship between delivery pressure and supply pressure of flow booster for ideal operation is described by Equation (6.2)

$$P_{DF} = xP_{HP} + (1-x)P_{LP}$$

where x is the switching ratio of the flow booster.

From this equation, the delivery pressure would be varied with the ratio x. Figure 7.18 shows the simulated delivery pressure with different switching ratio. Large pressure

pulsations occurred because the valve switched between the high supply pressure of 100 bar and the low supply pressure of 10 bar.

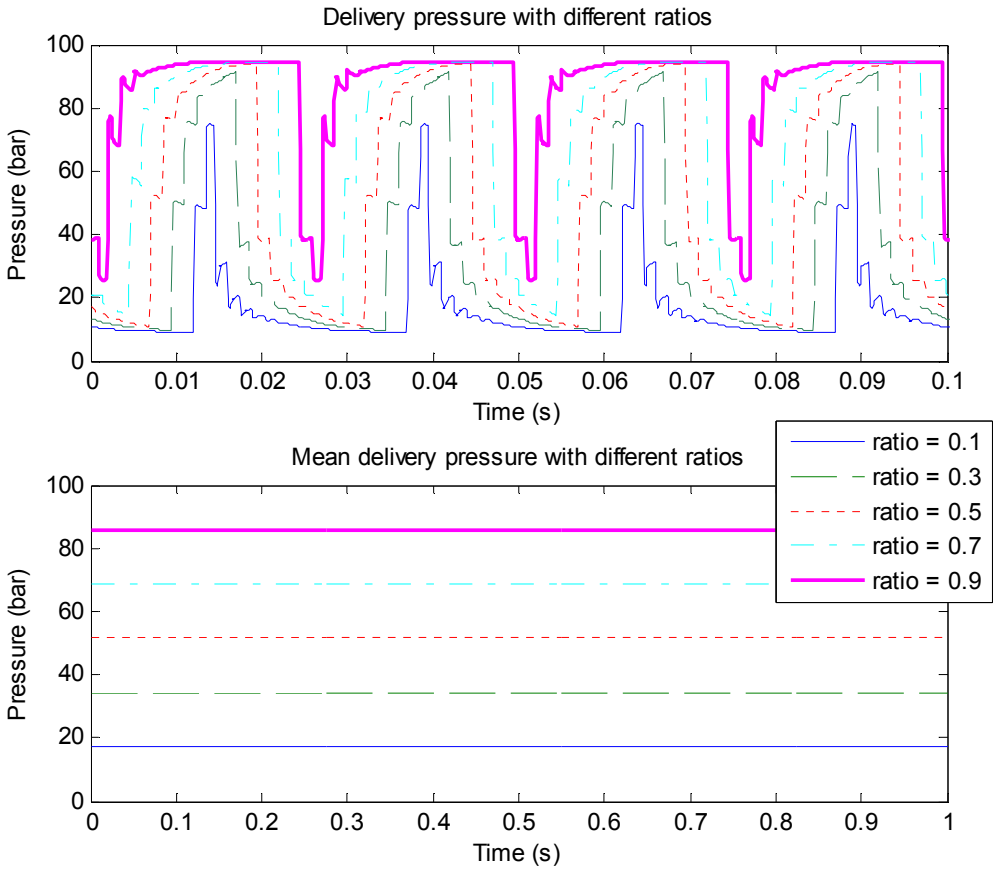

Figure 7.18 Delivery pressure at downstream line of flow booster with different switching ratios

It is expected in this case that the amplitude of secondary path went up with the increasing mean pressure of system and some phases changed due to the varying system dynamics, which resulted from the varying end impedance. The frequency responses of secondary path with different switching ratios are plotted in Figure 7.19 where the results are as expected, although phase and amplitude differences occurred at the range of frequency from 600Hz to 800Hz.

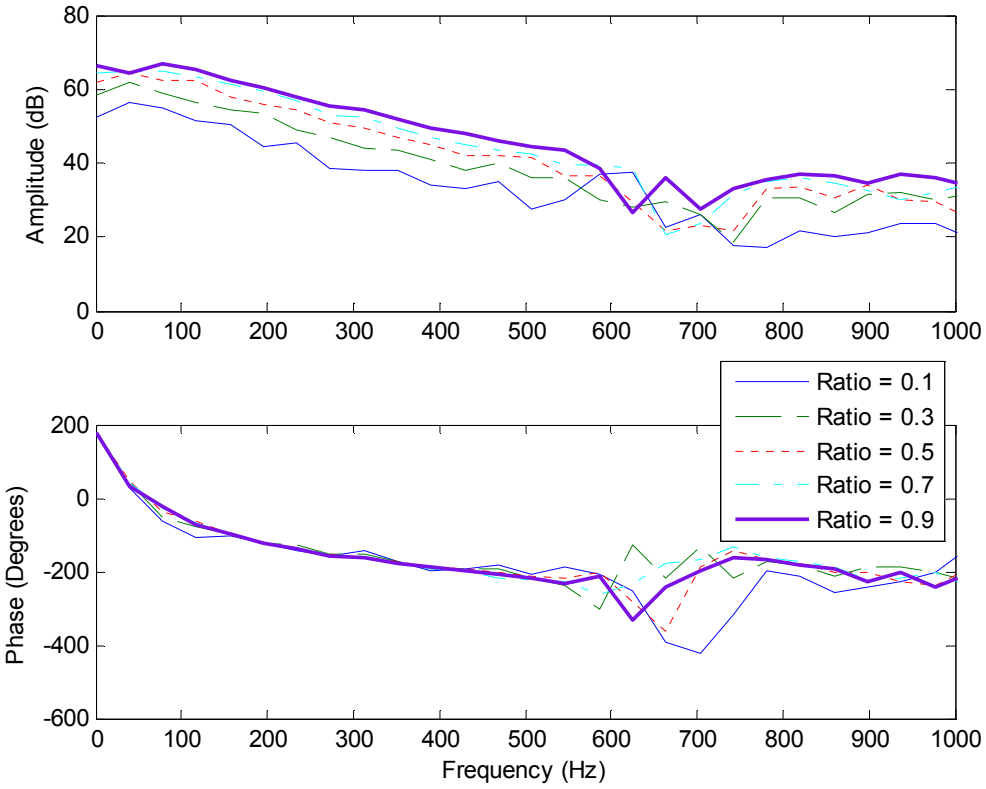

Figure 7.19 Amplitude and phase characteristics of secondary path with different switching ratios

Again the switching frequency of flow booster was fixed to 40Hz. The amplitude of pressure ripple at the frequency of 40Hz is plotted in Figure 7.20 (above) where the switching ratio x was changed from 0.1 to 0.9 in steps of 0.2 as shown in Figure 7.20 (bottom). The ratio increased by 0.2 in every 4s and the simulation time was 20s. The opening of the loading valve was modelled as $0.1cm^2$. The designed controller was applied for system noise cancellation in different ratios. The result is shown in Figure 7.20 (middle) where the fast adaptive speed and good cancellation were achieved by using FXLMS algorithm with FBLMS online identification method.

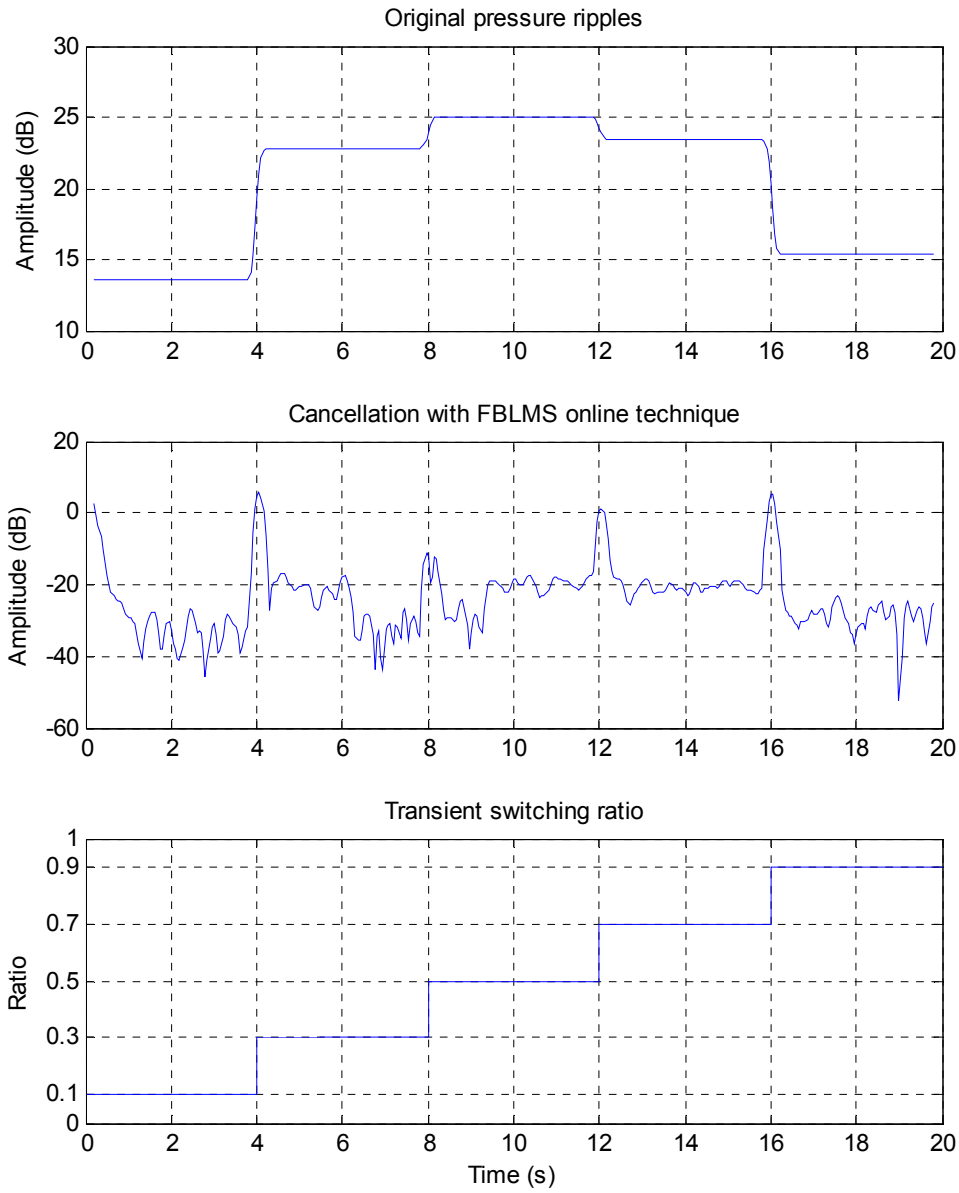

Figure 7.20 Pressure pulsation cancellation at the fundamental frequency with varying switching ratio of flow booster

The tap weights of different sub-controllers for fundamental frequency and the 3rd harmonics attenuation are plotted in Figure 7.21 for a good demonstration of the adaptive process.

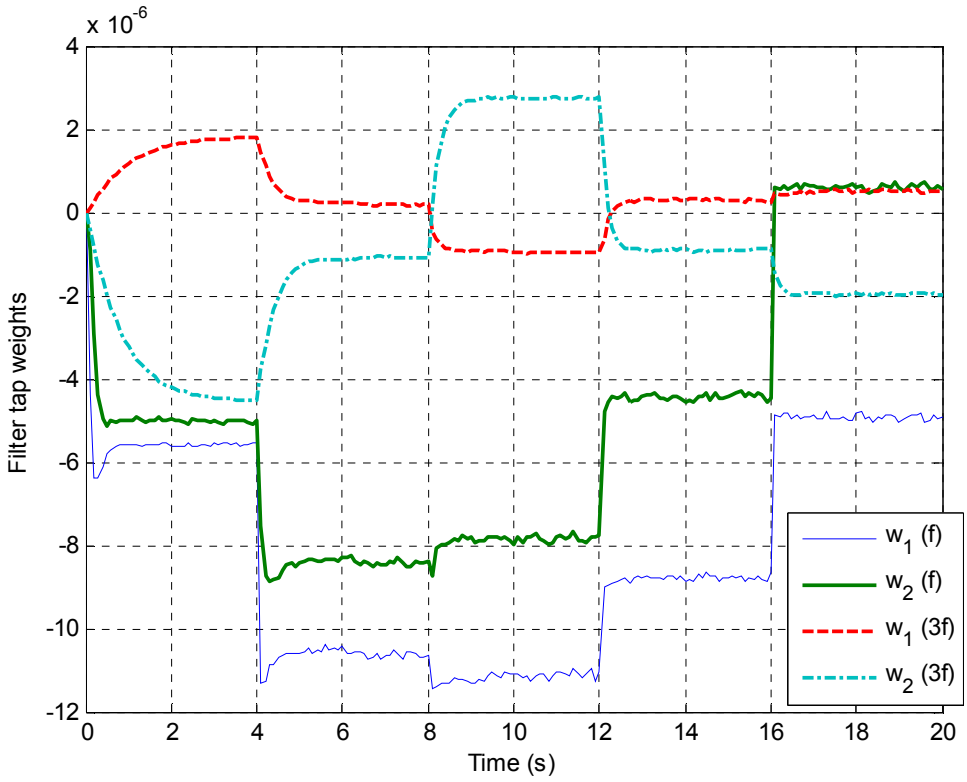

Figure 7.21 Filter tap weights of the sub-controller for fundamental frequency and the 3rd harmonic cancellation with varying switching ratio

Compared with the results in Figure 7.17, the weights changed faster in this case. This is because the fundamental frequency of the pressure pulsation stayed the same. That could speed up the adaptive process and reduce the potential instability of system. It can be concluded that the designed noise canceller based on flow booster is effective to attenuate the pressure pulsation which is caused by pulse nature of the flow and is able to perform robustly when the high-speed switching valve is subjected to the changing switching ratio. Also, the system is more robust and reliable for varying switching ratio compared with the changing switching frequency.

7.3.2.7 FBLMS online method for multiple harmonics cancellation with varying load

Different system loading could affect the performance of noise controller. However, it is a normal condition for a flow booster working under different loading requirements in real time. So it is significant to validate the performance and robustness of the controller when it is worked with varying loading.

A simple loading system was modelled by using a standard orifice equation with changing opening. The opening was ramped from 0.01cm^2 at 0s to 0.1 cm^2 at 20s. Figure 7.22 shows the amplitude of pressure pulsation before and after cancellation at the frequency of 40Hz. As can be seen, the residual pressure after cancellation maintained at the roughly constant level -20dB (Figure 7.22 (middle)) with the changing load.

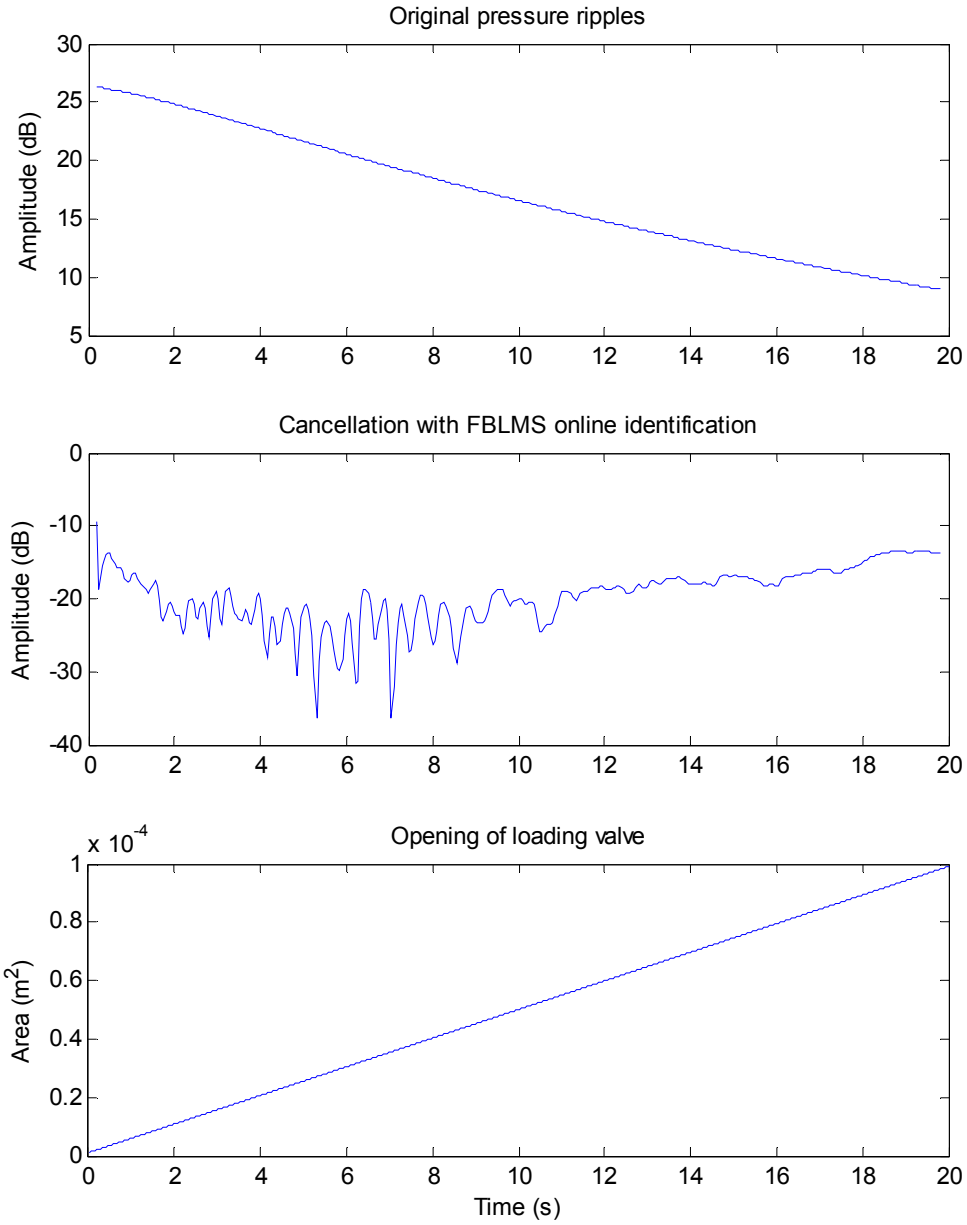

Figure 7.22 Pressure pulsation cancellation at the frequency of 40Hz with varying system load

The filter tap weights for fundamental frequency cancellation are shown in Figure 7.23 where the weights changed with the varying loading.

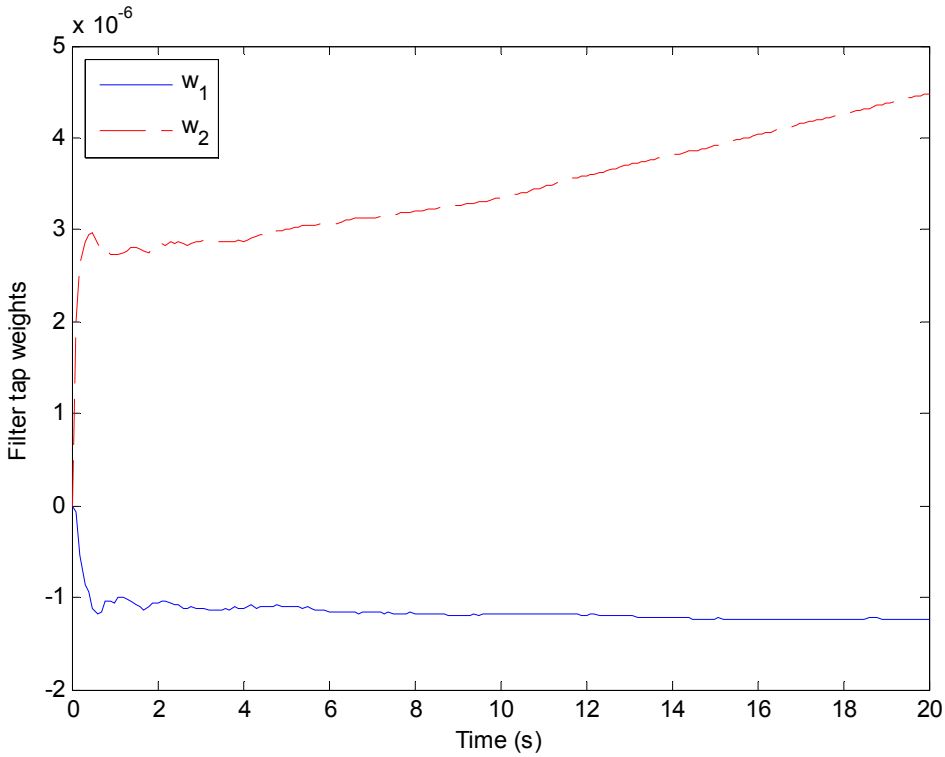

Figure 7.23 Filter tap weights of the sub-controller for fundamental frequency cancellation with changing load

In conclusion, the designed controller was implemented for single and multiple harmonics attenuation of pressure pulsation based on a flow booster. Excellent cancellation (around 40dB) was achieved within the proposed by-pass control structure. Effects from changing switching frequency, switching ratio and system loading were researched based on simulation. According to the results, it can be concluded that the designed controller is effective for pressure pulsation cancellation and is robust under varying system conditions. This noise canceller was applied and validated in the experimental studies described in Chapter 8.

7.4 Implementation for pressure pulsations cancellation with an in-series arranged controller

The same designed controller was implemented on the in-series structure as described in Section 7.3. The noise attenuator was arranged in-line between the main flow booster

part and the load system. The effectiveness and robustness of the controller were investigated in this section and the advantages and disadvantages of these two structures were compared on the basis of performance of cancellation and system stability.

7.4.1 Secondary path identification

The dynamics of the secondary path varied due to the change of arrangement of the noise canceller. The opening of the piezoelectric valve and loading valve directly affected the boundary conditions of the system.

Consideration should be made for the appropriate opening range of both piezoelectric and loading valves. When the opening of the loading valve is large, it can be seen as an open end and the impulse response of the secondary path is highly related to the opening of piezoelectric valve; when the opening of piezoelectric valve is large, it may perform less effectively because of small damping effect. The same parameters used in the by-pass structure were re-applied using this structure. The impulse response of the secondary path identified by LMS offline technique is shown in Figure 7.24. The dynamics of the piezoelectric valve were represented using the same transfer function as described in Equation 7.1. The switching ratio equals to 1 in order to provide a fixed supply pressure of 100 bar. The impulse response essentially converged after 0.015s with the filter length of 256, but more accurate results could be achieved by using longer filter length in order to obtain more complete characteristics of secondary path. The standard deviation of white noise was $1\times10^{-6}\text{m}^2$ and the convergence factor of identification filter was $\mu = 1\times10^{4}$. As can be seen, the power of white noise was smaller than that was used in by-pass structure, which resulted in the larger convergence factor in order to achieve the similar convergence speed of identification. The sample frequency was 10 kHz and the simulation time was 30s.

For LMS online technique, where the pressure pulsation was introduced in the system by switching the fast-speed valve, the impulse response is plotted in Figure 7.24. The switching ratio x_f was fixed at 0.5 and switching frequency was 40Hz. As before, the curve from the LMS offline technique is shown as an ideal result for comparison. It can be clearly noted that the filter did not converge and a large amplitude difference occurred between the results achieved using the LMS online and offline techniques.

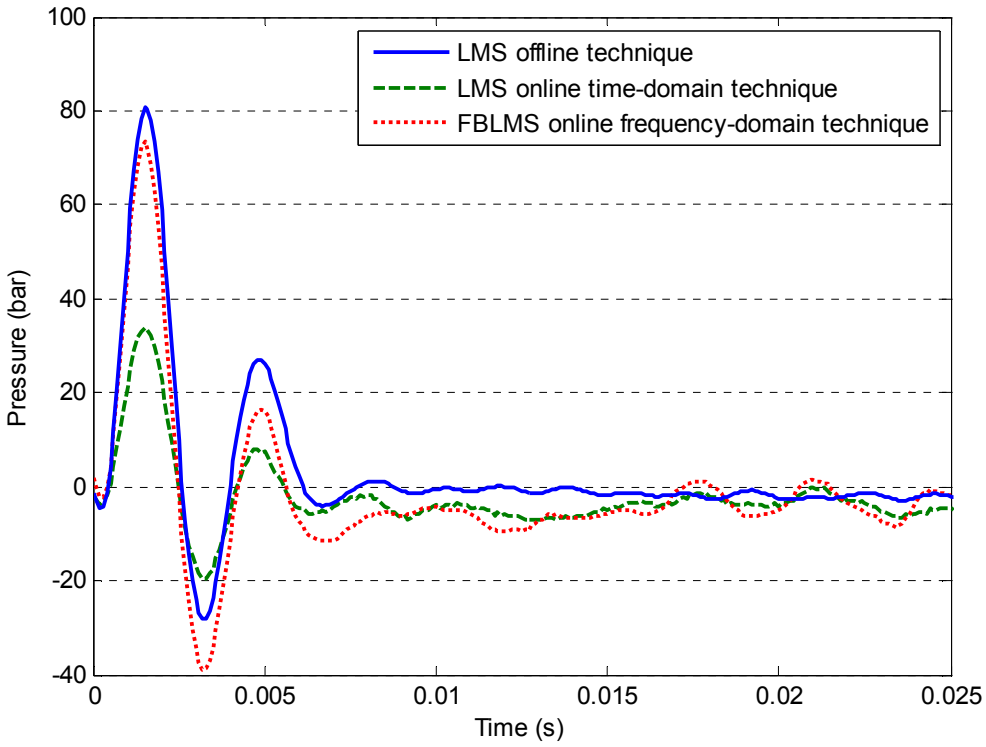

Figure 7.24 Amplitude and phase of secondary path $S(z)$ of flow booster with an in-series arranged controller

The result achieved by using the FBLMS algorithm was also plotted in Figure 7.24. It can be seen that the impulse responses match well on the comparison of the theoretical result although small amplitude differences occurred. This is expected due to the effects from the white noise and the selection of the identification convergence rate μ_c. Larger convergence rate μ_c and longer simulation time could be helpful to obtain more accurate results. However, it can prove that the FBLMS online identification technique is able to obtain accurate dynamics of the secondary path when pressure pulsation occurred in the system. Figure 7.25 shows the amplitude and phase characteristics of the secondary path $S(z)$ using these three techniques.

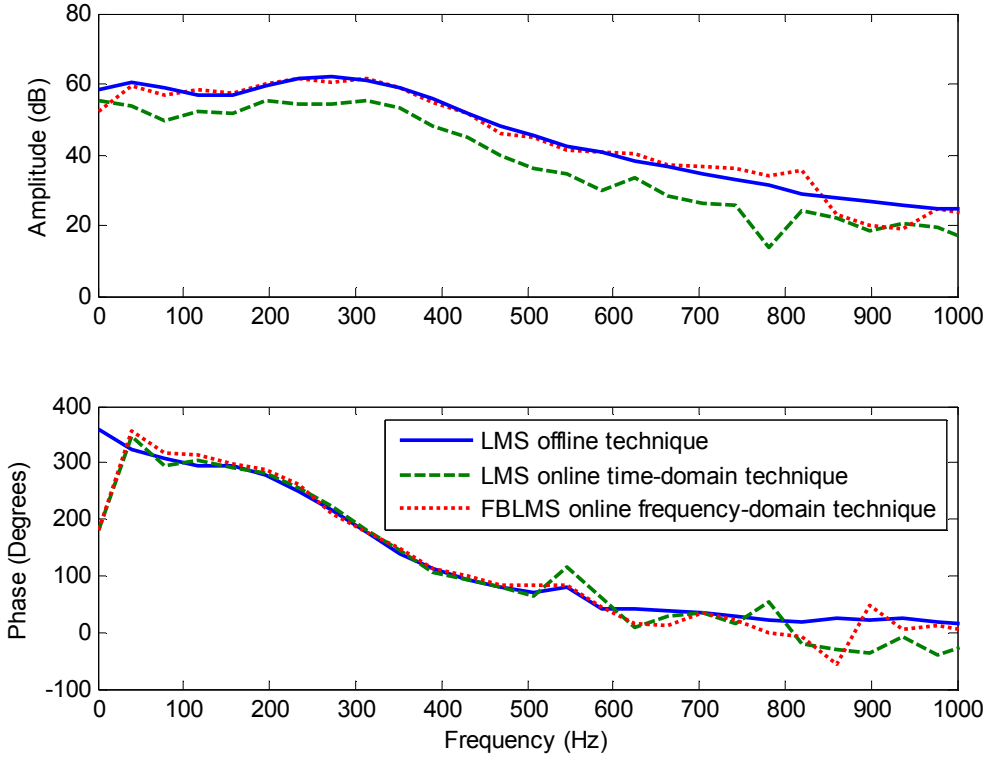

Figure 7.25 Amplitude and phase characteristics of secondary path using LMS offline, LMS online and FBLMS online techniques

In conclusion, the LMS offline and FBLMS online techniques both are effective for $S(z)$ identification of flow booster with an in-series arranged noise canceller. The LMS offline identification process can only be operated without pressure pulsations and it obtains the accurate dynamics of the secondary path. When pressure pulsations occurred in the flow booster, the FBLMS online technique is effective to operate and achieve reasonable secondary path dynamics, although the convergence speed of adaptive filter might decrease by the presence of pressure pulsations. However, this structure might have a limitation of flowrate requirement. When the opening of the piezoelectric valve was small, only low flowrate passed through the valve and it may result in the noise attenuator losing effectiveness. Details of pressure pulsation cancellation are discussed in the following section.

7.4.2 Active pressure pulsation cancellation

Figure 7.26 shows the schematic of pressure pulsation cancellation based on a flow booster system with an in-series arranged controller. The piezoelectric valve was arranged in line with the fast-speed valve, tube and loading valve. Two switched ports were connected to a high supply pressure and a low supply pressure alternately and cyclically, which was based on the driving signal produced by a pulsed wave generator. The control algorithm of the noise canceller was designed and the FXLMS algorithm was used to generate an adaptive control signal for the piezoelectric valve.

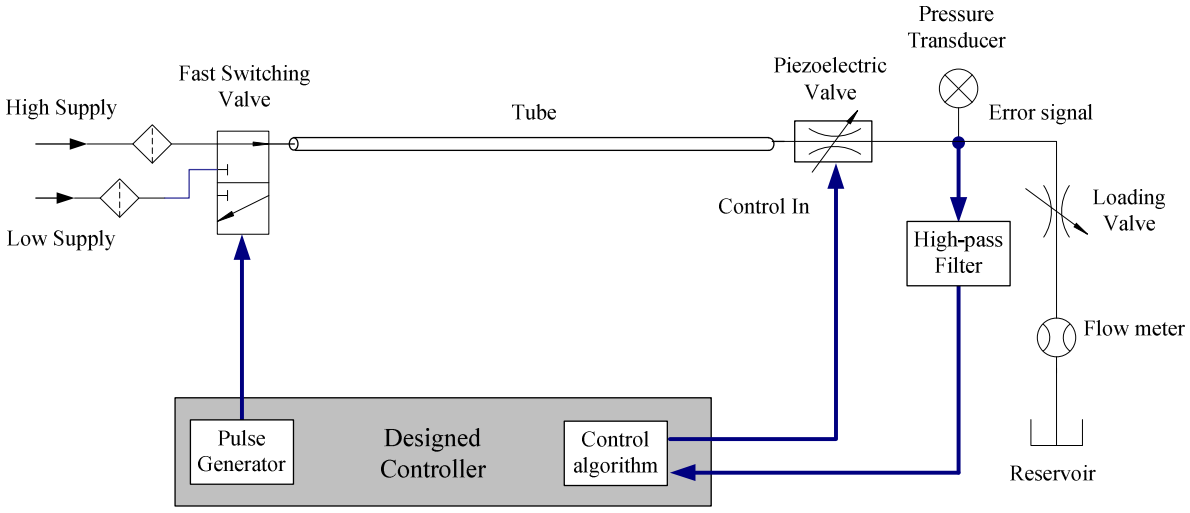

Figure 7.26 Schematic of the in-series structure based on a flow booster system with noise attenuator

As studied for the by-pass structure in section 7.3, firstly the application of single frequency cancellation was discussed to validate the system performance and effectiveness. Then the controller was expanded to general application by connecting two-weight adaptive filters in parallel to attenuate multiple harmonics. The system stability and robustness were investigated in terms of varying switching frequency and ratio, and loading requirement.

7.4.2.1 LMS offline method for single frequency cancellation

The simulation model was set up to represent the system as shown in Figure 7.27. The volume between the switching valve and the inertance tube was modelled using the pressure build-up equation, Equation (6.7) as described in Chapter 6.

$$P = \frac{B}{V}\int (Q_{VALVE} - Q_{TUBE})dt$$

The same equation was used to model the volume between the piezoelectric valve and loading valve to configure the valve models with two pressure inputs and flow outputs to avoid algebraic loops. Both volumes used in the model were 5mL. Other parameters for the model are listed in Table 7.1.

Simulated results of pressure pulsation cancellation using LMS offline identification method for a single frequency are shown in Figure 7.27, for the switching frequency $f = 40$ Hz. The switching ratio of the switching valve was 0.5. The dynamics of the secondary path S(z) were identified using the LMS time-domain technique as shown in Figure 7.25.

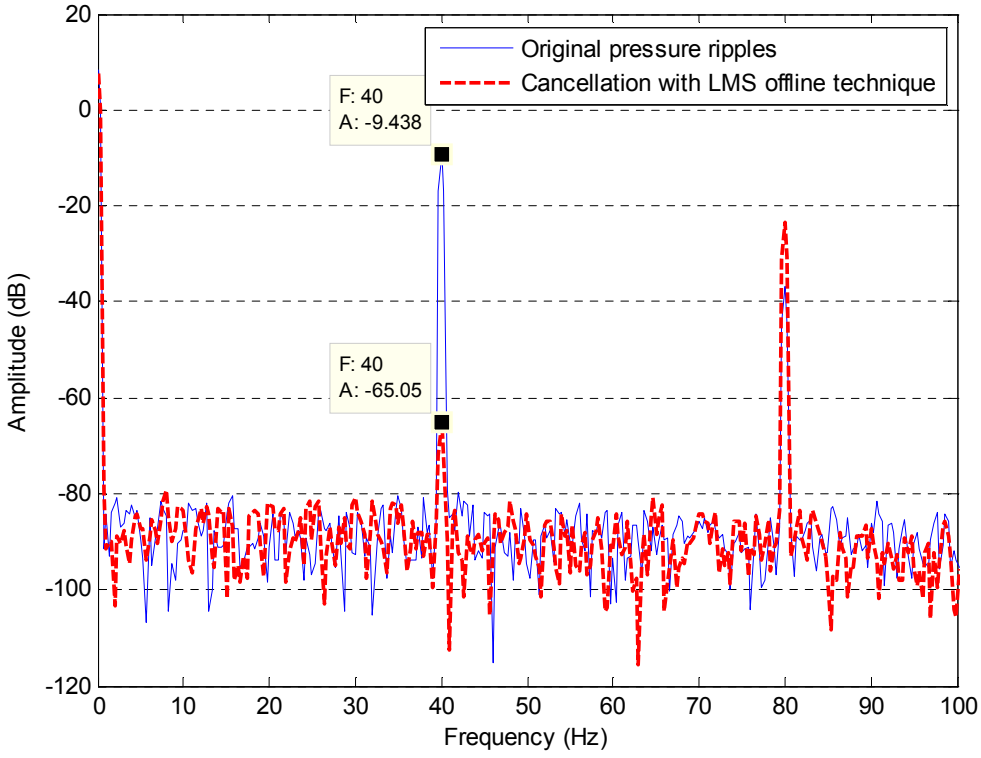

Figure 7.27 Single frequency cancellation using LMS offline technique

For the noise attenuator, the initial values of the weights equal zero. The leakage factor was chosen as 0.9999. The convergence factor of noise canceller was $\mu_c = 3\times10^{-17}$. A Hamming window was used to minimize the maximum side lobe in spectral analysis. The pressure pulsation was decreased by 55.6 dB at the frequency of 40Hz.

7.4.2.2 FBLMS online method for single frequency cancellation

The FBLMS online technique was applied in combination with the noise canceller with FXLMS algorithm. As before, the first 10s period was used for secondary path identification with a constant supply pressure. The switching valve and the noise controller were switched on at 10s. The amplitude and phase characteristics at 5s and 20s are shown in Figure 7.28. It is shown that the phases agreed well but amplitude difference occurred at different times due to the convergence process of the filter. The amplitude difference can be compensated by using larger convergence rate μ_c of the cancellation filter. However, fast convergence speed may result in system instability when the identification filter has not been completely converged. As can be seen in Figure 7.28, good agreement between the amplitude and phase obtained from the LMS offline technique and the FBLMS online technique was achieved when the FBLMS online technique operated for 20s.

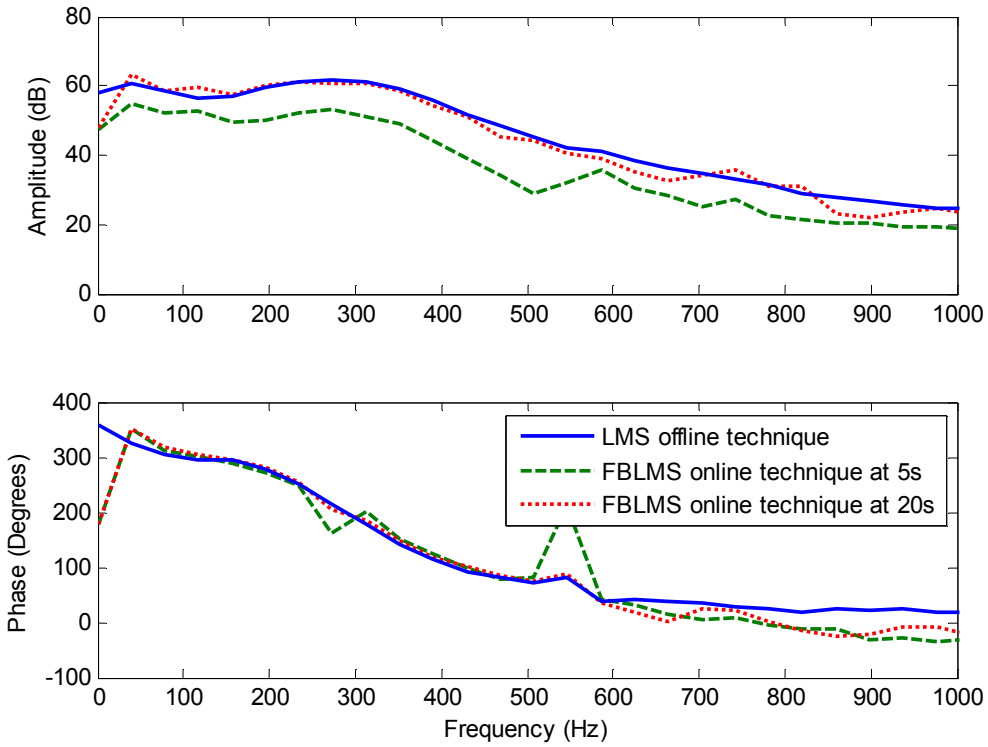

Figure 7.28 Amplitude and phase characteristics of secondary path S(z) of flow booster with an in-series controller

The FBN cancellation is plotted in Figure 7.29, where the amplitude of pressure pulsation decreased from -9.4 dB to -51.8 dB at the fundamental frequency 40Hz. The background noise of original pressure ripples rise to -60 dB compared to the Figure 7.27 where the background noise was below -80dB. This is because of the use of white noise for online secondary path identification.

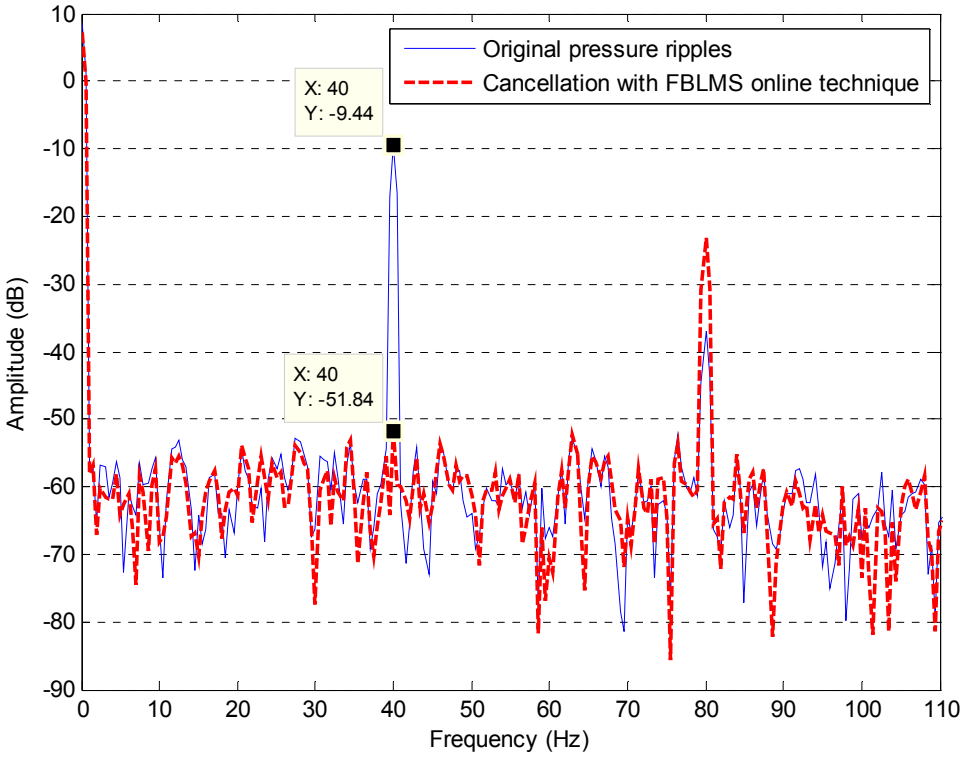

Figure 7.29 Single frequency cancellation using FBLMS online technique

7.4.2.3 LMS offline method for multiple harmonics cancellation

The multiple harmonics cancellation of pressure pulsation in the flow booster system based on the in-series structure was investigated. The designed controller was constructed from two-weight adaptive filters in parallel using different convergence rates, and was arranged in line with the flow booster and load. Different convergence factors were applied in adaptive notch filters at different frequencies, as listed in Table 7.7. Three harmonics of pressure ripple 40Hz, 80Hz and 120Hz were taken into account in this case. This is because numerical problems occurred in Simulink when more than three harmonics were considered. The solver used was 'ode23tb(stiff)' and the relative tolerance was 1×10^{-4}. However three harmonics were sufficient for proof of principle.

Table 7.7 Convergence rates used for difference harmonics by using LMS offline time-domain technique

Frequency (Hz)	40	80	120
Convergence rate μ	3×10^{-17}	2×10^{-17}	2×10^{-17}

Figure 7.30 shows the cancellation of multiple pressure pulsation harmonics using LMS offline technique. Good attenuation was achieved at three harmonics.

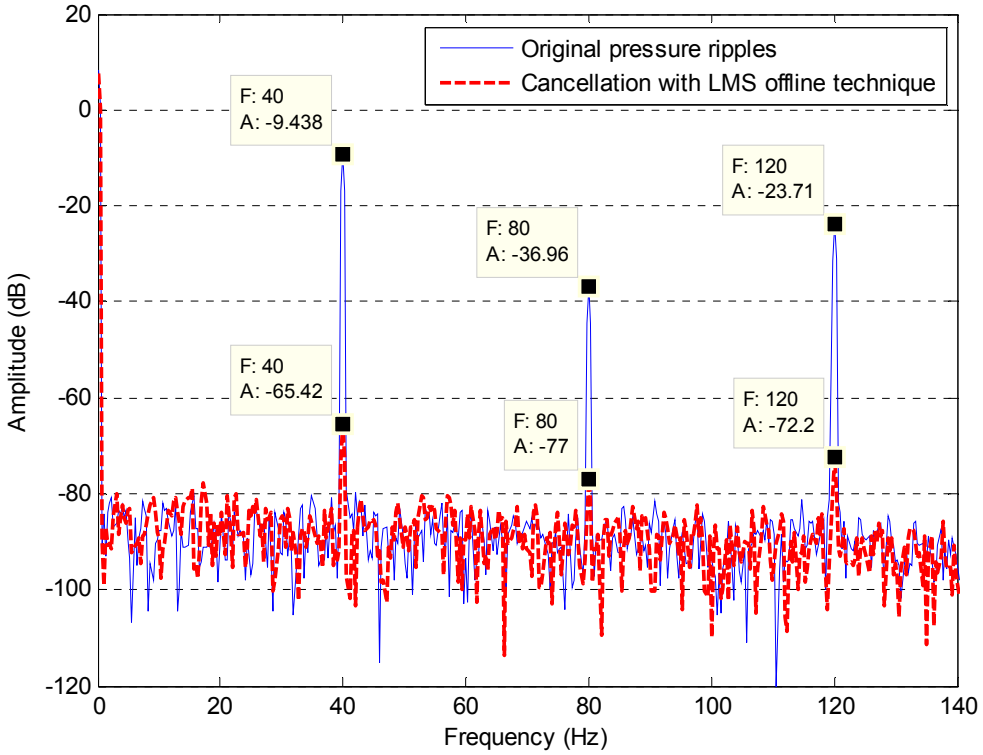

Figure 7.30 Multiple harmonics cancellation of FBN using LMS offline time-domain technique with in-series structure

The amplitudes of original pressure pulsation and after cancellation in dB at different frequencies are listed in Table 7.8. The maximum attenuation of 56.0dB was achieved at 40Hz and the average cancellation was 48.2dB.

Table 7.8 Results of cancellation at different frequencies using LMS offline time-domain technique

Frequency (Hz)	40	80	120
Original pressure pulsation (dB)	-9.44	-37.0	-23.7
After cancellation (dB)	-65.4	-77.0	-72.2
Total cancellation (dB)	56.0	40.0	48.5

Figure 7.31 shows the filter tap weights of different sub-controllers. The filter coefficients are plotted at 0.025s time interval in 10s. It can be seen that after 2s the

filters converged and the tap weights reached their optimal values which are described in Table 7.9.

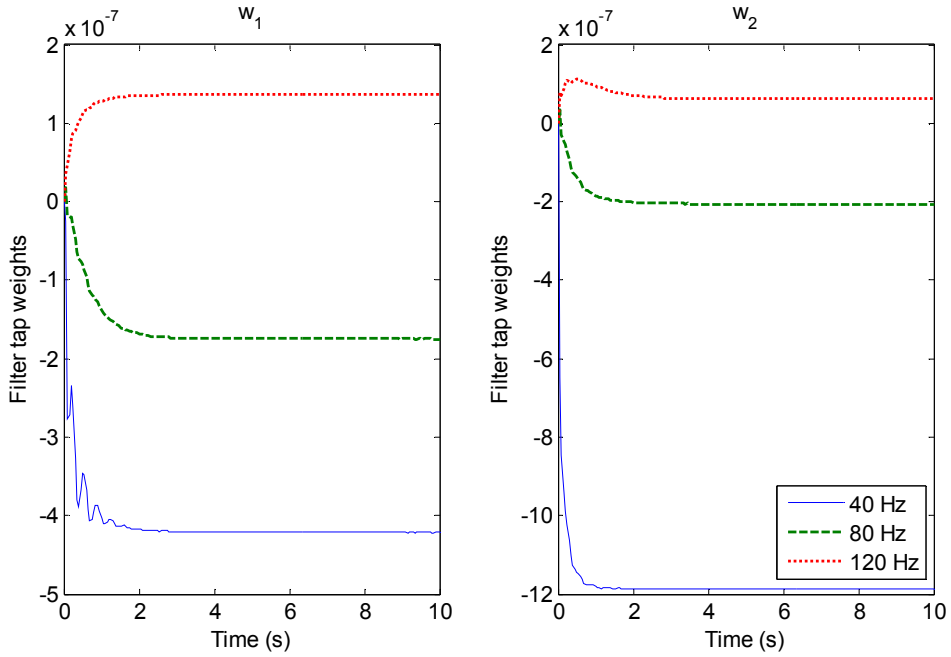

Figure 7.31 Filter tap weights of different sub-controller using LMS offline technique

Table 7.9 Optimal value of weights for different harmonics by using LMS offline time-domain technique

Frequency (Hz)	40	80	120
Optimal value of w_1	-4.21×10^{-7}	-1.75×10^{-7}	1.37×10^{-7}
Optimal value of w_2	-1.19×10^{-6}	2.06×10^{-7}	0.62×10^{-7}

7.4.2.4 FBLMS online method for multiple harmonics cancellation

The FBLMS online identification method was applied with the convergence rates of sub-controller listed in Table 7.10. The results are shown in Figure 7.32 where the cancellations were achieved at different frequencies.

Table 7.10 Convergence rates used for different harmonics using FBLMS online frequency-domain technique

Frequency (Hz)	40	80	120
Convergence rate μ_c	4×10^{-17}	2.5×10^{-17}	2.5×10^{-17}

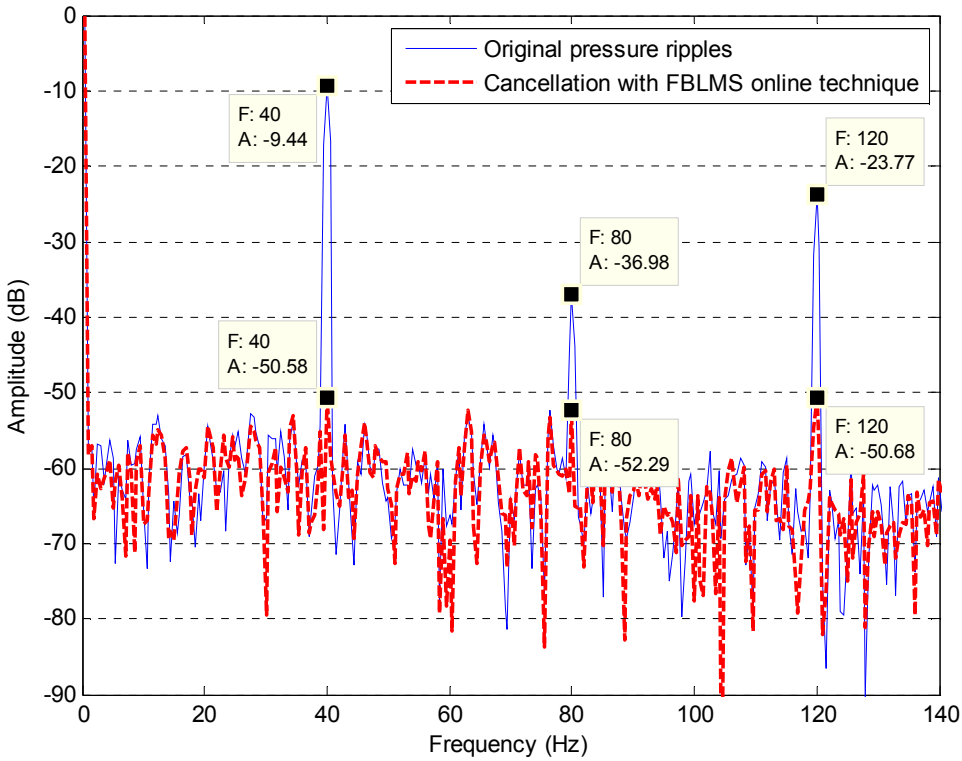

Figure 7.32 Multiple harmonics cancellation of pressure ripple using FBLMS online technique based on the in-series structure

Table 7.11 shows the amplitudes of original pressure and the total cancellation. The maximum cancellation 41.2dB was achieved at the frequency of 40Hz. Because of the rise in background noise, the attenuations at the frequencies of 80Hz and 120Hz were not as obvious as the results obtained by using LMS offline technique.

Table 7.11 Results of cancellation at different frequencies using FBLMS online frequency-domain technique

Frequency (Hz)	40	80	120
Original pressure pulsation (dB)	-9.4	-37.0	-23.8
After cancellation (dB)	-50.6	-52.3	-50.7
Total reduction (dB)	41.2	15.3	26.9

Good cancellation of pressure pulsation in simulation leads to a conclusion that the designed noise canceller is very effective for pressure pulsation attenuation with the proposed in-series structure. However, the introduction of white noise could affect the

controller performance. Besides, increased power consumption is expected for two reasons. Non-zero load flowrate is essentially necessary since the controller relies upon a pressure drop across the piezoelectric valve for noise cancellation. Moreover, the mean delivery pressure would decrease as the piezoelectric valve would result in a pressure drop. Based on these, a high-speed valve with high flowrate and low pressure drop is desired in terms of the canceller requirement and system efficiency with this structure.

7.4.2.5 FBLMS online method for multiple harmonic cancellation with a transient switching frequency

A transient frequency was implemented to validate the effectiveness and stability of the in-series controller. The FXLMS algorithm with FBLMS online identification technique was used for pressure ripple cancellation and system identification.

Figure 7.33 shows spectrograms of the pressure pulsation cancellation with varying switching frequency of the flow booster. The original pressure pulsation is plotted in Figure 7.33 (a) and the residual pressure ripple after cancellation is shown in Figure 7.33 (b). The switching frequency of the valve was varied from 80Hz to 20Hz over 20s with a step of 20Hz. A step signal is employed to model the sudden changing of switching frequency. Both the volumes between the inertance tube and piezoelectric valve, and between the piezoelectric valve and the loading valve, were 0.01L. As can be seen, the noise attenuator is capable of adapting to the varying conditions quickly and achieving good cancellation at the target frequencies.

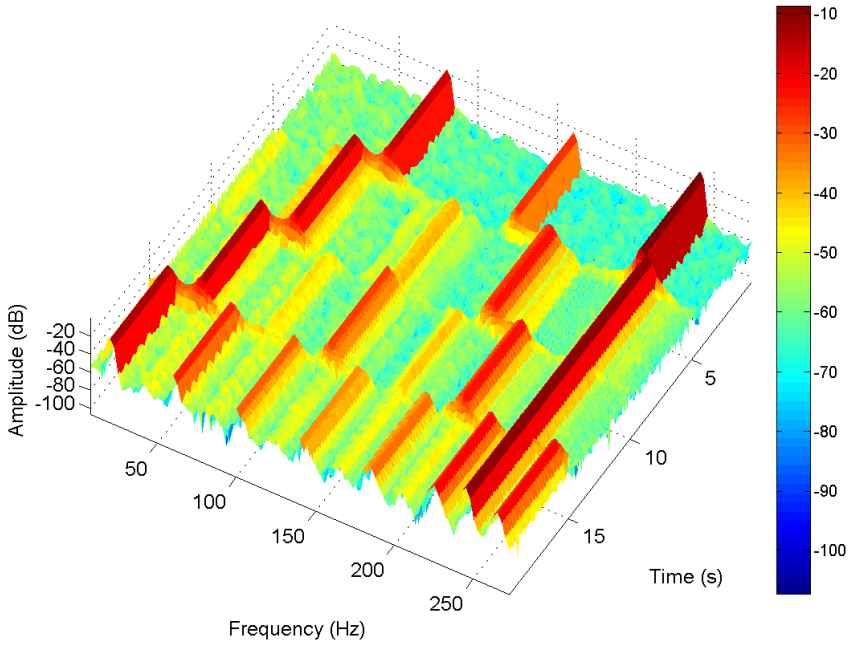

[a] Original pressure pulsation

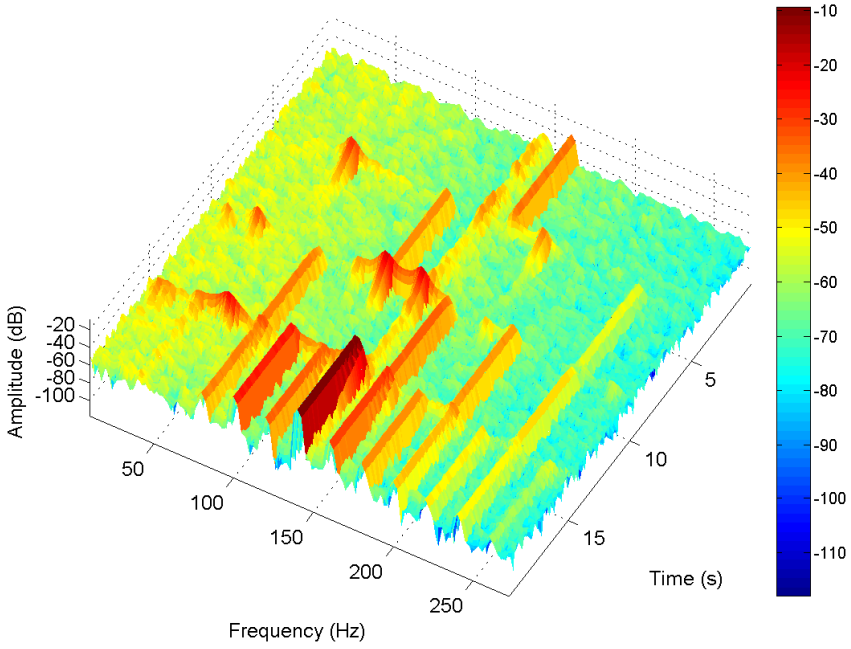

[b] After cancellation

Figure 7.33 Spectrogram showing transient cancellation of 3 harmonics with the fundamental frequency changing from 80Hz to 20Hz over 20s

It also can be seen that the controller needs to re-adapt with the different switching frequency. As in the by-pass structure, a re-adaption process is needed for attenuation. This can be seen as a disadvantage of the narrowband noise cancellation structure as the re-adaption process may result in reduced effectiveness of controller or even system instability.

Pressure harmonics at the frequency of 160Hz in the first 5s and 120Hz from 5s to 10s are still apparent. This is because of the compromise between the stability when the switching frequency varied to 40Hz and 20Hz and the performance of attenuation. Table 7.12 shows the fixed convergence factors of the notch filters. The convergence rates selected were based on the system stability with the switching frequency of 40Hz. Therefore, an automatic and appropriate control algorithm for changing convergence rates is needed in future research.

Table 7.12 Convergence rates used for difference harmonics with varying switching frequency

	Fundamental Frequency (Hz)	Harmonics of fundamental frequency (Hz)	
Frequency (Hz)	80	160	240
	60	120	180
	40	80	120
	20	40	80
Convergence rate μ	2.5×10^{-17}	1×10^{-17}	2×10^{-17}

The tap weights of the sub-controllers for fundamental frequency and the 3rd harmonics cancellation are plotted in Figure 7.34 where two weights w_1 and w_2 of the filter adapted with the changing conditions and obtained their optimal values quickly with a short period of re-adaption. The weights for the fundamental frequency are presented as $w_1(f)$ and $w_2(f)$ and for the 3rd harmonic are described as $w_1(3f)$ and $w_2(3f)$ in Figure 7.34.

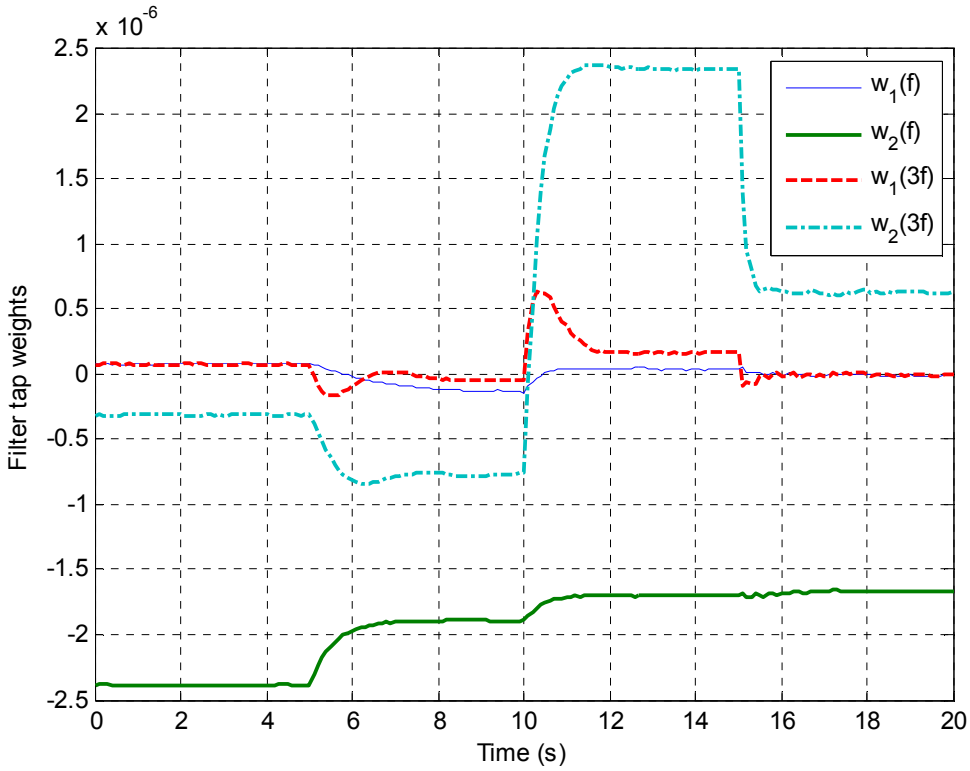

Figure 7.34 Filter tap weights of the sub-controller for fundamental frequency and the 3rd harmonic cancellation with varying switching frequency

7.4.2.6 FBLMS online method for multiple harmonics cancellation with a transient switching ratio

The amplitude of pressure ripple at the frequency of 40Hz was plotted in Figure 7.35 (above) where the switching ratio *x* was changed from 0.1 to 0.9 in step of 0.2 as shown in Figure 7.35 (bottom). The ratio increased by 0.2 in every 4s and the simulation time was 20s. The convergence rate used for the fundamental frequency was 2.5×10^{-17}. The simulated opening of the loading valve was fixed at 0.1 cm^2.

The noise canceller was applied with different ratios based on the in-series structure. The result was plotted in Figure 7.35 (middle) where fast adaptive speed and good cancellation were obtained. The average cancellation achieved was 40dB.

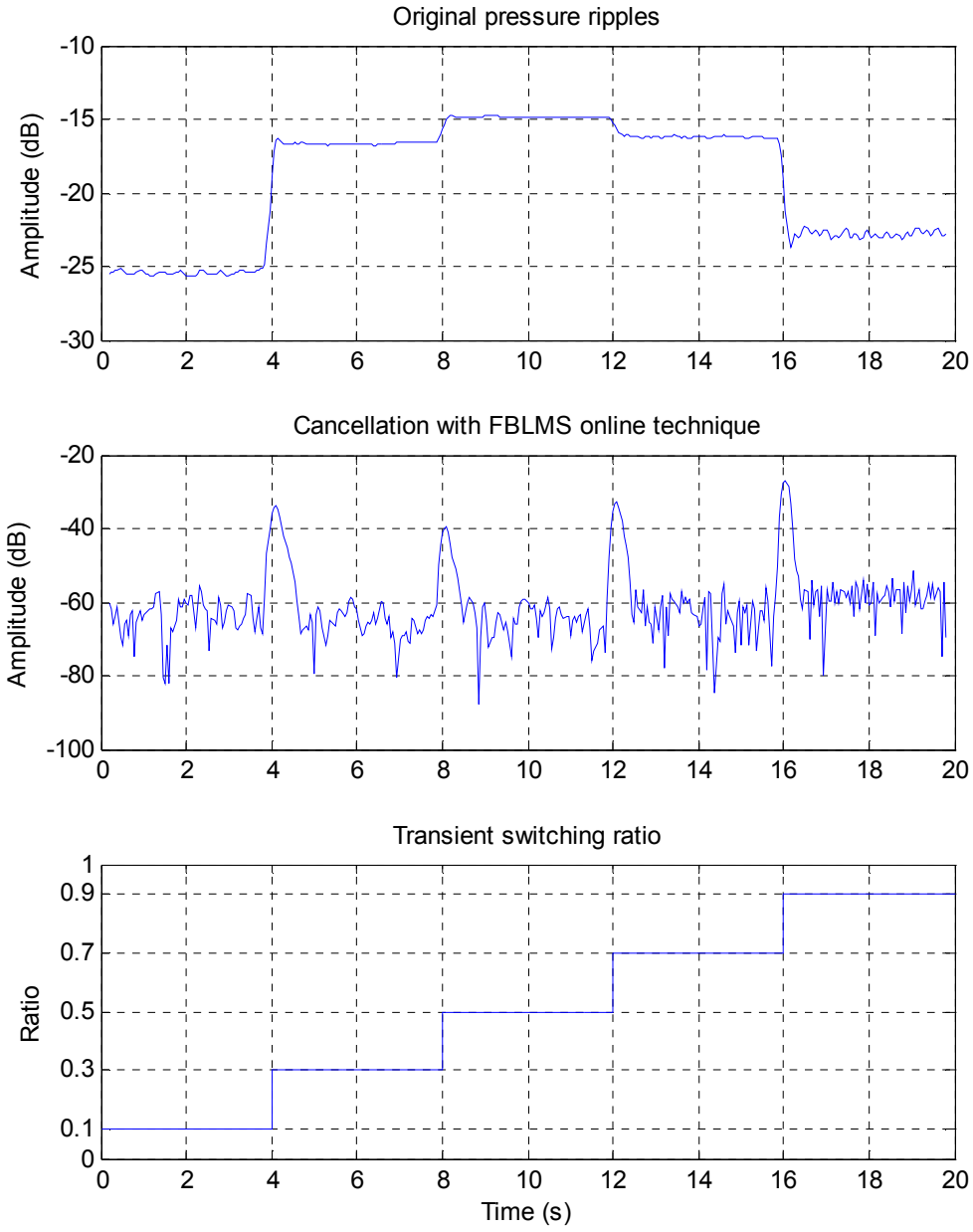

Figure 7.35 Pressure pulsation cancellation at the fundamental frequency with varying switching ratio of flow booster using the in-series structure.

Figure 7.36 shows the frequency response of the secondary path when the switching ratio varied. It can be seen that the amplitude went up with the increasing mean pressure and the phases changed with the varying system dynamics. Phase and amplitude differences occurred above the frequency of 700Hz.

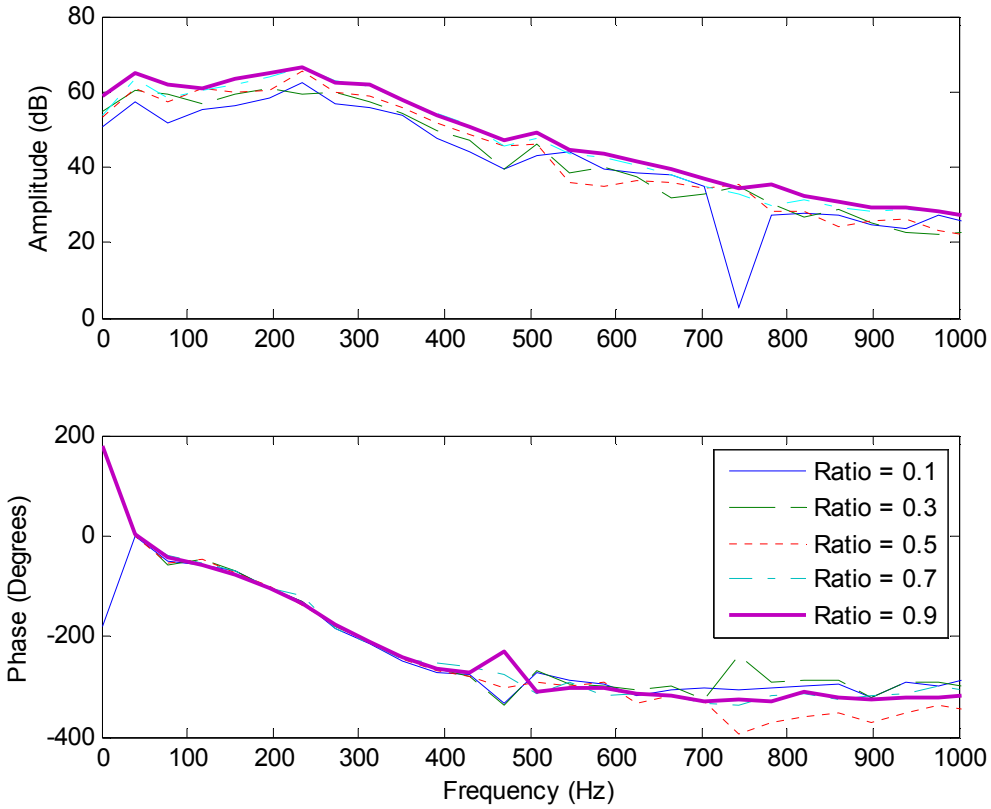

Figure7.36 Amplitude and phase characteristics of secondary path with different switching ratios

The tap weights of adaptive notch filter for the fundamental frequency are shown in Figure 7.37, where the weights adapt quickly with the changing switching ratios.

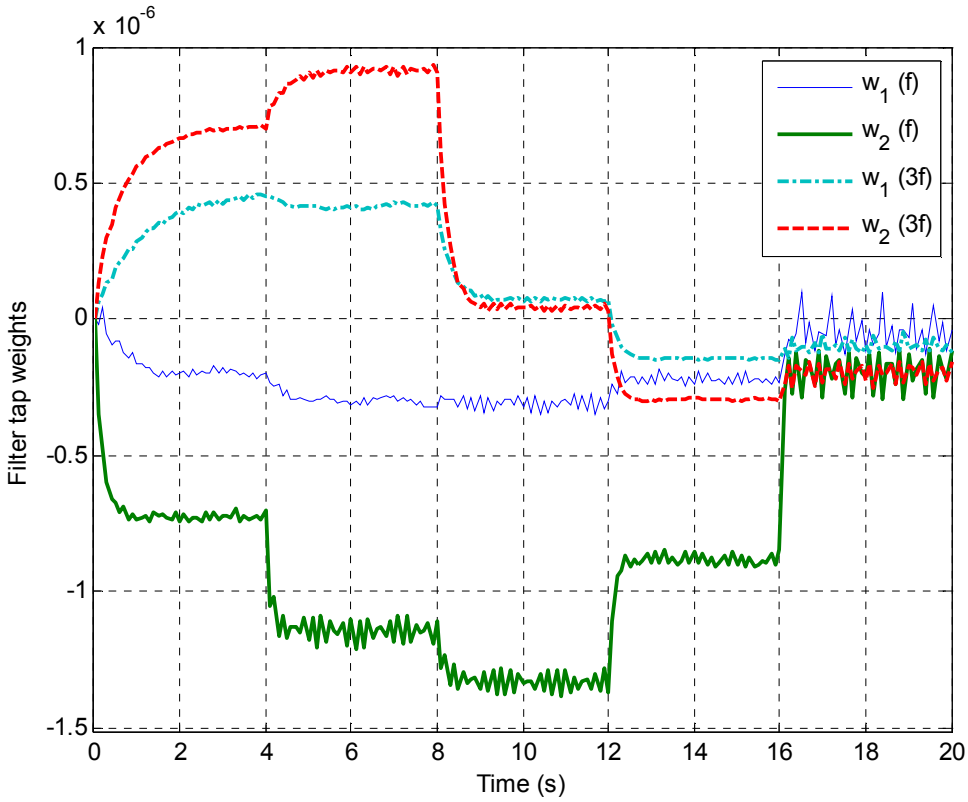

Figure 7.37 Filter tap weights of the sub-controller for the fundamental frequency and the 3rd harmonic with varying switching ratio using the in-series structure

7.4.2.7 FBLMS online method for multiple harmonics cancellation with varying loading

The same loading system as used in by-pass structure was used on the flow booster with the in-series noise canceller. The simulated opening was ramped from 0.01cm^2 at 0s to 1cm^2 at 20s. The downstream boundary condition was determined by the loading valve at the beginning when the valve was closed then depended on the opening of piezoelectric valve as the loading valve was gradually open in this process and can be seen as an open end eventually. It can be seen in Figure 7.38 (top) that the original pressure amplitude varied greatly during the 20s. This varying condition may cause changing dynamics of the secondary path of the system. The amplitudes of FBN before and after cancellation at the frequency of 40Hz and 120Hz are plotted in Figure 7.38.

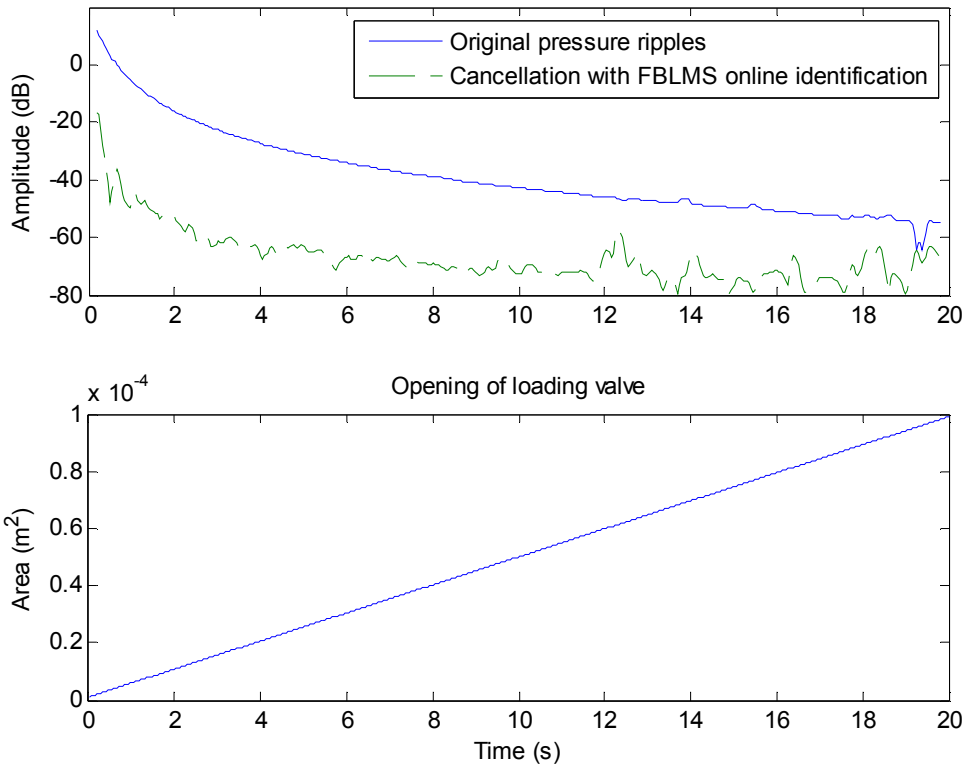

Figure 7.38 Pressure pulsation cancellation at the frequency of 40Hz with varying system load with in-series structure

Figure 7.39 shows the amplitude and phase characteristics at 1s and 6s. It can be seen that different dynamics were achieved at these two times. The FBLMS online identification method is capable of achieving different dynamics of secondary path with the changing system conditions. The tap weights of the filter for fundamental frequency cancellation are plotted in Figure 7.40.

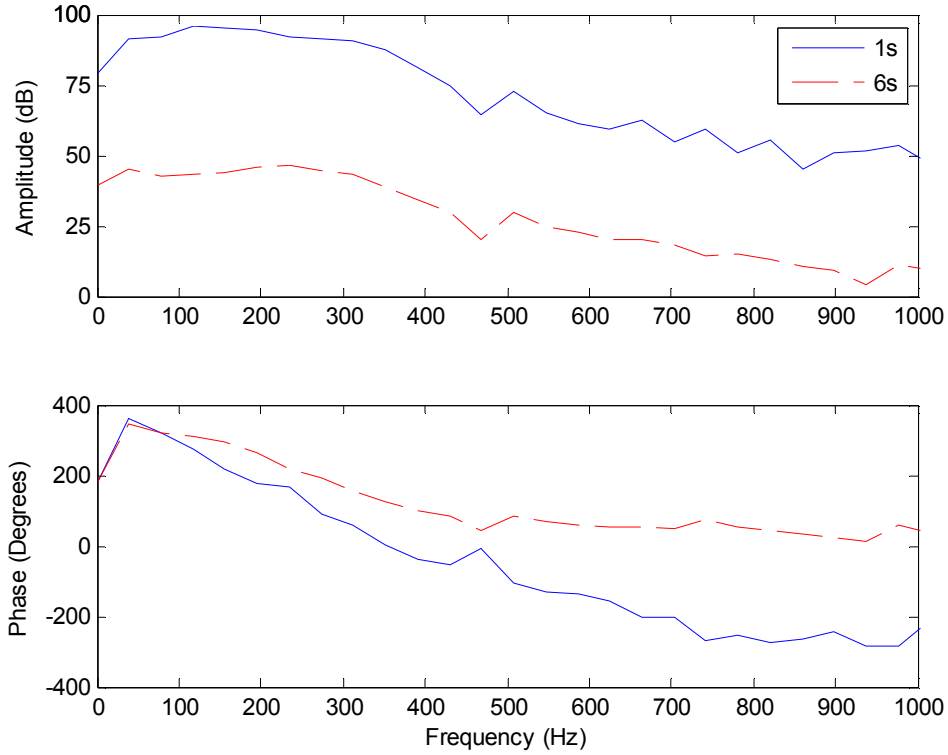

Figure 7.39 Amplitude and phase characteristics of secondary path $S(z)$ with changing loading using the in-series structure

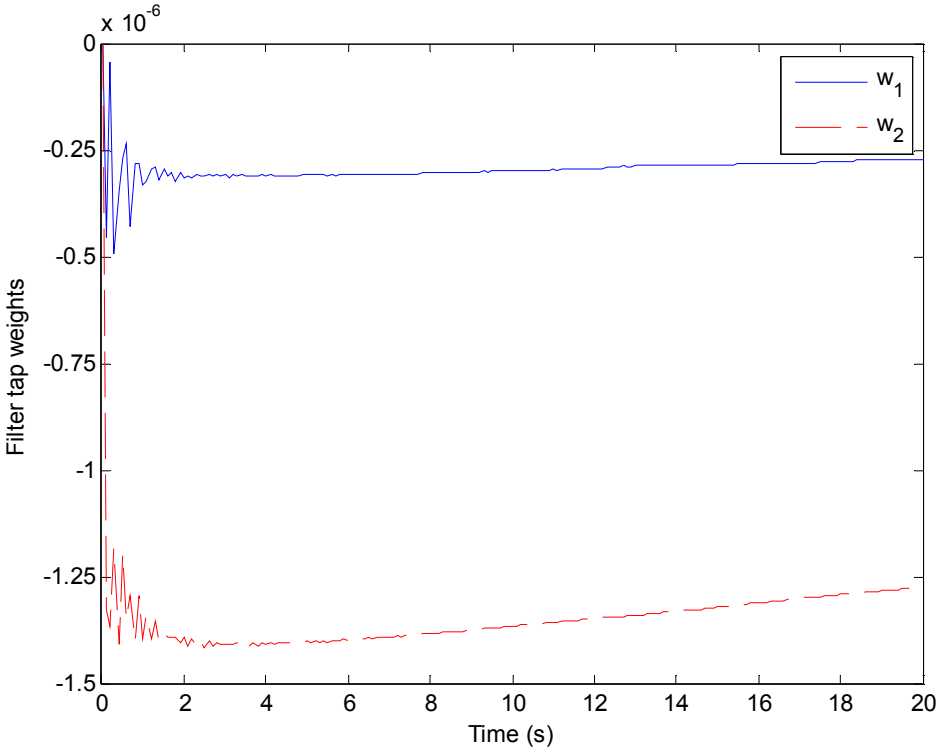

Figure 7.40 Filter tap weights of the sub-controller for fundamental frequency cancellation with changing load using the in-series structure

It can be concluded that the designed controller is able to attenuate the pressure pulsation generated in the flow booster when it is arranged in series with the system. Excellent cancellation (around 40dB) was achieved according to the simulated results. Moreover, the system performance and robustness were discussed in terms of changing switching frequency, switching ratio and system loading requirement. Results show that the identification filter could adapt quickly and effectively for changing system dynamics. However, this structure has its limitations compared with the by-pass structure. Comparisons and details are discussed in Section 7.5.

7.5 Comparison of two structures

As described in Section 7.3 and Section 7.4, the designed controller with two different structures performs effectively and robustly for FBN cancellation in a flow booster. The noise canceller and the transducer for measuring residual pressure were arranged at appropriate positions as shown in Figure 7.6 and Figure 7.26 to maintain an ideal constant delivery pressure.

Comparisons between these two structures are discussed in term of performance of noise canceller, system stability and applied limitation. The convergence rates of the filter were compromised between the FBN cancellation and system stability. Therefore, the attenuation achieved as shown in Table 7.3, Table 7.6, Table 7.8 and Table 7.11 could be seen as the maximum cancellation on condition of stability. Similar parameters were applied in simulation for the controller and the flow booster in both structures.

Based on these assumptions, it can be concluded that:

- Pressure pulsation could be reduced by up to 50dB by using the noise attenuator with both the by-pass and the in-series structures.
- The designed controller is able to attenuate the pressure ripple effectively and adapt quickly with the changing conditions. It is capable of maintaining stable performance when the switching frequency and ratio are varied. This is mainly because the phase changes of the secondary path $S(z)$ are not very dramatic when the flow booster is subjected to the varying conditions, although the amplitude would change with the system mean pressure.

- The introduction of white noise would increase the background noise but the cancellation should still be acceptable compared with the peak amplitude at the cancelled frequencies. However, it can be found that the amplitude of background noise from the by-pass structure was lower than from the in-series structure. It can be concluded that less effects caused by the white noise were observed when the noise canceller was arranged as a by-pass to the main system.
- For the by-pass structure, load pressure is required for the noise canceller to generate the anti-noise signal; whilst load flowrate is required for the noise attenuator for the in-series structure. That means the in-series structure would have a limitation when there is lack of flow passing through the piezoelectric valve. In that case the piezoelectric valve can not provide enough power for pressure pulsation cancellation. The by-pass structure is not restricted by the structure itself because the noise problem is only considered with the presence of the load pressure. Pressure pulsation may not be a problem when there is no load pressure in the system.
- For the in-series structure, with the fixed supply and return pressures, the mean delivery pressure would decrease in the process of controlling because pressure drop occurred in the piezoelectric valve. The ideal controller should have a high flowrate and small pressure drop. This is expected to decrease the power consumption of the controller. For the by-pass structure, the mean delivery flowrate would decrease when the attenuator is switched on. This is because a by-pass flowrate is needed for the piezoelectric valve.
- The dynamics of the secondary path were mainly determined by the opening of the loading valve in the by-pass structure. However, the effects from the control valve would be significant for the secondary path dynamics with the in-series structure.

Table 7.13 briefly describes the comparison between the by-pass and the in-series structures.

Table 7.13 Comparison of two different proposed structures

	By-pass structure	In-series structure
FBN cancellation	Good	Good
Stability and robustness	Good	Good
Background noise	Small	Medium
Effects from the opening of control valve	Small	Highly related
Flowrate requirement	No	Yes
Pressure requirement	Yes	Yes

From the analysis and simulation, it can be concluded that the by-pass structure can be more widely and effectively used for pressure pulsation cancellation in a flow booster compared with the in-series structure. Also less effect comes from the auxiliary noise which was used for secondary path identification and the opening of control valve within this structure. Moreover, it does not require flowrate passing through the control valve. Therefore, the by-pass structure can be seen as a general and effective approach for pressure ripple cancellation with good performance and few limitations.

7.6 Concluding remarks

The designed noise attenuator has been applied for pressure pulsation cancellation in a flow booster system with by-pass and in-series structures. The system performance was investigated via simulation in term of attenuation ability, robustness and stability when the working conditions were varied. Simulated results show an excellent cancellation was achieved as expected and the controller is capable of performing robustly with changing conditions. Based on these investigations, it can be concluded that the designed controller is able to obtain good pressure pulsation cancellation effectively and robustly. Experimental validation is demonstrated in chapter 8.

8 Experimental studies: flow booster rig tests

8.1 Experimental rig

The designed controller based on the FXLMS algorithm combined with LMS offline or online identification filter was applied to the flow booster rig. The rig comprised a proportional valve (Parker Hannifin), a 1.7m inertance tube with a diameter of 0.7cm and a loading valve. The proportional valve was switched rapidly between the high pressure supply port (pump supply) and low pressure supply port (reservoir) using a pulsed signal A needle valve was used at the downstream end to adjust the system load.

The experimental tests were conducted on two different rig structures with the pressure pulsation cancellation valve in series and by-pass configurations. A novel piezoelectric valve (Branson et al., 2011) was used as the actuator to produce the anti-noise in the system, because of its fast response and high bandwidth. An E-481 high-power piezo amplifier was used to drive the piezoelectric actuator. The designed controller was implemented on a dSPACE DS1005 controller board with a DS2002 A/D Board and a DS2103 D/A Board.

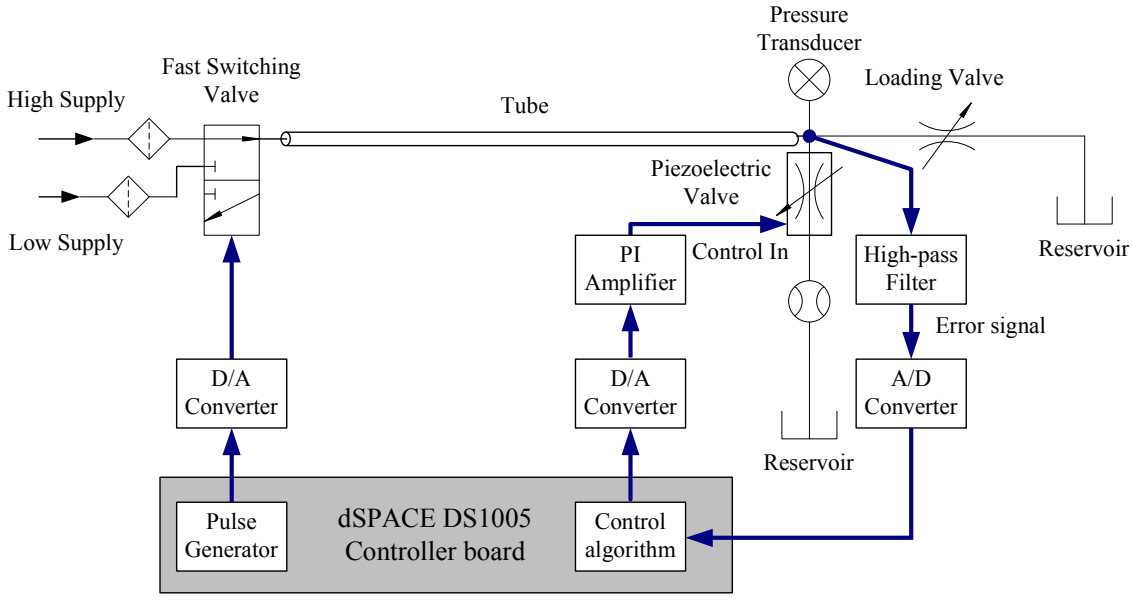

Figure 8.1 Schematic of the experimental test rig with by-pass structure

Figure 8.1 shows the schematic of the experimental test rig with the by-pass structure. A pre-determined pulsed signal was generated to control the servo valve switching

cyclically. A pressure transducer with a range of 0 to 135bar was arranged at the conjunction of the tube and piezoelectric valve. In order to avoid bias of the error signal, a digital high pass filter was built based on dSPACE with 1Hz cut-off frequency. A flowmeter was fixed at the downstream line of the piezoelectric valve to measure the flowrate passing through the by-pass branch. Another flowmeter was fixed after the loading valve to measure the load flowrate. Figure 8.2 shows a photograph of the rig with the by-pass structure.

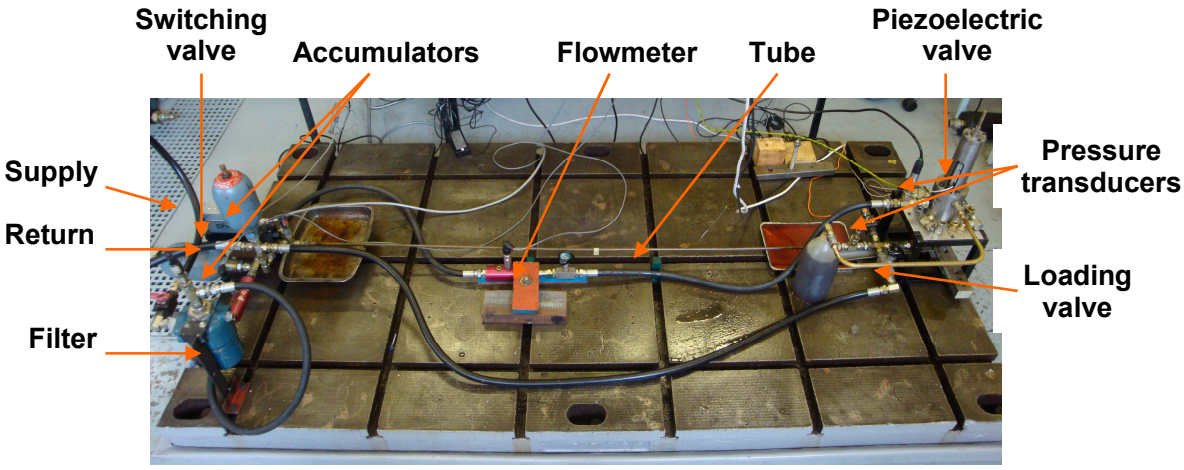

Figure 8.2 Photograph of the experimental rig with the by-pass structure

The schematic diagram of the experimental test rig with the in-series structure is shown in Figure 8.3, where the piezoelectric valve is arranged in line with the rigid tube and the loading valve. A pressure transducer with a range of 0 to 50 bar was fixed after the piezoelectric valve to measure the delivery pressure of the system. A flowmeter was installed after the loading valve.

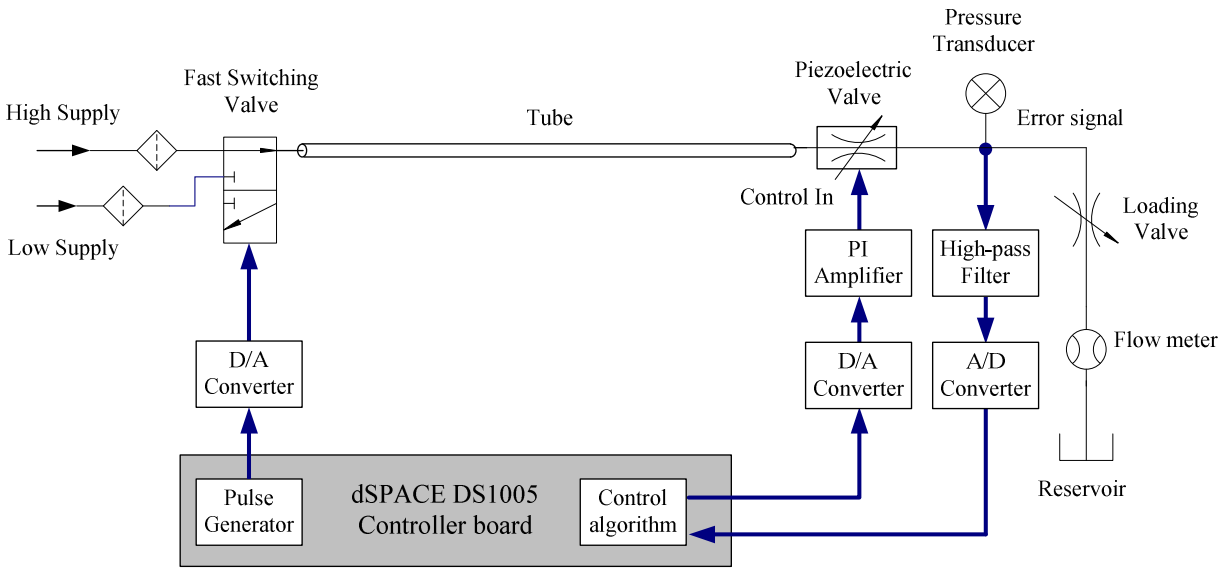

Figure 8.3 Schematic of the experimental test rig with the in-series structure

Figure 8.4 shows a photograph of the rig with the in-series structure.

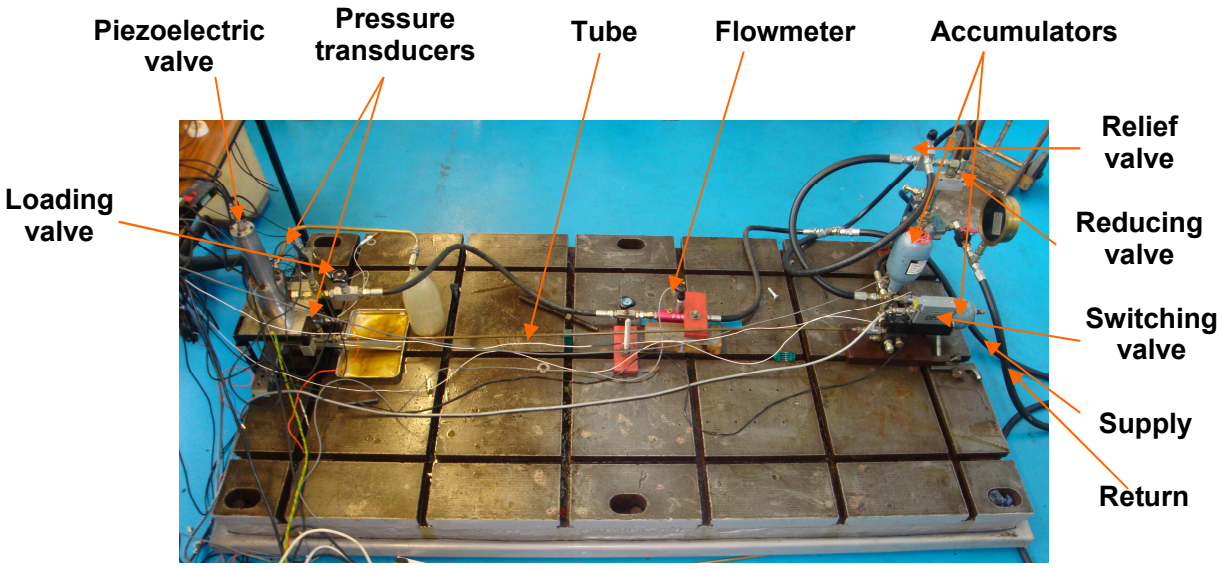

Figure 8.4 Photograph of the experimental rig with the in-series structure

8.2 Piezoelectric valve

As shown in Figure 8.1 and 8.3, a piezoelectrically actuated valve was applied as the actuator of the secondary source to produce an anti-noise signal for FBN cancellation. The piezoelectric actuators can operate at high force which is required for pressure pulsation attenuation. A piezoelectric valve designed as part of University of Bath's

EPSRC funded actuation project (Reference no. EP/D060478/1) was selected as the noise canceller for this application.

8.2.1 Introduction

The principle and design of the piezoelectric actuated valve were described by Branson et al. (2010). The Horbiger plate method, which is based on the use of annular grooves in two mating plates, was applied to form multiple metering edges for allowing large flow path areas at relatively small plate separation distances (Winkler and Scheidl, 2007, Hoerbiger.A, 1938, Kehler.K, 1940). Figure 8.5 shows the schematic of the prototype of the piezoelectric actuated valve and its photograph.

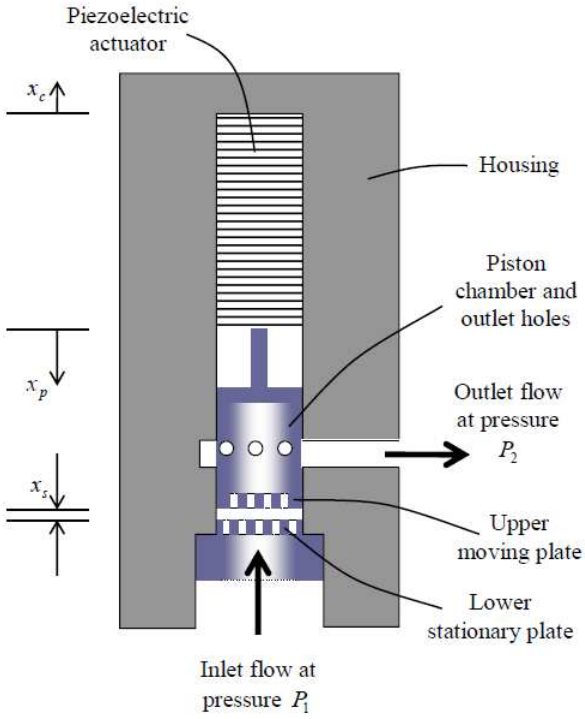

(a) Schematic cross-section (Branson et al., 2010)

(b) Photograph

Figure 8.5. The prototype piezoelectrically actuated valve

As can be seen, the valve is directly activated using a piezoelectric actuator to achieve a fast dynamic response. According to the experimental results, it has been proved that the designed valve has a high bandwidth and high flowrate under low pressure drops (Branson et al., 2011). Based on this, it can be concluded that the valve is capable for FBN cancellation in terms of its fast dynamic response and good performance.

8.2.2 Steady state performance

The steady state flow characteristics for the piezoelectric valve as a function of applied voltage and pressure drop across the valve are shown in Figure 8.6. The applied voltage of the piezoelectric actuator ranged from -200v to 800v. It can be seen that flow increases as the pressure drop increases and applied voltage decreases. When the applied voltage equals -200v, the piezoelectric valve is fully opened; when the applied voltage equals 800v, the valve is closed off.

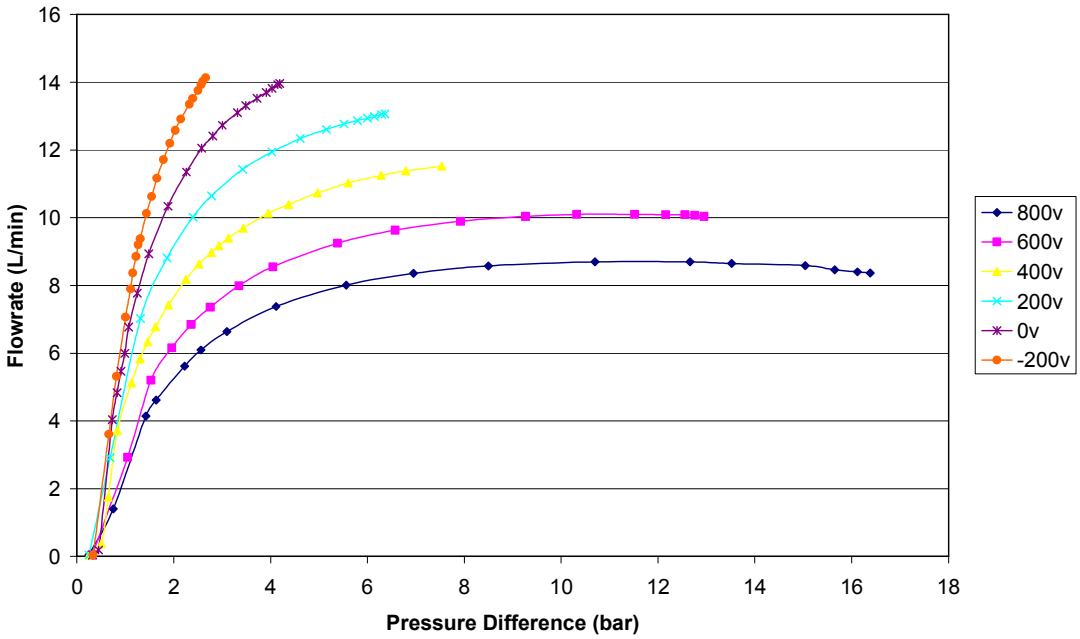

Figure 8.6 Steady state flow characteristics for the piezoelectric valve [1]

It can be noticed that a constant flowrate leakage occurred even the valve is at the closed off position (Branson et al., 2010). At an applied voltage of 400V a flowrate of 10L/min was achieved at pressure drop of 4bar. This state was applied as an initial condition for the noise attenuator in further experiments.

[1] 0v does not mean that the absolute output voltage equals to zero. It represented the initial offset value of the piezo amplifier.

8.3 System identification with by-pass structure

The accuracy of secondary path dynamics is very significant for the controller performance. The LMS offline and FBLMS online techniques were selected and used for identification, and experimentally validated.

A frequency analyzer was used to obtain the frequency response of the secondary path by sweeping voltage-controlled sinusoidal waves through a range of frequencies. The results achieved were used for comparison with the results achieved from LMS offline technique.

The opening of piezoelectric valve was controlled by the voltage from the amplifier, which was set at -200V, 0V, 400V, 700V and 800V for different opening conditions. The high pressure supply was fixed at 30bar and the return pressure was approximately 3 bar. The servo valve was connected to the high pressure supply port in order to get a constant pressure for the secondary path identification. The needle valve was fully closed. Experiments were performed to validate the identification filter with the LMS algorithm, which was effective to obtain accurate system dynamics.

Figure 8.7 ([a] – [d]) shows the amplitude and phase characteristics of the secondary path using the frequency analyzer and the LMS offline technique with a driving voltage of -200V, 0V, 400V, 700V and 800V. It can be seen that both the amplitude and phase curves obtained from the LMS offline technique agree well with the results achieved from the frequency analyzer. This experimentally proves that the LMS filter was effective for the identification of the unknown plant. Moreover, it can also be found that the secondary path mainly performed two different dynamics with different driving voltages of the piezoelectric valve, as shown in Figure 8.7 [a] and Figure 8.7 [d].

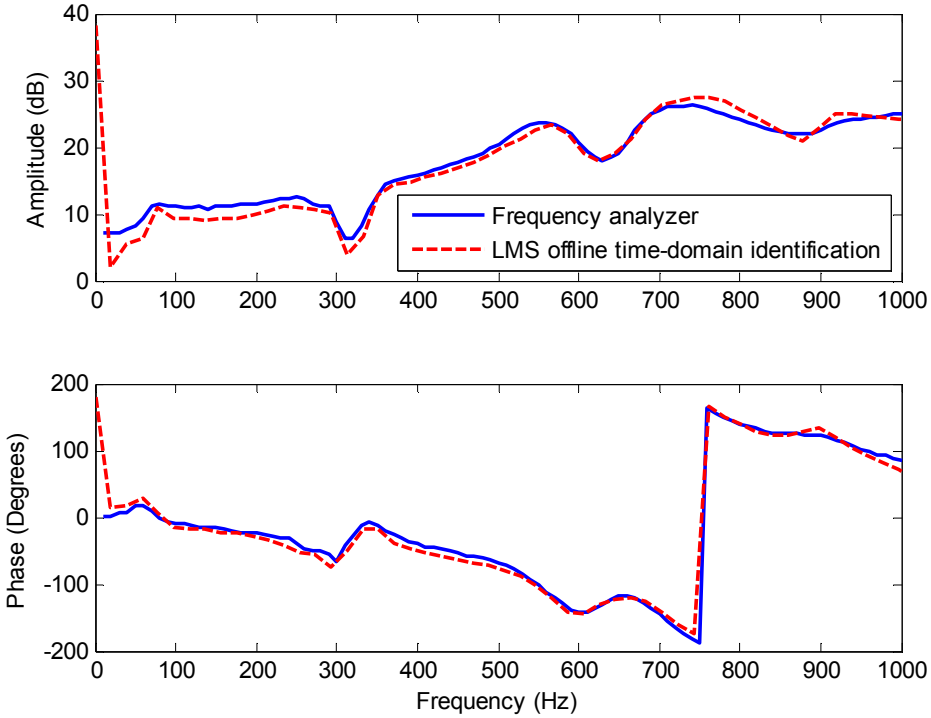

[a] piezoelectric actuator voltage = -200V

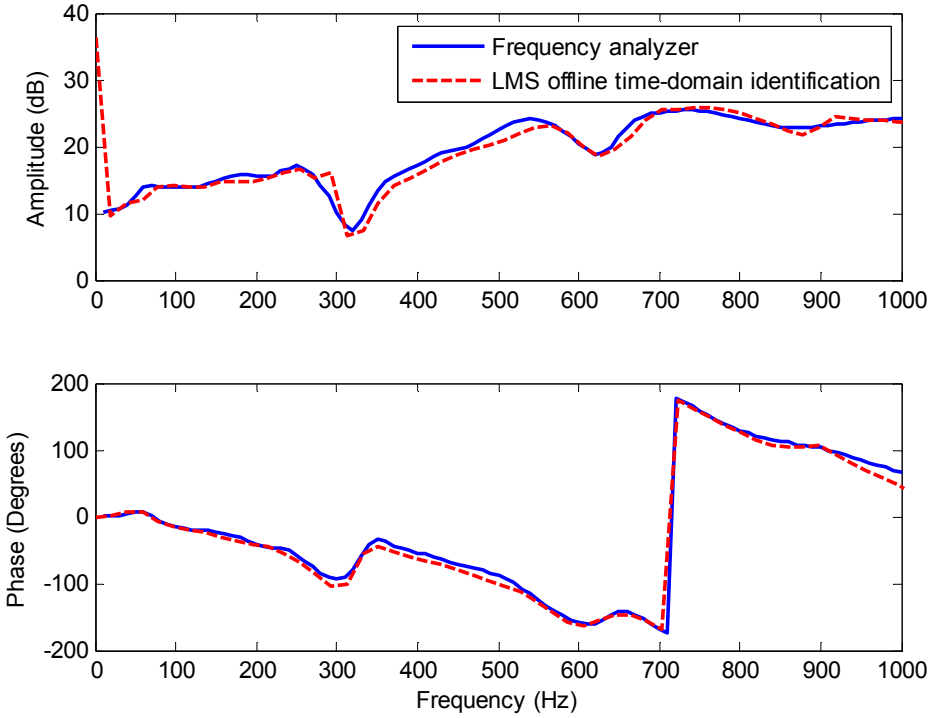

[b] piezoelectric actuator voltage = 0V

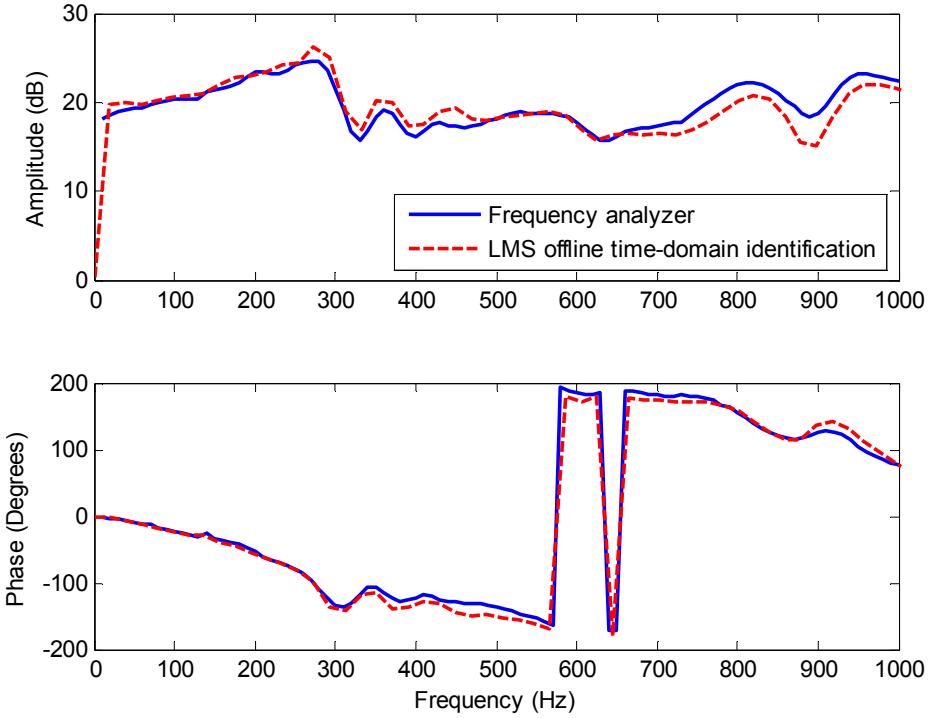

[c] The piezoelectric actuator voltage = 400V

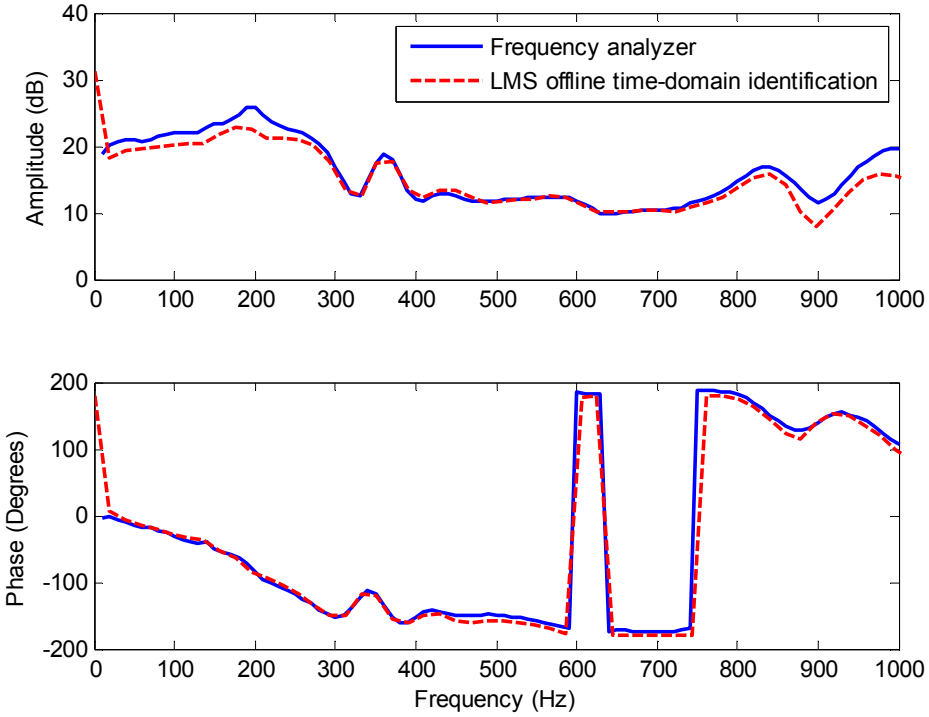

[d] piezoelectric actuator voltage = 700V

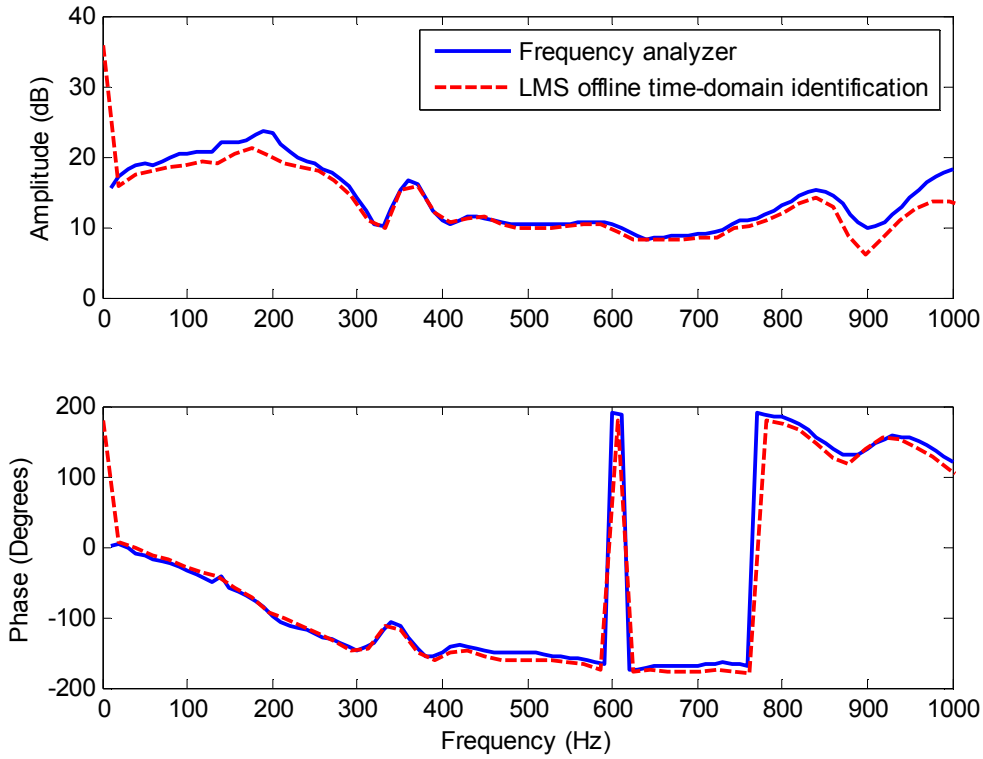

[e] piezoelectric actuator voltage = 800V

Figure 8.7 Comparison of frequency responses achieved from the frequency analyzer and LMS offline technique with different applied voltages

The impulse response of Figure 8.7[c] is shown in Figure 8.8 [a], with the loading valve closed (0 L/min). Relatively high damping is apparent in the secondary path. Compared with this, the impulse response achieved at the condition of opened loading valve with 3L/min flowrate is shown in Figure 8.8 [b]. As can be seen, lower damping occurred with a higher natural frequency, but it was still acceptable for the noise canceller. In order to present the general conditions, the loading flowrate was selected at 3L/min in further experiments.

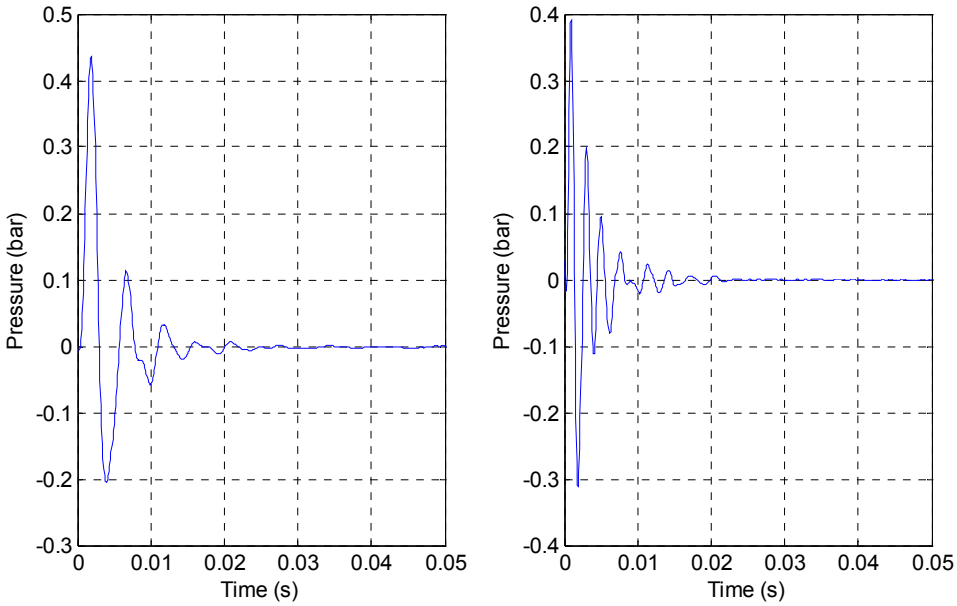

[a] Loading flowrate = 0L/min [b] Loading flowrate = 3L/min

Figure 8.8 Secondary path identification with different loading conditions

The same principle can be used as an alternative explanation for the opening of the piezoelectric valve in the by-pass branch; higher damping is preferred for system control and stability. Therefore, the piezoelectric valve was adjusted to the half open condition with the driving signal of 400V. The full opening of the piezoelectric valve could work but it was expected to have poorer cancellation performance. Details can be found in Appendix 2.

8.4 Pressure pulsation cancellation in a flow booster system with by-pass controller

The by-pass structure was initially implemented for pressure pulsation cancellation with the flow booster. This section presents the performance of the noise attenuator using both the LMS offline and FBLMS online identification techniques.

The high supply and low supply pressures of rig were fixed at 25 bar and 20 bar respectively. A reducing valve and a relief valve were applied to the high supply port in order to obtain the appropriate pressure as the low supply port, as shown in Figure 8.9. In this case the pressure difference was just 5 bar in order to avoid or reduce system cavitation.

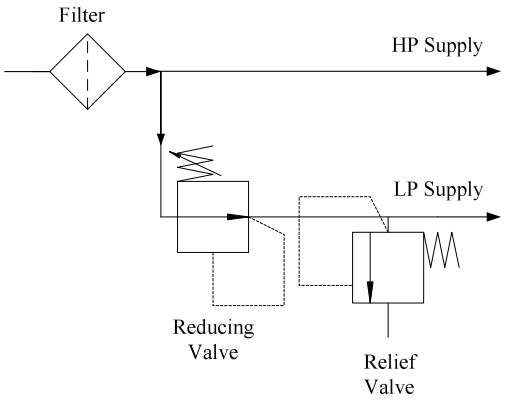

Figure 8.9 Supply pressure ports

Because of the introduction of a reducing valve and a relief valve, it was expected that dynamic differences would occur when the servo valve was connected to different supply ports. Figure 8.10 shows the frequency responses of secondary path for the servo valve connecting to high and low supply pressures using LMS offline identification technique. The length of filter was 512 and the sample frequency was 10 kHz. The loading valve was adjusted at the appropriate position to obtain the loading flowrate of 3 L/min when the servo valve connected to the high supply pressure and roughly 2 L/min when the valve connected to the low pressure port. The low flowrate was chose also in order to avoid cavitation. Figure 8.11 shows the impulse responses of secondary path.

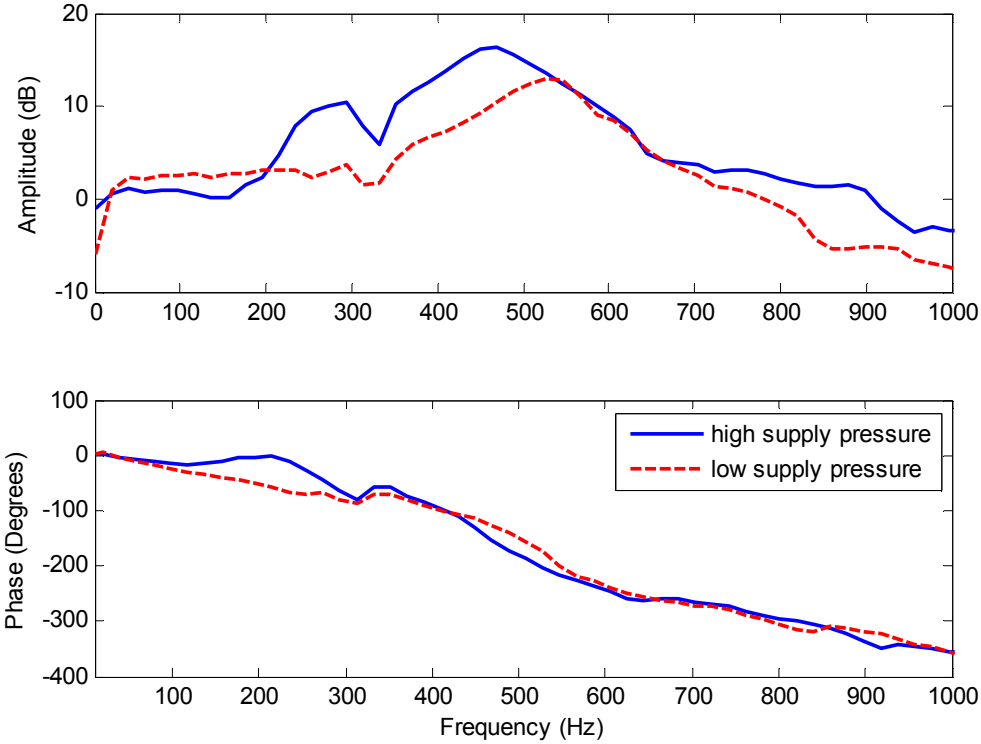

Figure 8.10 Frequency responses of secondary path when the servo valve was connected to the high and low supply pressures

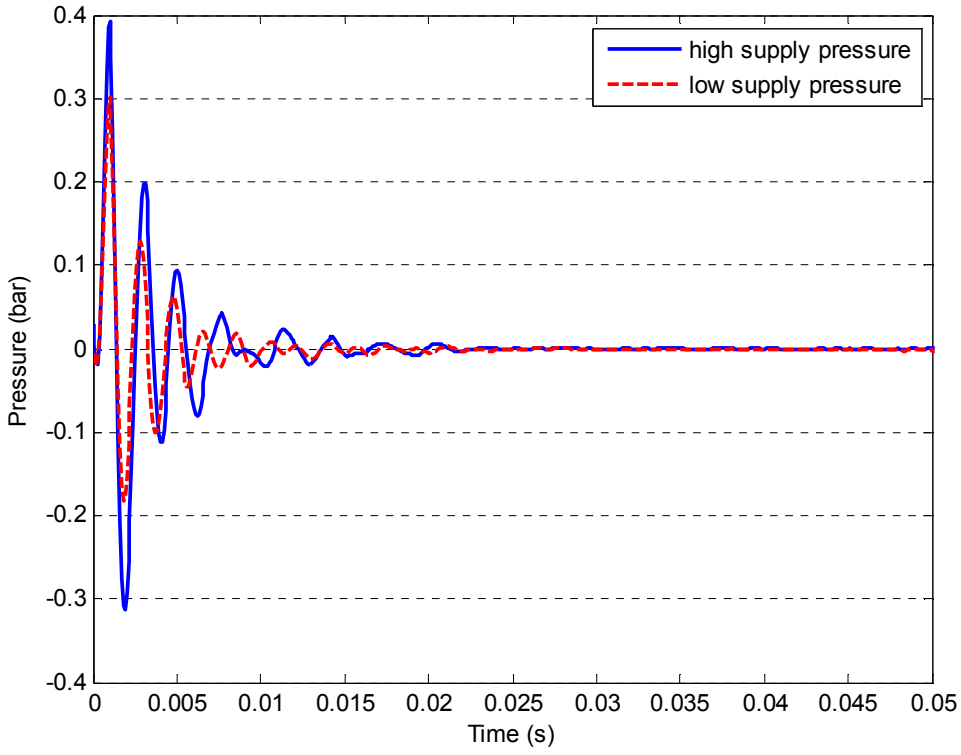

Figure 8.11 Impulse responses of secondary path when the servo valve was connected to the high and low pressure supplies

As can be seen in Figure 8.10, amplitude differences occurred but the phases almost remained the same in the frequency range from 0 to 1000Hz. This can be seen as an advantage for further experiments because of the stable phase characteristics when the switching valve connected to two different ports.

8.4.1 FXLMS canceller with LMS offline identification technique

Figure 8.12 shows a single harmonic of pressure pulsation cancellation using the LMS offline technique. The servo valve switched using 50% duty cycle pulse signal with the amplitude of 10V. It means the servo valve was fully open to both high supply and low supply ports cyclically. The loading and by-pass flowrates both were 2.7L/min at the switching condition. The sample time step was 0.1ms.

For the cancellation with LMS offline identification technique, the results in Figure 8.10 were used as the secondary path characteristics. The convergence rate of the noise canceller was 4×10^{-3}.

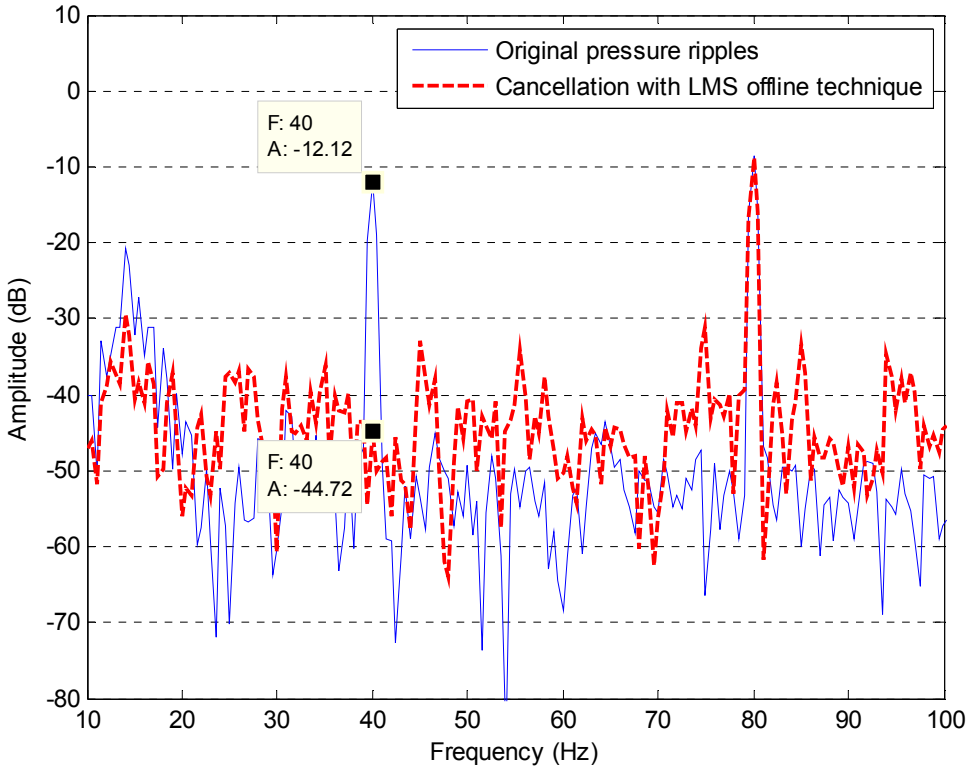

Figure 8.12 Single frequency cancellation using LMS offline identification technique

A Hamming window was used to minimize the maximum side lobe in spectral analysis. The pressure pulsation was decreased by 32.6dB at the frequency of 40Hz. For multiple harmonics cancellation, different convergence factors were applied in the parallel adaptive notch filters of different frequencies, as listed in Table 8.1. The cancelled frequencies were multiples of the fundamental frequency of 40Hz and three harmonics were considered in terms of the ability of computation of the dSPACE 1005 system.

Table 8.1 Convergence rates used for different harmonics using LMS offline time-domain technique

Frequency (Hz)	40	80	120
Convergence rate μ	5×10^{-3}	8×10^{-4}	3×10^{-4}

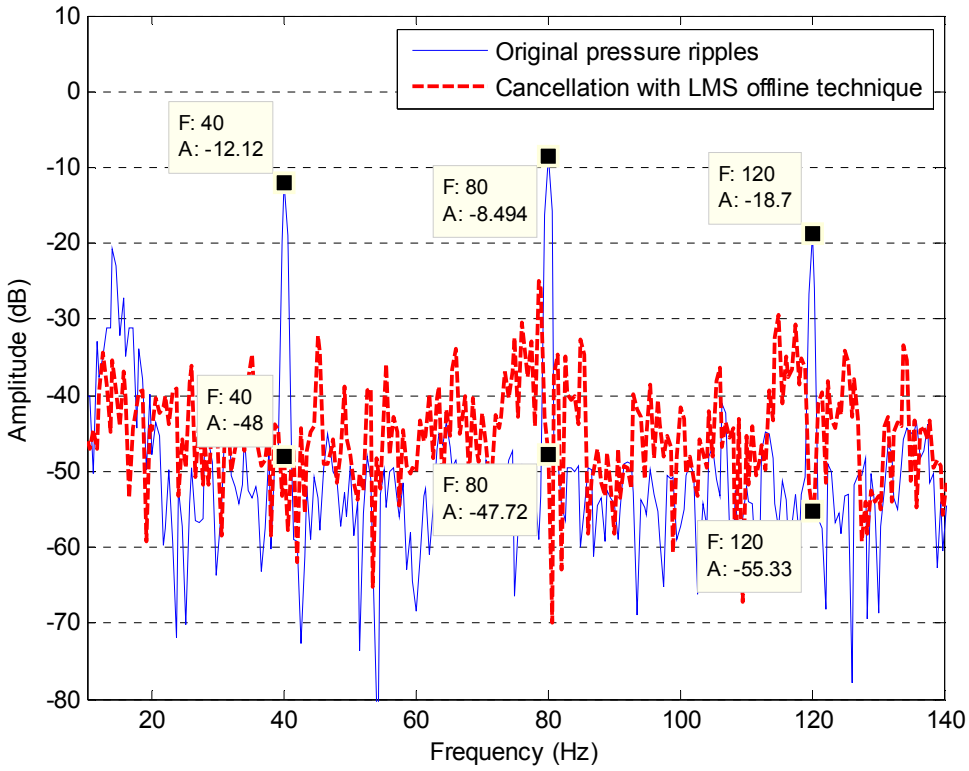

Figure 8.13 Multiple frequency cancellation using LMS offline identification technique

Figure 8.13 shows the cancellation of multiple pressure pulsation harmonic using the LMS offline technique. The amplitudes of the original pressure pulsation and after cancellation at different frequencies are listed in Table 8.2. It can be found that the maximum cancellation of 39.2 dB was achieved at the frequency of 80Hz.

Table 8.2 Results of cancellation at different harmonics using LMS offline time-domain technique

Frequency (Hz)	40	80	120
Original pressure pulsation (dB)	-12.1	-8.5	-18.7
After cancellation (dB)	-48	-47.7	-55.3
Total reduction (dB)	35.9	39.2	36.6

Compared to the result plotted in Figure 8.12, the cancellation at the fundamental frequency of 40Hz has been increased by 3dB in this case. That is because a larger convergence rate was used for the adaptive notch filter. Better cancellation performance was achieved as expected. The attenuations at the frequencies of 40Hz, 80Hz and 120Hz were effective and the average cancellation was over 35dB.

8.4.2 FXLMS canceller with FBLMS online identification technique

In this section, the pressure ripple canceller was applied with the FBLMS online identification technique. The length of the identification filter was 256 and the sample time step was 0.2ms. For the single frequency cancellation, the convergence rate of noise canceller was set at 5×10^{-4}. To achieve accurate identification results, a short period (less than 20s) within non-switching condition was introduced, which means the switching valve was driven by +10V and the port was connected to a pressure supply of 25 bar initially. After a short period, the servo valve switched cyclically and alternately to the HP port and LP port, and large pressure pulsations were generated in the system. The frequency responses of the secondary path at 15s and 30s are shown in Figure 8.14 with the comparison of the result from the LMS offline technique. The phases agreed well but amplitude differences occurred at the times of 15s and 30s. The amplitude increased and went towards the result of the LMS offline technique. It is expected that the amplitude would match to the result of the LMS offline technique when the identification filter was completely converged. This experimentally shows that the identification filter is able to obtain accurate secondary path dynamics in real time even within the disturbance from the large pressure ripples.

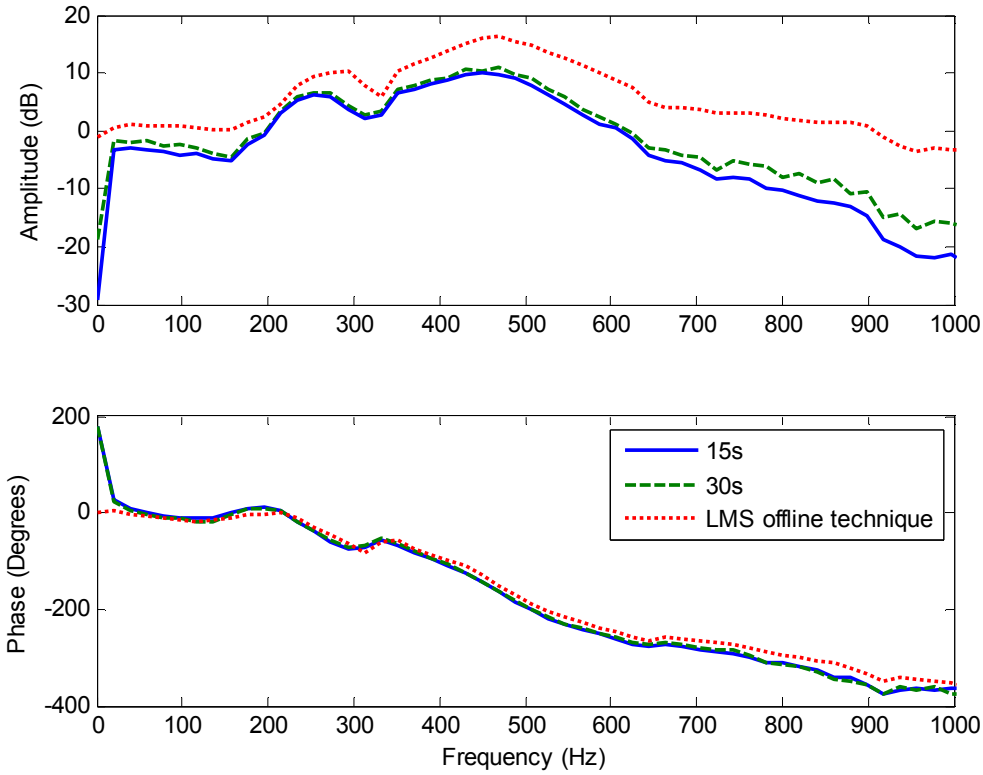

Figure 8.14 Frequency response of secondary path at the different working seconds

The pressure pulsation cancellation is plotted in Figure 8.15 where the amplitude of pressure ripple at the frequency of 40Hz dropped from -12.3dB to -45.3dB. The total cancellation was 33dB which was roughly similar to the result by using the offline identification. However, longer adaptive time was needed in this case because a smaller convergence rate was implemented for system stability for the online system.

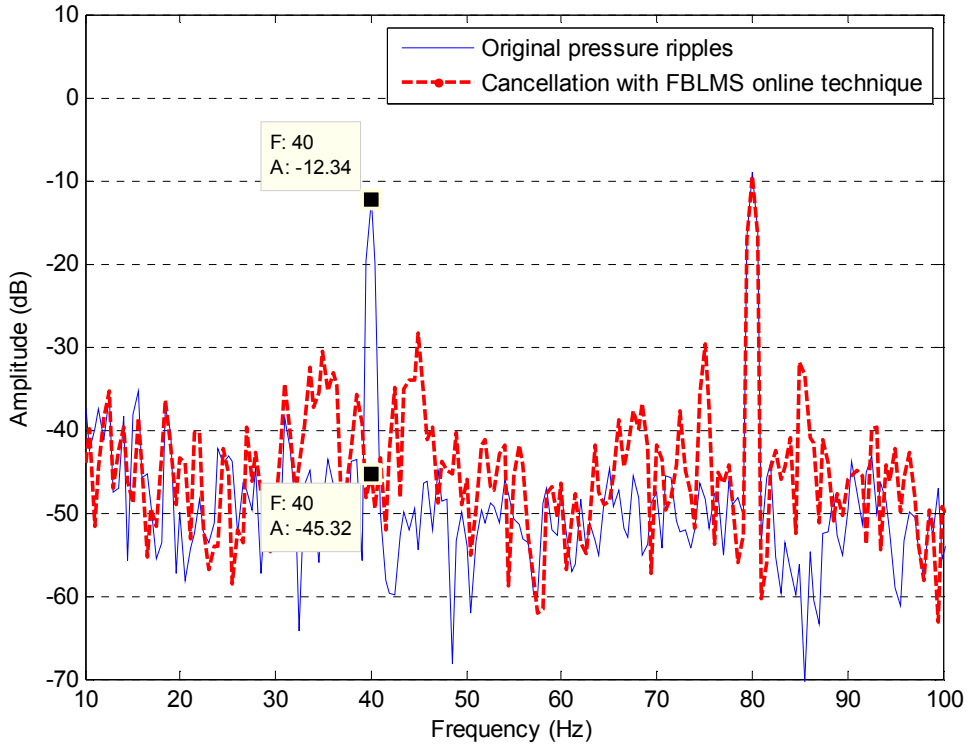

Figure 8.15 Single frequency cancellation using FBLMS online identification technique

For multiple harmonic cancellation, different convergence factors were applied in the parallel adaptive notch filters of different frequencies, as listed in Table 8.3. Three harmonics at 40Hz, 80Hz and 120Hz were considered for cancellation and the results are shown in Figure 8.16. Table 8.4 shows the amplitudes of original pressure and the total cancellation. The maximum cancellation 35.2dB was achieved at the frequency of 80Hz and the average cancellation was over 30dB.

Table 8.3 Convergence rates used for difference harmonics using FBLMS online frequency-domain technique

Frequency (Hz)	40	80	120
Convergence rate μ_c	5×10^{-4}	7×10^{-4}	3×10^{-4}

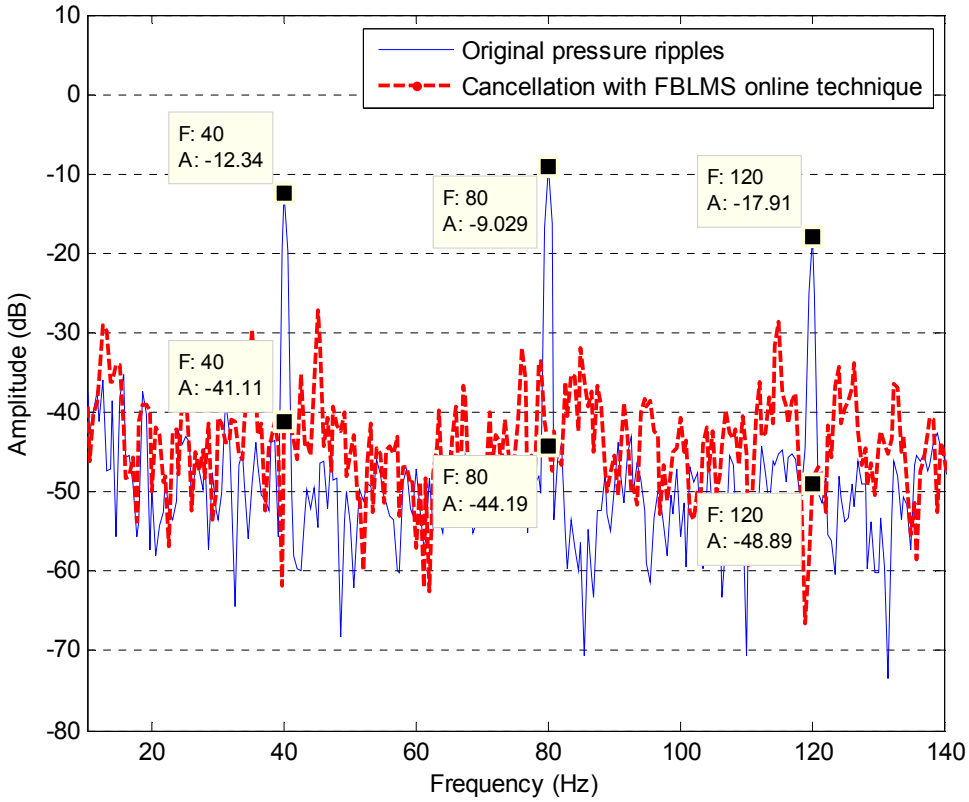

Figure 8.16 Multiple frequency cancellation using FBLMS online identification technique

Table 8.4 Results of cancellation at different harmonics using LMS offline time-domain technique

Frequency (Hz)	40	80	120
Original pressure pulsation (dB)	-12.3	-9.03	-17.9
After cancellation (dB)	-41.1	-44.2	-48.9
Total reduction (dB)	28.8	35.2	31

In conclusion, the designed controller of FXLMS algorithm with the combination of the LMS offline and FBLMS online techniques were successfully validated by experimental tests based on the flow booster rig. Excellence pressure pulsation cancellation was achieved by using these two combinations. The FBLMS online identification method was also validated for its effectiveness for varying system dynamic and accuracy. It can be concluded that the designed controller is suitable and effective for pressure pulsation cancellation of the flow booster.

8.4.3 Stability tests

System stability is very important to real applications. The controller would be useless without good stability even if it has fast response and accurate control performance. In this section, the stability of the controller was tested in terms of transient changes to the switching frequency, switching ratio and system load.

8.4.3.1 Transient switching frequency

The switching frequency of the valve was varied from 40 Hz to 10 Hz over 20s with steps of 10Hz. A step signal was employed to provide the sudden frequency changes at time 5s, 10s and 15s. The flowrate through the loading valve and the piezoelectric valve were 3.0L/min and 3.1L/min respectively. The shorter length of 128 was selected for the FBLMS identification filter and the sample time step was fixed at 0.3ms in dSPACE due to more complex computation process required in this case.

The convergence rates are listed in Table 8.5. Here the convergence rates selected are compromises for different frequencies. For example, the value 2×10^{-3} used in the filter for the fundamental frequency cancellation should satisfy frequencies 40Hz, 30Hz, 20Hz and 10Hz. Varying convergence rate could be considered in order to achieve better noise cancellation, as mentioned in Chapter 7. However, the varying convergence rate can result in the risk of instability. Therefore, in real applications sometime the compromise should be made between the cancellation performance and system stability.

Table 8.5 Convergence rates used for different fundamental frequency and harmonics in experiment

	Fundamental Frequency (Hz)	Harmonics of fundamental frequency (Hz)	
Frequency (Hz)	40	80	120
	30	60	90
	20	40	60
	10	20	30
Convergence rate μ_c	2×10^{-3}	9×10^{-4}	9×10^{-4}

Figure 8.17 shows spectrograms of the FBN cancellation during a frequency transient. The original pressure ripple is plotted in Figure 8.18 (a) and the residual pressure pulsation of system after cancellation is shown in Figure 8.18 (b). The sub-controllers for different frequencies were all fully adapted before the frequency was changed. As can be noted, the noise canceller with three sub-controllers arranged in parallel is able to adapt the changing conditions quickly and obtain good cancellation at the target frequencies.

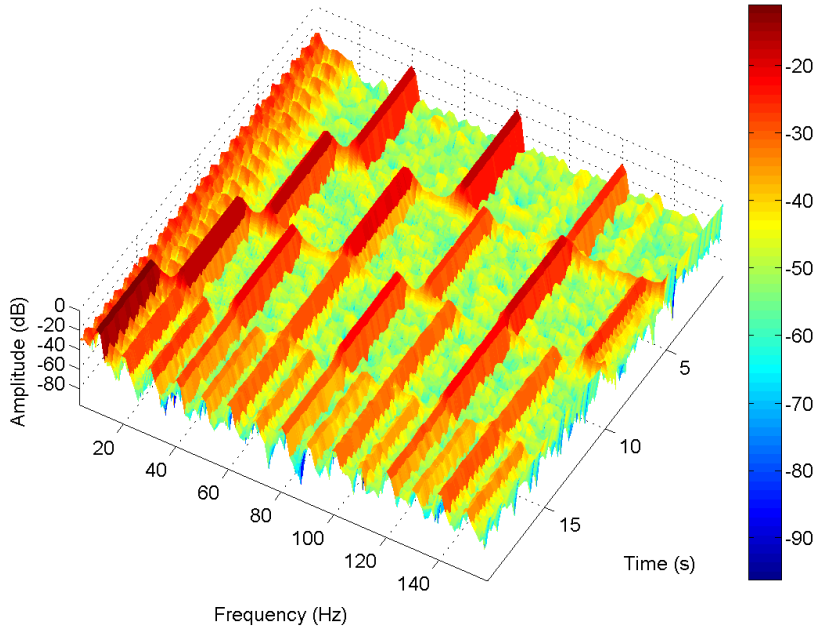

[a] Original pressure pulsation

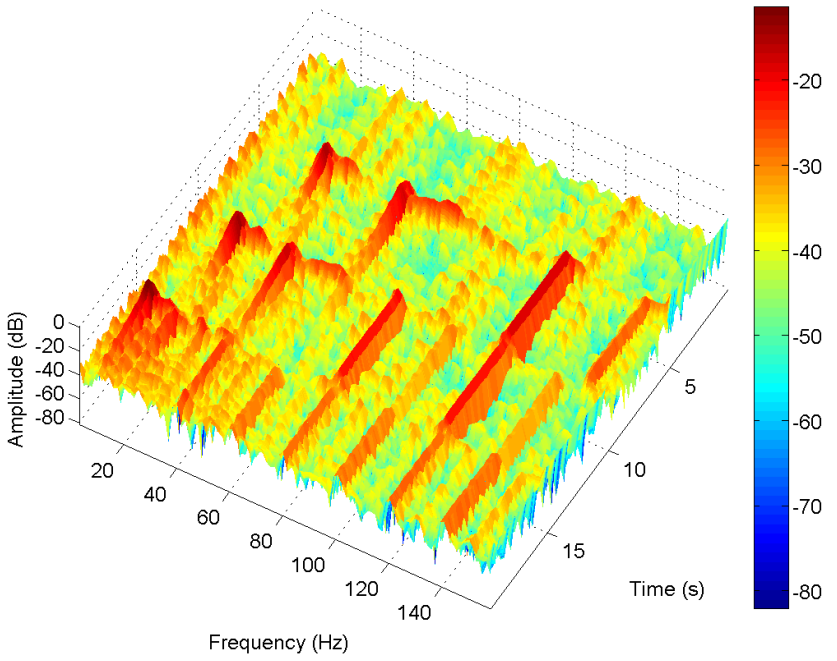

[b] After cancellation

Figure 8.17 Spectrogram showing transient cancellation of 3 harmonics with the fundamental frequency changing from 40Hz to 10Hz over 20s

The controller re-adapted when the switching frequency varied. This is mainly because the frequency of the reference signal for the FXLMS algorithm used for the noise

attenuator changes synchronously based on the switching frequency. It is also because the amplitude of the primary noise changed with different operating conditions. The noise canceller adapts using the updated frequency for the reference signals.

The tap weights of the sub-controllers for fundamental frequency are plotted in Figure 8.18 where two weights w_1 and w_2 of the filter adapted with the changing conditions and obtained their optimal values quickly with a short period of re-adaptation. The designed controller has excellent ability for pressure ripple cancellation and good robustness while adapting with varying switching frequency.

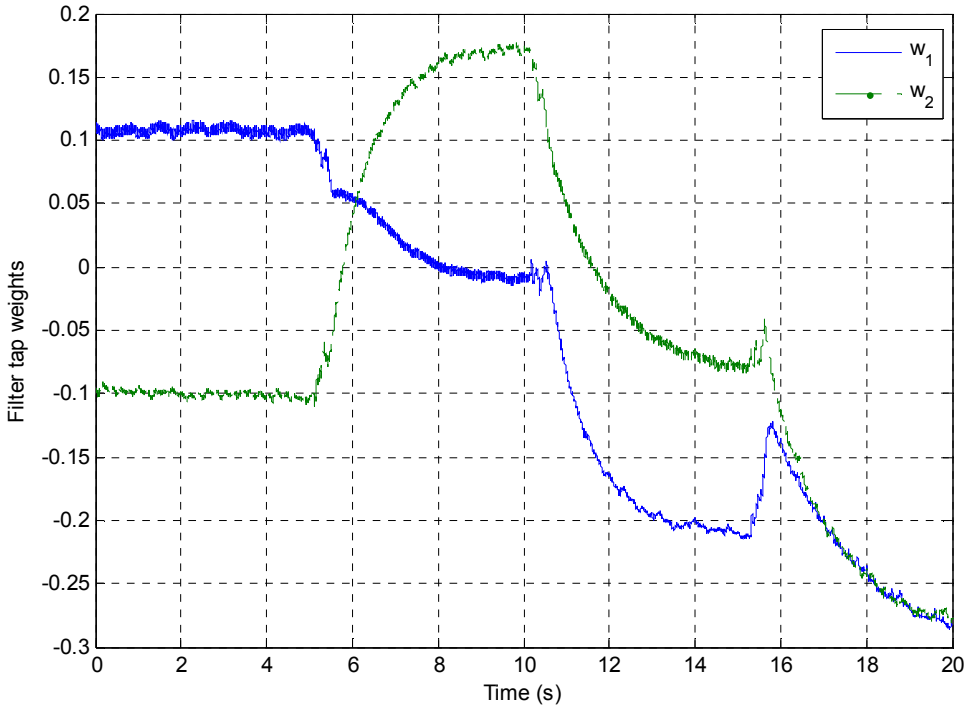

Figure 8.18 Filter tap weights of the sub-controller for fundamental frequency with transient switching frequency

8.4.3.2 Transient switching ratio

The switching frequency of the flow booster was fixed at 40Hz again. The amplitude of pressure ripple at the frequency of 40Hz is plotted in Figure 8.19 (above) where the switching ratio x was changed from 0.1 to 0.9 in steps of 0.2 as shown in Figure 8.19 (bottom). The ratio increased by 0.2 in every 4s and the time was 20s. The flowrates passed through the loading valve and the piezoelectric valve were 3.3L/min and 2.9L/min respectively. The convergence rates used for different harmonics are shown in

Table 9.6. The length of the identification filter was 256 and the sample time step was 0.2ms.

Table 8.6 Convergence rates used for difference harmonics with varying switching ratios

Frequency (Hz)	40	80	120
Convergence rate μ	3×10^{-4}	5×10^{-4}	2×10^{-4}

The cancellation of different ratios at the fundamental frequency is shown in Figure 8.19 (middle) where fast adaptive speed and good cancellation were achieved and the amplitude after cancellation remained around 40dB.

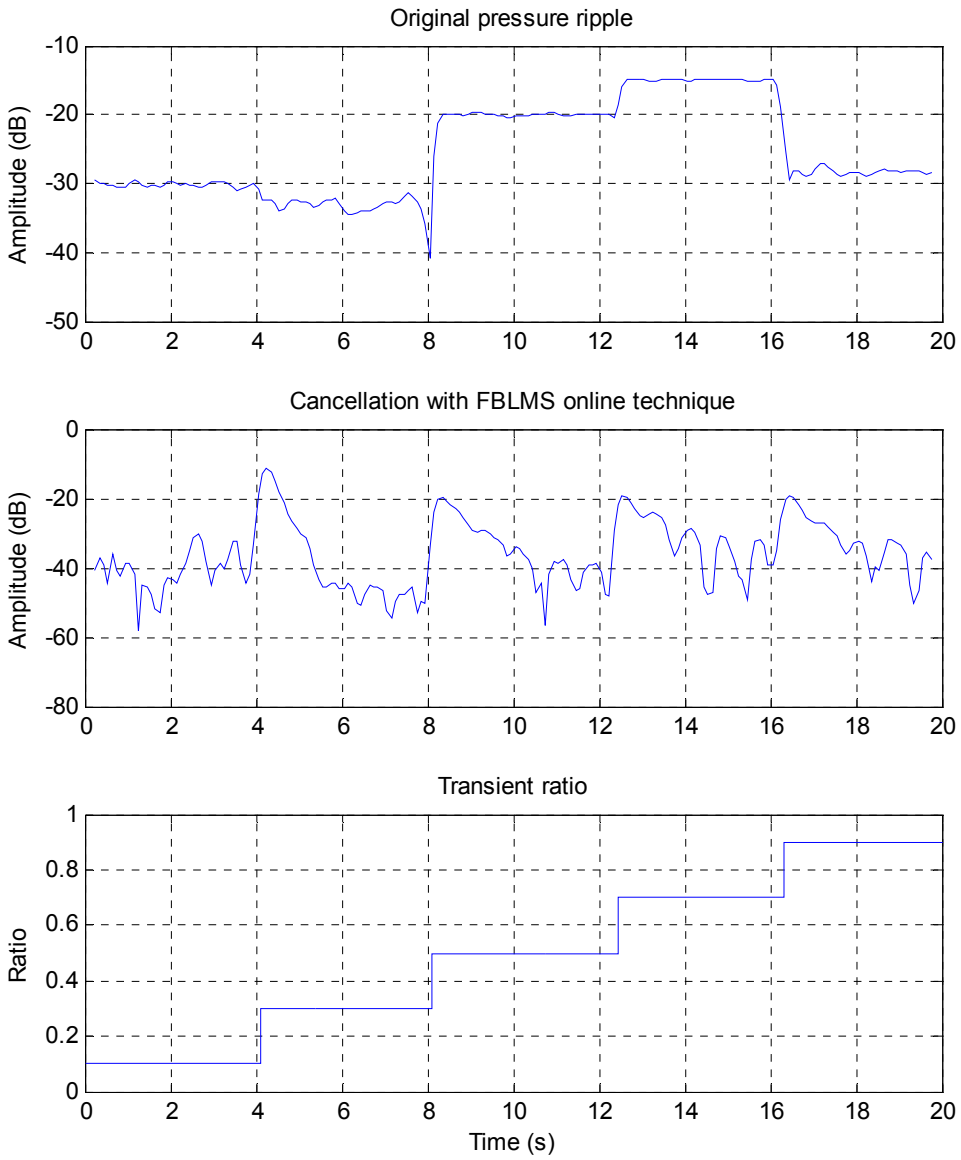

Figure 8.19 Pressure pulsation cancellation at the fundamental frequency with varying switching ratios of the flow booster

The tap weights of different sub-controllers for fundamental frequency are plotted in Figure 8.20 for a good demonstration of adaptive process. As can be seen, the weights adapted quickly and went to the steady state within less than 2s.

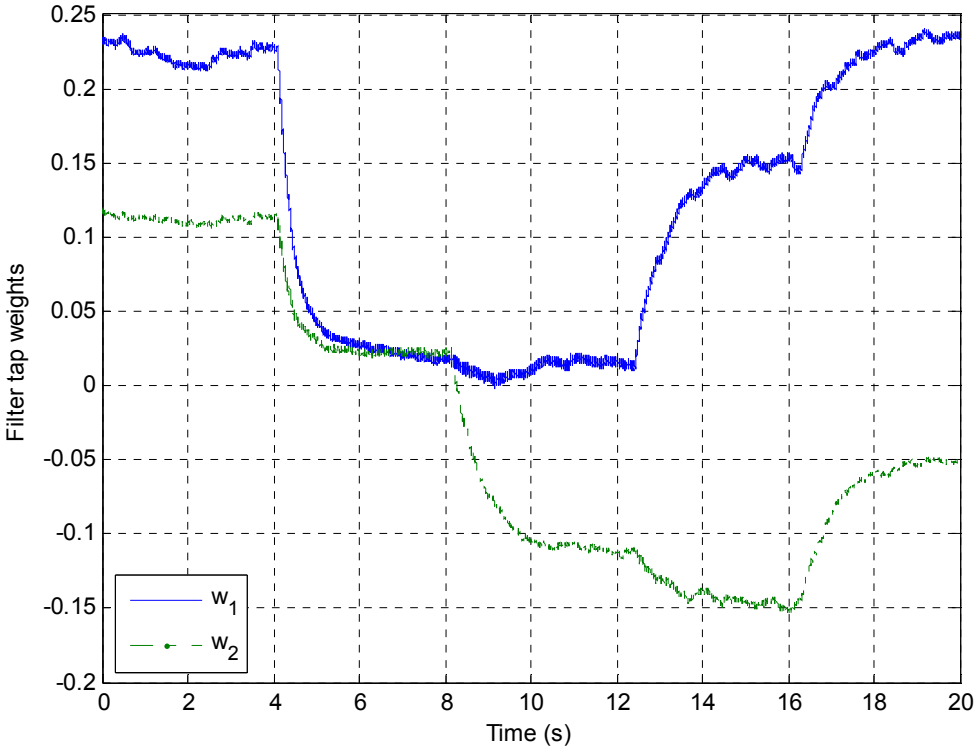

Figure 8.20 Filter tap weights of the sub-controller for fundamental frequency cancellation with varying switching ratio

It can be concluded that the designed noise canceller based on the flow booster is effective for attenuating the pressure pulsation and is able to perform robustly when the high-speed switching valve is subjected to a changing switching ratio.

8.4.3.3 Varying loading

Next the flow booster with the noise canceller was subjected to the varying loading conditions. Because the needle valve was adjusted manually, it was difficult to adjust the opening proportionally. Therefore, instead of the proportional change, the needle valve was changed from open to closed. Specifically, the flowrate through the needle valve varied from 3L/min to 0L/min at 5s, as shown in Figure 8.21 (bottom).

Figure 8.21 shows the amplitude of pressure pulsation before (above) and after cancellation (middle) at the frequency of 40Hz with varying system load. As can be seen, the residual pressure after cancellation maintained at the roughly constant level -45 dB with the changing load. The total cancellation was approximately 25 dB. It can be

said that the designed controller is effective and robust under suddenly changing loading conditions, which can occur in real applications.

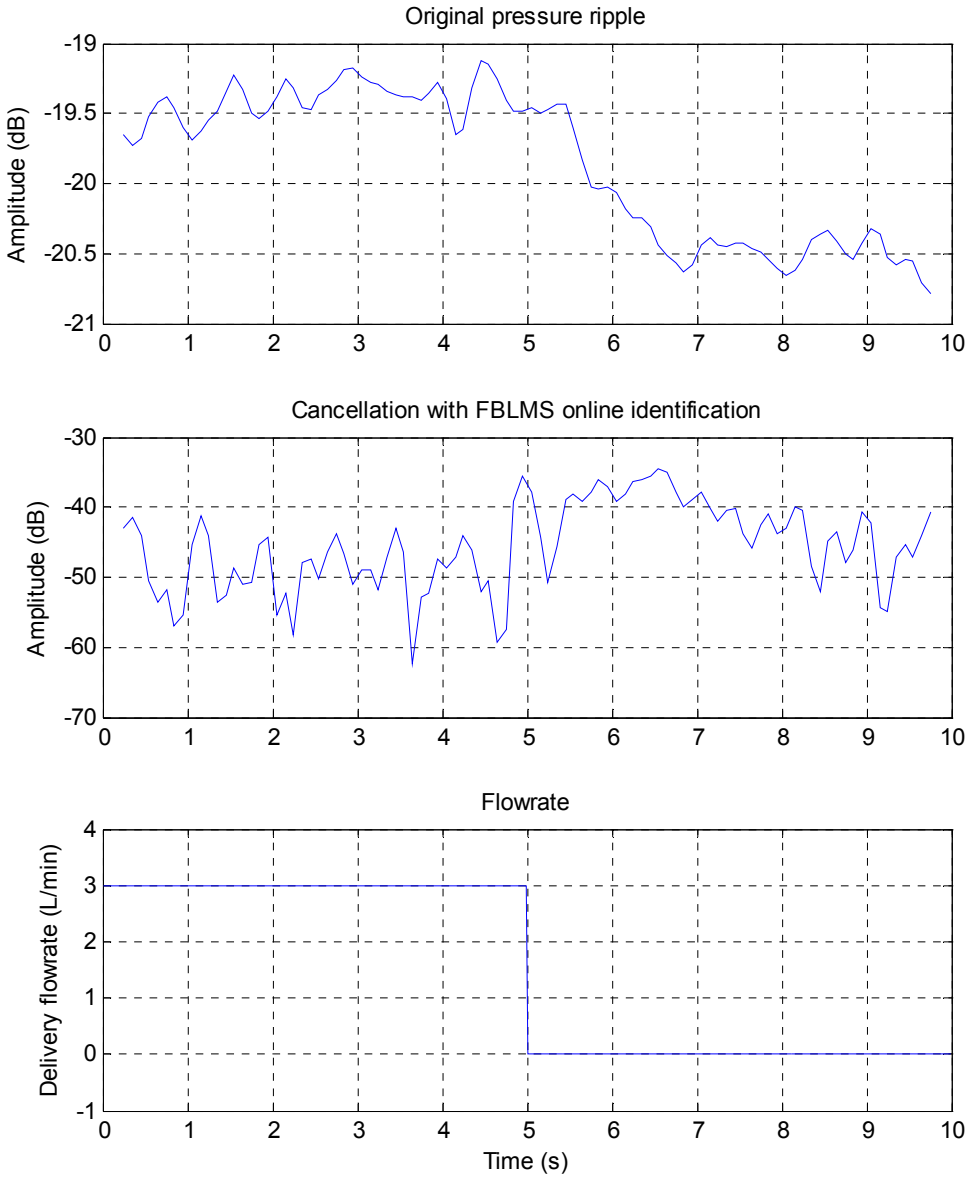

Figure 8.21 Pressure pulsation cancellation at the frequency of 40Hz with varying system load

In conclusion, the designed controller was implemented for single and multiple harmonics attenuation of FBN based on the flow booster rig. Excellent cancellation (around 35dB) was achieved within the noise controller and the proposed by-pass control structure. The investigation of effects from the changing switching frequency, the switching ratio and the system loading was researched based on experimental work.

According to the results, it can be concluded that the designed controller is effective for FBN cancellation and robust under varying system conditions.

8.5 Experiments of pressure pulsation cancellation on flow booster system with in-series controller

In this section, the in-series structure is implemented for pressure pulsation cancellation based on the flow booster. The performance of noise attenuator arranged in line with the main rig using both the LMS offline and FBLMS online identification techniques is presented.

8.5.1 FXLMS canceller with LMS offline identification technique

The high supply and low supply pressures of rig were fixed at 25 bar and 20 bar respectively. Figure 8.22 shows the single harmonic pressure pulsation cancellation using the LMS offline technique. The servo valve switched fully open to the high supply and low supply ports using 50% duty cycle pulse signal with the amplitude of 10V. The loading flowrate was 3L/min at the switching condition. The length of the filter used for identification was 512 and the sample time step was 0.1ms. The impulse response of secondary path when the noise canceller was arranged in line with the main rig is plotted in Figure 8.3 and the frequency response is shown in Figure 8.23.

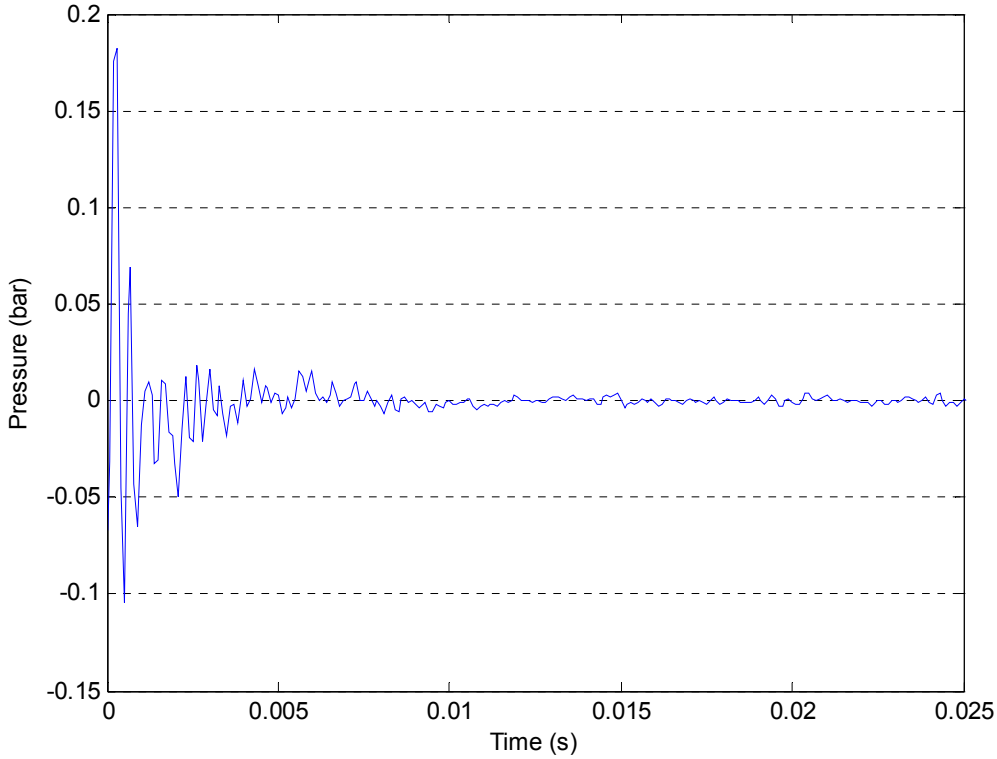

Figure 8.22 Impulse response of secondary path based on the in-series structure

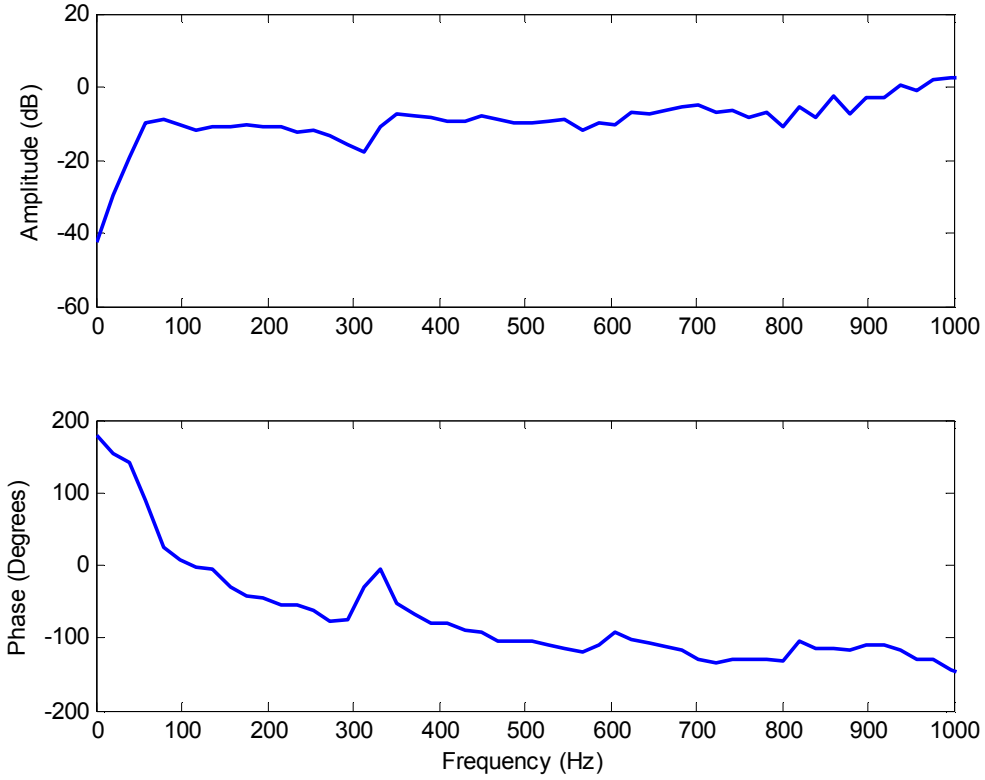

Figure 8.23 Amplitude and phase responses of secondary path in in-series structure

For the noise cancellation filter, the convergence rate for the fundamental frequency cancellation was fixed at 2×10^{-4}. Figure 8.24 shows the amplitude of pressure ripples before and after cancellation. It can be seen that the amplitude decreased from 10.6 dB to -19.3dB.

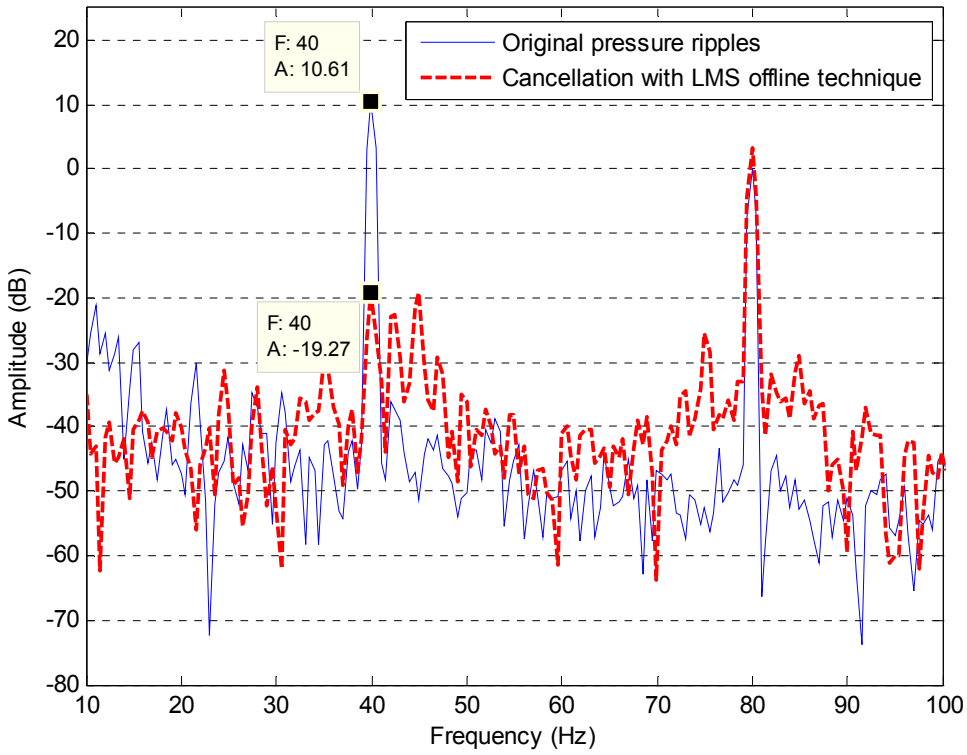

Figure 8.24 Single frequency cancellation by using LMS offline technique using the in-series structure

For multiple harmonic cancellation, different convergence factors were applied in the paralleled adaptive notch filters of the frequencies 40Hz, 80Hz and 120Hz, as listed in Table 8.7. The opening of the loading valve was maintained the same as in the single frequency cancellation test, but the flowrate passing through was slightly higher at 3.2L/min due to the decreasing viscosity in the test rig.

Table 8.7 Convergence rates used for different harmonics with the LMS offline identification method

Frequency (Hz)	40	80	120
Convergence rate μ	6×10^{-4}	6×10^{-5}	6×10^{-5}

Figure 8.25 shows the cancellation at the harmonics of 40Hz, 80Hz and 120Hz based on the in-series structure and Table 8.8 lists the amplitude of pressure ripple before and after cancellation. It can be seen that the maximum cancellation of 49dB occurred at the frequency of 120Hz. The average cancellation was over 30dB. It was also found that the loading flowrate dropped to 2.7 L/min from 3.2L/min with the use of the pressure ripple canceller. This can be explained by the inaccuracy of the downstream flowmeter or the non-linear characteristics of the system.

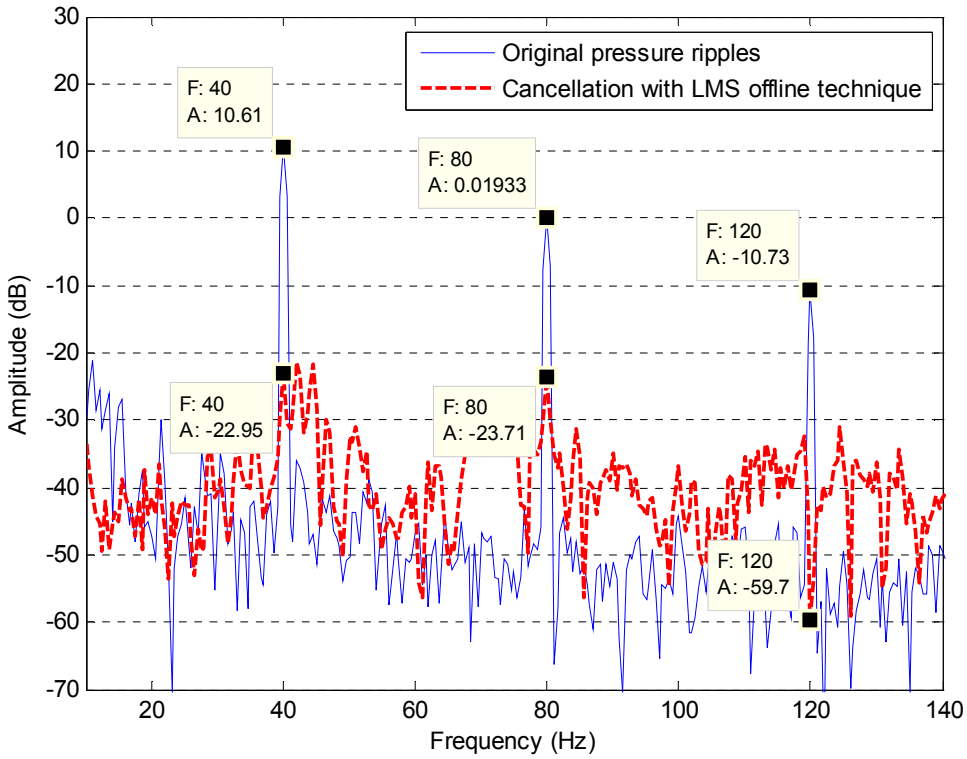

Figure 8.25 Multiple frequencies cancellation using LMS offline technique with in-series structure

Table 8.4 Results of cancellation at different harmonics using LMS offline time-domain technique

Frequency (Hz)	40	80	120
Original pressure pulsation (dB)	10.6	0.02	-10.7
After cancellation (dB)	-23.0	-23.7	-59.7
Total cancellation (dB)	33.6	23.7	49

8.5.2 FXLMS canceller with FBLMS online identification technique

The pressure ripple canceller was applied with FBLMS online identification technique with the in-series test rig structure in this section. For single frequency cancellation, the convergence rate of noise canceller was set at 5×10^{-3}. As in the by-pass structure tests, a short period (20s) with non-switching condition was introduced to achieve accurate identification of the secondary path. The switching valve was driven by +10V and the port was connected to a 25 bar supply pressure in the initial conditions. After that, the high-speed valve switched and the controller switched on.

The frequency responses of the secondary path at 15s and 30s are shown in Figure 8.26 where reasonable dynamics were achieved. The identification filter obtained the accurate results in real time even with the disturbance from the large pressure ripples at 20s. Good agreement of phases was obtained at 15s and 30s. However, the identification filter was not completely converged on the comparison of the characteristics of the amplitude at 30s with that achieved by using LMS offline identification method. Longer experimental time would be needed for more accurate secondary path dynamics. The upstream boundary condition would change with and without the high-speed valve switching. It may cause different characteristics of the secondary path. However, the phases were very similar at the low frequency range as can be seen in Figure 8.26. Good system stability is expected due to the stable phase characteristics.

The length of the identification filter was 256 and the sample time step was 0.2ms.

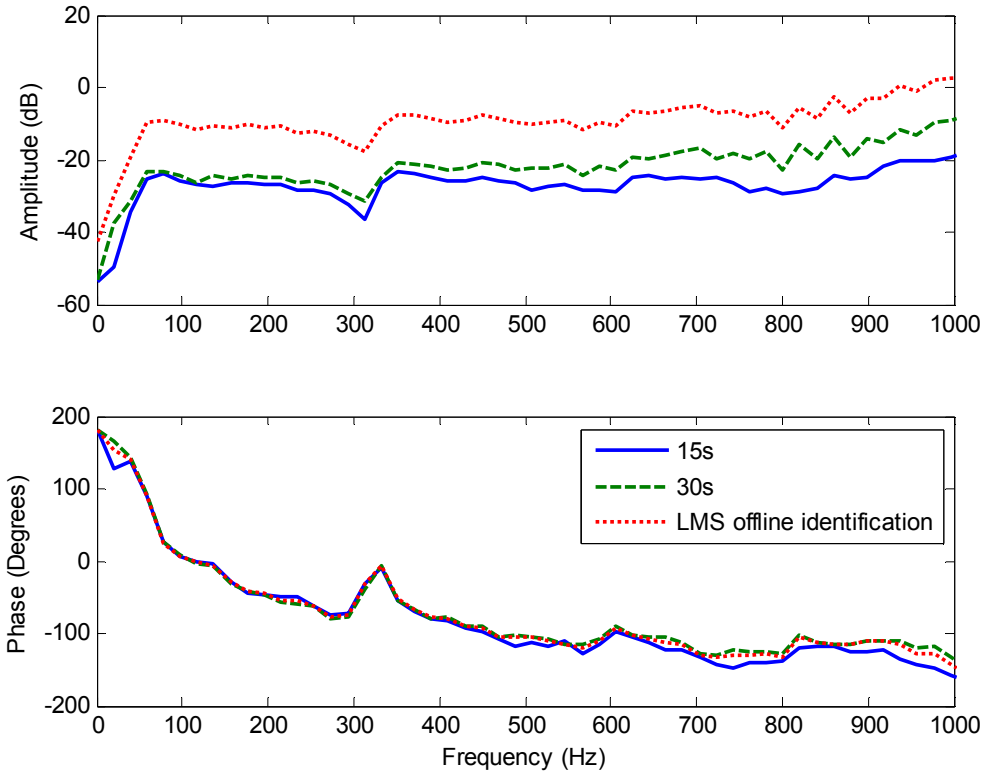

Figure 8.26 Frequency response of secondary path at different working times

The pressure ripple cancellation is plotted in Figure 8.27 where the amplitude of the FBN at the frequency of 40Hz dropped from 11.3dB to -27.0dB. The total cancellation was 38.3dB which was slightly higher than the result achieved from the LMS offline identification method. This was because a higher convergence rate was chosen for the cancelling filter compared with the value used in Figure 8.24. The convergence rate chosen was based on the estimation of the online identification result. For example, the cancellation was achieved at 30s as plotted in Figure 8.27 and at the same second the amplitude achieved was far less than the actual amplitude. In this case, the larger convergence factor of the cancelling filter can be selected and applied for faster adaptive speed and better attenuation performance. However, this can only used when the secondary path dynamic could be expected. It may result in instability if the convergence rate was larger than its optimum value. One solution that may be effective for this situation is using varying convergence rate in the adaptive process. A larger convergence rate could be used for lower amplitude characteristics normally at the beginning of the identification process and a smaller convergence factor could be applied when the identification filter completely converged with the output of the actual

amplitude. This may need to have online measurement or detection of the amplitude of the secondary path.

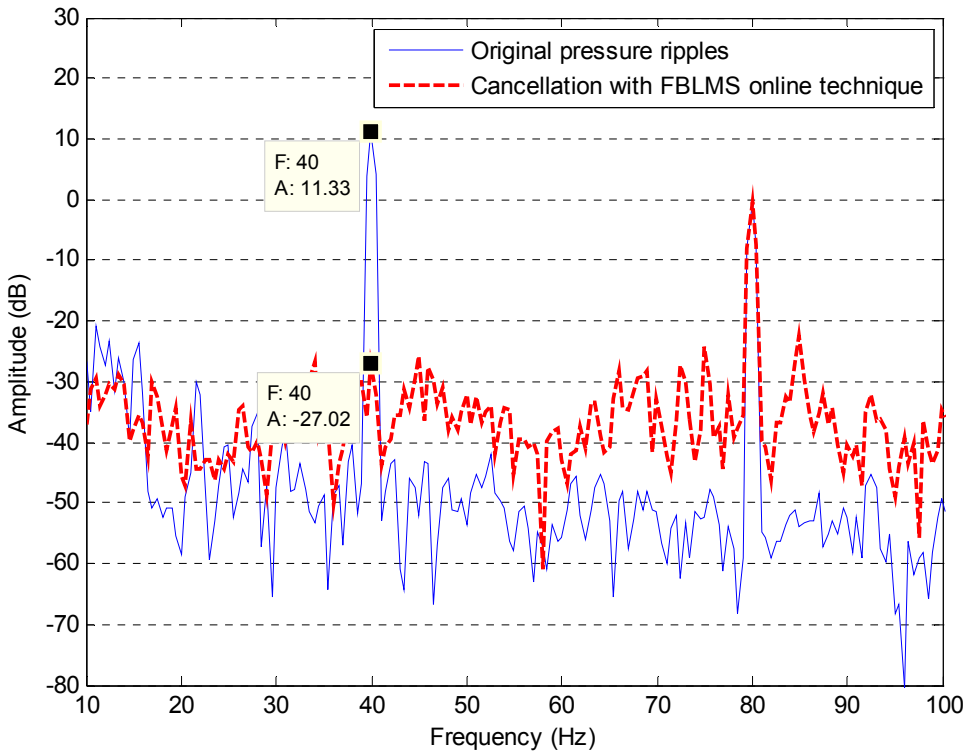

Figure 8.27 Single frequency cancellation by using FBLMS online identification technique using the in-series structure

For multiple harmonics cancellation, different convergence factors were applied in the paralleled adaptive notch filters of different frequencies, as listed in Table 8.5. Three harmonics 40Hz, 80Hz and 120Hz were considered in cancellation and the results are plotted in Figure 8.28. Table 8.6 shows the amplitudes of original pressure and the total cancellation. The loading flowrate was varied from 3.2/min to 2.8L/min after switching on the noise attenuator.

Table 8.5 Convergence rates used for different harmonics by using FBLMS online frequency-domain technique

Frequency (Hz)	40	80	120
Convergence rate μ	6×10^{-3}	6×10^{-3}	6×10^{-3}

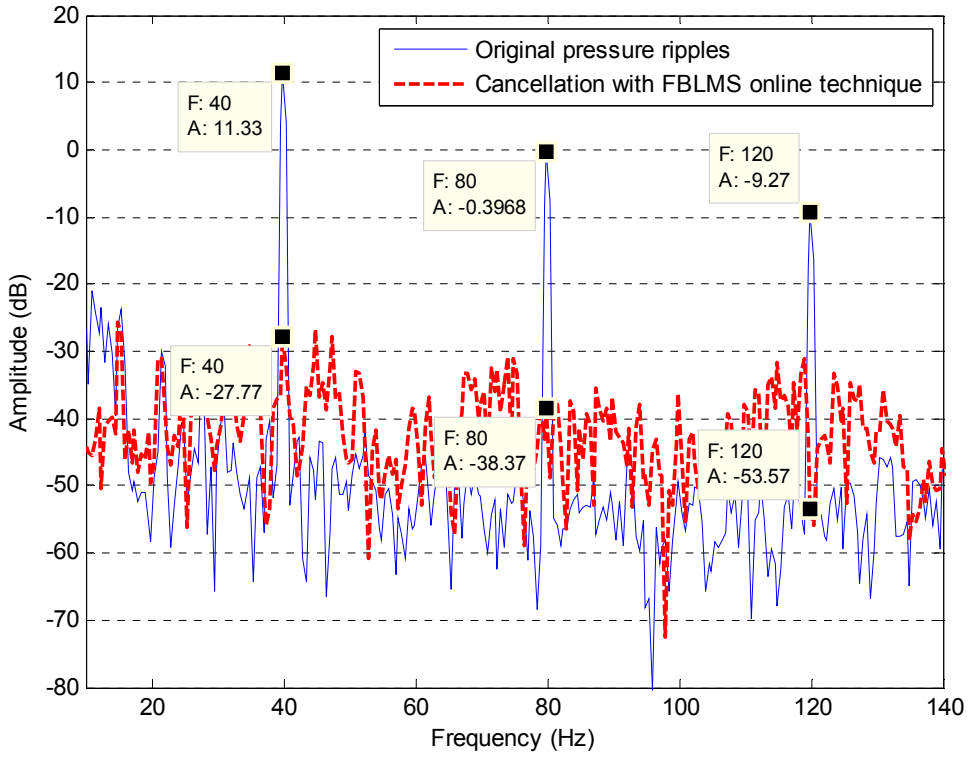

Figure 8.28 Multiple frequencies cancellation by using FBLMS online identification technique using the in-series structure

Table 8.6 Results of cancellation at different harmonics using LMS offline time-domain technique

Frequency (Hz)	40	80	120
Original pressure pulsation (dB)	11.3	-0.40	-9.3
After cancellation (dB)	-27.8	-38.4	-53.6
Total cancellation (dB)	39.1	38	44.3

In conclusion, the designed controller of FXLMS algorithm with the combination of the LMS offline and FBLMS online techniques were successfully validated by experimental tests based on the flow booster rig with the in-series structure. Excellent pressure pulsation cancellation was achieved by using these two combinations. The FBLMS online identification method was validated for its effectiveness for varying system dynamic and accuracy. It can be concluded that the designed controller with the in-series arrangement of the flow booster is effective for system pressure pulsation cancellation.

8.5.3 Stability tests

As was done in the rig using the by-pass structure, the system stability was investigated in terms of the transient changes to the frequency, switching ratio and system load.

8.5.3.1 Transient switching frequency

The switching frequency of the valve was varied from 40 Hz to 10 Hz over 20s with the step of 10Hz. A step signal was employed to provide the sudden frequency changes at time 5s, 10s and 15s. The flowrates passed through the loading valve and the piezoelectric valve were 2.7L/min and 3.0L/min respectively. The length of the identification filter was 128 and the sample time step was fixed at 0.3ms.

The convergence rates were listed in Table 8.7.

Table 8.7 Convergence rates used for different fundamental frequencies and harmonics in experiment

	Fundamental Frequency (Hz)	Harmonics of fundamental frequency (Hz)	
Frequency (Hz)	40	80	120
	30	60	90
	20	40	60
	10	20	30
Convergence rate μ	5×10^{-2}	7×10^{-3}	7×10^{-3}

Figure 8.29 shows spectrograms of the pressure pulsation cancellation during a frequency transient. The original pressure ripple is plotted in Figure 8.29 (a) and the residual pressure pulsation of system after cancellation is shown in Figure 8.29 (b). The sub-controllers for different frequencies were all fully adapted before the frequency was changed. As can be noted, the noise canceller with three sub-controllers arranged in parallel is capable of adapting to the changing conditions quickly and obtaining good cancellation at the target frequencies.

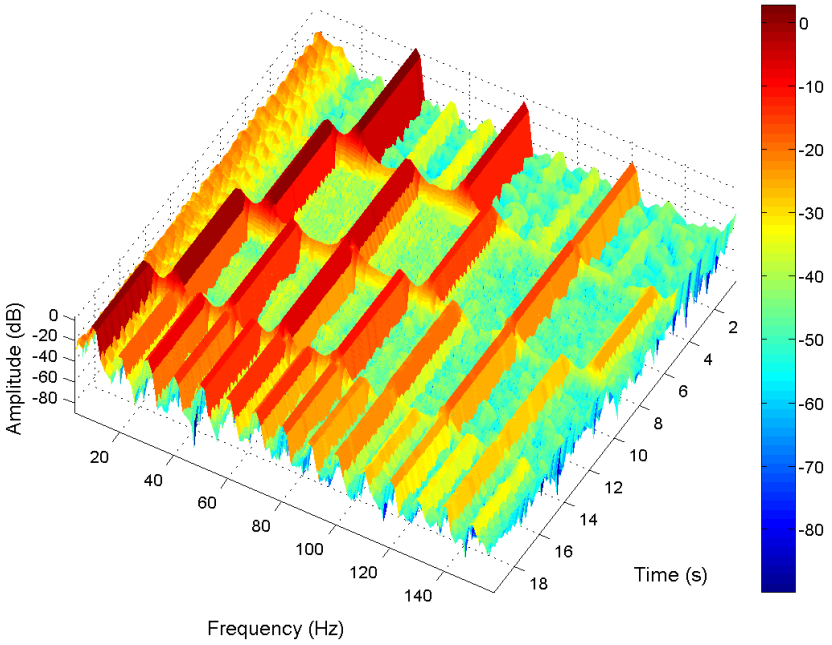

[a] Original pressure pulsation

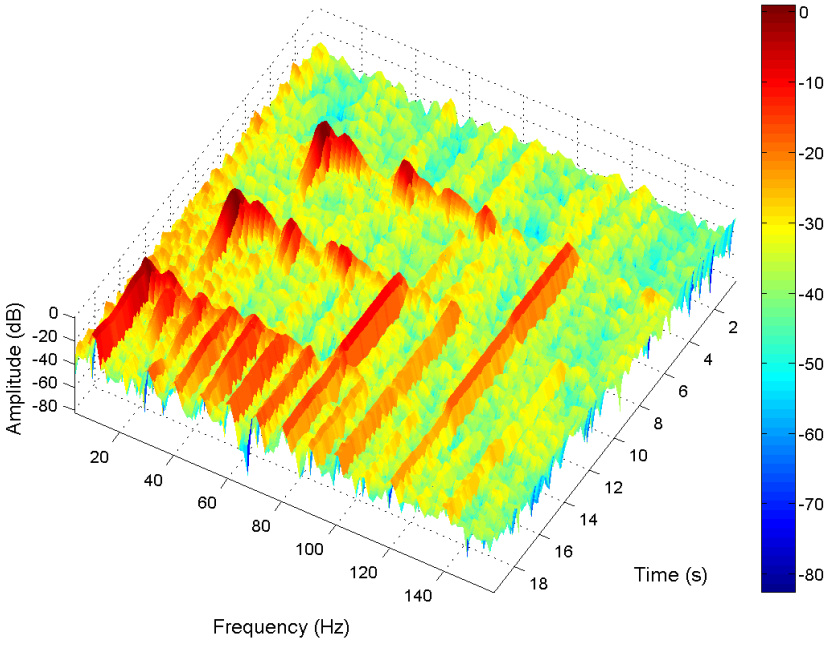

[b] After cancellation

Figure 8.29 Spectrogram showing transient cancellation of 3 harmonics with the fundamental frequency changing from 40Hz to 10Hz over 20s

Similar to the tests based on the by-pass structure, the controller re-adapted when the switching frequency varied. The filter tap weights of the sub-controllers for fundamental

frequency are plotted in Figure 8.30 where two weights w_1 and w_2 of the filter adapted with the changing conditions and obtained their optimal values quickly with a short period re-adaptation. The designed controller has excellent ability for pressure ripple cancellation and good robustness for adapting with the varying switching frequency.

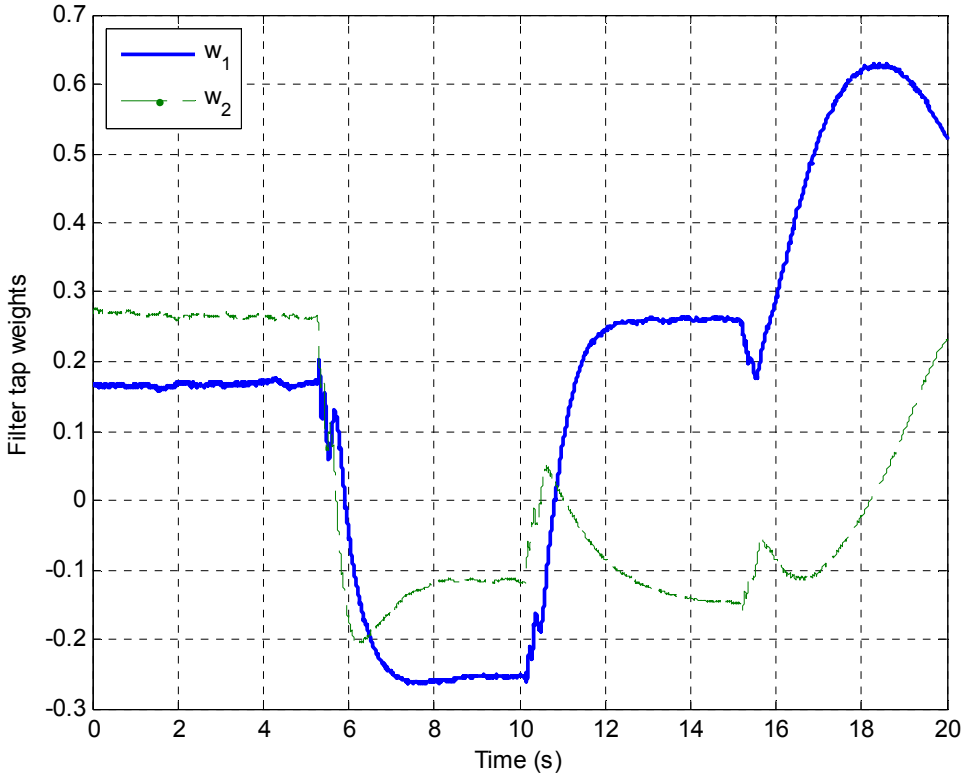

Figure 8.30 Filter tap weights of the sub-controller for fundamental frequency with the transient switching frequency based on the in-series structure

The cancellation at the frequency of 10Hz was significantly poorer compared with the cancellation at other frequencies, as shown in Figure 8.29. It was also can be seen in Figure 8.30 that the weights w_1 and w_2 can not obtain a steady or optimum value in the time period from 16s to 20s. This resulted in the noise attenuator performing poor cancellation. The frequency response of the secondary path is plotted in Figure 8.31 where the range of the frequency was from 0Hz to 200Hz. In order to achieve more information of the secondary path, the impulse response was extended by adding a zero vector with length of 768 at the end assuming the identification filter was completely converged.

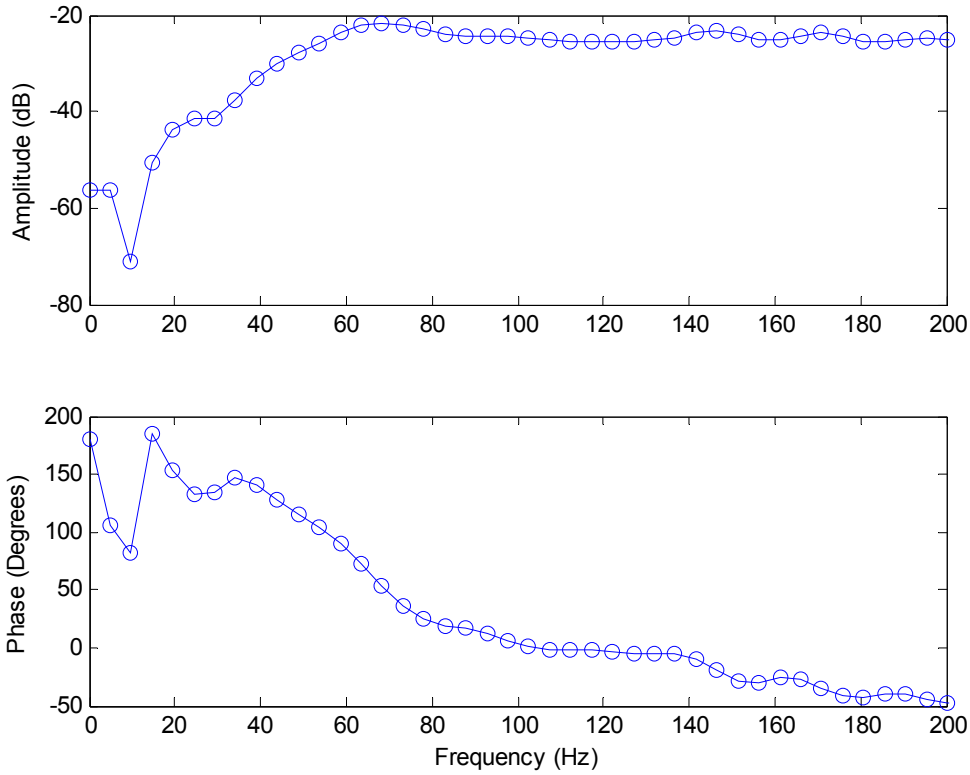

Figure 8.31 Frequency response of secondary path plotted from 0Hz to 200Hz

It can be seen that an anti-resonance exists around the frequency of 10Hz. This could cause the poor response of the noise canceller at these specific frequencies. Therefore, the designed controller became less effective for pressure pulsation cancellation due to the dynamics of the secondary path. A larger convergence rate setting could be helpful to solve this problem but it also may result in instability when the system switching frequency increased. This also may be the case of this specific test rig or structure.

8.5.3.2 Transient switching ratio

The switching frequency of 40Hz was re-applied to the flow booster rig. Figure 8.32 shows the frequency responses of the secondary path with and without the noise canceller at the beginning of the experiments. The amplitude of pressure ripple at the frequency of 40Hz is plotted in Figure 8.33 (top) where the switching ratio x was changed from 0.1 to 0.9 in steps of 0.2 as shown in Figure 8.33 (bottom). The ratio increased by 0.2 in every 4s and the time was 20s. The flowrates through the loading valve and the piezoelectric valve were 3.3L/min and 2.9 L/min respectively. The convergence rates used for different harmonics are shown in Table 8.8. The length of the identification filter was 256 and the sample time step was 0.2ms.

Table 8.8 Convergence rates used for difference harmonics with varying switching ratios

Frequency (Hz)	40	80	120
Convergence rate μ_c	5×10^{-2}	3×10^{-2}	3×10^{-2}

The convergence rates selected were based on the characteristics of the secondary path. Larger values can be used at the first few seconds due to the low amplitude obtained from the identification filter.

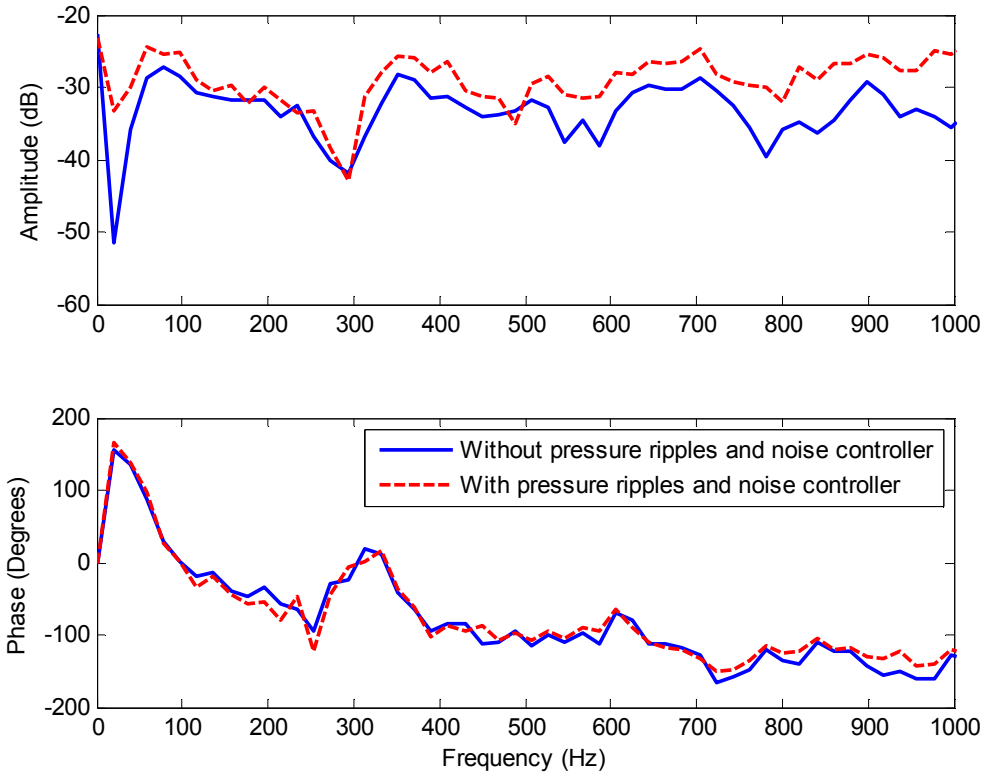

Figure 8.32 Amplitude and phase characteristics of the secondary path using FBLMS online technique in the first few seconds

The cancellation of different ratios at the fundamental frequency is shown in Figure 8.33 (middle) where fast adaptive speed and good cancellation were achieved and the amplitude after cancellation remained around -40dB.

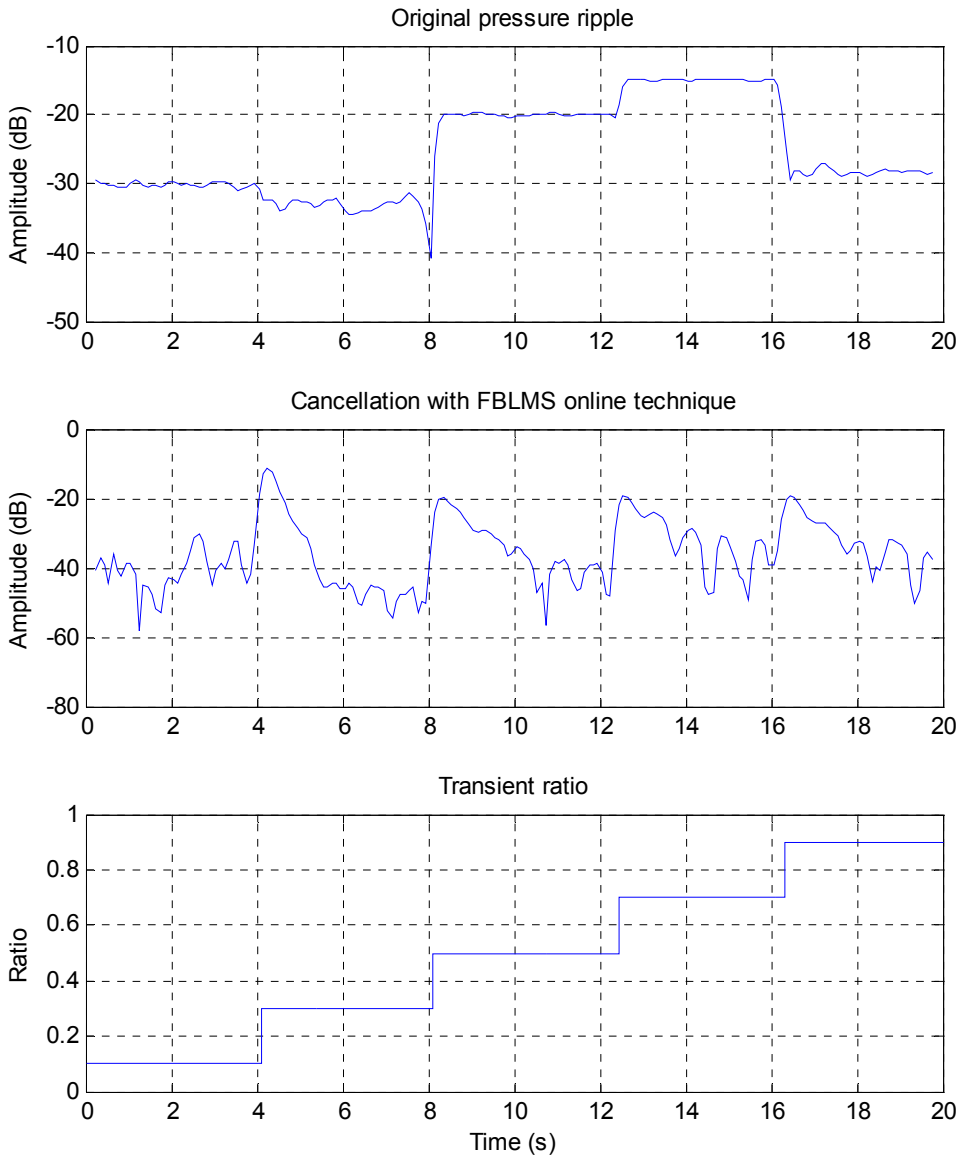

Figure 8.33 Pressure pulsation cancellation at the fundamental frequency with varying switching ratios of the flow booster using in-series structure

The tap weights of different sub-controllers for fundamental frequency are plotted in Figure 8.34 where the weights adapted quickly and went to the steady state or their optimum values within 1s.

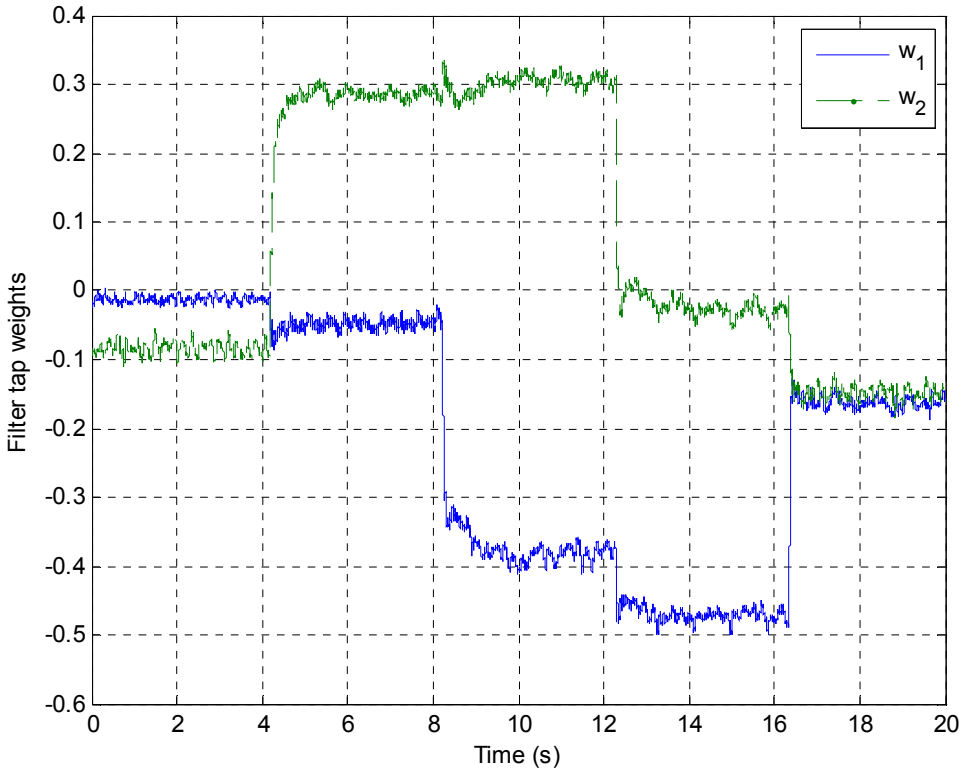

Figure 8.34 Filter tap weights of the sub-controller for fundamental frequency cancellation with varying switching ratio

In conclusion, the designed noise canceller which was arranged in line with the flow booster is effective to attenuate the pressure pulsation and is able to perform robustly when the fast-speed switching valve is subjected to changing switching ratio.

8.5.3.3 Varying loading

Next the flow booster with the noise canceller was subjected to varying loading conditions. The needle valve opening was changed manually from its open condition to a nearly closed condition. Specifically, the flowrate passing through the needle valve varied from 3L/min to 1.2L/min at 5s, as shown in Figure 8.35 (bottom).

Figure 8.35 shows the amplitude of pressure pulsation before (above) and after cancellation (middle) at the frequency of 40Hz with varying system load. It can be seen that the residual pressure after cancellation maintained at the roughly constant level -45dB with the changing load. The total cancellation was approximately 45dB. The

designed controller arranged in line with the main rig is effective and robust under sudden changing loading conditions, which may commonly occur in real applications.

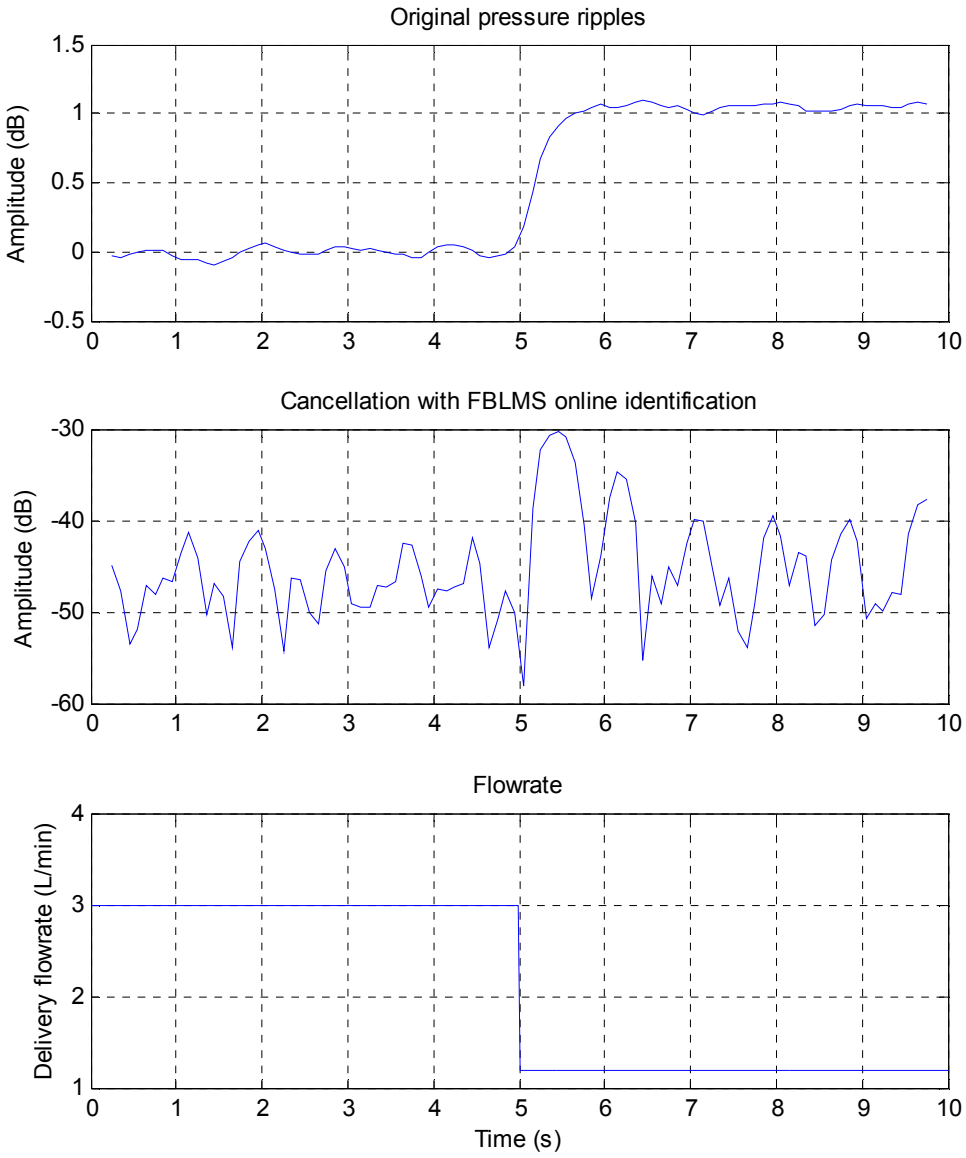

Figure 8.35 Pressure pulsation cancellation at the frequency of 40Hz with varying system load

In conclusion, the system stability has been investigated in terms of the transient switching frequency, the changing switching ratio and changing loading of system. Fast response and good control performance were achieved. It was also proved that the in-series arrangement is able to obtain good pressure pulsation cancellation.

8.5 Discussion

The designed noise attenuator has been implemented for pressure pulsation cancellation based on the flow booster within the by-pass and in-series structures in experiments. The piezoelectric valve is able to provide the accurate control signal to the hydraulic test rig and excellent cancellation was achieved.

However, the following statements need to be considered:

- With the in-series structure, the working supply pressure can be not quite high enough due to the limitation of the piezoelectric valve itself. The high supply pressure used was 25 bar and the low supply pressure was 20 bar in all experiments. A valve with better performance may be helpful for higher pressure testing.
- Small pressure differences of 5 bar and low loading flowrate of 3L/min were used in the experiments in order to avoid system cavitation. This restricts of system characteristics changes. For example, it was difficult to do the experiments with dramatic loading changes which may cause instability of the controller.
- The designed controller with only three sub-controllers arranged in parallel was compiled and run successfully with the dSPACE 1005 control board. The number of the sub-controllers is dependent on the computation speed of the hardware.
- The switching valve which has been used is not quite fast enough with a maximum switching frequency of 40Hz. The dSPACE 1005 control board speed is another limitation, this would be more significant with a faster valve.
- A faster valve which can provide very fast switching frequency could be useful for further testing with a wider cancelled frequency range. Also it would provide less resistance for this switched hydraulic system.
- The by-pass structure could be widely and successfully used for pressure pulsation cancellation in hydraulic systems. It has less restriction compared with the requirements of the in-series structure.
- It is difficult to estimate the performance of the piezoelectric valve when the oil temperature increased. But different characteristics of the valve can be noticed in a few seconds within the high temperature. A temperature sensor is used to protect the actuator.

8.6 Concluding remarks

The designed noise attenuator has been implemented for pressure pulsation cancellation based on a flow booster with by-pass and in-series structures. The system performance was investigated via experiments in terms of attenuation ability, robustness and stability when it was subjected to the varying working conditions. Results show excellent cancellations were achieved and the controller is capable of performing robustly with changing conditions. It can be concluded that the designed controller is able to obtain a good pressure pulsation cancellation effectively and robustly based on the SIHS.

9 Conclusions and future work

9.1 Conclusions

The work described in this thesis forms a successful development and implementation study for the control of pressure pulsation in the switched inertance hydraulic system. The research was supported by Centre for Power Transmission and Motion Control (PTMC).

The proposed controller has been successfully tested with an experimental vibration rig, where it has been shown to be capable of controlling a single harmonic and multiple harmonics of vibration. Moreover, it performed stably and robustly in response to transient changes to the fundamental frequency.

It has also been initially and successfully implemented with a flow booster where it was shown that excellent cancellations of pressure pulsation can be achieved using by-pass and in-series arrangements of the controller.

A novel method was also developed for the measurement of unsteady flowrate along the pipe. It is very useful to estimate the dynamic flow of the piping system. Good results were obtained using this technique on the pipe rig.

This thesis details work conducted to develop an effective controller for active FBN cancellation. The FXLMS algorithm was applied in the filter for noise attenuation together with the adaptive LMS filter for system identification. About 40dB cancellation of FBN can be achieved according to the experiments. However, some concerns still need to be presented here:

- The controller was composed of two filters, one for system identification and the other one for noise cancellation. Different lengths and convergence rates of the filters were selected. For narrowband noise cancellation, like FBN, normally the lengths of the filter used for identification is longer than the notch filter used for noise cancellation. Also there may be a large difference in value between the

convergence rates of identification μ_i and of cancellation μ_c. Careful selection should be made for choosing the convergence rates for each filter.

- For online identification within FBLMS algorithm, an unrelated white noise was required in the process which may reduce the overall effectiveness of the attenuation and increase the background noise.
- The identification process is computationally intensive due to the long length filter.
- For noise cancellation filter, the frequency of the reference signal was used from the system switching frequency directly. No extra device was used for detecting the frequency for the reference signal as was done in the vibration rig. This effectively eliminates the frequency mismatch problem which may occur in the system and which would result in poor cancellation performance. However, in a more general case for FBN cancellation, the frequency of FBN may still need to be estimated.
- The controller is able to attenuate the FBN for the switched inertance hydraulic system with by-pass and in-series structures. From the simulations and experiments, it can be concluded that the by-pass structure can be more widely and effectively used for FBN cancellation based on a flow booster compared with the in-series structure.
- In experiments, the rig sometimes exhibited non-linear behaviour which may be caused by the dynamic system and the secondary path actuator. This may be the reason for less FBN cancellation achieved in experimental tests compared with simulations.
- Cavitation from the piezoelectric valve itself may also increase the system background noise. An accumulator arranged at the downstream of the piezoelectric valve could be helpful for reducing these effects.
- Regarding the hardware, the dSPACE 1005 control board is able to present the principle of the control method and the controller performance. However, only three harmonics were considered in experimental tests due to its computational limitations.

It can be concluded that the active noise control method is feasible and effective for attenuating pressure pulsations in hydraulic systems. It has the advantage of being effective for low frequency cancellation compared with passive attenuation methods which may be only effective in certain frequency ranges. Secondly, a well-designed

active attenuator can eliminate the bulky size and weight problems caused by the passive control methods. Thirdly, system dynamics would not be impaired by using the active device, whilst the usage of passive attenuators, such as accumulator, silencer and hose, may introduce additional compliance and resistance and reduce the dynamic response. Moreover, the active controller is versatile and suitable for different hydraulic systems with suitable control parameters. Therefore, this active method is a good solution for a system that requires low frequency cancellation by using a reasonably small attenuator without impairment of its dynamics.

On the other hand, like passive attenuators, active devices may also tend to be expensive for hydraulic systems. Experience of the control theory and design is needed for the implementation of active attenuators. The passive solution can be built into the system and there is no control element, which eliminates any issues with stability and robustness. The system with active controllers is more sensitive to external disturbance than that using passive attenuators.

The nature of digital hydraulic systems can cause pressure pulsation problems due to the digital input signals which result in the pulsed nature of the pressure or flow. In these systems, reducing the noise level and maintain their original dynamics are important features, active noise control method is a very promising solution for attenuating the noise due to its competitive advantages.

9.2 Recommendations for future work

The work presented in this thesis gives a number of different areas in which further research could be concerned.

- The controller is designed based on adaptive LMS algorithms in this work. Further research could be aimed at modifying the control algorithm in order to improve the control accuracy and reduce the computation. For example, considering the behaviour of system non-linear characteristics may improve the performance of the noise canceller.
- The piezoelectric valve used as the secondary path actuator has a small maximum pressure, which limited the experimental testing pressure. A better

performance actuator could be designed and implemented for further experimental work.

- The loading system was demonstrated using a manually adjusted needle valve on the test rig in this work. More complex loading systems could be implemented for further research, in which the performance of the noise canceller could be tested for more challenged working conditions.
- The location of the downstream pressure transducer could be moved in an attempt to optimize the controller performance for the specific system. An optimal position could be found in terms of appropriate cost functions of the system or controller. The cost functions would balance cancellation performance against power consumption.
- The power consumption of the system was considered in this work, but not in detail. Future work could be aimed at the area of the power consumption of the active noise controller.
- The unsteady flowrate measurement method is a very useful and effective technique for estimating the dynamic flowrate. It could be applied on a SIHS for further investigation of system characteristics. Moreover, it also could be implemented based on Kojima's method to attenuate the pressure pulsation in SIHSs or conventional hydraulic piping systems.

References

1977. Guidelines for the Design of Quiet Hydraulic Fluid Power Systems, *Association of Hydraulic Equipment Manfuacturers*.

2009. Hydraulic system design, section 14: Fluid-borne noise. *Centre for Power Transmission and Motion Control.* University of Bath.

Akhtar, M., Abe, M. and Kawamata, M. A new variable step size LMS algorithm-based method for improved online secondary path modeling in active noise control systems. *IEEE Transactions on Audio, Speech, and Language Processing*,14(2), pp. 720-726.

Alasty, A., Esmailzadeh, E and Ohadi, A. 2002. Hybrid active noise control of a one-dimensional acoustic duct. *Journal of Vibration and Acoustics,* 124**,** pp. 10-19.

Bai, M. and Lin, H. 1997. Comparison of active noise control structures in the presence of acoustical feedback by using the H_∞ synthesis technique. *Journal of Sound and Vibration,* 206**,** pp. 453-471.

Bai, M. and Lin, H. 1998. Plant uncertainty analysis in a duct active noise control problem by using the H_∞ theory.*Journal of the Acoustical Society of America,* 104**,** pp. 237-247.

Bao, C., Sas, P. and Van Brussel, H. 1993a. Adaptive active control of noise in 3-D reverberant enclosures. *Journal of Sound and Vibration,* 161**,** pp. 501-514.

Bao, C., Sas, P. and Van Brussel, H. 1993b. Comparison of two-on-line identification algorithms for active noise control. *Proceedings of the 2nd Conference on Recent Advances in Active Control of Sound and Vibration.* pp.38-54.

Bouchard, M., Paillard, B. and Le Dinh, C. 1999. Improved training of neural networks for the nonlinear active control of sound and vibration. *IEEE Transactions on Neural Networks,* 10**,** pp. 391-401.

Boucher, C., Elliott, S. and Nelson, P. 1991. Effect of errors in the plant model on the performance of algorithms for adaptive feedforward control*., IEE Proceedings of Radar and Signal Processing*., pp. 313-319.

Branson, D., Johnston, D. N., Tilley, D., Bowen, C. and Keogh, P. 2010. Piezoelectric Actuation in a High Bandwidth Valve. *Ferroelectrics,* 408**,** pp. 32-40.

Branson, D., Wang, F., Johnston, D. N., Tilley, D. G., Bowen, C. R. and Keogh, P. S. 2011. Piezoelectrically actuated hydraulic valve design for high bandwidth and flow performance. *Proceedings of the Institution of Mechanical Engineers, Part I: Journal of Systems and Control Engineering,* 225**,** pp. 345-359.

Brown, F., Tentarelli, S. and Ramachandran, S. 1988. A hydraulic rotary switched-inertance servo-transformer. *Journal of Dynamic Systems, Measurement, and Control,* 110**,** pp. 144-150.

Brown, F. T. 1988. Switch reactance hydraulics: a new way to control fluid power. *Proc. National Conference on Fluid Power, Chicago***,** pp. 25-34.

Burgess, J. 1981. Active adaptive sound control in a duct: A computer simulation. *Journal of the Acoustical Society of America,* 70**,** pp. 715-726.

Chang, C. and Luoh, F. 2007. Enhancement of active noise control using neural-based filtered-X algorithm. *Journal of Sound and Vibration,* 305**,** pp. 348-356.

Cioffi, J. 1987. Limited-precision effects in adaptive filtering. *IEEE Transactions on Circuits and Systems,*34**,** pp.821-833.

Clark, G., Mitra, S. and Parker, S. 1981. Block implementation of adaptive digital filters. *IEEE Transactions on Acoustics, Speech and Signal Processing*, 29**,** pp. 744-752.

Crouse, J. 1988. Active attenuator and method. US Patents, No. 4750523.

Das, D. and Panda, G. 2004. Active mitigation of nonlinear noise processes using a novel filtered-s LMS algorithm. *IEEE Transactions on Speech and Audio Processing,* 12(3)**,** pp. 313-322.

Dekker, N., Edwards, J. and James, A. 1989. Active noise control. US Patents, No. 4876722.

Efe, M. and Kaynak, O. 2000. Stabilizing and robustifying the learning mechanisms of artificial neural networks in control engineering applications. *International Journal of Intelligent Systems,* 15**,** pp. 365-388.

Eghtesadi, K., Hong, W. and Leventhall, H. 1983. The tight-coupled monopole active attenuator in a duct. *Noise Control Engineering Journal,* 20**,** pp. 16–20.

Elliott, S. and Nelson, P. 1985. The application of adaptive filtering to the active control of sound and vibration. *NASA Technical Report.*

Elliott, S., Stothers, I. and Nelson, P. 2003. A multiple error LMS algorithm and its application to the active control of sound and vibration. *IEEE Transactions on Acoustics, Speech and Signal Processing,*35**,** pp. 1423-1434.

Elliott, S. and Sutton, T. 1996. Performance of feedforward and feedback systems for active control. *IEEE Transactions on Speech and Audio Processing,* 4**,** pp. 214-223.

Eriksson, L. and Allie, M. 1989. Use of random noise for on-line transducer modeling in an adaptive active attenuation system. *Journal of the Acoustical Society of America,* 85(2)**,** pp. 797–802.

Eriksson, L. J. 1991. Active acoustic attenuation system with overall modeling. US Patents, No. 4987598.

Fahy, F. 2001. Foundations of engineering acoustics, *Academic Press*.

Franz, M. and Larsen, A. 1996. Apparatus and method for attenuation of fluid-borne noise. US Patents, No. 5492451.

Freudenberg, J., Hollot, C., Middleton, R. and Toochinda, V. 2003. Fundamental design limitations of the general control configuration. *IEEE Transactions on Automatic Control,* 48**,** pp. 1355-1370.

Gan, W. and Kuo, S. 2002. An integrated audio and active noise control headset. *IEEE Transactions on Consumer Electronics,* 48**,** pp. 242-247.

Glover Jr, J. 1977. Adaptive noise canceling applied to sinusoidal interferences. *IEEE Transactions on Acoustics, Speech and Signal Processing,* 25**,** pp. 484-491.

Goldstein, A. 1965. On steepest descent. *DTIC Online Document*.

Haraguchi, M. and Hu, H. 2009. Stability analysis of a noise control system in a duct by using delay differential equation. *Acta Mechanica Sinica,* 25(1)**,** pp. 131-137.

Henderson, R. 1981. Quieter Fluid Power Handbook: Silencing Fluid-Borne Noise. *BHRA Fluid Engineering*. pp. 33-44.

Hillis, A. 2005. Adaptive control of active engine mounts. *PhD thesis, University of Bristol.*

Hinamoto, Y. and Sakai, H. 2005. Analysis of the filtered-X LMS algorithm and a related new algorithm for active control of multitonal noise. *IEEE Transactions on Audio, Speech, and Language Processing,*14**,** pp. 123-130.

Hinamoto, Y. and Sakai, H. 2007. A Filtered-X LMS Algorithm for Sinusoidal Reference Signals—Effects of Frequency Mismatch. *IEEE Signal Processing Letters,* 14**,** pp. 259-262.

Hoerbiger.A. 1938. *Annular Automatic Valve*. US Patents No. 2127688.

Hong, J., Akers, J., Venugopal, R. and Lee, M. 1996. Modeling, identification, and feedback control of noise in an acoustic duct. *IEEE Transactions on Control Systems Technology,* 4**,** pp. 283-291.

Hong, J. and Bernstein, D. 1998. Bode integral constraints, colocation, and spillover in active noise and vibration control. *IEEE Transactions on Control Systems Technology,* 6**,** pp. 111-120.

Hong, W., Eghtesadi, K. and Leventhall, H. 1987. The tight coupled monopole (TCM) and tight coupled tandem (TCT) attenuators: Theoretical aspects and experimental attenuation in an air duct. *Journal of the Acoustical Society of America,* 81**,** pp. 376-388.

Horne, M. and Hansen, R. 1982. Sound propagation in a pipe containing a liquid of comparable acoustic impedance.*Journal of the Acoustical Society of America,* 71(6)**,** pp. 1400-1405.

Huebner, R. 1996. Attenuation of fluid borne noise. US Patents, No. 5560205.

Hughes, M. 1981. Quieter Fluid Power Handbook: Air Borne Noise from Pipework. *BHRA Fluid Engineering***,** 5. pp. 17-22.

Jeon, H., Chang, T. and Kuo, S. 2010. Analysis of Frequency Mismatch in Narrowband Active Noise Control. *IEEE Transactions on Audio, Speech, and Language Processing,* 18**,** pp. 1632-1642.

Johnston, D. and Edge, K. 1989. Simulation of the pressure ripple characteristics of hydraulic circuits.*Proceedings of the Institution of Mechanical Engineers, Part C: Journal of Mechanical Engineering Science,* 203**,** pp. 275-282.

Johnston, D. and Edge, K. 1991. In-situ measurement of the wavespeed and bulk modulus in hydraulic lines.*Proceedings of the Institution of Mechanical Engineers, Part I: Journal of Systems and Control Engineering,* 205**,** pp. 191-197.

Johnston, D. N. 1987. Measurement and Prediction of the Fluid Borne Noise Characteristics of Hydraulic Components and Systems. *PhD thesis, University of Bath.*

Johnston, D. N. 2006. Efficient methods for numerical modeling of laminar friction in fluid lines. *Journal of Dynamic Systems, Measurement, and Control,* 128(4)**,** pp. 829-835.

Johnston, D. N. 2009. A switched inertance device for efficient control of pressure and flow. *Bath/ASME Fluid Power and Motion Control Symposium.* Hollywood, USA. pp. 1-8.

Johnston, D. N. and Drew, J. 1996. Measurement of positive displacement pump flow ripple and impedance. *Proceedings of the Institution of Mechanical Engineers, Part I: Journal of Systems and Control Engineering,* 210**,** pp. 65-74.

Johnston, D. N. and Pan, M. 2010. Use of Pipeline Wave Propagation Model for Measuring Unsteady Flowrate. *Proc. Fluid Power and Motion Control, September*, *Bath.,* pp.307-320.

Johnston, D. N. and Tilley, D. 2003. Fundamentals of fluid-borne noise. *Centre for Power Transmission and Motion Control.* University of Bath.

Johnston, N. 2007. Hydraulic system noise prediction and control. *Handbook of Noise and Vibration Control***,** pp. 946-955.

Johnston, N. 2012. The transmission line method for modelling laminar flow of liquid in pipelines. *Proceedings of the Institution of Mechanical Engineers, Part I: Journal of Systems and Control Engineering*.

Kaiser, O., Pietrzko, S. and Morari, M. 2003. Feedback control of sound transmission through a double glazed window. *Journal of Sound and Vibration,* 263**,** pp. 775-795.

Kehler.K. 1940. Automatic Annular Valve. US patents, No. 2186489.

Klees, G. 1967. Attenuating device. US Patents, No. 3323305.

Kojima, E., Shinada, M. and Yamaoka, T. 1993. Development of an active attenuator for pressure pulsation in liquid piping systems (trial construction of the system and fundamental experiments on attenuation characteristics). *JSME international journal. Series B, fluids and thermal engineering,* 36**,** pp. 230-237.

Krus, P., Weddfelt, K. and Palmberg, J. O. 1994. Fast pipeline models for simulation of hydraulic systems. *Journal of Dynamic Systems, Measurement, and Control,* 116(1)**,** pp. 132-137.

Kuo, S., Kuo, K. and Gan, W. 2010. Active noise control: Open problems and challenges. *International Conference on Green Circuits and Systems, IEEE, Shanghai.* pp. 164-169.

Kuo, S. and Morgan, D. 1995. Active noise control systems: algorithms and DSP implementations, *John Wiley & Sons, Inc. New York, USA*.

Kuo, S. and Morgan, D. 1999. Active noise control: a tutorial review. *Proceedings of the IEEE,* 87**,** pp. 943-973.

Kuo, S. and Nallabolu, S. 2007. Analysis and Correction of Frequency Error in Electronic Mufflers using Narrowband Active Noise Control. *IEEE International Conference on Control Applications*, *Singapore*. pp. 1353-1358.

Kuo, S. and Vijayan, D. 1997. A secondary path modeling technique for active noise control systems. *IEEE Transactions on Speech and Audio Processing,* 5**,** pp. 374-377.

Labview 2008. LabVIEW.Adaptive Filter Toolkit 1.0 Help. *National Instruments*.

Lan, H., Zhang, M. and Ser, W. 2002. An active noise control system using online secondary path modelingwith reduced auxiliary noise. *IEEE Signal Processing Letters,* 9**,** pp. 16-18.

Lin, J. and Luo, Z. 2002. Internal model-based LQG/ H_∞ design of robust active noise controllers for an acoustic duct system. *IEEE Transactions on Control Systems Technology,* 8(5)**,** pp. 864-872.

Lopez, E., Colunga, P., Bustamante, R., Nakano-Miyatake, M. and Perez-Meana, H. 2010. Evaluation of a hybrid active noise control system with acoustic feedback. *The 53rd IEEE International Midwest Symposium on Circuits and Systems*. *Seattle, US*, pp. 873-876.

Lueg, P. 1936. Process of silencing sound oscillations. *US Patents, No. US 714582 A*.

Maillard, J., Lago, T. and Fuller, C. 1999. Fluid wave actuator for the active control of hydraulic pulsations in piping systems. *Proceedings of the International Modal Analysis Conference IMAC,1999*, pp. 1806-1812.

Morari, M. and Zafiriou, E. 1989. *Robust process control*, Prentice Hall.

Morgan, D. 1980. An analysis of multiple correlation cancellation loops with a filter in the auxiliary path. *IEEE Transactions on Acoustics Speech and Signal Processing,* 28**,** pp. 454-467.

Olson, H. and May, E. 1953. Electronic sound absorber. *Journal of the Acoustical Society of America,* 25(6), pp. 1130-1136.

Oppenheim, A. V. and Schafer, R. W. 1989. Discrete-time signal processing. *Prentice Hall*.

Petersen, I. and Pota, H. 2002. Experiments in feedback control of an acoustic duct. *Proceedings of the 2000 IEEE International Conference on Control Applications, Anchorage,USA*, pp. 261-266.

Phillips, E. 1999. Method and apparatus for reduction of fluid borne noise in hydraulic systems.*Journal of the Acoustical Society of America,* 105(3)**,** pp. 1447.

Radcliffe, J. and Southward, S. 1993. Global active noise control of a one-dimensional acoustic duct using a feedback controller. *Journal of Vibration and Acoustics,* 115**,** pp. 488-494.

Sakai, H. and Hinamoto, Y. 2005. An exact analysis of the LMS algorithm with tonal reference signals in the presence of frequency mismatch. *Signal Processing,* 85**,** pp. 1255-1262.

Haykin, S. 1996. Adaptive filter theory. *New Jersey, Prentice-Hall Inc*.

Skaistis, S. 1988. Noise control of hydraulic machinery, *CRC Press*.

Snyder, S. and Hansen, C. 1989. Active noise control in ducts: Some physical insights. *Journal of the Acoustical Society of America,* 86 (1)**,** pp. 184-194.

Snyder, S. and Hansen, C. 2002. The effect of transfer function estimation errors on the filtered-x LMS algorithm. *Signal Processing, IEEE Transactions on,* 42**,** pp. 950-953.

Snyder, S. and Tanaka, N. 1995. Active control of vibration using a neural network. *IEEE Transactions on Neural Networks,* 6**,** pp. 819-828.

Sommerfeldt, S. D. 1989. Adaptive Vibration Control of Vibration Isolation Mounts, Using an LMS-Based Control Algorithm. *Journal of the Acoustical Society of America,* 88 (2)**,** pp. 1184.

Hydraulic fluid power - determination of pressure ripple levels generated in systems and components. Part 1: Precision method for pumps. *ISO 10767-1:1996.*

Strauch, P. and Mulgrew, B. 1998. Active control of nonlinear noise processes in a linear duct. *IEEE transactions on signal processing,* 46 (9), pp. 2404-2412.

Streeter, A., Ray, L. and Collier, R. D, 2004. Hybrid feedforward-feedback active noise control. *American Control Conference, Boston, USA, 2004*. *IEEE*, 3, pp. 2876-2881.

Swanson, D. C. 1989. Active noise attenuation using a self-tuning regulator as the adaptive control algorithm. *Proc. Inter-noise,1989*, pp. 467-470.

Tan, L. and Jiang, J. 2001. Adaptive Volterra filters for active control of nonlinear noise processes. *IEEE transactions on signal processing,* 49 (8)**,** pp.1667-1676.

Taylor, R. 1981. Quieter Fluid Power Handbook: Pump noise and its treatment. *BHRA Fluid Engineering***,** pp. 53-66.

Tilley, D. 1981. Quieter Fluid Power Handbook: Fluid-Borne Noise in Hydraulic Systems. *BHRA Fluid Engineering*, pp. 67-76.

Tseng, W., Rafaely, B. and Elliott, S. 1998. Combined feedback–feedforward active control of sound in a room. *Journal of the Acoustical Society of America,* 104 (6)**,** pp. 3417-3425.

Vitkovsky, J. P., Lambert, M. F., Simpson, A. R. and Bergant, A, 2000. Advances in unsteady friction modelling in transient pipe flow. *Proceedings of 8th International Conference on Pressure Surges - Safe Design and Operation of Industrial Pipe System, Hague, Netherlands, April 2000*. pp.471-482.

Wang, L. 2008. Active control of fluid-borne noise. *PhD thesis, University of Bath, 2008.*

Widrow, B. 1971. Adaptive filters. *Aspects of Network and System Theory***,** pp. 563-587.

Widrow, B., Glover Jr, J., Mccool, J., Kaunitz, J., Williams, C., Hearn, R., Zeidler, J., Dong Jr, E. and Goodlin, R. 2005. Adaptive noise cancelling: Principles and applications. *Proceedings of the IEEE,* 63**,** pp. 1692-1716.

Widrow, B., Shur, D. and Shaffer, S. 1981. On adaptive inverse control. *The Fifteenth Asilomar Conference on Circuits, Systems and Compters, November 1981*. pp. 185-189.

Widrow, B. and Stearns, S. D. 1985. Adaptive signal processing. Englewood Cliffs, NJ, Prentice-Hall, Inc., 1985.

Winkler, B. and Scheidl, R. 2007. Development of a fast seat type switching valve for big flow rates. *The Tenth Scandinavian International Conference on Fluid Power, SICFP'07, Tampere, Finland, May, 2007*, pp. 137-146.

Wu, J. and Lee, T. 2005. Application of H-infinity hybrid active controller for acoustic duct noise cancellation. *International Journal of Vehicle Noise and Vibration,* 1**,** pp. 183-193.

Wylie, E. B., Streeter, V. L. and Suo, L. 1993. Fluid transients in systems, Prentice Hall Englewood Cliffs, New Jersey.

Xiao, Y., Ikuta, A., Ma, L., Xu, L. and Ward, R. 2004a. Statistical properties of the LMS Fourier analyzer in the presence of frequency mismatch. *IEEE Transactions on Circuits and Systems—I: Regular Papers,* 51**(**12). pp. 2504-2515.

Xiao, Y., Ma, L. and Khorasani, K. 2004. A robust narrowband active noise control system for accommodating frequency mismatch. *The Seventh European Signal Processing Conference, September, 2004, Vienna, Austria.* pp. 917-920.

Xiao, Y., Ma, L., Khorasani, K., Ikuta, A. and Xu, L. 2005. A filtered-X RLS based narrowband active noise control system in the presence of frequency mismatch. *Circuits and Systems, IEEE International Symposium*, 1, pp. 260-263 .

Yang, F., Gupta, A. and Kuo. 2009. Parallel multi-frequency narrowband active noise control systems. *Acoustics, Speech and Signal Processing, IEEE International Conference, 2009*. pp. 253-256.

Yuan, J. 2004. A hybrid active noise controller for finite ducts. *Applied Acoustics,* 65**,** pp. 45-57.

Zhang, M., Lan, H. and Ser, W. 2001. Cross-updated active noise control system with online secondarypath modeling. *IEEE Transactions on Speech and Audio Processing,* 9**,** pp. 598-602.

Zhang, X., Ren, X., Na, J., Zhang, B. and Huang, H. 2010. Adaptive nonlinear neuro-controller with an integrated evaluation algorithm for nonlinear active noise systems. *Journal of Sound and Vibration*. 329, pp. 5005–5016.

Appendix 1 Oscillations of weight taps

1.1 System structure

Figure A-1 shows the block diagram of Filtered-X adaptive notch filter for narrowband noise cancellation. Two orthogonal components $x_0(n)$ and $x_1(n)$ are used as reference signals for two-weight adaptive notch filter and the control signal $y(n)$ is summed from the weighted reference inputs. For the frequency present in the reference signal, the adaptive weight vector **w(n)** = $[w_0(n), w_1(n)]$ are required for cancellation.

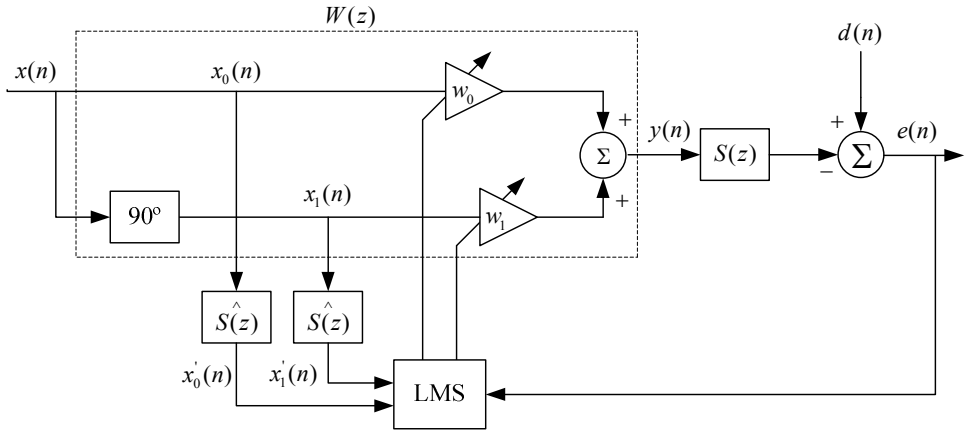

Figure A-1 Single-frequency ANC system using FXLMS algorithm (Elliott et al., 2003)

The weights are updated by the equations based on LMS algorithm:

$$\mathbf{w}_0(n+1) = \mathbf{w}_0(n) + \mu \mathbf{x}_0'(n) e(n) \tag{A-1}$$

$$\mathbf{w}_1(n+1) = \mathbf{w}_1(n) + \mu \mathbf{x}_1'(n) e(n) \tag{A-2}$$

where $\mathbf{x}_0'(n)$ and $\mathbf{x}_1'(n)$ are the reference signals filtered by the cancellation path estimate $\hat{S}(z)$.

$$x_0'(n) = x_0(n)\hat{s}(n) \tag{A-3}$$

$$x_1'(n) = x_1(n)\hat{s}(n) \tag{A-4}$$

Assuming the reference inputs are

$$x_0(n) = A_0 \sin(\omega_0 n) \tag{A-5}$$

$$x_1(n) = A_1 \cos(\omega_0 n) \tag{A-6}$$

at the reference frequency ω_0. A_0 and A_1 are the amplitude of $x_0(n)$ and $x_1(n)$.

The filtered reference signals can be expressed as

$$x_0^{'}(n) = A_0 A_s \sin(\omega_0 n + \phi_s) \tag{A-7}$$

$$x_1^{'}(n) = A_1 A_s \cos(\omega_0 n + \phi_s) \tag{A-8}$$

where A_s and ϕ_s are the amplitude and phase of the estimated cancelling path $\hat{S}(z)$.

Thus, the cancelling signal y(n) can be written as:

$$y(n) = w_0(n)\mathbf{x}_0(n) + w_1(n)\mathbf{x}_1(n) \tag{A-9}$$

1.2 Effect of error signal *e*(*n*)

From equation (A-1) and (A-2), it can be seen that the weights updating depends on the convergence factor μ, filtered reference $x^{'}(n)$ and error signal $e(n)$. Usually, the reference signal $x(n)$ is given beforehand and it is uncorrelated to the error signal $e(n)$ and primary noise $d(n)$.

Assuming the residual error signal $e(n)$ is

$$e(n) = A_e \sin(\omega_0 n + \phi_e) \tag{A-10}$$

Substituting equation (A-7) and (A-8) to (A-1) and (A-2), the weights w_0 and w_1 can be given as:

$$\mathbf{w}_0(n+1) = \mathbf{w}_0(n) + \mu A_0 A_s \sin(\omega_0 n + \phi_s) A_e \sin(\omega_0 n + \phi_e) \tag{A-11}$$

$$\mathbf{w}_1(n+1) = \mathbf{w}_1(n) + \mu A_1 A_s \cos(\omega_0 n + \phi_s) A_e \sin(\omega_0 n + \phi_e) \tag{A-12}$$

When the weight vector $\mathbf{w}(n) = [w_0(n) \quad w_1(n)]$ converged to the optimum weight vector $\mathbf{w}^*(n) = [w_0^*(n) \quad w_1^*(n)]$, with ideal cancellation the mean value of the error signal $e(n)$ would equal to 0.

Taking the offset C into account of the residual error signal $e(n)$, for it is normally existing in practical application. So the error signal $e^{'}(n)$ can be expressed as:

$$e^{'}(n) = A_e \sin(\omega_0 n + \phi_e) + C \tag{A-13}$$

Equation (A-11) and (A-12) are modified as follows:

$$\mathbf{w}_0^{'}(n+1) = \mathbf{w}_0^{'}(n) + \mu A_0 A_s \sin(\omega_0 n + \phi_s)(A_e \sin(\omega_0 n + \phi_e) + C) \quad \text{(A-14)}$$

$$\mathbf{w}_1^{'}(n+1) = \mathbf{w}_1^{'}(n) + \mu A_1 A_s \cos(\omega_0 n + \phi_s)(A_e \sin(\omega_0 n + \phi_e) + C) \quad \text{(A-15)}$$

When the notch filter is ideally converged, $e^{'}(n) = C$

$$\mathbf{w}_0^{'}(n+1) = \mathbf{w}_0^{'}(n) + \alpha A_0 \sin(\omega_0 n + \phi_s) \quad \text{(A-16)}$$

$$\mathbf{w}_1^{'}(n+1) = \mathbf{w}_1^{'}(n) + \alpha A_1 \cos(\omega_0 n + \phi_s) \quad \text{(A-17)}$$

where

$$\alpha = \mu A_s C \quad \text{(A-18)}$$

which means the notch filtered converged to an optimum vector w* with sinusoidal oscillations.

In order to eliminate the oscillations, a high-pass filter can be used to pre-process the error signal *e*(*n*) to zero offset.

Appendix 2 Cancellation of different openings of the piezoelectric valve

- **By-pass structure**

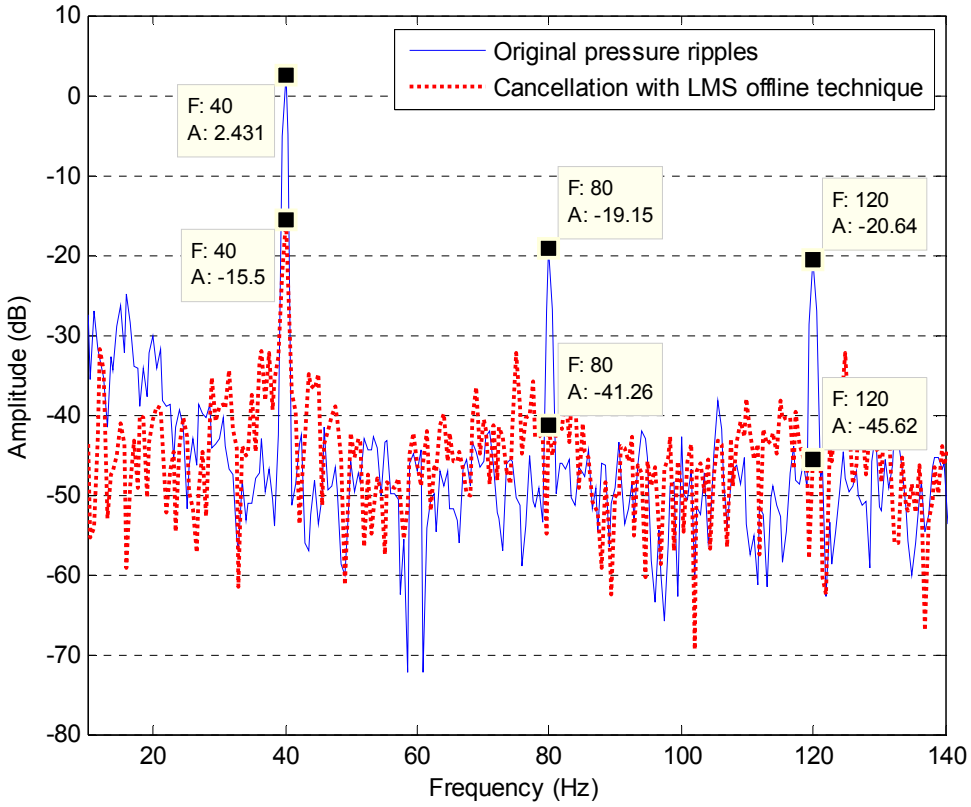

Figure A2-1 Multiple frequencies cancellation using LMS offline identification technique with the driving voltage of the piezoelectric valve of 0V (0V + offset voltage)

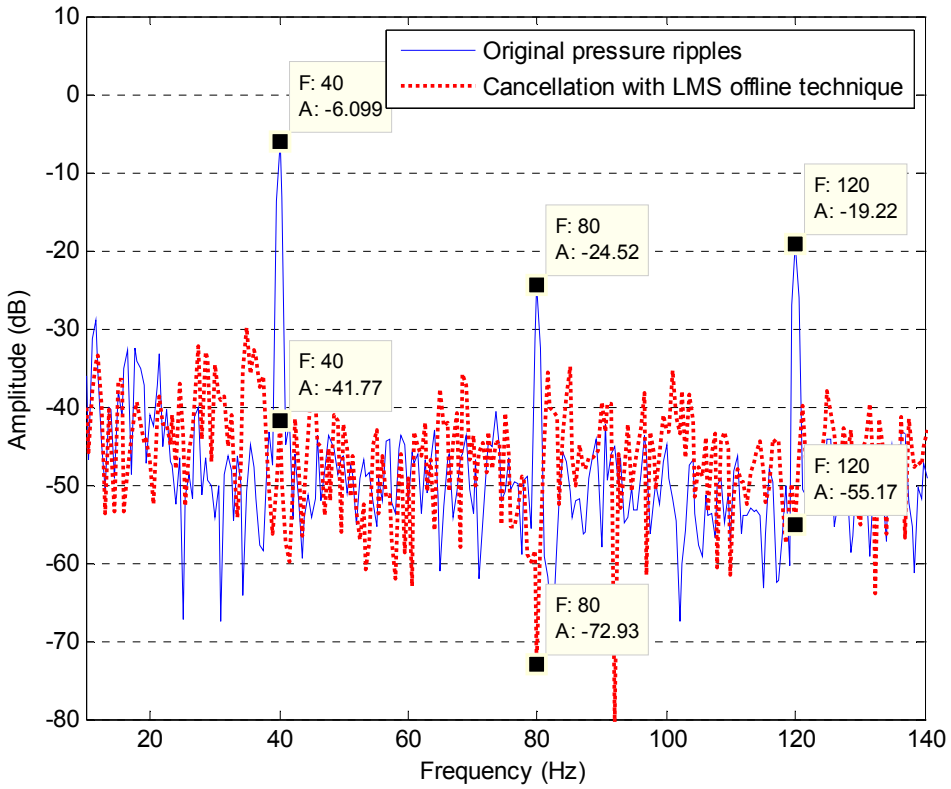

Figure A2-2 Multiple frequencies cancellation using LMS offline identification technique with the driving voltage of the piezoelectric valve of 400V (400V + offset voltage)

Appendix 3 Publications

Johnston, D. N. and Pan, M. 2010. Use of Pipeline Wave Propagation Model for Measuring Unsteady Flowrate. Proc. Fluid Power and Motion Control, September, Bath., pp.307-320.

Use of Pipeline Wave Propagation Model for Measuring Unsteady Flowrate

Nigel Johnston, Min Pan
Department of Mechanical Engineering
University of Bath

ABSTRACT

A novel method for estimation of unsteady flowrate using pressure at two or three points along a pipeline is described in this paper. The pressure data are processed using a wave propagation model to determine the unsteady flow. Computer simulations show that the proposed method is effective for unsteady flowrate measurement to a high bandwidth. However, if the pressure values from two transducers are used, inaccuracies exist at certain frequencies when the transducer spacing coincides with multiples of half a wavelength. The accuracy can be improved by adding a third transducer with unequal spacing. The comparison and analysis of two-transducer and three-transducer techniques are investigated through simulation. This method may be applied to real time flowrate measurement, control systems or active noise cancellation systems.

1. INTRODUCTION

The estimation of unsteady flowrate is significant for the theoretical analysis of pipe system and practical applications. Many systems and methods have been proposed as the means to obtain the unsteady flowrate by determining the velocity of fluid. The techniques commonly applied in the past for measuring the velocity of fluids in unsteady flow consist essentially of Hot Wire Anemometer (HWA), Laser Doppler Velocimetry (LDV) or Particle Image Velocimetry (PIV) [1][2][3]. These methods are expensive and sophisticated, and they are particularly ill-suited to use on an industrial site [4]. Besides, the LDV and PIV cannot be used to determine the flowrate in real time. In fact, these techniques require post-processing of the acquired images in order to obtain the speed of the fluid. Furthermore the HWA and LDV methods measure the velocity at a point and not the volume flow rate; to determine the flow, assumptions have to be made about the velocity profile and corrections made.

On the other hand, many researchers presented measuring methods based on the mechanics of fluids in unsteady flow, estimating the flow from the pressure gradient, which is estimated from two pressure transducers a small distance apart [4][5][6]. These techniques make it possible to measure the flowrate in real time, combining low price, simplicity of implementation and reliability, as high bandwidth pressure transducers are readily available and relatively easy to use. However, because of a simplified approximation to the wave behaviour, and the introduction of a pressure gradient calculation, it is necessary for the transducers to be closely spaced. This means that the pressure gradient is calculated from the difference between two similar measurements, magnifying the errors. Thus the flowrate measuring accuracy is degraded and the bandwidth is limited.

In this paper, methods are described for measuring the unsteady flowrate in a piping system, avoiding the limitations of previous two-transducer methods. The proposed methods are based on the wave propagation model to determine the flowrate using measured pressures as boundary conditions. This paper is organized as follows. Section 2 describes the mathematical model of pipeline using pipeline wave propagation model. The two-transducer and three-transducer techniques are presented in Section 3, together with simulated results. Conclusions are given in Section 4.

2. PIPELINE WAVE PROPAGATION MODEL

The motion equation in a pipeline and continuity equation are

$$\frac{\partial q}{\partial t}+\frac{q}{A}\frac{\partial q}{\partial x}+\frac{A}{\rho}\frac{\partial p}{\partial x}+f(q)=0 \tag{1}$$

$$\frac{\partial p}{\partial t}+\frac{q}{A}\frac{\partial p}{\partial x}+\frac{\rho c^2}{A}\frac{\partial q}{\partial x}=0 \tag{2}$$

On the assumption that $q/A<<c$, the second terms in these equations can be neglected. So the equation (3) and (4) can be obtained as follows by using ordinary differential equations.

$$\frac{dq}{dt}+\frac{A}{\rho c}\frac{dp}{dt}+f=0 \quad when \quad \frac{dx}{dt}=c \tag{3}$$

$$\frac{dq}{dt}-\frac{A}{\rho c}\frac{dp}{dt}+f=0 \quad when \quad \frac{dx}{dt}=-c \tag{4}$$

These equations apply along the characteristic lines as shown in figure 1, which effectively represent waves travelling in the two directions. Assuming the pressure of point A and B are p_A and p_B, and the flows are q_A and q_B respectively. After a timestep Δt, the pressure and flow at point P can be calculated by using the value of p_A, p_B, q_A and q_B from the previous time step. The finite difference method is introduced to get the approximate equations along the pipe.

$$c^+:\ q_p-q_A+\frac{A}{\rho c}(p_p-p_A)+\Delta t f(q_A)=0 \tag{5}$$

$$c^-:\ q_p-q_B-\frac{A}{\rho c}(p_p-p_B)+\Delta t f(q_B)=0 \tag{6}$$

where $f(q_A)$ and $f(q_B)$ represent the friction at point A and B.

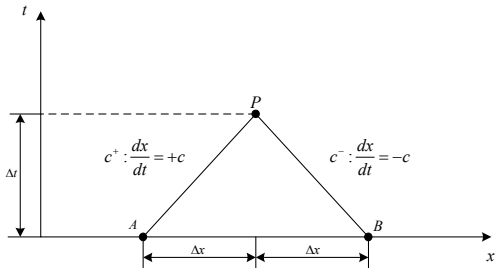

Figure 1 Characteristics line of pipe

This numerical method is known as the Method of Characteristics (MOC) and is a widely used, simple method which has very high accuracy (see, for example, [7, 8]).

For steady laminar flow $f(q)$ can be approximated as

$$f(q)=\frac{8\nu}{r^2}q \tag{7}$$

In practice, the friction term includes an unsteady or frequency dependent part except at steady state .The laminar flow with the sum of a steady term and a series of unsteady terms in the Fourier domain can be derived approximately as follows.

$$F_{APP}(Q)=\frac{\nu}{r^2}\left[8+4\sum_{i=1}^{k}\left(\frac{m_i j\omega}{\frac{\nu m_i}{r^2}+j\omega}\right)\right]Q \tag{8}$$

in which k indicates the number of terms, and n_i and m_i are weighting factors for the i^{th} term. A method of determining values of n_i and m_i was proposed by Johnston [9]. Values of m_1, m_2 and n_1 were listed for a range of values of β, and other values were determined using the equations:

$$m_i = \beta m_{i-1} \quad \text{for } 3 \le i \le k \tag{9}$$

$$n_i = \beta^2 n_{i-1} \quad \text{for } 2 \le i \le k \tag{10}$$

The value of β can be chosen depending on the required accuracy, with small values of β giving the highest accuracy but requiring the highest number of terms k. The number of terms k can be determined by the expression $k = ceil\left(\frac{2\log r - \log(n_i \nu \Delta t)}{2\log\beta}\right) + 1$.

In order to use equation (8) as the friction model for simulation using the MOC in time domain, approximating equations can be represented by using inverse Fourier Transformation.

$$f(t+\Delta t) = \frac{8\nu}{r^2} q(t+\Delta t) + \frac{4\nu}{r^2} \sum_{i=1}^{k} y_i(t+\Delta t) \tag{11}$$

$$y_i(t+\Delta t) = y_i(t) e^{-\frac{n_i \nu \Delta t}{r^2}} + m_i [q(t+\Delta t) - q(t)] e^{-\frac{n_i \nu \Delta t}{2r^2}} \tag{12}$$

Substituting the equation for $f(t+\triangle t)$ into equation (5) and (6) yields the flowrate and pressure at any point along the pipe. The pressure and flowrate at the new timestep can be evaluated by rearrangement of equations (5) and (6) to give (13) and (14).

$$p_p = \frac{1}{2}\left[p_A + p_B + \frac{\rho c}{A}(q_A - q_B) + \Delta t \cdot \frac{\rho c}{A}(f_B - f_A) \right] \tag{13}$$

$$q_p = \frac{1}{2}\left[q_A + q_B + \frac{A}{\rho c}(p_A - p_B) - \Delta t (f_A + f_B) \right] \tag{14}$$

3. FLOWRATE MEASUREMENT METHOD

3.1 Two-transducer technique

The method was evaluated by simulation of a simple system as shown in Figure 2. Two transducers are arranged along the pipe to measure the pressure ripples p_1 and p_2.

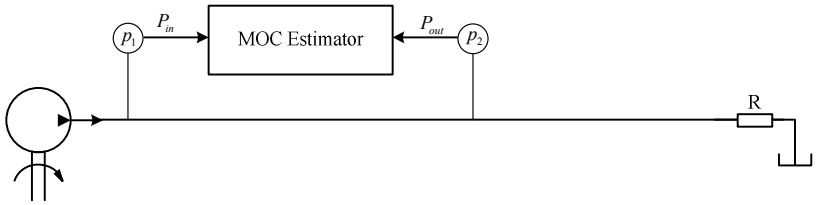

Figure 2 System schematic of two-transducer technique

The system was itself simulated using the MOC. Whilst this is clearly an idealised situation, it gives the opportunity to compare the estimated flow (determined by the MOC estimator) with the 'actual' flow (determined by the MOC system model). R represents the resistance of the load. The pressure ripples are generated by the pump at the upstream end. The pressure pulsations from (virtual) transducers 1 and 2 provide inputs P_{in} and P_{out} for the MOC estimator.

Figure 3 shows the results of flow measurement using the two-transducer technique. The simulation parameters used are presented in Table 1.

Table 1 Simulation parameters

Length	2.6 m
Diameter	0.01 m
Viscosity	30 cst
Density	870 kg/m^3
Speed of sound	1300 m/s
Number of nodes	21
Grid spacing	0.13 m
Friction terms k	4
Time step	0.1 ms
Simulation time	4 s
Upstream boundary	Flow chirp, 0-800 Hz over 4 seconds, 0.01 L/s amplitude
Pressure "transducer" locations	0.13m, 1.43m (nodes 2 and 12)
Downstream boundary resistance	2×10^9 Ns/m^5

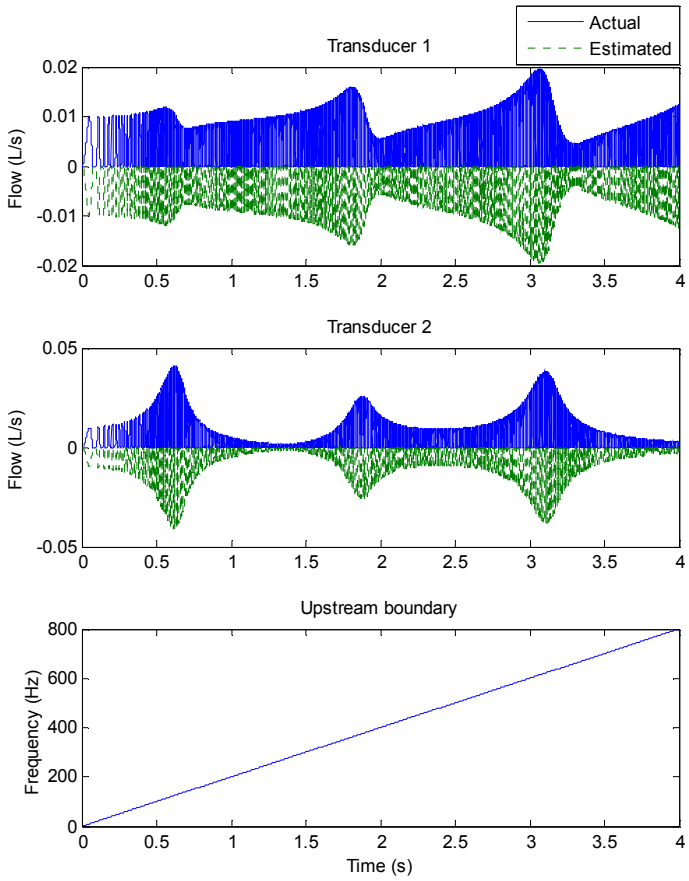

Figure 3 Comparison of actual and estimated flows at transducer 1 and 2 using two-transducer technique

For clarity only the positive half of the signal of actual value and the negative half of the signal of estimated value were shown. The bottom plot presented the upstream boundary with frequency variation with the sample time. It can be found that the estimated flowrate detected at the locations of two transducers by applying this method is identical to the actual theoretical values in the ideal conditions without disturbances. This would be expected as the MOC estimator is identical to the MOC system model.

However, the performance of the two-transducer technique can be degraded under imperfect conditions, particularly at the half-wavelength spacing (and integer multiples of half-wavelength). The spacing is defined as the distance between two (virtual) pressure transducers. In this case, the spacing is 1.3m from transducer 1 to transducer 2, and this is equal to a half wavelength at 500 Hz. In practice imperfections, errors and uncertainties might arise from transducer calibration factors and phase shifts, variations in fluid properties, and random noise. Figure 4 shows the effect of a 1% error in the calibration factor of (virtual)

pressure transducer 2. This was estimated using Fast Fourier Transforms (FFT) of the actual and estimated flows at the two transducers. Large errors are apparent at about 500 Hz and 1000 Hz.

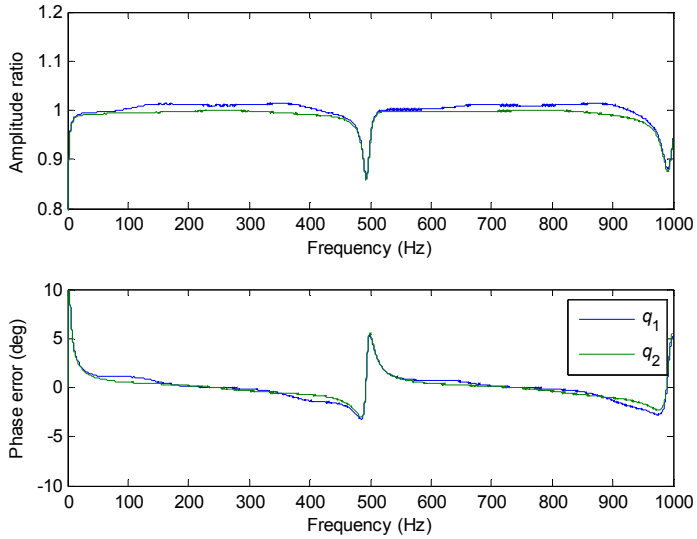

Figure 4 Errors at transducers 1 and 2 with a 1% error in calibration factor

The effect of a 1% difference between the speed of sound in the simulated pipeline and in the MOC estimator was also considered. This was done by changing the timescale of the data to the MOC estimator by 1%, remapping the predicted data to the new timestep by interpolation. Figure 5 shows the results of this. Large errors occur around 500 Hz and 1000 Hz. The noise on the data is a numerical artifact caused by changing the timestep and remapping the data, and can be ignored. In subsequent results presented in this paper, this noise has been removed by smoothing the data.

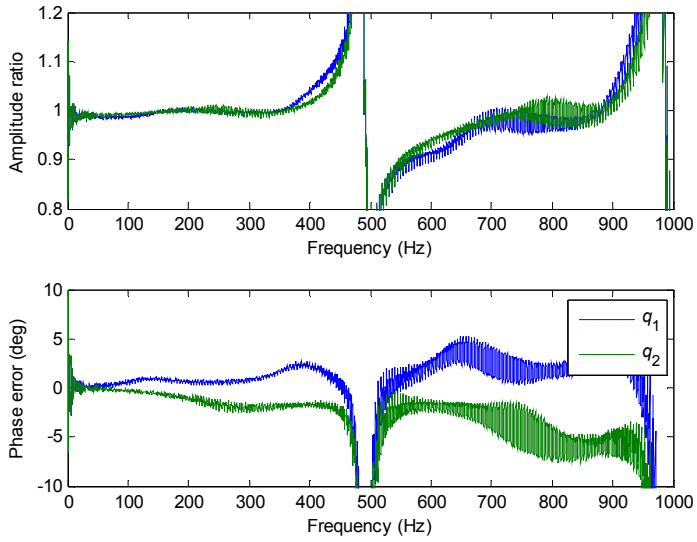

Figure 5 Errors at transducers 1 and 2 with a 1% error in speed of sound

Around the half-wavelength condition the errors in the predicted flows are much greater than the applied errors in the calibration factor and the speed of sound. The half-wavelength spacing problem can be shown easily if friction is neglected. From equation (15)

$$Q_1 = (P_1 \cos\frac{\omega\Delta x}{c} - P_2) \Big/ \sin\frac{\omega\Delta x}{c} \tag{15}$$

where P and Q are the Fourier transforms of pressure and flowrate, Δx is the spacing. When Δx equals to a multiple of a half-wavelength,

$$\Delta x = n \cdot (\lambda/2) \ \ (n = 1, 2, 3\ldots\ldots) \tag{16}$$

$$\frac{\omega \Delta x}{c} = \frac{\omega \cdot n \cdot \frac{\lambda}{2}}{c} = \frac{2\pi f \cdot n \cdot \frac{\lambda}{2}}{c} = n\pi \ (n = 1, 2, 3\ldots\ldots) \tag{17}$$

From equation (16) and (17), $\sin(w\Delta x/c) = 0$. So equation (15) for Q_1 is indeterminate and the pressure boundary conditions can be satisfied by an infinite range of flows. In practice, the friction in the system makes the denominator in equation (15) non-zero but very small, so that the equation becomes ill-conditioned around these frequencies. In order to eliminate this problem, an improved method is presented in the next section.

3.2 Three-transducer technique

The three-transducer technique uses two MOC estimators between three transducers as shown in figure 6. The spacing between transducers 1 and 2 and between 2 and 3 are different to avoid a half-wavelength condition arising in both estimators at any point within a wide frequency range. This is a similar approach to that used in the 'Secondary Source method', which is a technique for measuring flow ripple in the frequency domain [10, 11].

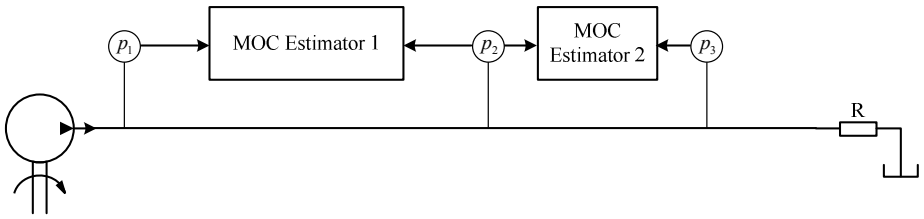

Figure 6 System schematic of three-transducer technique

The identical parameters were re-applied as used in two-transducer technique, and a third transducer was situated at the location of 2.21m. First, two MOC estimators were applied independently without the coupling resistance *R*. The amplitude ratios at the first transducer are shown in Figure 7, using two separate MOC estimators with a 1% error in the calibration factor of transducer 2. Figure 8 shows the same for 1% error in the speed of sound. In both cases it can be seen that large errors are apparent at about 500 Hz and 1000 Hz for the pair of transducers 1 and 2, and 800 Hz for the pair of transducers 2 and 3. Taking the average reduces the error by about half, but the errors are still large as the error from the ill-conditioned pair dominates. Therefore, a method of coupling the calculations is necessary in order to avoid the ill-conditioning.

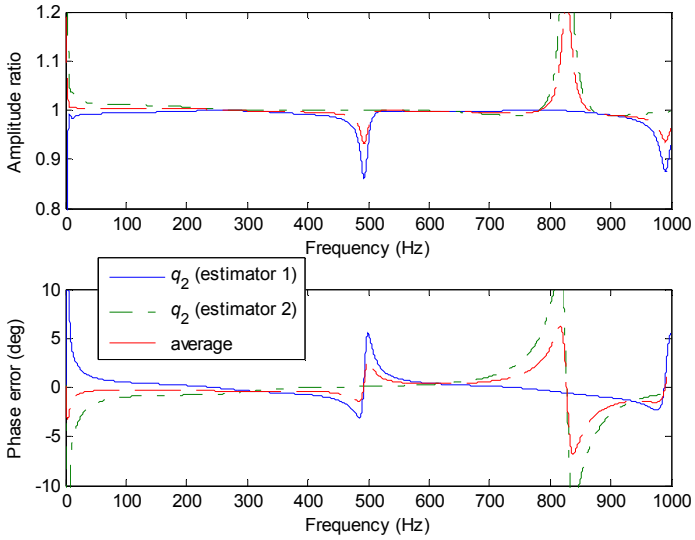

Figure 7 Errors at transducer 2 by using different transducer pairs, with a 1% error in calibration factor for transducer 2

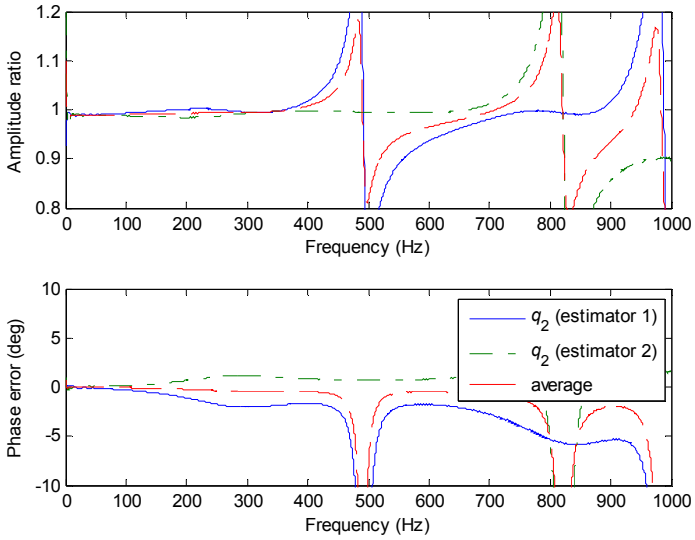

Figure 8 Errors at transducer 2 by using different transducer pairs with a 1% error in speed of sound

However the two estimators and the second pressure transducer cannot be coupled directly as the difference in predicted flows has to be accounted for. A 'loose' coupling is proposed, where the two MOC estimators are coupled together directly, but are only indirectly coupled to the pressure transducer measurement via a (virtual) hydraulic resistance R. This is shown in Figure 9. Under perfect, idealised conditions the two flows q_2 and q_2' would be equal and the pressure p_{12} would be equal to the measured pressure p_2 from the second transducer. However under realistic, imperfect conditions, the two estimated flows q_2 and q_2' would not be equal, and the pressure p_{12} would be given by the equation

$$p_{12} = p_2 + (q_2 - q_2')R \tag{18}$$

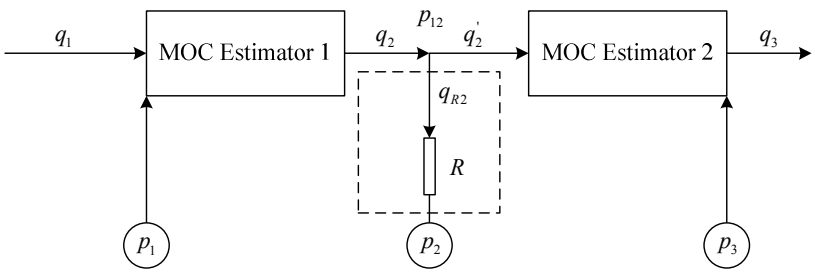

Figure 9 Coupling of MOC estimators

The flowrate q_1 and q_2 can be calculated by using the pressure p_1 and p_{12} with MOC estimator 1, whilst MOC estimator 2 is applied to predict the flowrate q_2' and q_3 from pressures p_{12} and p_3. A reasonable value of the resistance R needs to be chosen. A low value of R results in the two MOC estimators being decoupled, and a high value of R results in pressure transducer 2 being decoupled and the two MOC estimators effectively behaving as a single one using the measured pressures at points 1 and 3. It has been found that reasonably good results are obtained if R is of a similar order to the magnitude of the characteristic impedance of pipe. In this case, best results were obtained with R equal to half the magnitude of the characteristic impedance, $R = 7.7 \times 10^9$ Ns/m^5, but the optimum value may depend on the system.

Figures 10 and 11 show the amplitude and phase errors of q_1, q_2, q_2' and q_3 relative to the actual flows at these points. The half-wavelength problem at the frequency 500Hz has almost been eliminated, though errors increase above about 800 Hz in figure 11. The errors resulting from the error in the calibration factor (figure 10) are smaller than those resulting from the speed of sound error (figure 11) (note the different scales).

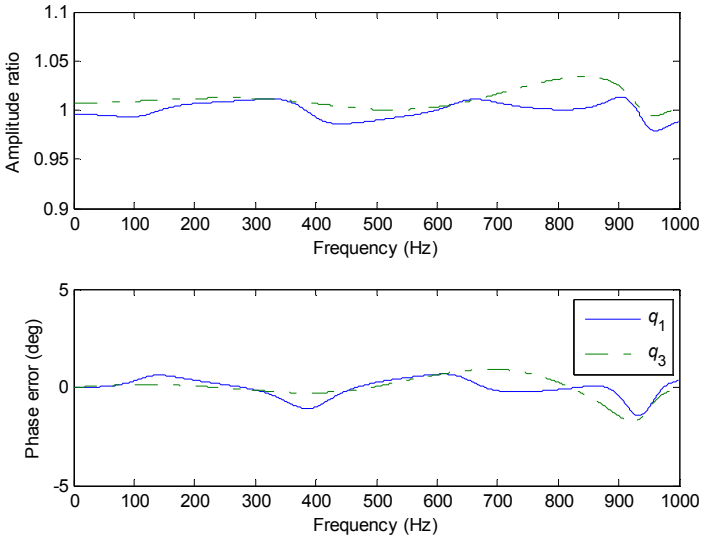

(a) Errors at transducers 1 and 3

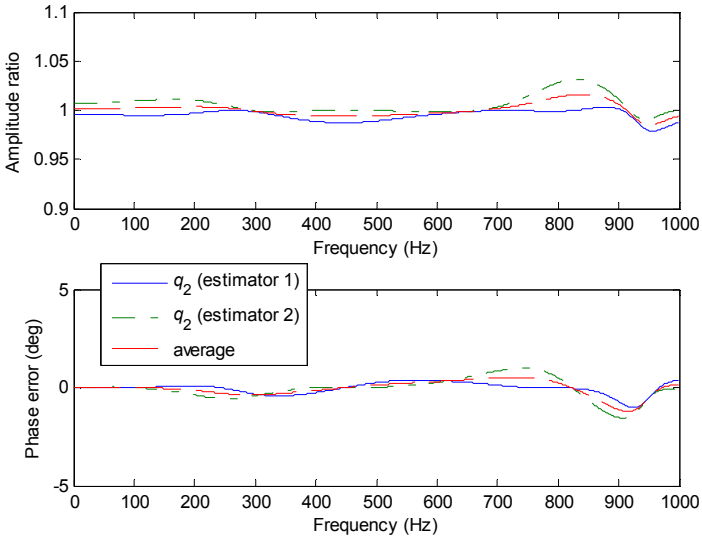

(b) Errors at transducer 2

Figure 10 Errors using three-transducer technique with a 1% error in calibration of transducer 2

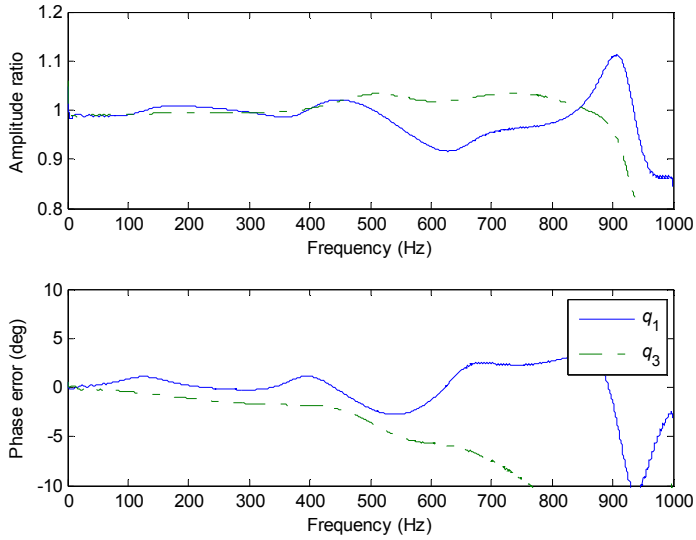

(a) Errors at transducers 1 and 3

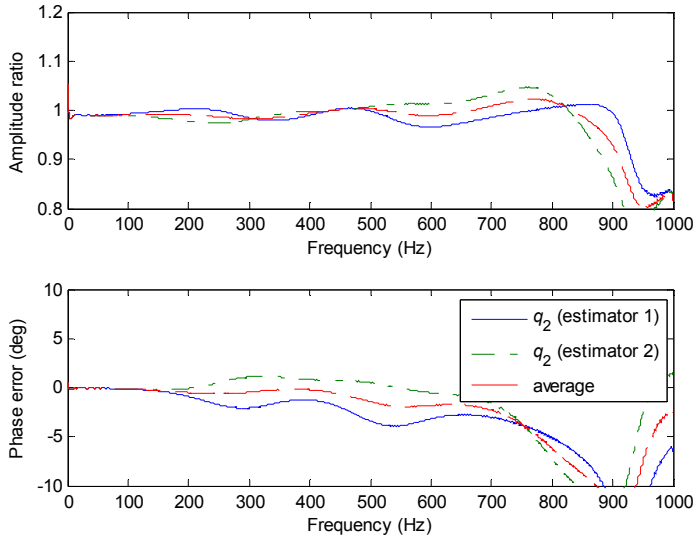

(b) Errors at transducer 2

Figure 11 Errors using three-transducer technique with a 1% error in speed of sound

In practice there may be considerable uncertainty in the speed of sound. However, a technique exists for establishing the speed of sound using three pressure transducers [10-12], and the same three transducers can be used as for the flow measurement. It has previously been found to be possible to determine the speed of sound very accurately using this method, provided that pressure ripple excitation is available with a high bandwidth.

This technique has only been found to work if the two MOC estimators are coupled to the second transducer via a resistance. If the two MOC estimators were coupled at the first or third transducer the estimators were found to be unstable.

The results presented here are purely through simulation. The next stage will be to implement the technique experimentally. However the accuracy of experimental results will be more difficult to evaluate, as it will be difficult to establish the unsteady flow by other means in order to obtain a meaningful comparison.

4. CONCLUSIONS

A two-transducer and a three-transducer method for measuring the unsteady flowrate in pipeline system have been investigated through simulation. The methods are based on wave propagation models to identify the unsteady flow from pressure measurements. Because the analysis is based on precise wave propagation models, there is no restriction on the transducer spacing. Previous methods have used finite difference approximations and consequently have required the transducers to be close together, limiting the bandwidth and the accuracy.

The methods were evaluated by applying known errors to simulated pressure data. The two transducer method was found to be inaccurate when the transducer spacing was close to a multiple of half the wavelength. This problem can be eliminated by using three unequally spaced transducers. Further work is needed to implement and evaluate the techniques experimentally, and this is planned to take place shortly.

NOMENCLATURE

A	pipe internal cross-sectional area
c	speed of sound
F	Fourier transform
f	friction term
k	number of terms in approximated friction series
L	length of pipe
m_i, n_i	weighting factors in approximated friction series
nx	divided element numbers
p	pressure
q	flow rate
Q	Fourier transform of flow rate
r	pipe internal radius
R	load resistance, virtual resistance coupling middle transducer
R_f	steady friction term
t	time
$\triangle t$	time step
x	distance along pipe
α	frequency
β	Frequency ratio for friction terms
ρ	Fluid density
v	Kinematic viscosity
ω	Angular frequency

REFERENCES

[1] Comte-Bellot, G., "Hot-wire anemometry". Annual review of fluid mechanics, Vol.8, pp.209-231.1976.

[2] Kato et al. "Laser Doppler velocimetry". US Patent No. 5 587 785. 1996.

[3] Prasad, A.K.. "Particle Image Velocimetry". Current science, Vol.79, (1), pp.51-60. 2000.

[4] Foucault et al. "Unsteady flow meter". US Patent No. 7 519 483 B2. 2009.

[5] Kojima, E., Shinada, M.. "Development of an active attenuator for pressure pulsation in liquid piping systems," JSME International Journal, Series Ⅱ, Vol.34, pp.466-473, 1991.

[6] Peube et al. "Method and apparatus for measuring unsteady flow velocity". US Patent No. 5 493 512. 1996.

[7] Wylie, E.B. and Streeter, V.L., "Fluid Transients in Systems", Prentice-Hall Inc., USA, 1993

[8] Vitkóvsky, J., Lambert, M., Simpson, A., and Bergant, A., "Advances in Unsteady Friction Modelling in Transient Pipe Flow," BHR Group Conference on Pressure Surges, Safe Design and Operation of Industrial Pipe Systems, BHR Group Conf. Series, Pub. No. 39, May, Wiley, 2000

[9] Johnston, D.N., "Efficient methods for numerical modelling of laminar friction in fluid lines," Transactions of ASME, Vol .128, pp. 629-634. 2006.

[10] Johnston, D.N. and Drew, J.E., "Measurement of Positive Displacement Pump Flow Ripple and

Impedance", Proc. Inst. Mech. Engrs pt I, Vol 210, 1996, pp65-74
[11] ISO Standard 10767-1 (1996). "Hydraulic fluid power - determination of pressure ripple levels generated in systems and components. Part 1. Precision method for pumps."
[12] Johnston, D.N. and Edge, K.A., "In-situ measurement of the wavespeed and bulk modulus in hydraulic lines", Proc. Inst. Mech. Engrs, Part I, Vol. 205, 1991, pp191-197

In Preparation

Pan, M, Johnston, D. N and Hillis, A. Active control of pressure pulsation in a switched inertance hydraulic system, *to be submitted to Proceedings of the Institution of Mechanical Engineers, Part I: Journal of Systems and Control Engineering, 2012.*

Pan, M, Johnston, D. N and Hillis, A. 2012. Active control of pressure pulsation in a switched inertance hydraulic system based on a rectangular-wave reference signal, *to be submitted to ASME/Bath FPMC 2012 or DFP 2012.*

Kudzma, S, Pan, M, Johnston, D.N; Plummer, A, Hillis, A.J, Sell, N., A High Flow Fast Switching Valve for Digital Hydraulic Systems. *to be submitted to ASME/Bath FPMC 2012*.

Johnston, D.N, Pan, M, Wang, F.P, Kudzma, S, Use of pipeline wave propagation model for measuring unsteady flowrate in piping systems. *to be submitted to ASME Journal of Fluids Engineering.*